198038

NHTSA-98-3588

Evaluation of Motor Vehicle Fire Initiation and Propagation
Part 10: Propagation of a Mid-Underbody Gasoline Pool Fire in a 1998 Sport Utility Vehicle

NHTSA-98-3588-189

Jeffrey Santrock
General Motors Corporation

ABSTRACT

This report describes a vehicle fire propagation test conducted pursuant to an agreement between GM and the United States Department of Transportation. This fire test was conducted on June 11, 1998. The test vehicle was a crash-tested 1998 Ford Explorer. In the crash test, this vehicle was stationary and was struck in the left front (driver's side) by a moving barrier. The fuel tank in the test vehicle was punctured by the drive shaft during the crash test. Fluid was observed leaking from the fuel tank onto the ground under the test vehicle after impact. No fire was observed during this crash test, nor was evidence of fire present in the test vehicle detected during an inspection of the test vehicle after the crash test. An artificial method of creating an underbody gasoline pool was used in this test. Gasoline was pumped continuously during this test from an external reservoir onto the ground under the test vehicle to simulate the leaking fluid that was observed after the crash test. The gasoline was ignited with a propane torch and allowed to burn until flames were observed spreading across the headlining panel in the test vehicle. Flames entered the passenger compartment through drain holes and electrical pass-through openings in the floor panel. Fire suppression began at approximately 250 seconds after the gasoline was ignited.

DEPT. OF TRANSPORTATION
DOCKETS
02 OCT 22 AM 12: 10

Table of Contents

Appendicies

List of Figures

Report

List of Figures

Appendicles

List of Tables

Report

List of Tables

Appendicies

1 Introduction and Test Summary

The work described in this report was conducted by General Motors (GM) pursuant to an agreement between GM and the United states Department of Transportation. According to this agreement, GM and the National Highway Traffic Safety Administration (NHTSA) jointly developed fifteen separate vehicle fire safety research projects. One of these projects, entitled "Fire Initiation and Propagation Tests", involves conducting 1) vehicle crash tests to investigate potential ignition events that occur in vehicle crashes, and 2) subsequent vehicle fire tests to characterize fire propagation in these crash-tested vehicles. The vehicle models to be tested, and the crash- and fire-test methods to be used for Project B.3 are described in another report [1]. The objectives of the fire tests are:

- To determine the principal fire paths and time-lines for flame propagation into the passenger compartment under the test conditions;
- To identify which components burn and to measure the thermal environments around those components associated with their ignition under the test conditions; and
- To measure air temperatures, heat fluxes, and combustion gas concentrations in the passenger compartment under the test conditions.

These tests were conducted under carefully designed test conditions noted throughout this and other reports. They cannot be relied upon to predict the specific nature and characteristics of actual post-collision fires in the field.

The test vehicle was a 1997 Ford Explorer (VIN: 1FMDU34X4VUB02606). The test vehicle was crash tested on July 30, 1997 at the General Motors Proving Ground in Milford, Michigan [2]. In the crash test, this vehicle was stationary and was struck in the left front (driver's side) by a moving barrier. The moving barrier had a deformable aluminum honeycomb face as described in FMVSS214 [3]. The test vehicle was parked with the brakes on and positioned at a 23 ± 2° angle relative to the velocity vector of the moving barrier. The barrier face struck the front left corner of the test vehicle. The mass of the test vehicle was 2232 kg (4,921 lbs.). The mass of the barrier was 1638 kg (3611 lbs.). The barrier speed was 104.4 km/h (64.9 mph). The change in velocity of the test vehicle was 45 kmh (28 mph) in the direction of the barrier's initial longitudinal axis. The maximum velocity change occurred approximately 60 msec after impact. A more detailed description of this test can be found in another report [2].

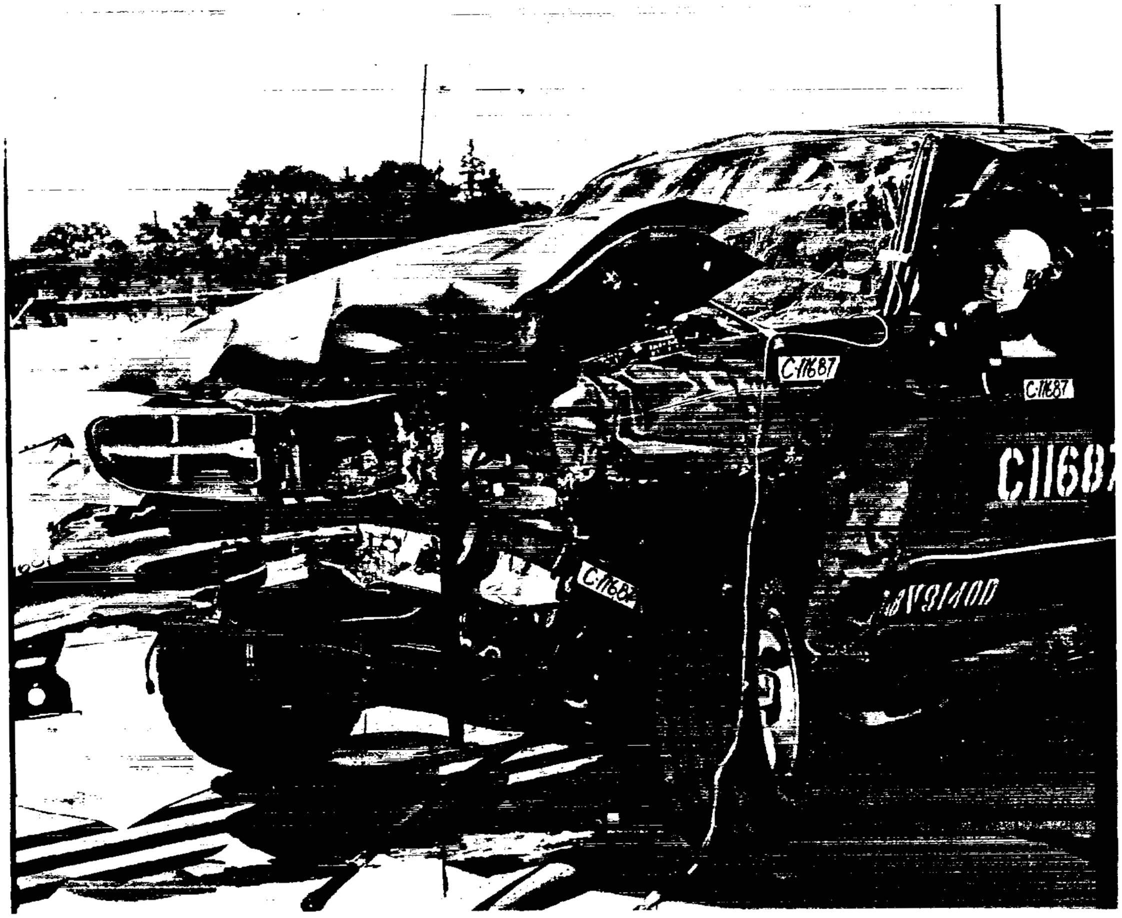

Figure 1. Fire Test F980611. Photograph of the test vehicle after the crash test.

Figure 1 is a photograph of the test vehicle after the crash test. The residual crush to the test vehicle was 730 mm on the left side of the test vehicle and 85 mm on the right side of the test vehicle. Both glass outer layers of the windshield were broken during this crash test, and the windshield remained attached to the test vehicle after this crash test (Fig. 1). The driver's door window was lowered during this crash test and could not be raised after this crash test because of crash-induced deformation of the door (Fig. 1). The hood outer panel separated from the hood inner panel during this crash test (Fig. 1). The front compartment floor pan panel and forward section of the roof (Fig. 1) were displaced and deformed during this crash test.

The fuel tank of the test vehicle was punctured by the universal joint connecting the rear propulsion shaft to the transfer case [2]. Figure 2 is a photograph of the front in board corner of the fuel tank removed from the test vehicle. The hole in the tank is outlined in yellow paint.

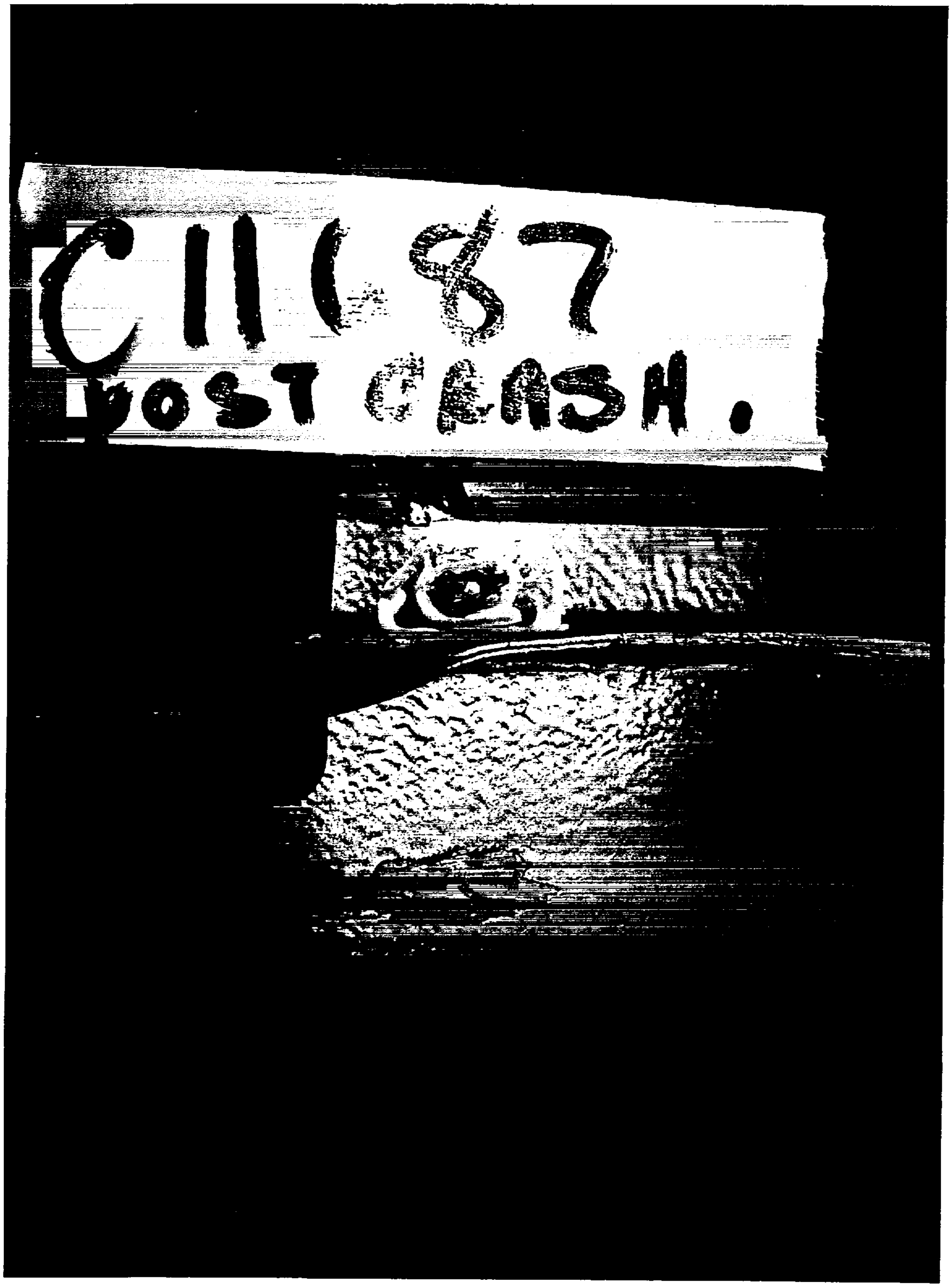

Figure 2. Fire Test F980611. Photograph of the front inboard (right) corner of the fuel tank removed from the test vehicle after the crash test.

Potential fire paths into the occupant compartment for an underbody gasoline fire with gasoline leaking from the hole in the front inboard corner of the fuel tank (Fig. 2) identified during inspection of the test vehicle after the crash test included electrical pass-throughs under the left front seat (Fig. 3), crash-induced openings around the deformed shift lever pass-through cover plate (Fig. 4), drain hole plugs in the floor panel, and crash-induced gaps between the bottoms of the left doors and door sills (Fig. 5). Thermocouples were installed at each of the these locations to aid in determining the fire propagation pathways into the passenger compartment during this fire test and the timing of flame-spread through each pathway. Figure 3 is a photograph of 2 electrical pass-throughs in the floor panel under the left front seat after the crash test. The pass-through closures (grommets) were EPDM. One of these electrical pass-throughs pulled out during the crash test, and is outlined with yellow paint. Figure 4 is a photograph of the deformed shift lever pass-through cover plate in the floor panel under the floor console. Openings around the cover plate are outlined with yellow paint. Figure 6 is a photograph of the front left side of the test vehicle after the crash test. Deformation of the door and vehicle structure during the crash test resulted in gaps between the bottom of the door and door sill, and between the back of the door and the latch pillar.

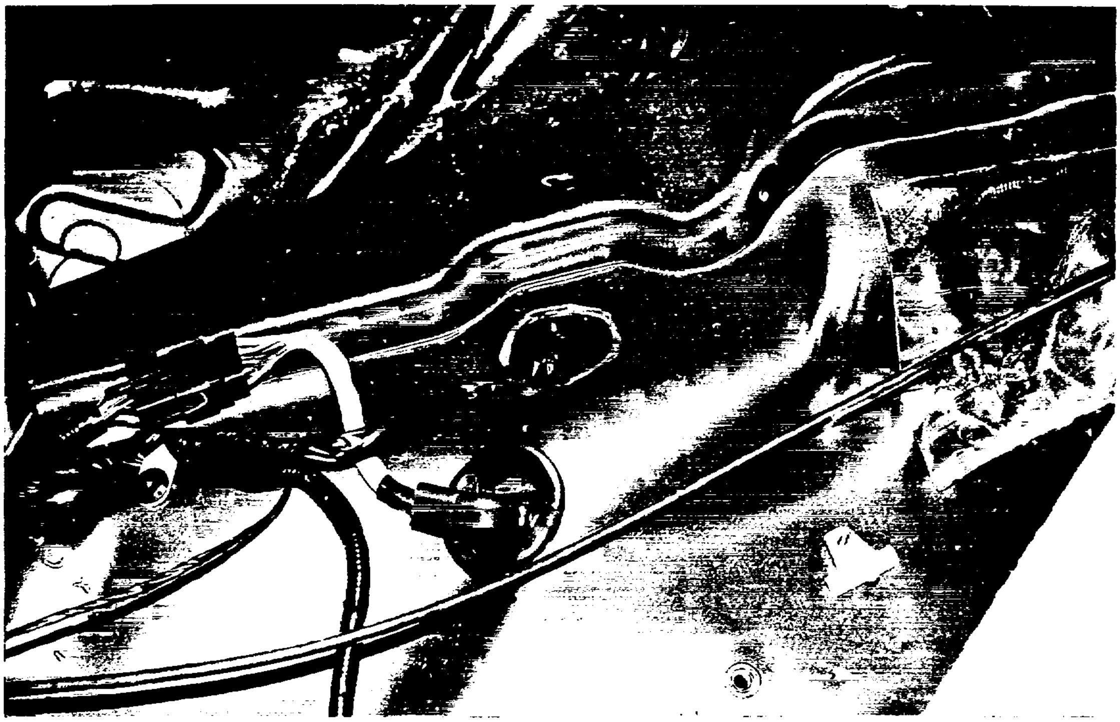

Figure 3. Fire Test F980611. Photograph of the area of the floor pan under the right front seat. A wire pass-through that was dislodged during the crash test is outlined with yellow paint.

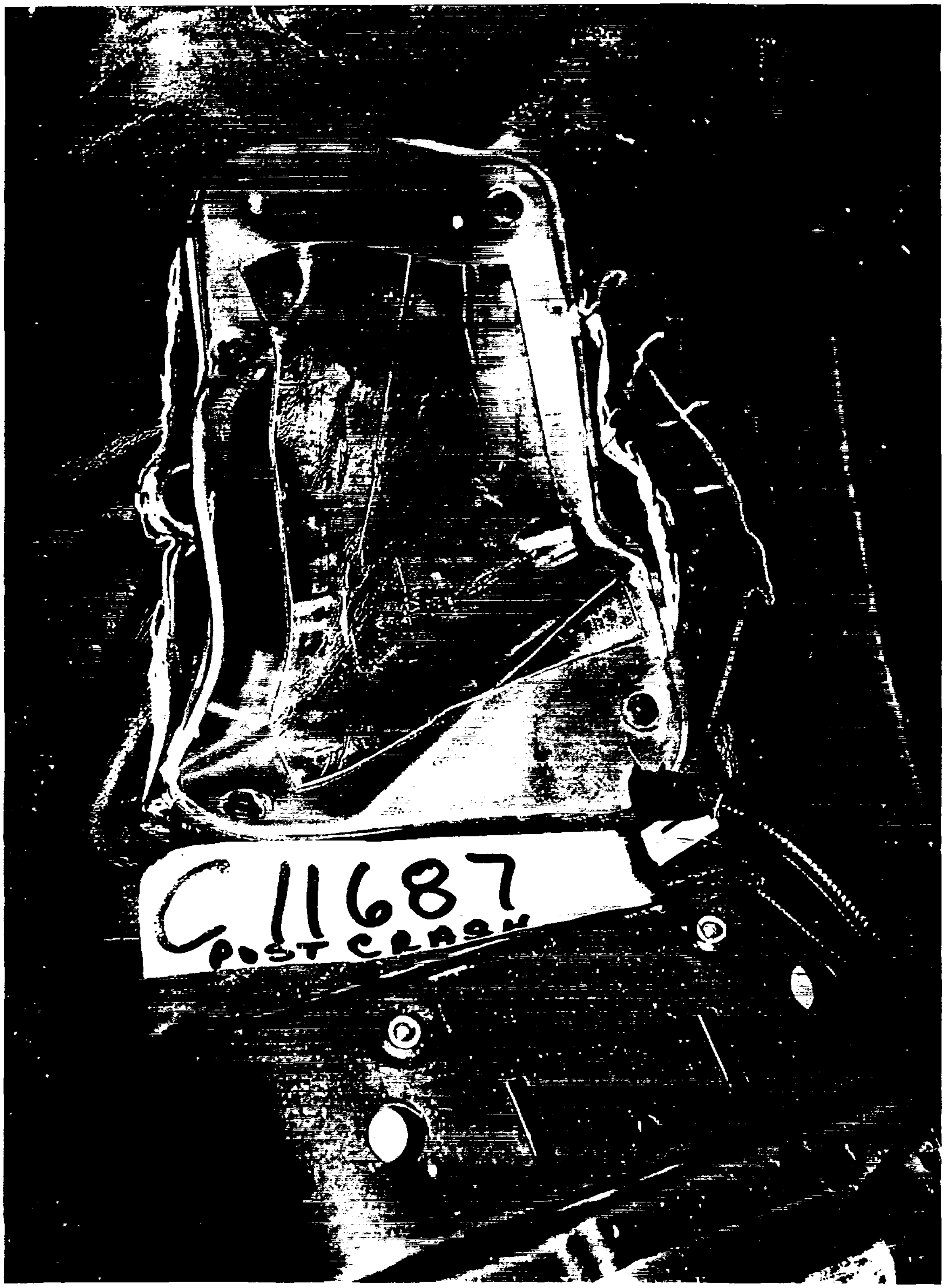

Figure 4. Fire Test F980611. Photograph of the shift lever pass-through cover plate in the floor panel of the test vehicles after the crash test. Openings around the cover plate are outlined with yellow paint.

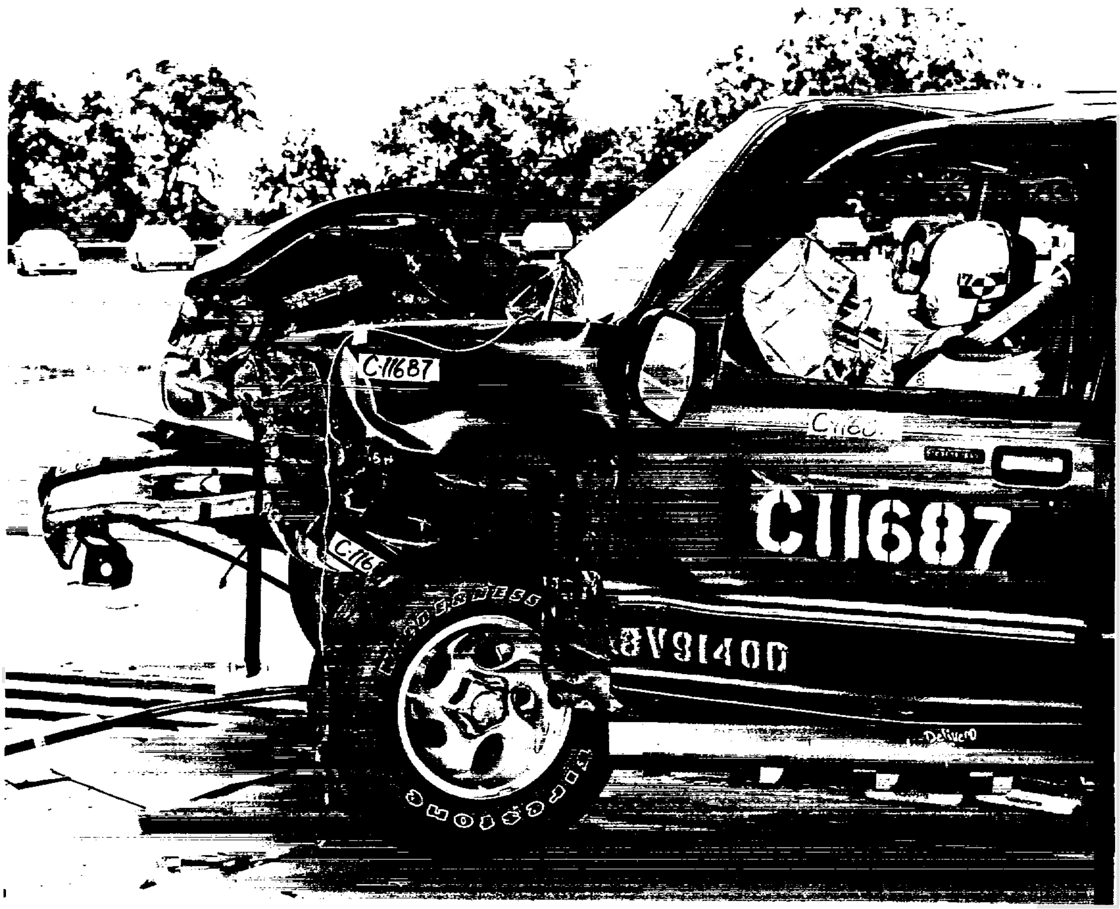

Figure 5. Fire Test F980611. Photograph of the front left side of the test vehicle after the crash test.

The fire test described in this report was conducted on June 11, 1998 at the Factory Mutual Test Center in West Glocester, Rhode Island. The fire test was designed to study propagation of an under-body gasoline pool fire into the passenger compartment. Table 1 summarizes the timing of flame-spread into the passenger compartment during this test.

The method of creating an underbody gasoline pool used in this test simulated the leak that was observed during the vehicle crash test. A modified service parts fuel tank was installed in the test vehicle for this fire test. The modified fuel tank contained a section of stainless steel tubing with the outlet on the front inboard side of the tank (see **APPENDIX A**). Gasoline was pumped continuously from an external reservoir during this test. Liquid gasoline flowing from the outlet of the tubing pooled in the fuel tank skid plate under the fuel tank and dripped onto the cement board surface of the fluid containment pan. The gasoline was ignited with a propane torch and allowed to burn until flames were observed inside the passenger compartment of the test vehicle. Flames entered the passenger compartment through the electrical pass-throughs in the floor panel under the left front seat and through drain holes in the floor panel. Conductive heating through the floor panel resulted in ignition of sections of the floor carpeting in the passenger compartment. Fire suppression began at approximately 250 seconds after the gasoline was ignited. A water mist was used to extinguish the flames after the flow of gasoline was stopped.

Table 1
Summary of Fire Development during in Fire Test F980611

Time[1] (sec)	**Event**
-28	Start of gasoline flow
0	Gasoline under the test vehicle was ignited using a propane torch
10	Flames enter passenger compartment through electrical pass-through opening in floor panel under left front seat
75	Flames burn through grommet in second electrical pass-through opening in floor panel under left front seat
130	Flames burn through floor carpet above electrical pass-through opening under left front seat
205	Flames burn through floor carpet above second electrical pass-through opening in floor panel under left front seat
235 - 250	Flames burn through top of left front seat cushion
250 - 260	End of test and beginning of fire suppression

[1] Time after ignition of the gasoline pool.

2 Vehicle Condition and Test Protocol

The crash-tested vehicle was prepared for the fire tests at the General Motors Research and Development Center (GM R&D Center) in Warren, Michigan, and shipped to the Factory Mutual Test Center in West Glocester, Rhode Island where this fire test was conducted. The test vehicle was returned to the GM R&D Center after the fire test, where it was systematically disassembled to permit closer inspection of the fire damage and identification of flame-spread paths into the passenger compartment that were not obvious from observations made during this fire test.

Descriptions of the measurement of the flow rate of fuel from the fuel tank in the test vehicle during the crash test and modifications to a service parts fuel tank installed in the test vehicle for this fire test are in **APPENDIX A**. A description of the video cameras used in during this test is in **APPENDIX B**. A description of the infrared cameras used in this test is in **APPENDIX C**. A description of the thermocouples installed in the test vehicle and data from these thermocouples are in **APPENDIX D**. A description of the aspirated thermocouples used in this test and data from these aspirated thermocouples are in **APPENDIX E**. A description of the heat flux transducer/radiometer assemblies installed in the test vehicle and data from these devices are in **APPENDIX F**. Description of the pressure and airflow measurement equipment and analysis procedures, and data from these measurements are in **APPENDIX G**. Description of the Fire Products Collector (FPC) at the Factory Mutual Global Test Center and analysis procedures, and data from this device are in **APPENDIX H**. A description of the Fourier Transform Infrared Gas Analysis System used during this test and results from this device are in **APPENDIX I**. Descriptions of the Gas Chromatography/Mass Spectrometry equipment and analysis procedures, and the results of these analyses are in **APPENDIX J**. Descriptions of the particulate sampling equipment and analysis procedures, and the results of these analyses are in **APPENDIX K**.

The vehicle was placed in a rectangular steel pan (length = 25 ft., width = 15 ft., height = 4 in.) to prevent spilled and leaking automotive fluids from spreading in the test facility. This fluid containment pan was fabricated from two sheets of carbon steel. Angle-braces were welded to the under-side of the pan to keep it from flexing under the weight of the vehicle. The corners of the support frame rested on load cells. Mass loss was determined from data acquired from the load cells during the test.

A layer of fiberglass-reinforced cement construction board (DuraRock, USG Corporation) was placed on bottom of the fluid containment pan. A thin layer of sand was used to level the concrete board so that the grade of the surface measured from the center to the edges along the major and minor axes was no greater than 1%. The joints between boards were sealed with latex caulking.

The test vehicle was placed in the center of the pan (Fig. 6). All doors were closed. Except for the left front door, the door window glasses were raised to their fully closed position in each door. An air horn was sounded to signal three events during the test: (1) the start of gasoline flow, (2) ignition of the gasoline pool by a propane torch, and (3) the end of the test and start of fire suppression. The air horn was used to synchronize the data acquisition systems used in this test. The air horn was audible on the videotapes and infrared imaging systems. One channel of the data acquisition system for vehicle instrumentation monitored a normally open switch, which was depressed at each sounding. The real-time clock in the FTIR data system was synchronized to the real-time clock in the vehicle instrumentation data system.

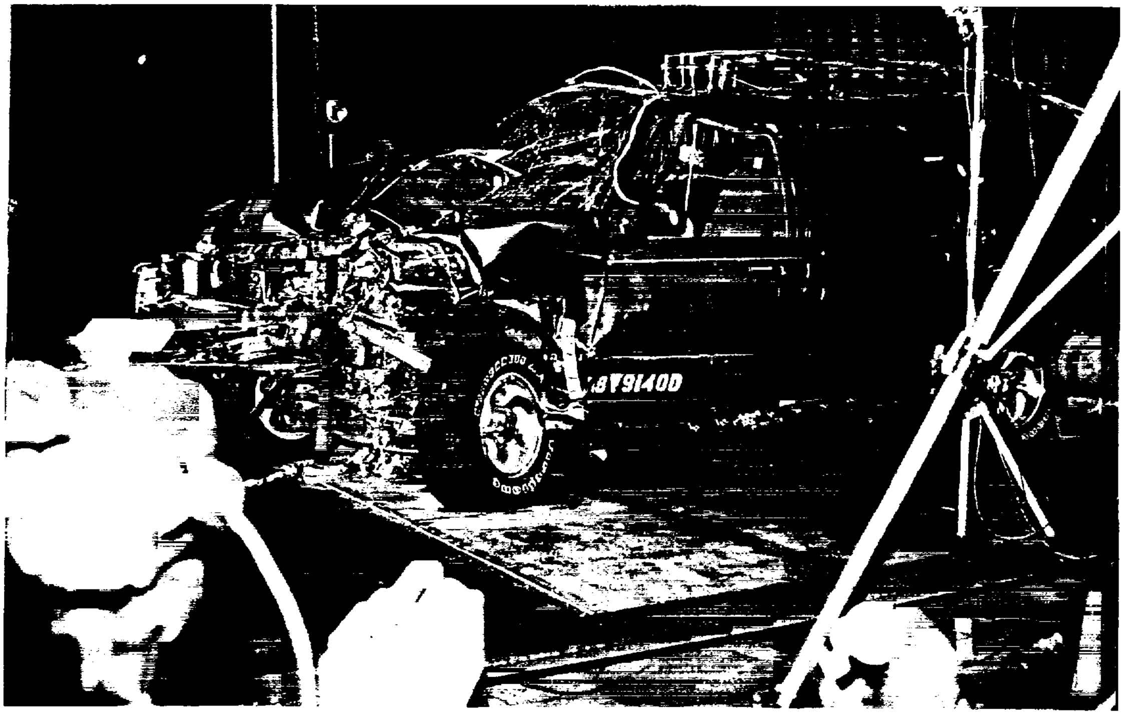

Figure 6. Fire Test F980611. Photograph of the test vehicle in the fluid containment pan before the fire test.

The original fuel tank was removed from the test vehicle after the crash test to measure the fluid flow rate from the hole, and a modified service parts fuel tank was installed in the test vehicle for this fire test. The dispersion and drip patterns of fuel flowing from the outlet of the tubing were similar to the dispersion and drip patterns of fuel flowing from the hole in the original fuel tank after the crash test (**APPENDIX A**). The tubing in the modified service parts fuel tank was connected to a gasoline delivery system for this fire test.

Technical personnel from the Building and Fire Research Laboratory of the National Institutes of Standards and Technologies designed, built, and operated the gasoline delivery system used in this test. Figure 7 shows a schematic diagram of the gasoline delivery system used in this test.

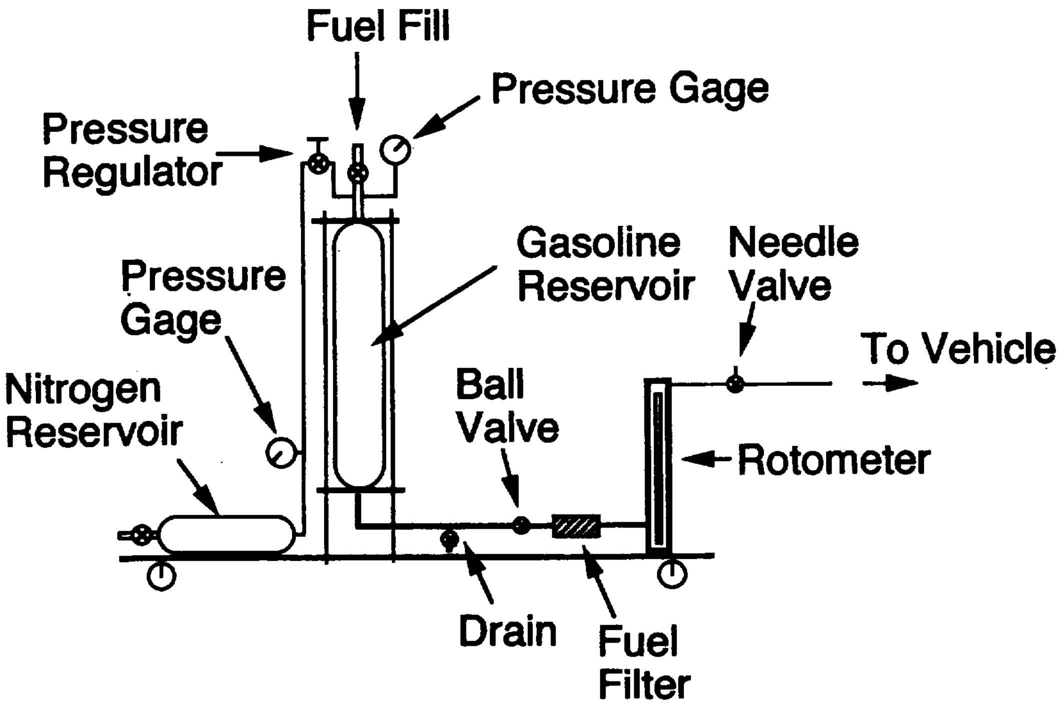

Figure 7. Fire Test F980611. Schematic diagram of the external gasoline reservoir and delivery system used to artificially supply gasoline to the test vehicle during this test.

The gasoline delivery system consisted of two stainless steel cylinders. One cylinder functioned as a fluid reservoir and had a capacity of 4 L, while the other cylinder functioned as a gas reservoir and had a capacity of 2 L. A pressure regulator in the line connecting the gas reservoir to the fluid reservoir controlled the head pressure in the fluid reservoir. The outlet line of the fluid reservoir contained a ball valve that was used to turn on and off the flow of gasoline during the test, a rotometer to indicate the flow of gasoline during the test, and a needle valve to control the flow of gasoline.Gasoline (4 L) was added to a steel fluid reservoir (4 L). The gas reservoir was filled with dry nitrogen gas. The pressure regulator was adjusted to maintain a head pressure of 275 kPa (25.0 psi) in the fluid reservoir. The delivery tube was purged with gasoline before the start of the test to eliminate air.

A valve approximately 3 feet from the outlet of the gasoline delivery tube was mounted near the right front door and opened to start the flow of gasoline during this test. The flow rate of gasoline through the delivery tube was determined from readings taken from the rotometer. The head pressure in the fluid reservoir and ball position in the rotometer was checked at 30 second intervals during the test to determine if the initial flow rate of gasoline had changed. The pressure regulator and needle valve were adjusted as necessary to maintain a constant flow rate of gasoline during the test.

3 Ignition

The valve connecting the gasoline delivery system to the tubing installed in the modified service parts fuel tank in the test vehicle was opened at the start of this fire test. Gasoline began flowing from the outlet of the tubing within 1 to 2 seconds. The needle valve on the gasoline delivery system was adjusted manually at the beginning of this test to give a target flow rate of approximately 300 cm^3/min of gasoline, and adjusted manually periodically during this test to maintain a constant flow rate of gasoline. The actual flow rate achieved during this fire test was 350 ± 10 cm^3/min,[1] which was 50 cm^3/min greater than the target flow rate and 60 to 70 cm^3/min greater than the fluid flow rate from the hole in the original fuel tank in the crash tested vehicle (**Appendix A**).

Gasoline flowed into the fuel tank skid plate and onto the cement board surface under the test vehicle. A propane torch was used to ignite gasoline vapor above the liquid gasoline pool under the test vehicle approximately 28 seconds after the start of gasoline flow. Figures 8 through 11 show a series of video stills from Cameras 1 through 4 at 2 seconds before ignition and about ½ second after ignition. Ignition occurred under the front of the fuel tank near the left side of the test vehicle (lower video stills, Fig.'s 8 through 11). Blue flames (Fig.'s 5 through 8) spread concentrically from the point of ignition through gasoline vapor retained in the bottom of the fluid containment pan[2] after it had vaporized. Flames were observed in the fuel tank skid plate after ignition.

---

[1] A series of measurements was performed after this test to determine the flow rate of gasoline from the delivery system during this test. In this series of measurements, 4 L of gasoline was added to the reservoir and the pressure regulator was adjusted to maintain a head pressure of 275 kPa (25.0 psi) in the fluid reservoir. The rotometer was adjusted to match the readings recorded during the test. The volume flow rate of gasoline from the system was determined by collecting the effluent from the outlet in a graduated cylinder for a measured period of time.

[2] The density of gasoline vapor is between 3 and 4, where $d_{AIR} = 1$ [4].

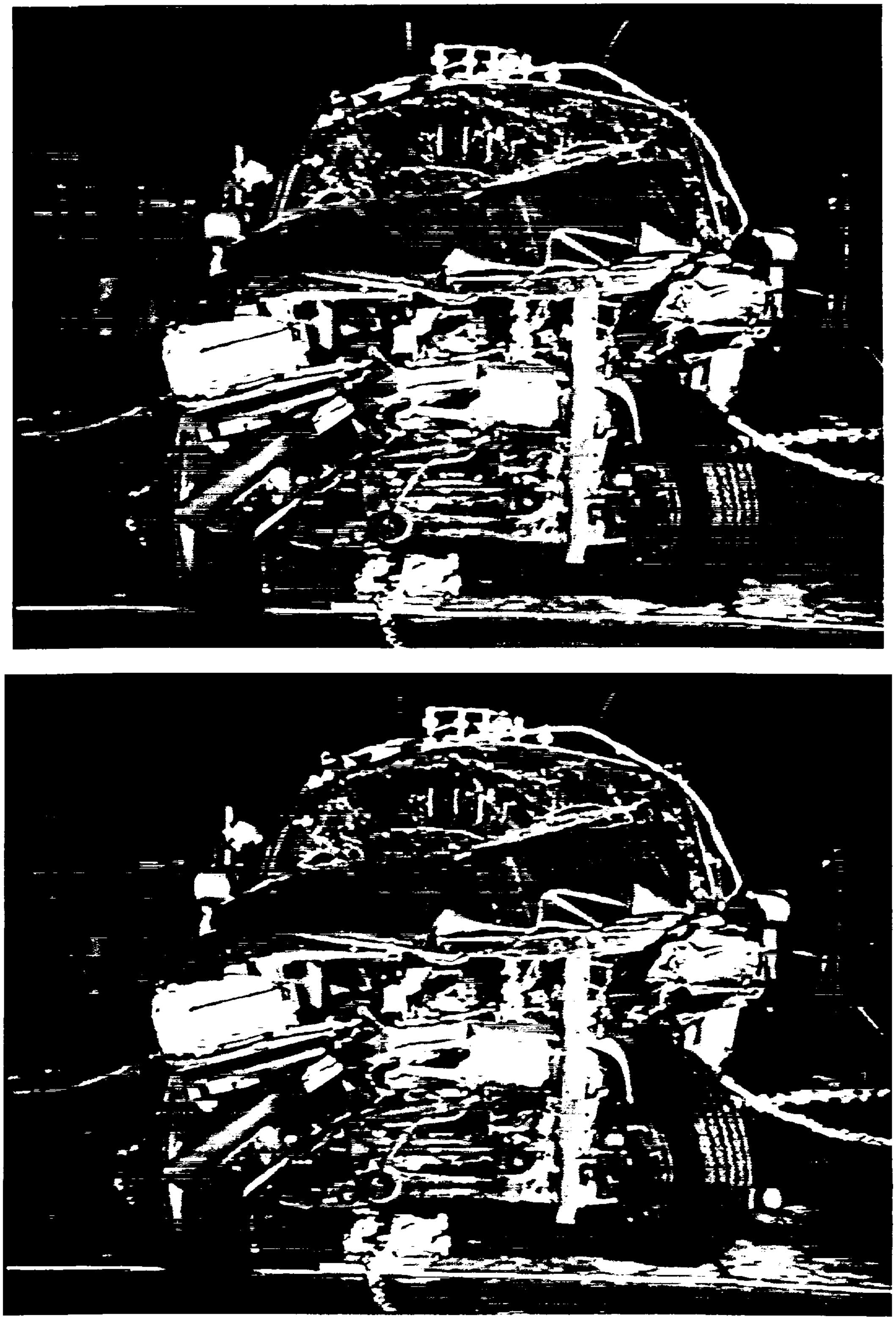

Figure 8. Fire Test F980611. Video stills from Camera 1 at 2 seconds before ignition (upper) and approximately ½ second after ignition (lower).

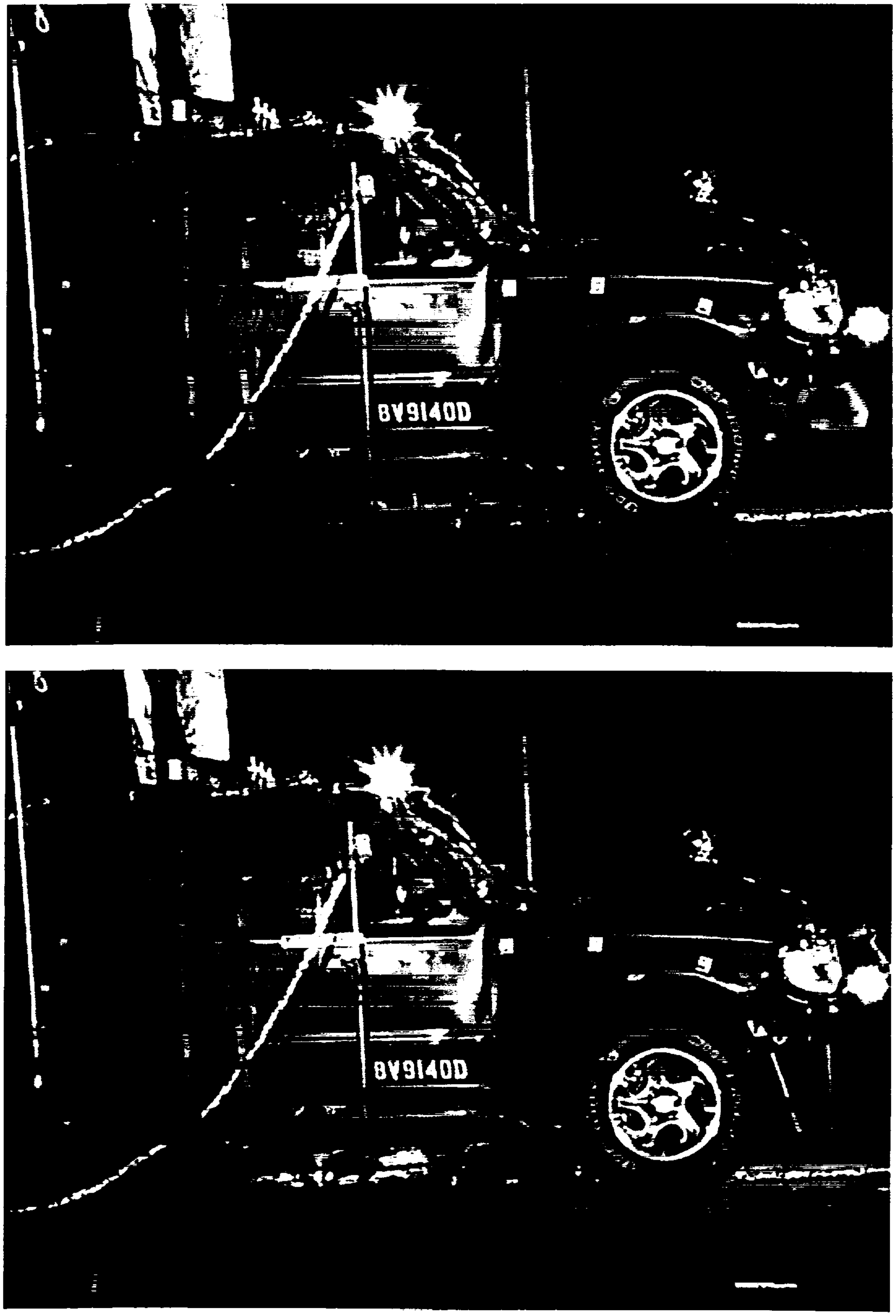

Figure 9. Fire Test F980611. Video stills from Camera 2 at 2 seconds before ignition (upper) and approximately ½ second after ignition (lower).

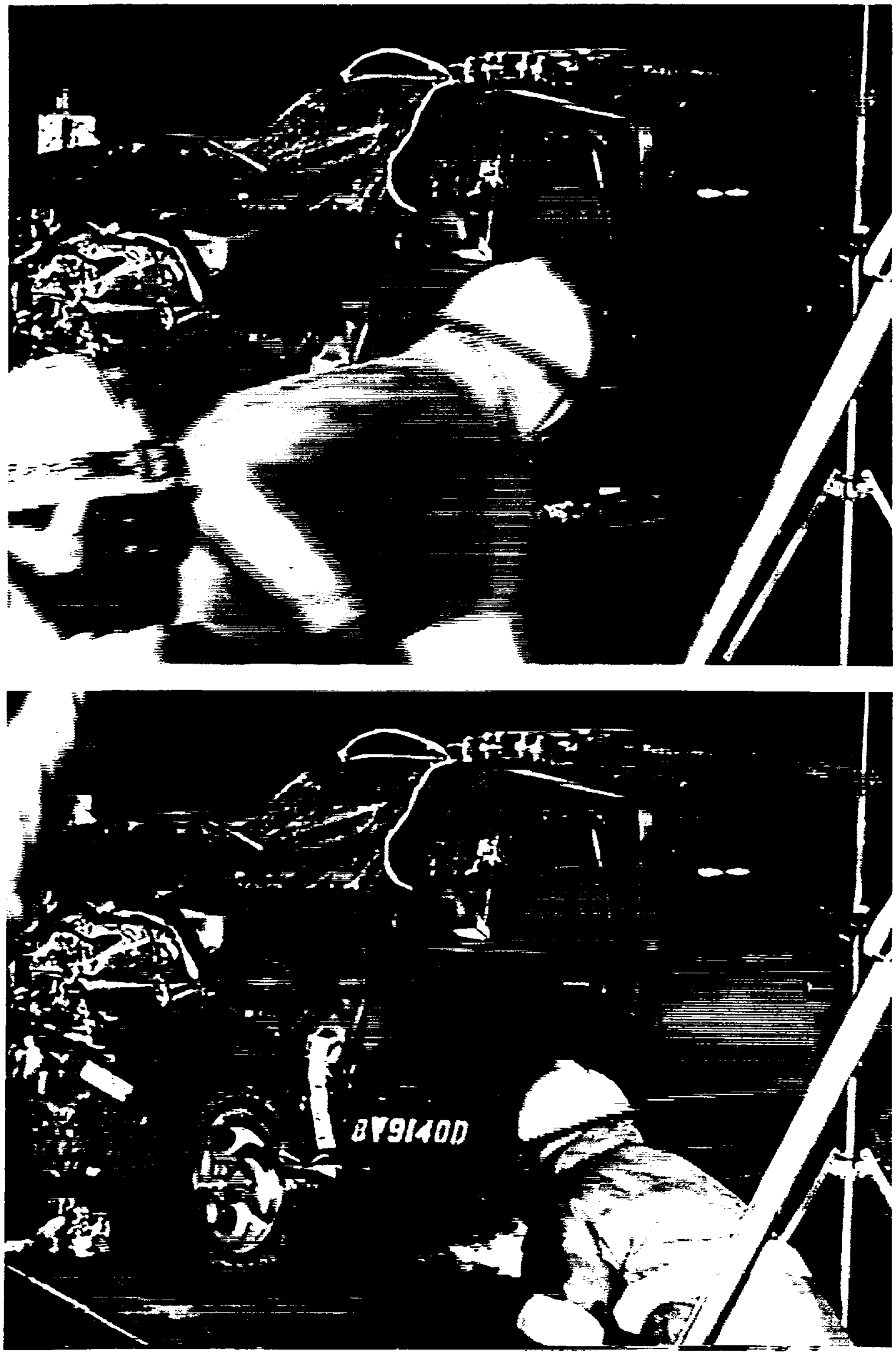

Figure 10. Fire Test F980611. Video stills from Camera 3 at 2 seconds before ignition (upper) and approximately ½ second after ignition (lower).

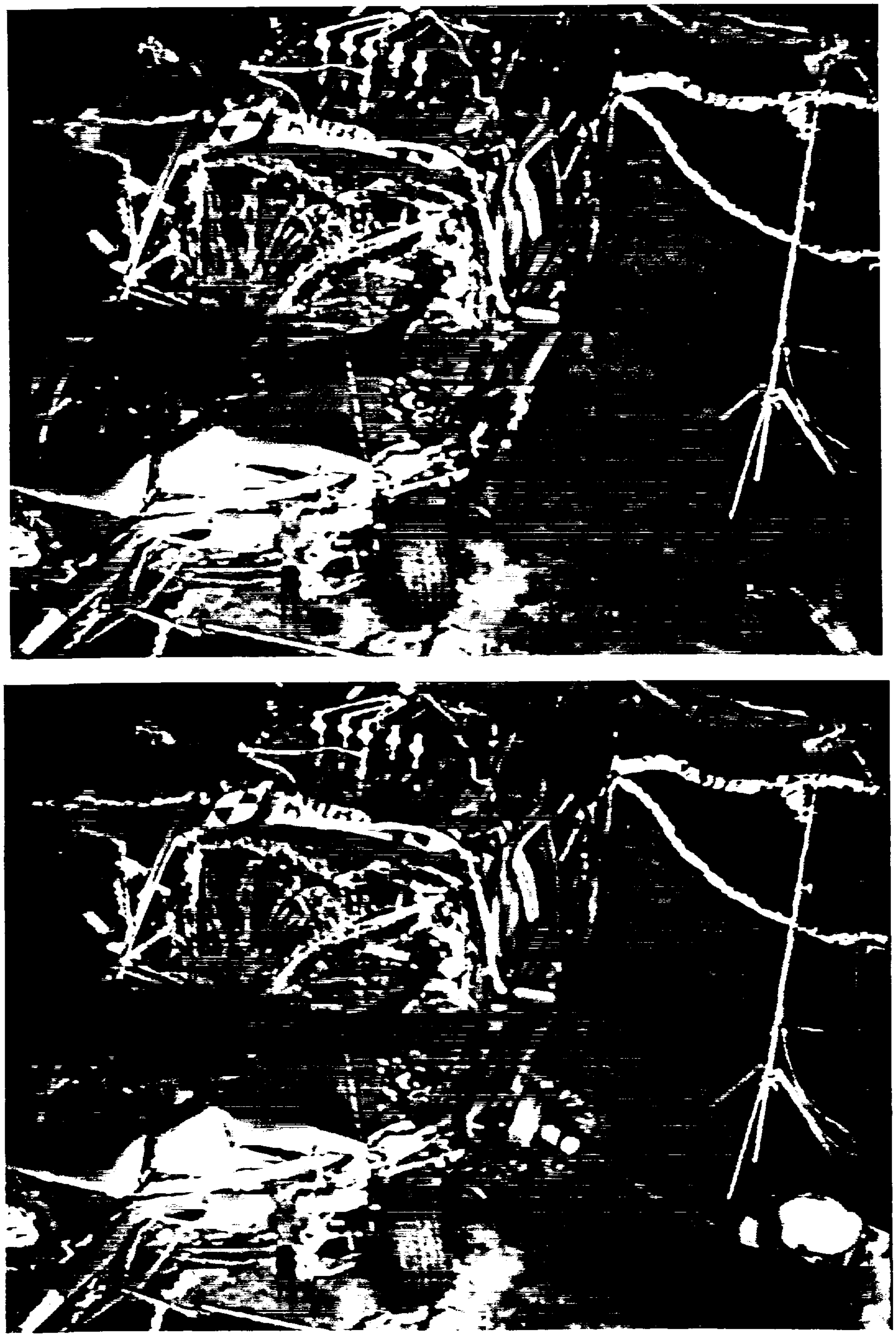

Figure 11. Fire Test F980611. Video stills from Camera 4 at 1 second before ignition (upper) and approximately ½ second after ignition (lower).

4 Behavior of the Underbody Gasoline Pool Fire in this Test

It was not possible to determine accurately the distribution of flames on the test vehicle underbody from the video record or thermocouple data acquired during this test. Gasoline pooled in the fuel tank skid plate and on the cement boards under the fuel tank ignited and burned in this test. Review of the videos from cameras 2 and 3 showed flames from the burning gasoline on the cement boards spreading out along the lower surface of the fuel tank skid plate. None of the video cameras in this test were positioned to view directly the underside of the test vehicle. The number of thermocouples located below the floor panel was not adequate to estimate the temperature distribution, and thus the distribution of flames on the lower surface of the test vehicle. It was therefore not possible to determine the area of the floor panel that was exposed to flames during this test.

Figures 12 through 22 show a series of video stills from Cameras 3 and Infrared thermograms from IR6 at 0, 15, 30, 60, 90, 120, 150, 180, 210, 240, and 243 seconds post-ignition. The diameter of the gasoline pool fire on the cement board under the test vehicle appeared to be about 15 inches in diameter[3] from the time of ignition through 30 seconds post-ignition (video stills, Fig.'s 12 through 14). Flames from the burning gasoline on the cement board surface appeared to contact and spread along the lower surface of the fuel tank skid plate (video stills, Fig.'s 12 through 14). The diameter of the gasoline pool and the height of the flames above the gasoline pool decreased between 30 and 243 seconds post-ignition (Fig.'s 15 through 22). This observed behavior suggests that the rate of consumption of liquid gasoline in the fuel tank skid plate by fire was greater than the flow rate of liquid gasoline onto the skid plate, resulting in a decrease in the flow of liquid gasoline out of the fuel tank skid plat onto the cement board surface under the test vehicle. By 210 seconds post-ignition, the size of the burning gasoline pool on the cement board surface decreased substantially (video still, Fig. 20). Flames from burning gasoline on the cement board surface did not appear to reach the lower surface of the fuel tank skin plate at this time (video still, Fig. 20).

The video stills and infrared thermograms in Figures 12 through 22 show that smoke and heated gases produced by the burning gasoline under the test vehicle flowed into and out of the engine compartment along the rear and left edges of the deformed hood. Flames were not visible in the engine compartment at any time during this test (Fig.'s 12 through 22).

---

[3] The diameter of the gasoline pool on the cement board under the front of the fuel tank was estimated by comparison to the left front wheel (diameter = 15 in.).

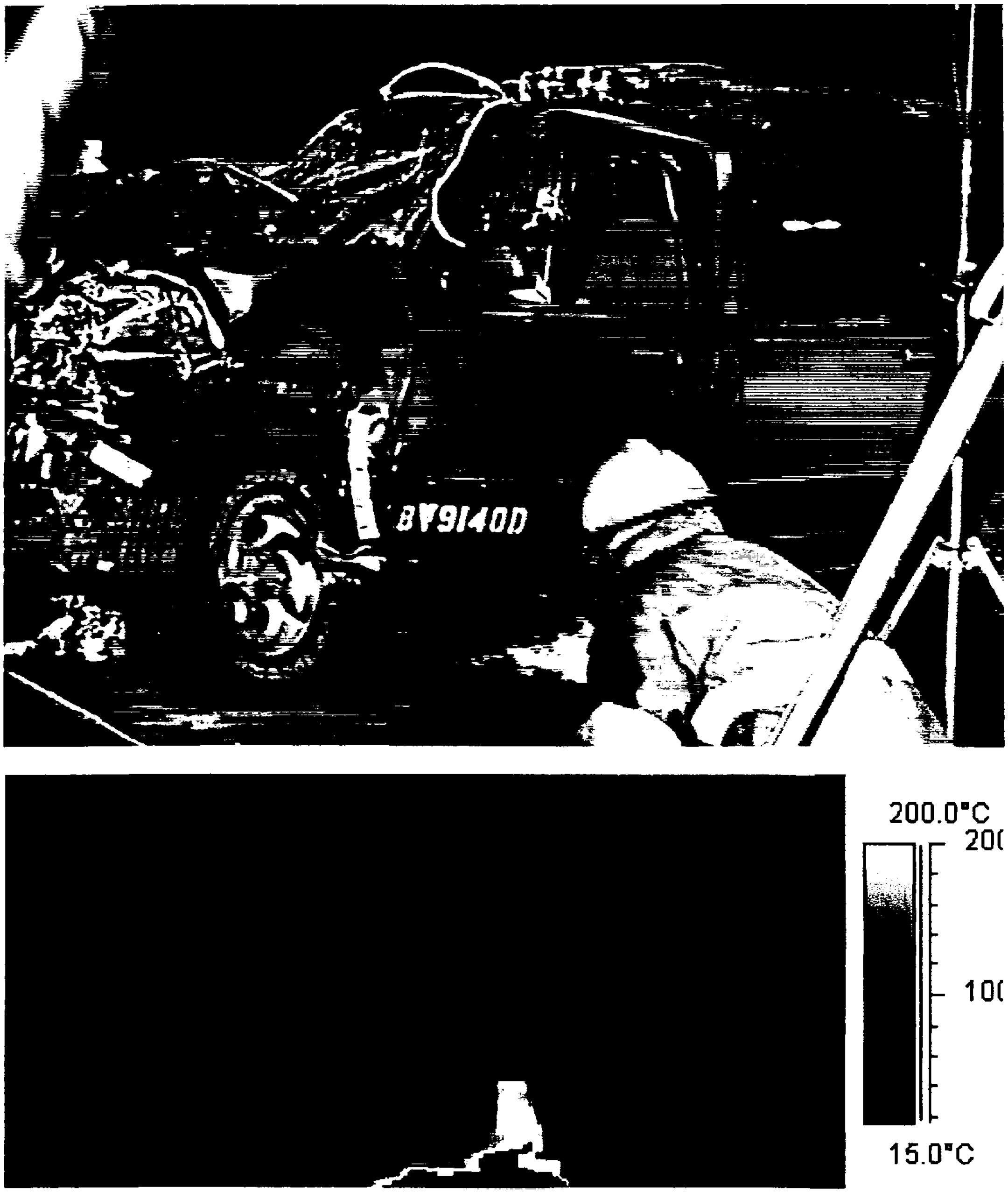

Figure 12. Fire Test F980611. Video still from Video Camera 3 (upper) and Infrared thermogram from IR6 (lower) at the time of ignition (0 seconds post-ignition).

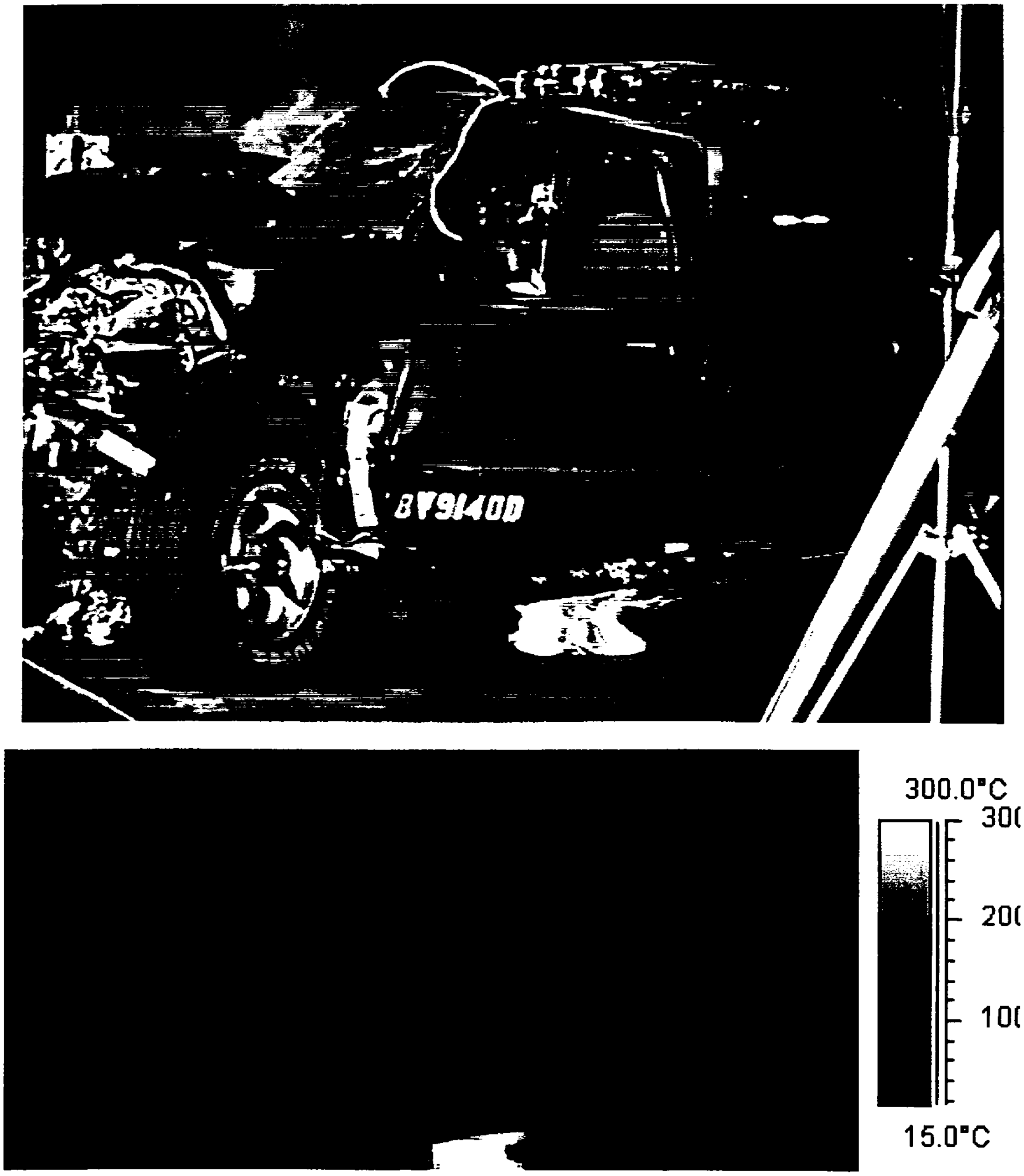

Figure 13. Fire Test F980611. Video still from Video Camera 3 (upper) and Infrared thermogram from IR6 (lower) at 15 seconds post-ignition.

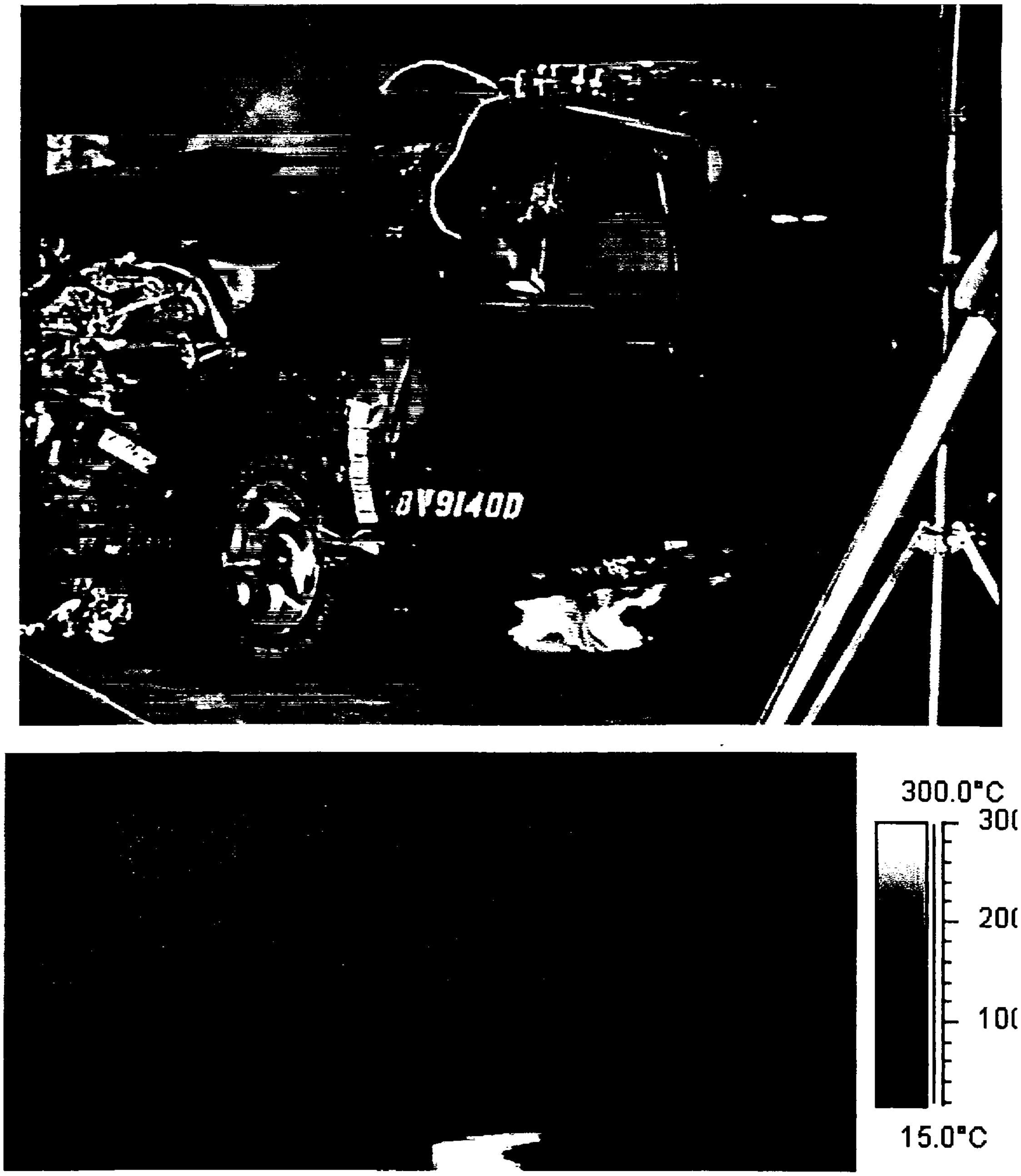

Figure 14. Fire Test F980611. Video still from Video Camera 3 (upper) and Infrared thermogram from IR6 (lower) at 30 seconds post-ignition.

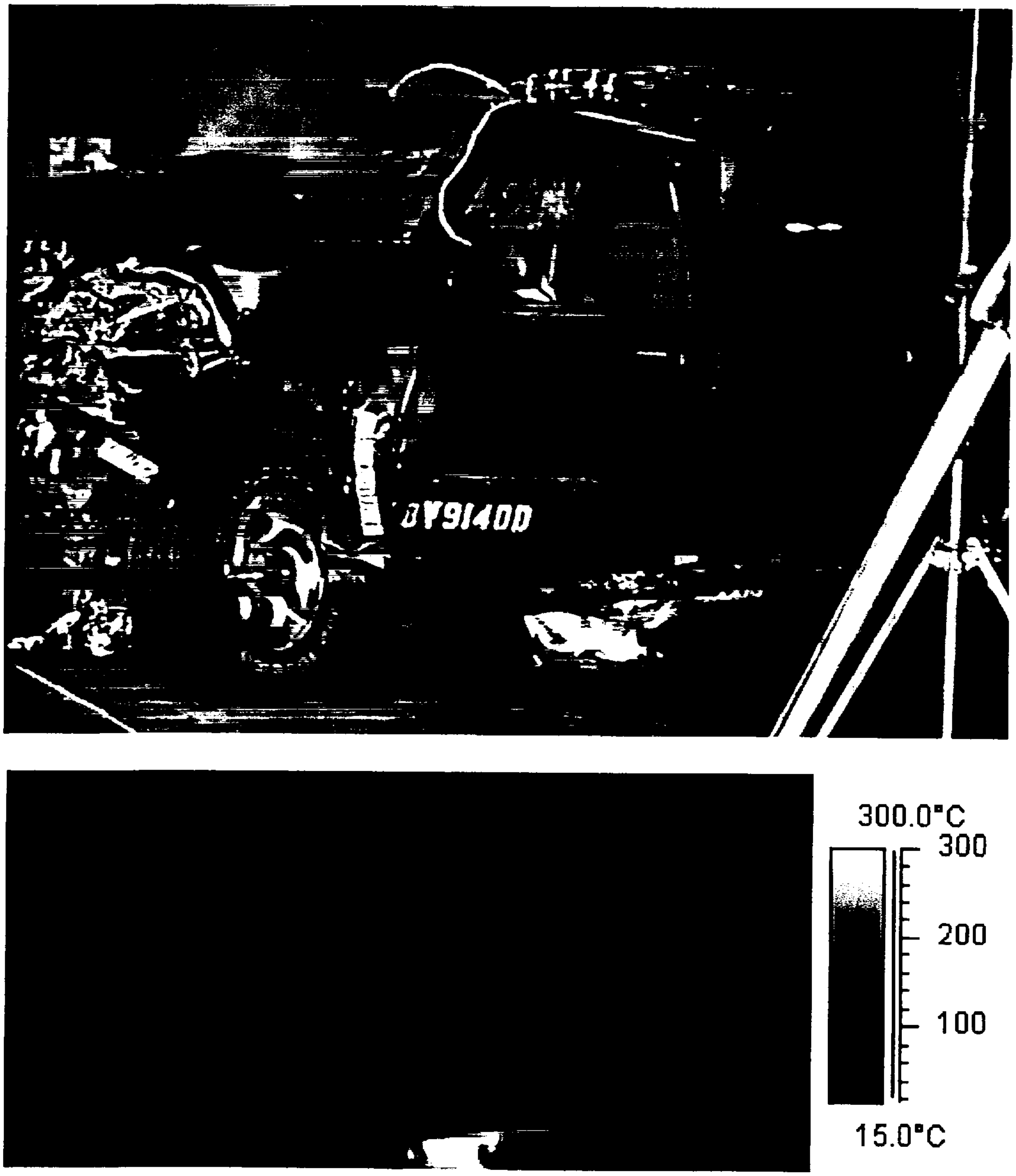

Figure 15. Fire Test F980611. Video still from Video Camera 3 (upper) and Infrared thermogram from IR6 (lower) at 60 seconds post-ignition.

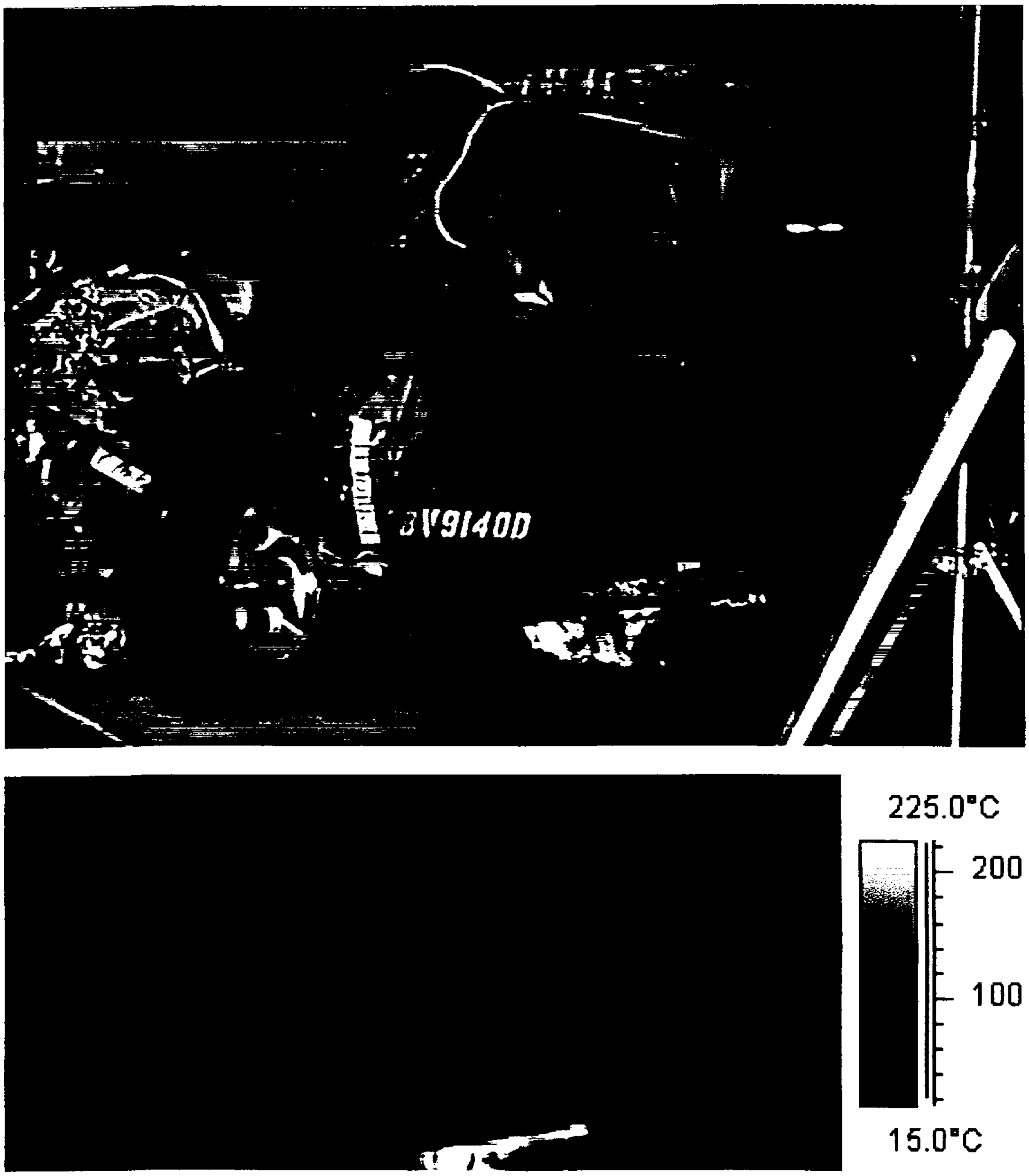

Figure 16. Fire Test F980611. Video still from Video Camera 3 (upper) and Infrared thermogram from IR6 (lower) at 90 seconds post-ignition.

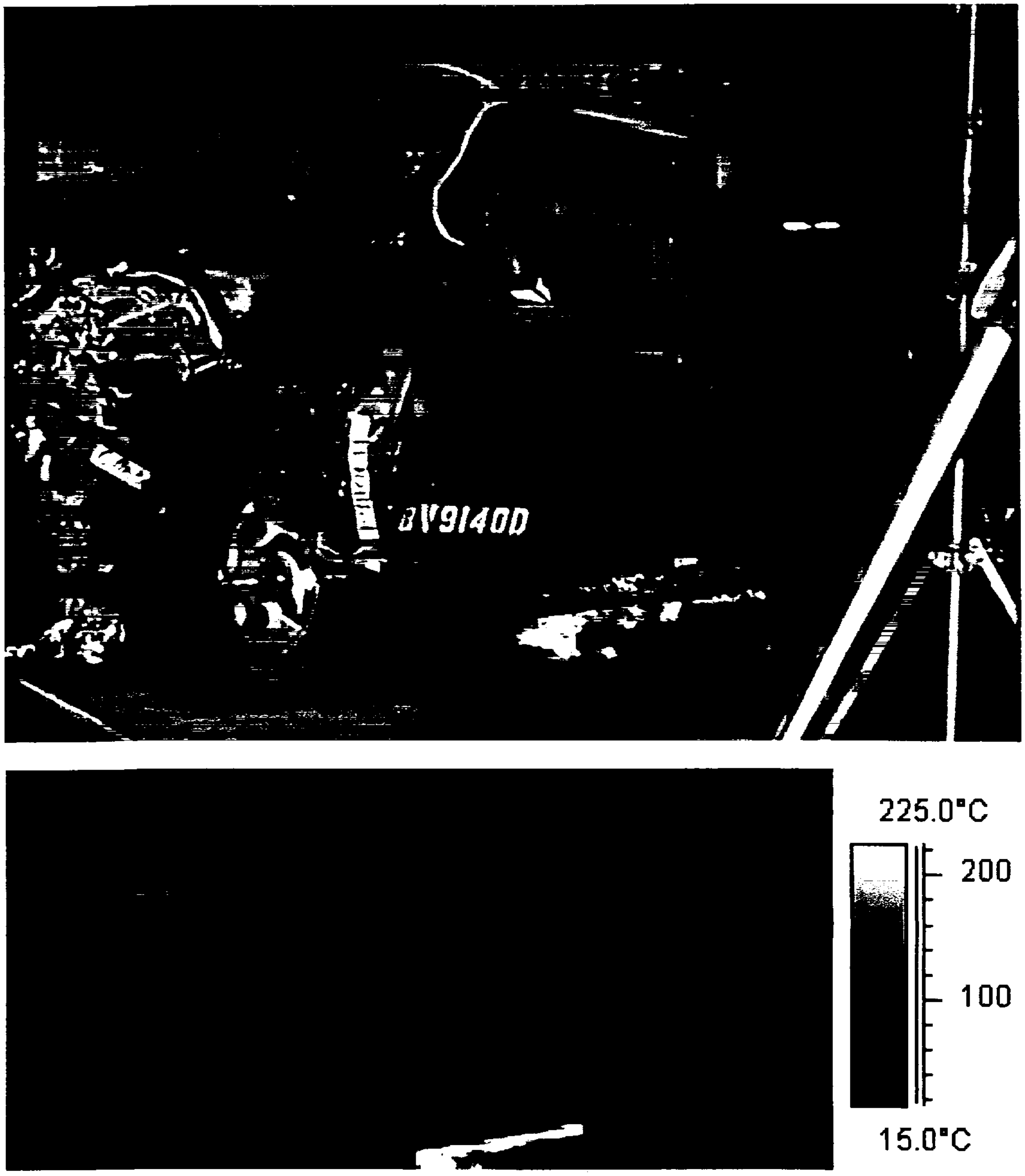

Figure 17. Fire Test F980611. Video still from Video Camera 3 (upper) and Infrared thermogram from IR6 (lower) at 120 seconds post-ignition.

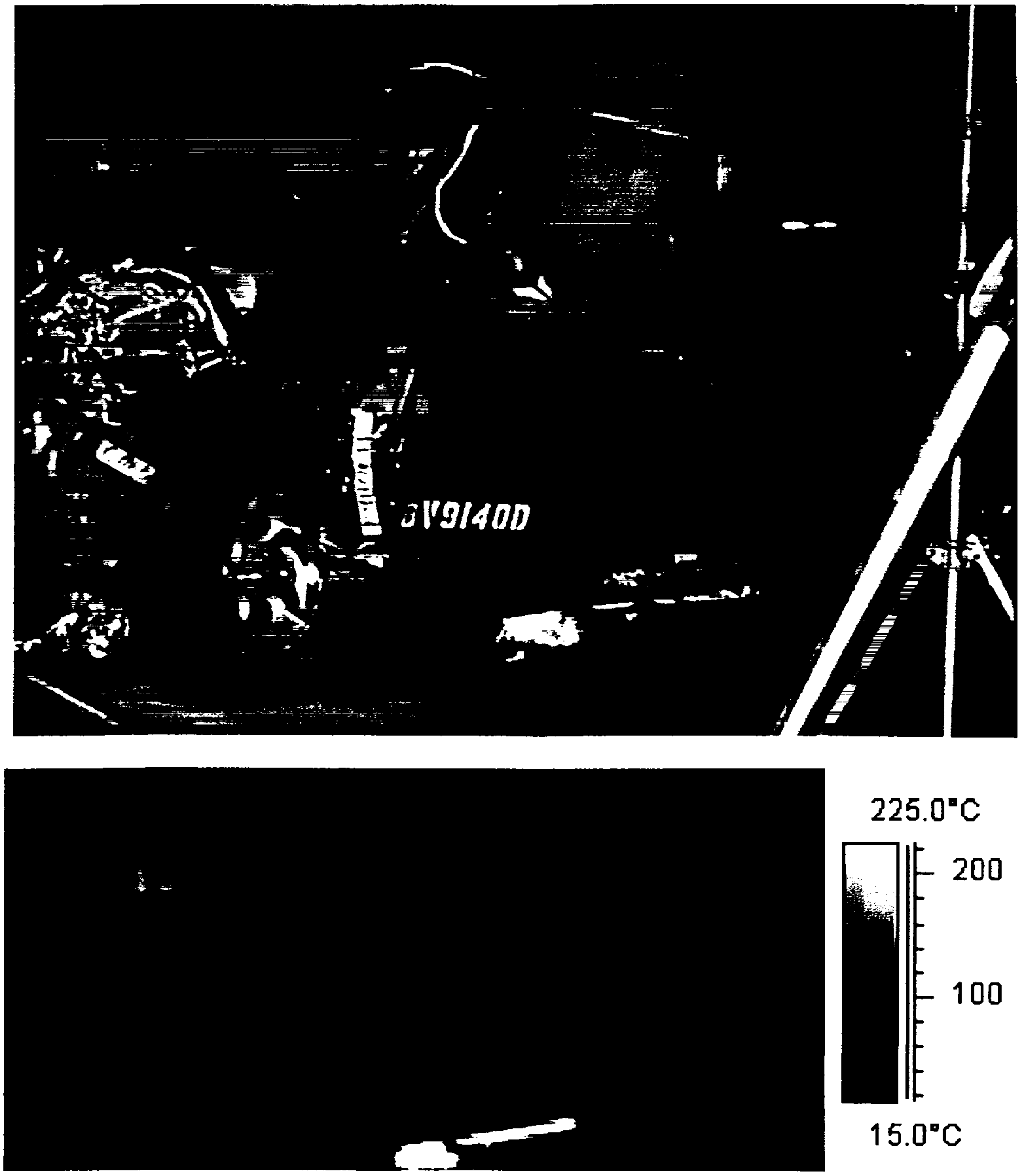

Figure 18. Fire Test F980611. Video still from Video Camera 3 (upper) and Infrared thermogram from IR6 (lower) at 150 seconds post-ignition.

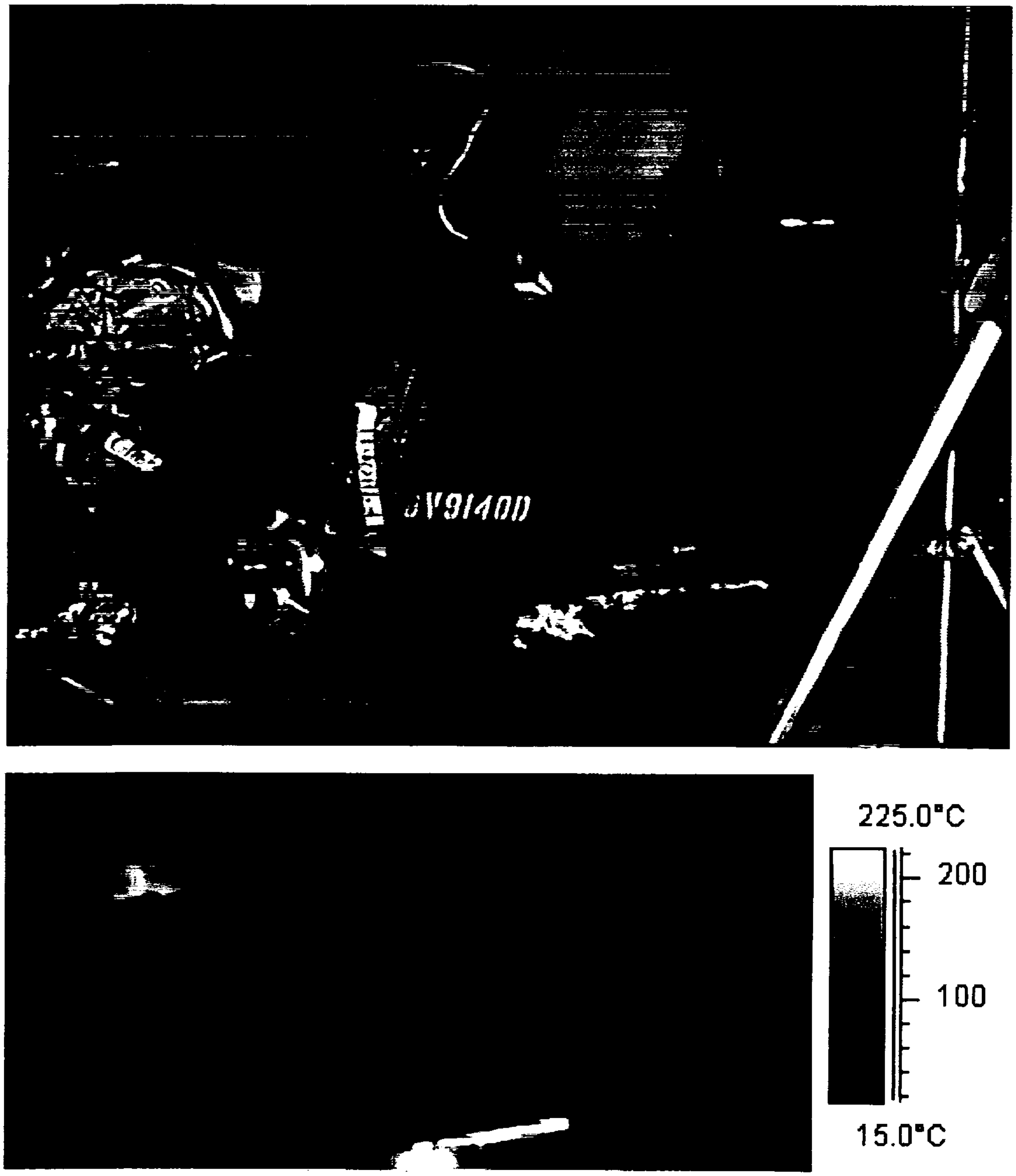

Figure 19. Fire Test F980611. Video still from Video Camera 3 (upper) and Infrared thermogram from IR6 (lower) at 180 seconds post-ignition.

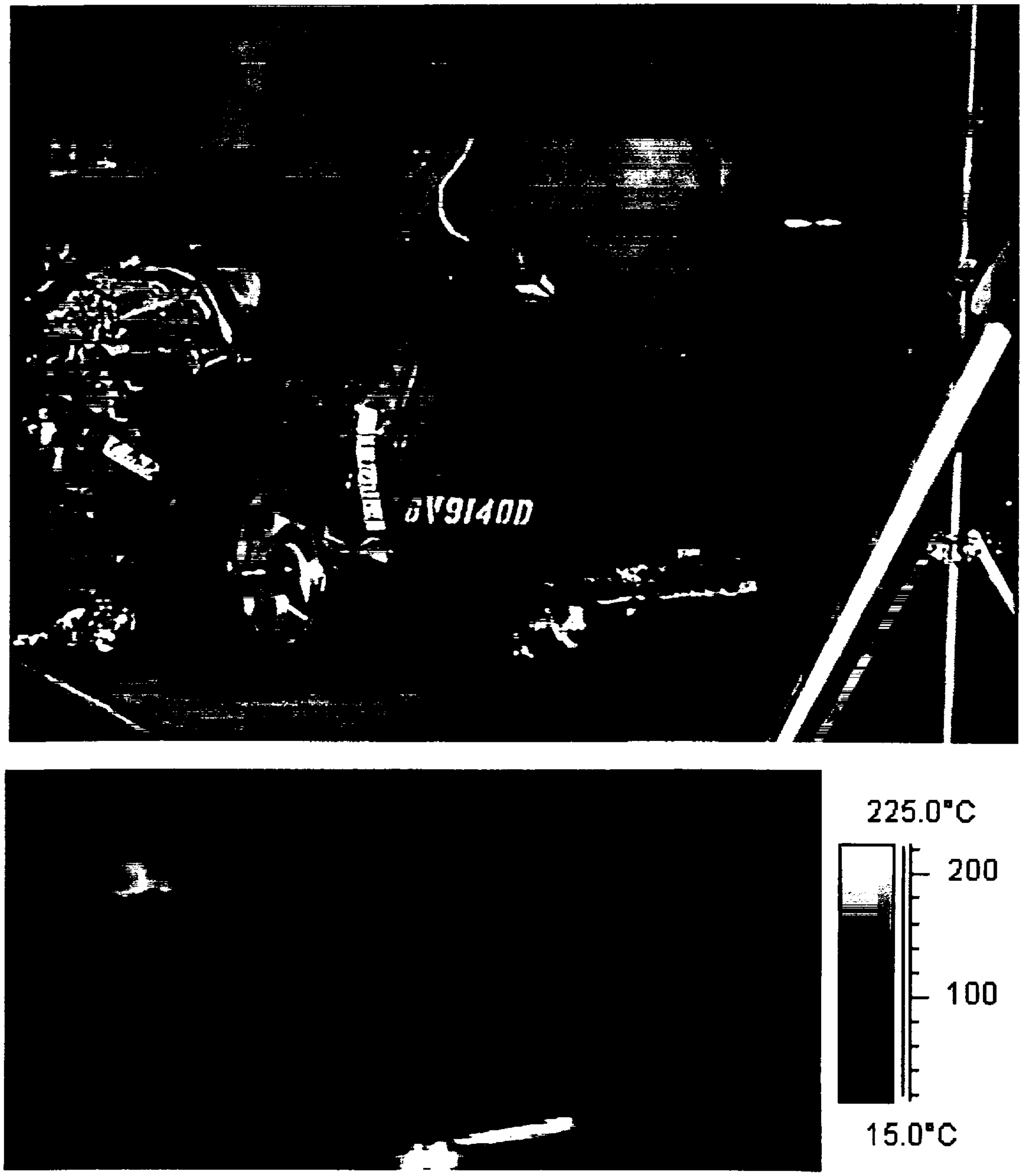

Figure 20. Fire Test F980611. Video still from Video Camera 3 (upper) and Infrared thermogram from IR6 (lower) at 210 seconds post-ignition.

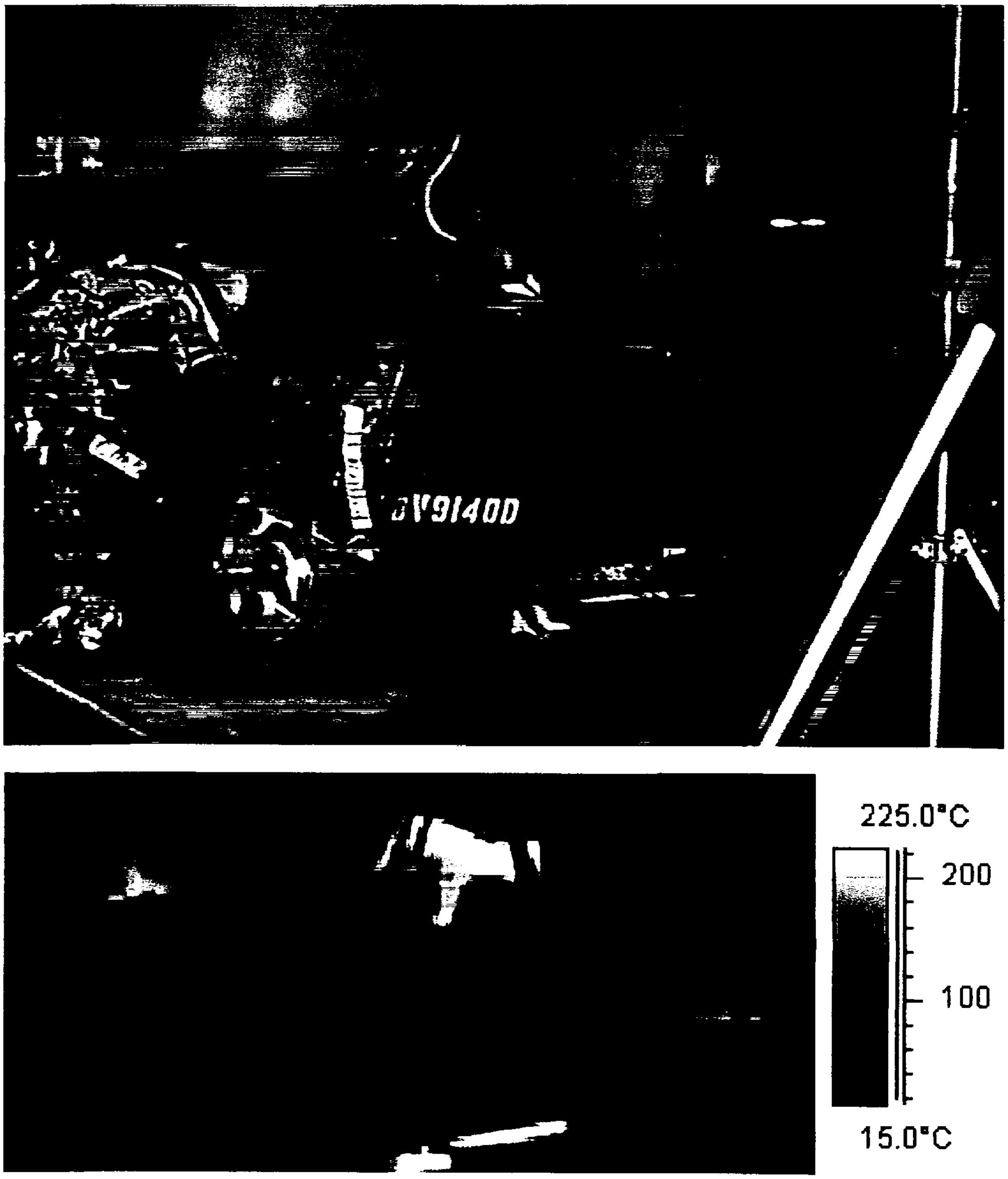

Figure 21. Fire Test F980611. Video still from Video Camera 3 (upper) and Infrared thermogram from IR6 (lower) at 240 seconds post-ignition.

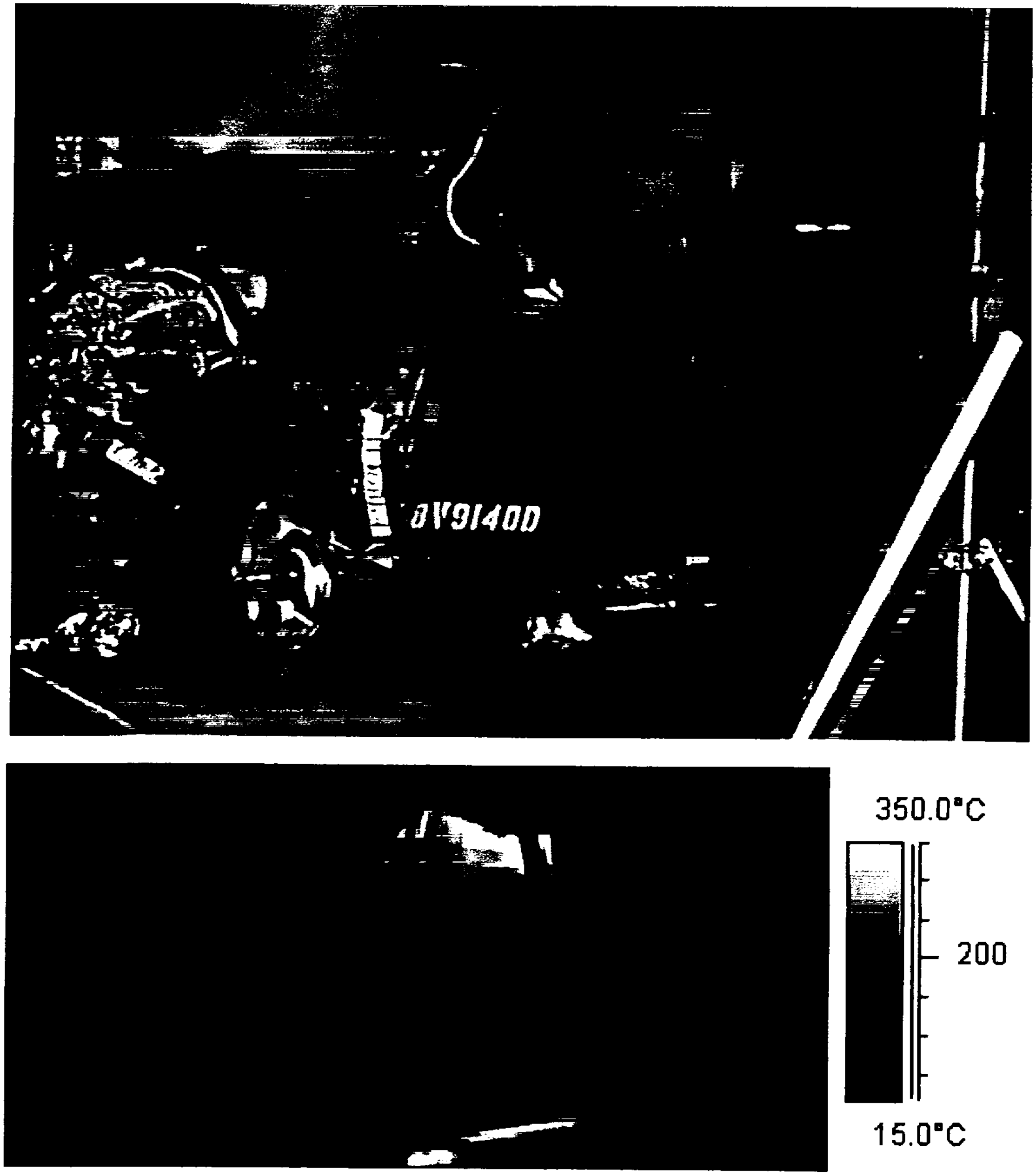

Figure 22. Fire Test F980611. Video still from Video Camera 3 (upper) and Infrared thermogram from IR6 (lower) at 243 seconds post-ignition.

The maximum temperature of smoke and gases in the upper part of the engine compartment of the test vehicle during this test was between 200 and 250°C (thermogram, Fig. 22).

Figure 23 shows video stills from Camera 5 at 2 seconds before ignition and 240 seconds post-ignition. The oil pan on the bottom of the engine, forward section of the transmission bell housing, the right exhaust take-down pipe, the left exhaust cross-over pipe, and a section of the right control arm are visible in these video stills (Fig. 23). The video record from Camera 5 did not show smoke or flames in this area at the time of ignition (upper video still, Fig. 23), shortly before the end of this test, (lower video still, Fig. 23), or at any time between ignition and 240 seconds post-ignition.

The Infrared thermograms in the figures showed heated gases in left rear wheelhouse from about 30 seconds post-ignition (Fig. 14) through the end of this test (Fig. 22). The maximum temperature of the gases in the left rear wheelhouse was between 150 and 200°C (thermogram, Fig. 22).

Smoke was visible in the passenger compartment by 60 seconds post-ignition (video still, Fig. 15), and was flowing out of the top of the window opening in the left front door by 120 seconds post-ignition (video still, Fig. 17). The infrared thermograms indicated that the temperature of the smoke and gases in the passenger compartment was < 40°C at 60 seconds post-ignition (thermogram, Fig. 15), increased to between 40 and 60°C by 180 seconds post-ignition (thermogram, Fig. 17), and was > 350°C at 243 seconds post-ignition (thermogram, Fig. 22). Flames appear to be visible in the area above the right rear seat by 243 seconds post-ignition (video still, Fig. 22).

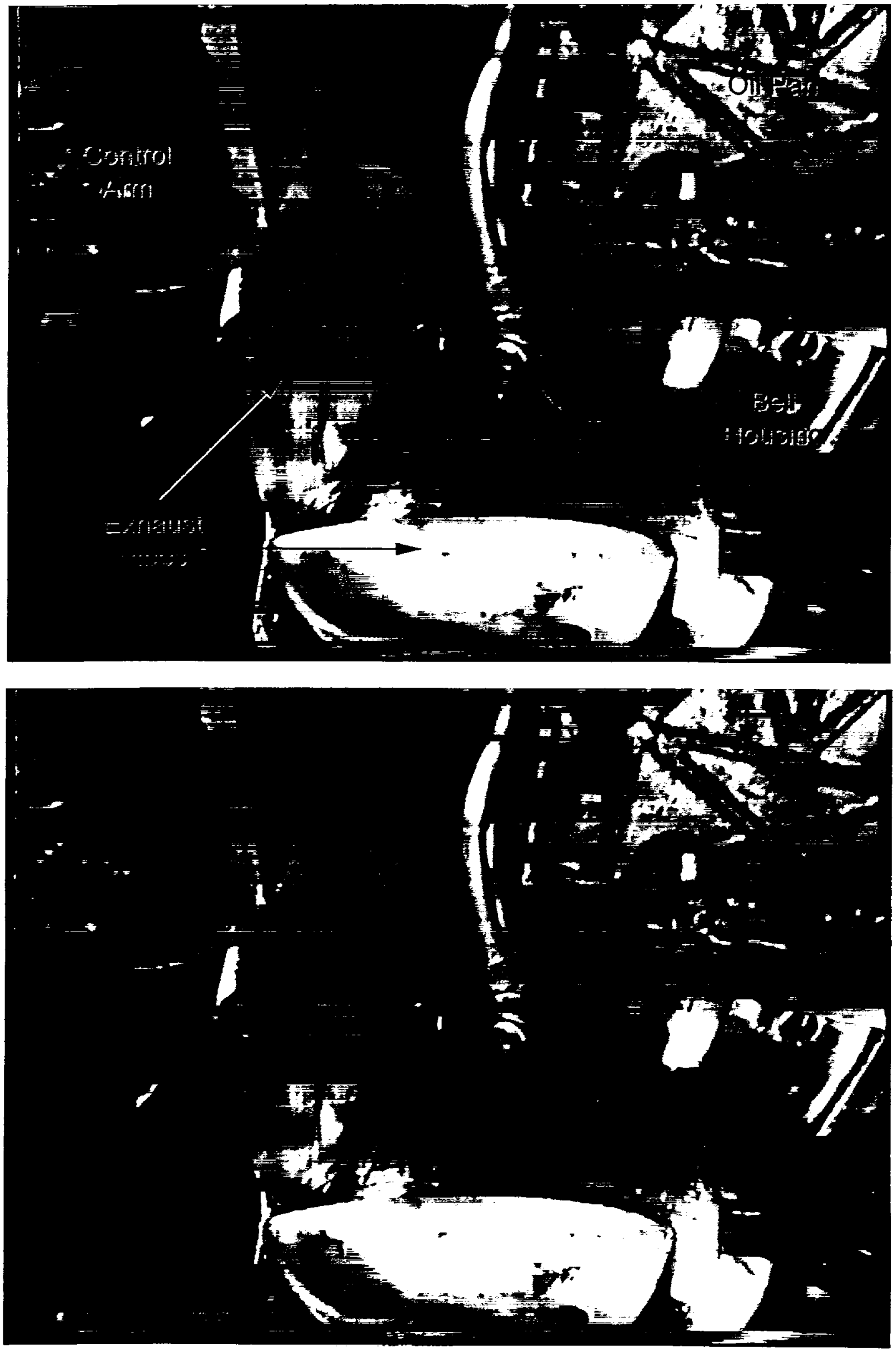

Figure 23. Fire Test F980611. Video stills from Camera 5 at 2 seconds before ignition (upper) and 240 seconds post-ignition (lower).

5 *Flame-Spread into the Passenger Compartment*

Heat and fire damage to the floor panel and floor carpet observed during inspection of the test vehicle after this test indicated that flames spread into the passenger compartment through a number of openings in the floor panel. Figure 24 shows photographs of the floor carpet and floor panel in the test vehicle after this test. The instrument panel, center console, seats, and interior trim panels were removed from the test vehicle after this fire test and before the photographs in Figure 24 were taken. The outlines in these photographs indicate the approximate foot-prints of the front seats, center console, and rear bench. The labels in both photographs indicate the following openings in the floor panel: crash-induced gaps around the shift lever pass-through cover plate (A); electrical pass-through openings under the left front seat (B); drain openings in the panel (C through I).

Photographs in Figure 24 show three areas of heat and fire damage to the floor carpet and floor panel caused by flame-spread through the electrical pass-through openings in the floor panel under the left front seat, where the carpet was over the drive train tunnel, and along the rear of the front compartment under the right side of the rear seat. Conduction through the floor panel also appears to have resulted in heat damage to the carpet in these areas. The timing of flame-spread through the electrical pass-through openings under the left front seat was determined by analysis of data recorded from thermocouples and heat flux transducers in the test vehicle, and by examination of the video record. The timing of flame-spread through drain holes in the floor panel could not be determined accurately from the thermocouple data recorded during this test. Temperature data recorded from Thermocouples F13, F14, F16, F17, and F18 indicate that flames did not spread into the passenger compartment through the gaps around the floor panel and the shift lever pass-through cover plate (see **APPENDIX C**).

5.1 Flame-Spread into the Passenger Compartment through Electrical Pass-Through Openings in the Floor Panel Under the Left Front Seat

An area of the floor carpet that was under the left front seat was burned and charred, and consumed by fire. Electrical pass-through openings are visible in the exposed floor panel (B, Fig. 24). Figure 25 contains diagrams showing the approximate locations of Thermocouples C1, C2, F9, F10, P5, P6, P7, S18, S19, and S20, and HFT2 in the test vehicle. Thermocouple F9 was located approximately ½ in. below the lower surface of the floor panel (Diagram A, Fig. 25). Thermocouple F10 was attached to the upper surface of the floor panel using a thermally conductive adhesive (Diagram A, Fig. 25). HFT2 was located in a clearance hole drilled in the floor panel such that the transducer element was facing downward and flush with the lower surface of the floor panel (Diagram A, Fig. 25). Thermocouples P6 and P7 were located in the

Figure 24. Fire Test F980611. Photograph of the floor carpet (upper) and floor panel (lower) in the test vehicle after this test.

electrical pass-through opening where the grommet dislodged from the opening during the crash test (Diagram A, Fig. 25). Thermocouple P5 was located above the grommet in the other electrical pass-through opening (Diagram A, Fig. 25). Thermocouples C1 and C2 were located on the upper surfaces of the floor carpeting above the electrical pass-through openings (Diagram B, Fig. 25). Thermocouples S18, S19, and S20 were located below the lower surface of the foam pan in the left front seat cushion (Diagram B, Fig. 25).

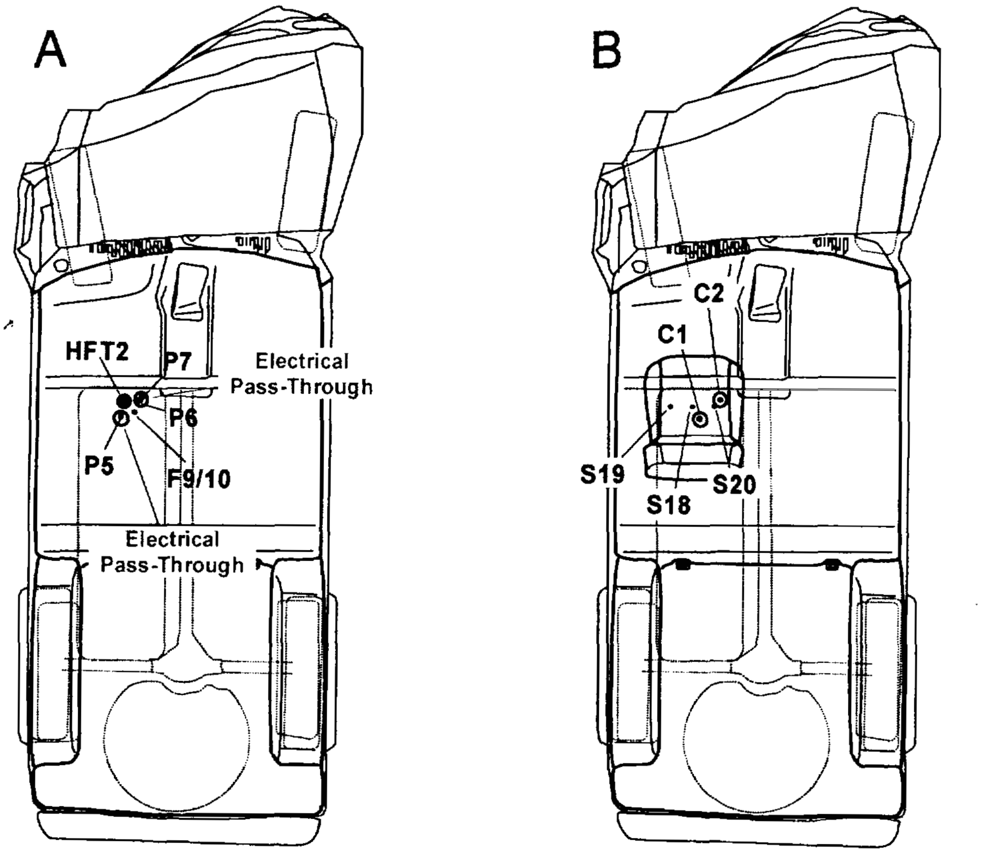

Figure 25. Fire Test F980611. Diagrams showing the approximate locations of Thermocouples F9 and F10 and a HFT2 in the floor pan (A), Thermocouples P5, P6, and P7 in electrical pass-through openings in the floor panel (A), and Thermocouples C1 and C2 on the floor carpet (B), and Thermocouples S18, S19, and S20 below the left front seat cushion (B) of the test vehicle.

Figure 26 shows plots of temperature data recorded from Thermocouples F9 and F10, and heat flux data recorded from HFT2. Figure 27 shows plots of data recorded from Thermocouples P6, P7, and C2. Figure 28 shows plots of data recorded Thermocouples P5 and C1.

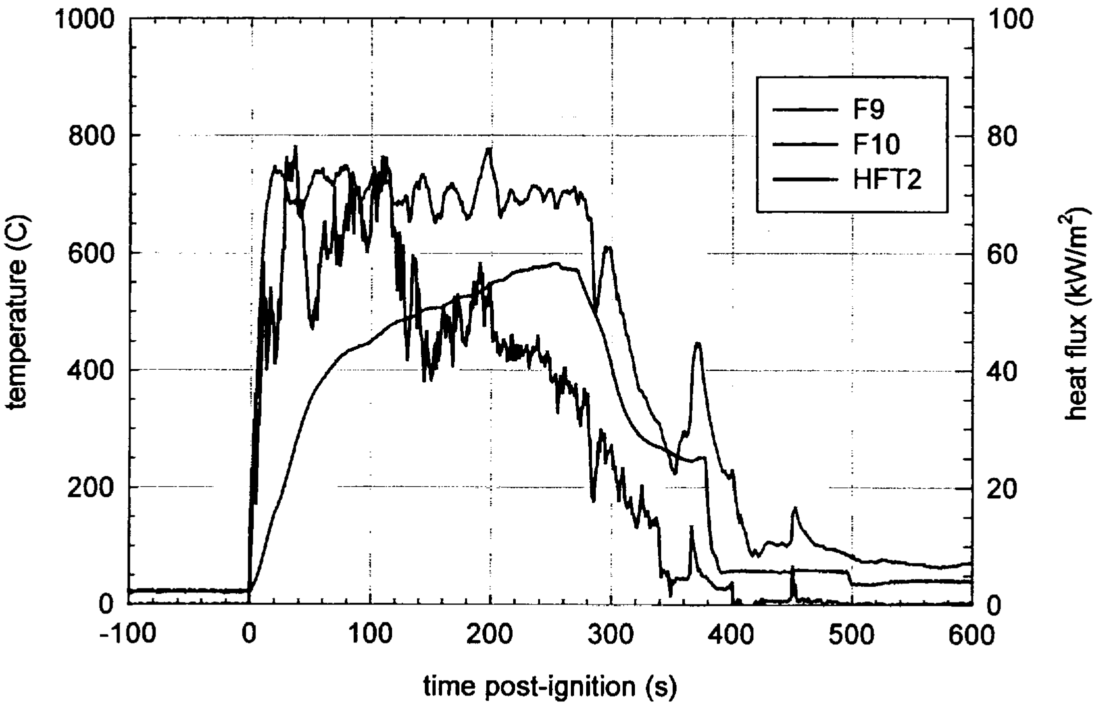

Figure 26. Fire Test F980611. Plots of temperature data recorded from Thermocouples F9 and F10, and heat flux data recorded from HFT2.

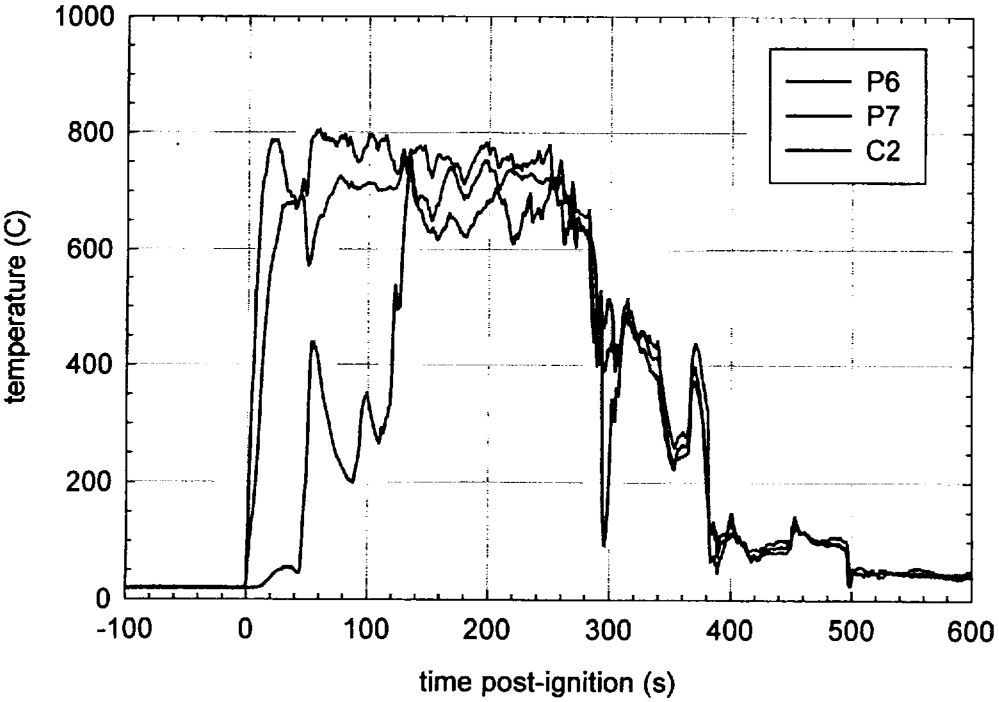

Figure 27. Fire Test F980611. Plots of temperature data recorded from Thermocouples P6, P7, and C2.

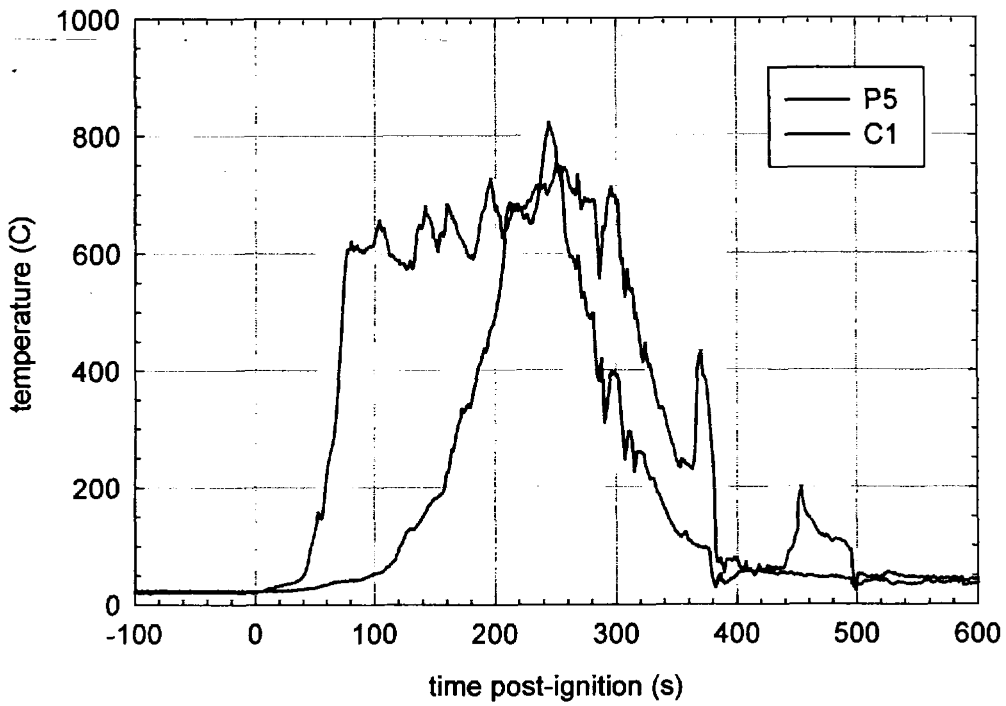

Figure 28. Fire Test F980611. Plots of temperature data recorded from Thermocouples P5 and C1.

Temperature data recorded from Thermocouple F9 indicates that the section of the floor panel under left front seat was exposed to flame temperatures[3] from about 10 through 185 seconds post-ignition (Fig. 26). The measured heat flux to this section of the floor panel during this time interval was between 40 and 80 kW/m^2 (Fig. 26).The maximum temperature of the floor panel was 582°C recorded between 250 and 255 seconds post-ignition (Fig 26).

Temperature data recorded from Thermocouples P6 and P7 indicate that flames entered the electrical pass-through opening where the grommet had dislodged during the crash test by 10 seconds post-ignition (Fig. 27). Flame temperatures were recorded by Thermocouple C2 starting at about 130 seconds post-ignition (Fig. 27), suggesting that flames burned through the carpet above this pass-through opening at this time.

Data recorded from Thermocouples P5 and C1 indicate that flames burned through the grommet that was not dislodged from the electrical pass-through under the left front seat at about 75 seconds post-ignition and burned through the carpet above this pass-through opening at about 205 seconds post-ignition (Fig. 28).

---

[3] As in previous reports, a value of 600°C was used in this report as the threshold to indicate the presence of flame.

Figure 29. Fire Test F980611. Video still from Camera 10 at 235 seconds post-ignition.

Figure 30. Fire Test F980611. Video still from Camera 10 at 240 seconds post-ignition.

Figure 31. Fire Test F980611. Video still from Camera 10 at 250 seconds post-ignition.

Figure 32. Fire Test F980611. Video still from Camera 10 at 245 seconds post-ignition.

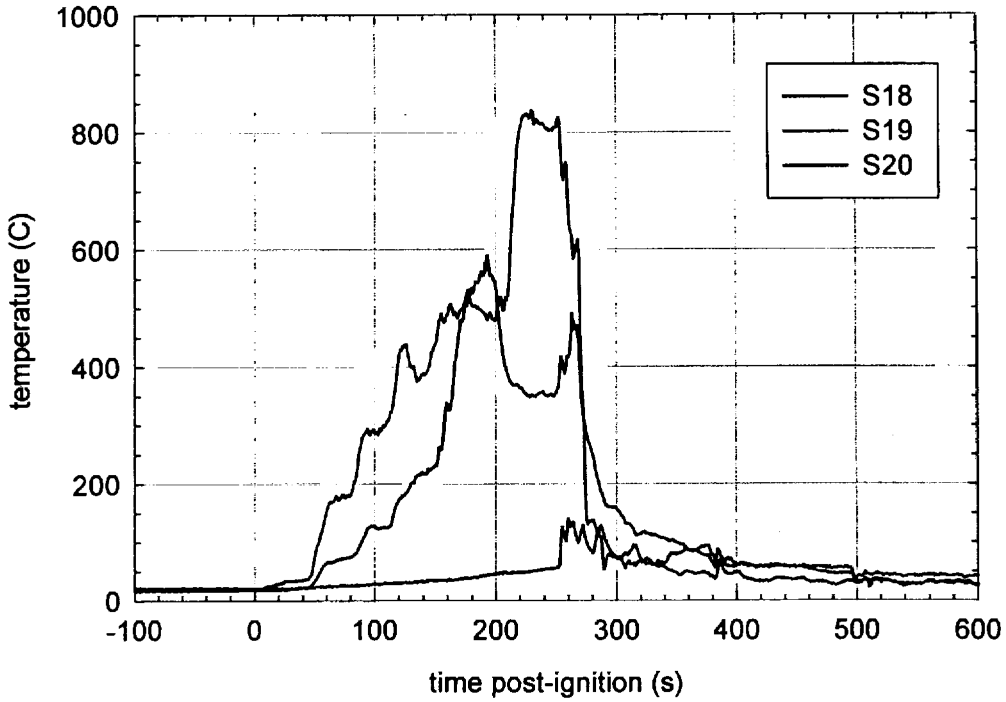

Figure 33. Fire Test F980611. Plots of temperature data recorded from Thermocouples S18, S19, and S20.

The video from Camera 10 showed that flames burned through the left front seat cushion between 235 and 250 seconds post-ignition (Fig.'s 29 through 32). Temperature data recorded from Thermocouples S18, S19, and S20 (Fig. 33) suggests that brackets for the power seat mechanism and support structure under the seat affected the distribution of flames on the pad in the seat cushion.

For example, temperature data record from Thermocouples S19 and S20 indicated that the lower surface of the foam pad on the right and left sides of the seat cushion was exposed to heated gases starting at about 20 seconds post-ignition (Fig. 33) and flames starting at about 200 seconds post-ignition (Fig. 33). Temperature data recorded from Thermocouple S18 indicated that that the lower surface of the foam pad in the center of the seat cushion, which was above a bracket for the power seat mechanism, was not exposed to flames at any time during this test (Fig. 33).

The video from Camera 10 showed a fire plume between the inboard side of the left front seat cushion and the center console between about 190 and 195 seconds post-ignition (Fig. 34). Examination of the floor panel and floor carpet in this area (B, Fig. 24) indicated that this fire

Figure 34. Fire Test F980611. Video still from Camera 10 at 193 seconds post-ignition.

plume was caused by flame-spread through the electrical pass-through opening with crash-dislodged grommet under the left front seat. Before burning through the carpet under the left front seat, flames entering this pass-through opening appeared to follow channels formed by folds in the floor carpet along the rise in the floor panel that formed the left side of the drive train tunnel. Flames burn through the carpet at the top of the rise along the left side of the center console, producing the fire plume observed in the video from Camera 10 at 193 seconds post-ignition (Fig. 34).

Fire damage in the test vehicle observed after this test was consistent with flame-spread through the electrical pass-through openings in the floor panel. Insulation of the electrical wires in the pass-through openings in the floor panel under the left front seat was melted, burned, and charred (Fig. 35). The grommet that was not dislodged in the crash test was melted, burned and charred (Fig. 35). The carpet backing[4] melted and solidified on sections of the wiring and the floor panel (Fig. 35). Dark, oily soot was deposited on sections of the floor panel around these

---

[4] The floor carpet backing was poly(ethylene) [5].

Figure 35. Fire Test F980611. Photograph of a section of the floor panel that was under the left front seat in the test vehicle after this test.

pass-through openings (Fig. 35). Examination of the left front seat after this test showed a hole burned through the foam pad and cover of the seat cushion directly above the electrical pass-through opening with crash-dislodged grommet (Fig. 36). The area of the center console that was adjacent to the electrical pass-through openings in the floor panel under the left front seat was melted and burned (Arrow, Fig. 37).

5.2 Flame-Spread into the Passenger Compartment through Drain Holes in the Floor Panel and Conduction through the Floor Panel

The floor carpet over the drive train tunnel that was under the rear of the center console was burned and charred, and consumed by fire (Fig. 24). A drain hole opening is visible in the exposed section of floor panel (C, Fig. 24). An area of the floor carpet that was under the rear bench seat was burned and charred, and consumed by fire. A drain hole opening is visible at the edge of the carpet (G, Fig. 24). When the floor carpet was removed from the test vehicle after this test, a number of other drain hole openings were observed in the floor panel (Fig. 24). Grommets were in place in all of these drain hole openings before this fire test, and appeared to have been partially or completely consumed by fire during this test.

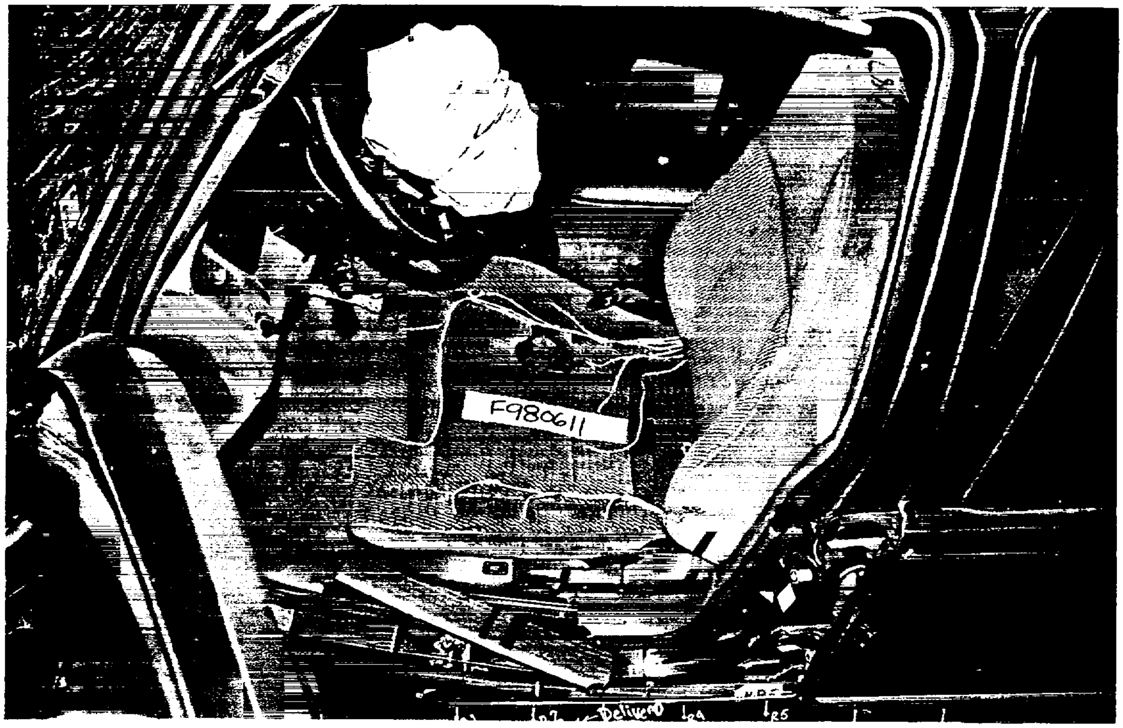

Figure 36. Fire Test F980611. Photograph of the left front seat in the test vehicle after this test.

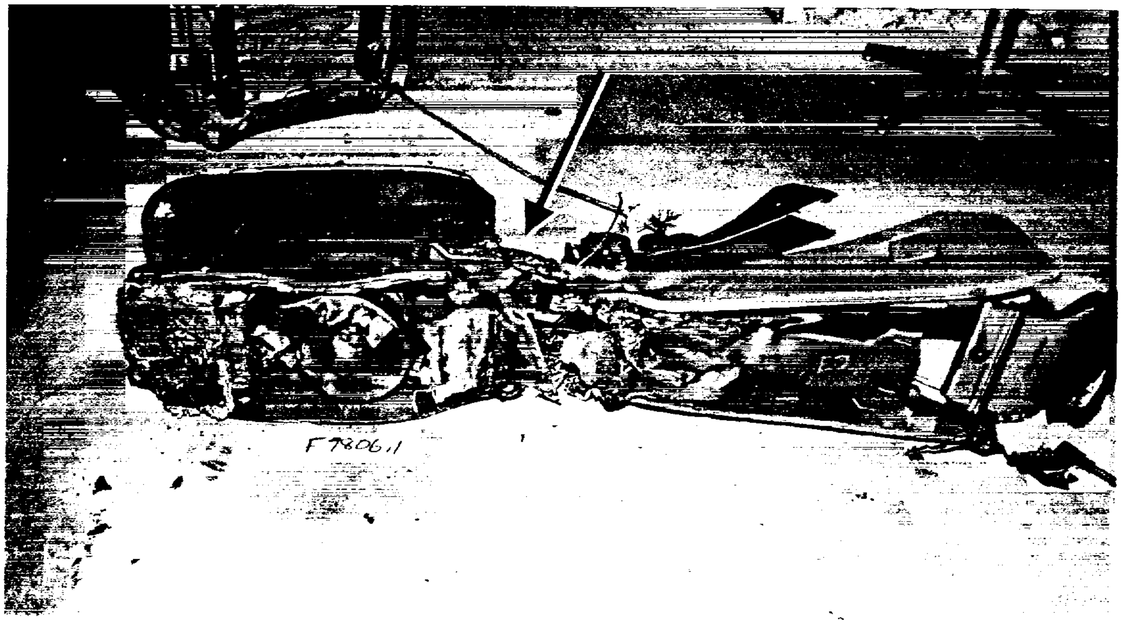

Figure 37. Fire Test F980611. Photograph of the bottom and right side of the center console removed from the test vehicle after this test. The arrow indicated the area of the center console that was adjacent to the electrical pass-through openings in the floor panel under the left front seat.

The timing of burn-through of each grommet and flame-spread through each drain hole opening could not be determined accurately from the thermocouple data recorded during this test.

Figure 38 contains a diagram showing the approximate locations of Thermocouples F1, F2, P1, P2, P3, and P4, and HFT1 in the test vehicle.

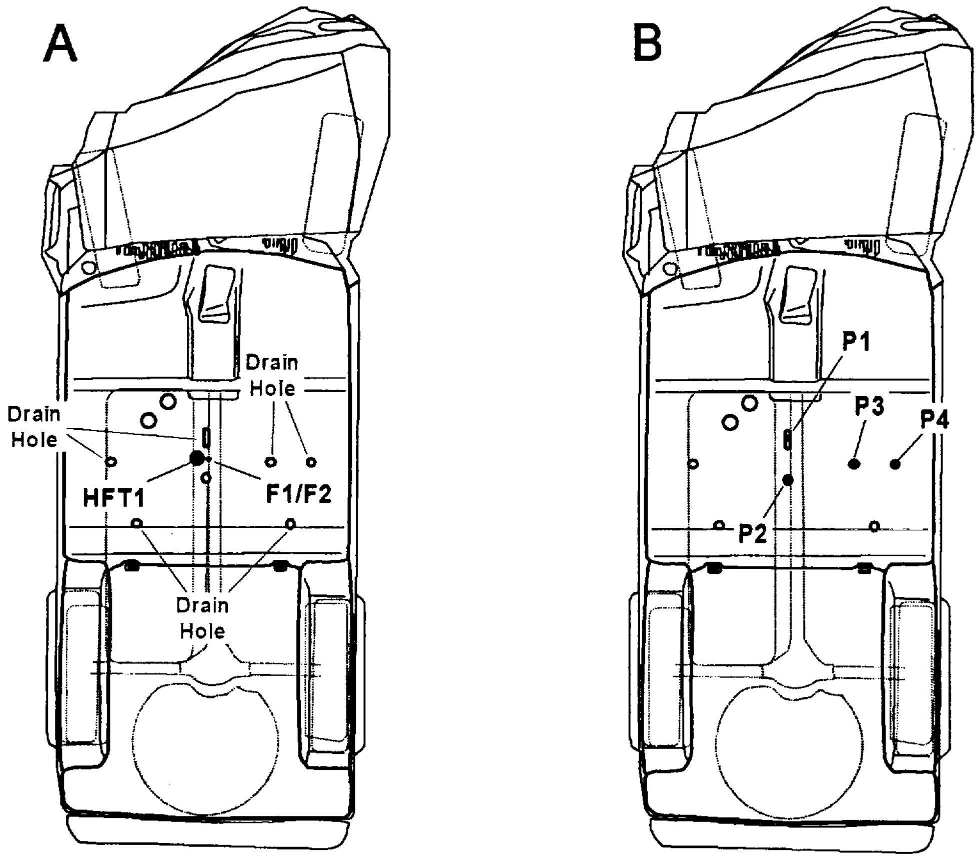

Figure 38. Fire Test F980611. Diagrams showing the approximate locations of Thermocouples F1 and F2 and HFT1 in the floor panel (A), and Thermocouples P1, P2, P3, and P4 on the upper surfaces of drain hole grommets (B) in the test vehicle.

Thermocouple F1 was located approximately ½ in. below the lower surface of the floor panel (Diagram A, Fig. 38). Thermocouple F2 was attached to the upper surface of the floor panel using a thermally conductive adhesive (Diagram A, Fig. 38). HFT1 was located in a clearance hole drilled in the floor panel such that the transducer element was facing downward and flush with the lower surface of the floor panel (Diagram A, Fig. 38). Thermocouples P1, P2, P3, and P4 were located on the upper surfaces of drain hole grommets in the floor panel (Diagram B, Fig. 38).

Figure 39 shows plots of temperature data recorded from Thermocouples F1 and F2, and heat flux data recorded from HFT1. Temperature data recorded from Thermocouple F1 indicates that the section of the floor panel in the drive train tunnel was exposed to flame temperatures from about 10 to 350 seconds post-ignition (Fig. 39). The measured heat flux to this section of the floor panel during this time interval was in the range of 40 to 95 kW/m^2 (Fig. 39). The maximum temperature of the floor panel was between 530 and 535°C recorded between 280 and 310 seconds post-ignition (Fig 39).

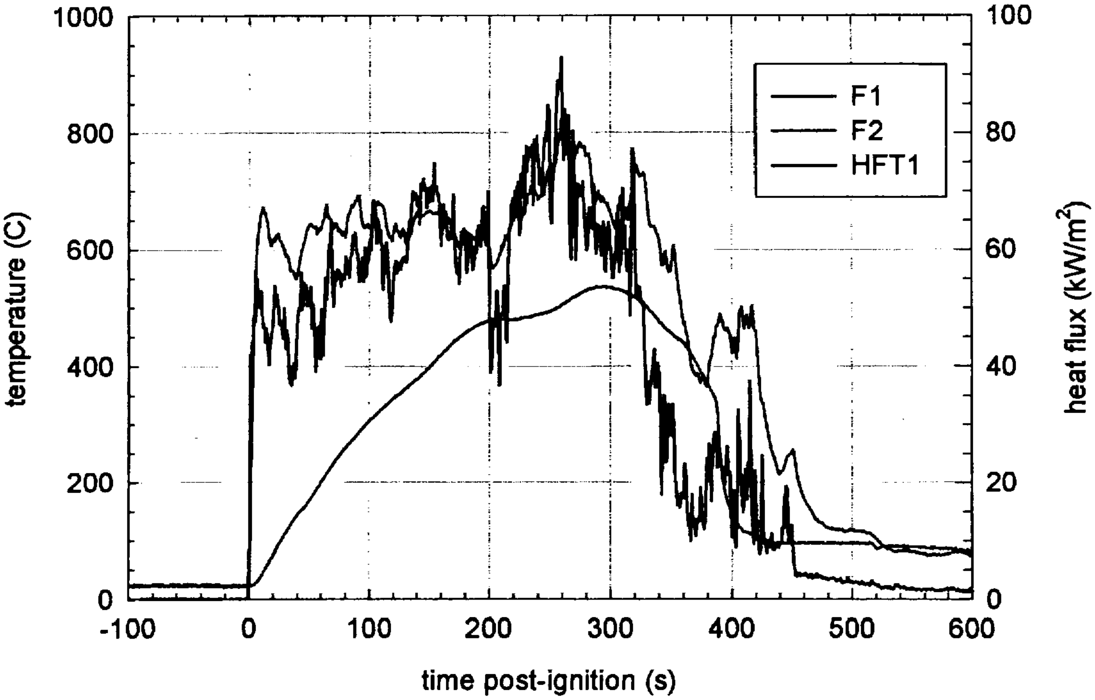

Figure 39. Fire Test F980611. Plots of temperature data recorded from Thermocouples F1 and F2, and heat flux data recorded from HFT1.

Figure 40 shows plots of data recorded from Thermocouples P1, P2, P3, and P42. Temperature data recorded from these thermocouples appears to have been affected by contact with the grommets in the drain holes and with the overlying carpet or carpet pad. For example, the maximum temperatures recorded from these thermocouples were 566°C (P1), 570°C (P2), 357 (P3), and 190°C (P4) from the time of ignition until 250 seconds post-ignition (Fig. 40) – the end of the test and beginning of fire suppression. These values were less than the 600°C threshold used to indicate the presence of flames in this report, and would seem to indicate that flames did not burn through the grommets in these drain holes during this test. Inspection of the test vehicle after this test revealed that the grommets in 5 of 7 drain holes in the floor panel in the front compartment of the test vehicle were partially or completely consumed by fire (Fig. 24). Heat and fire damage to the floor carpet (Fig. 24), rear section of the center console (Fig. 37), and rear panels in the front seat back covers (Fig. 41) indicate that flames spread into the passenger compartment through the drain hole labeled C in Figure 24. Heat and fire damage to the floor carpet (Fig. 24) and rear seats (Fig. 42) indicate that flames spread into the passenger comp

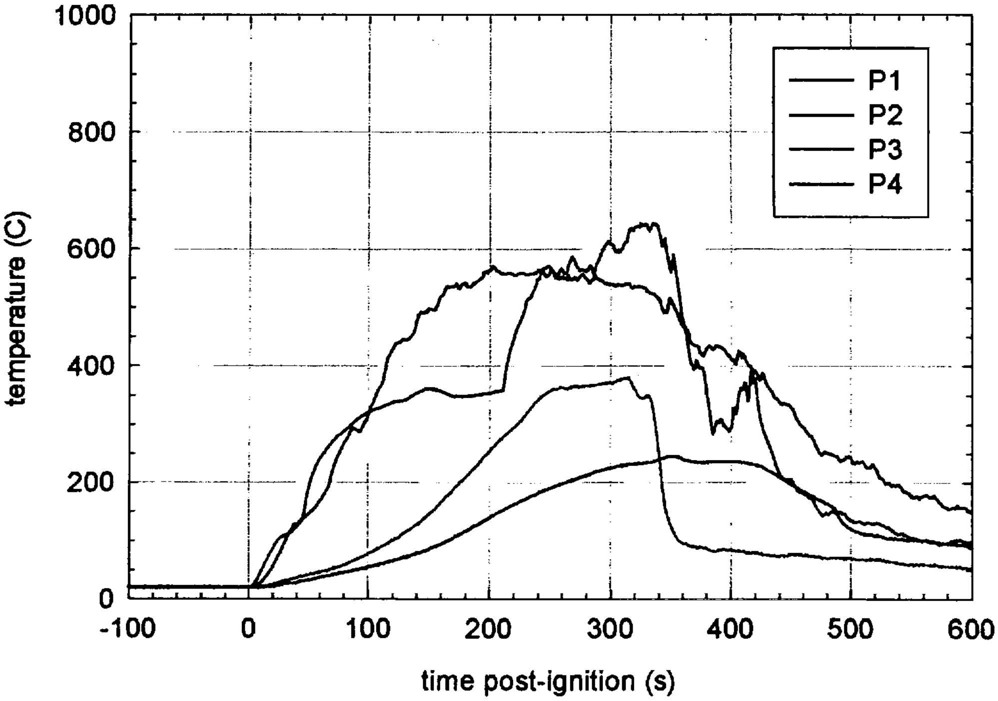

Figure 40. Fire Test F980611. Plots of temperature data recorded from Thermocouples P1, P2, P3, and P4.

The pattern of heat and fire damage to the floor carpet (Fig.'s 24 and 42) suggests that conduction through the floor panel heated sections of the carpet under the left front seat, over the drive train tunnel, and along the rear of the front compartment under the rear seats. Maximum temperatures recorded from thermocouples on the upper surface of the floor panel on the drive train tunnel at the rear of the center console were 502, 536, and 616°C and under the left front seat were 346 and 582°C (**APPENDIX C**). The carpet pad under the floor carpet was charred where it was over the drive train tunnel (Fig. 43).

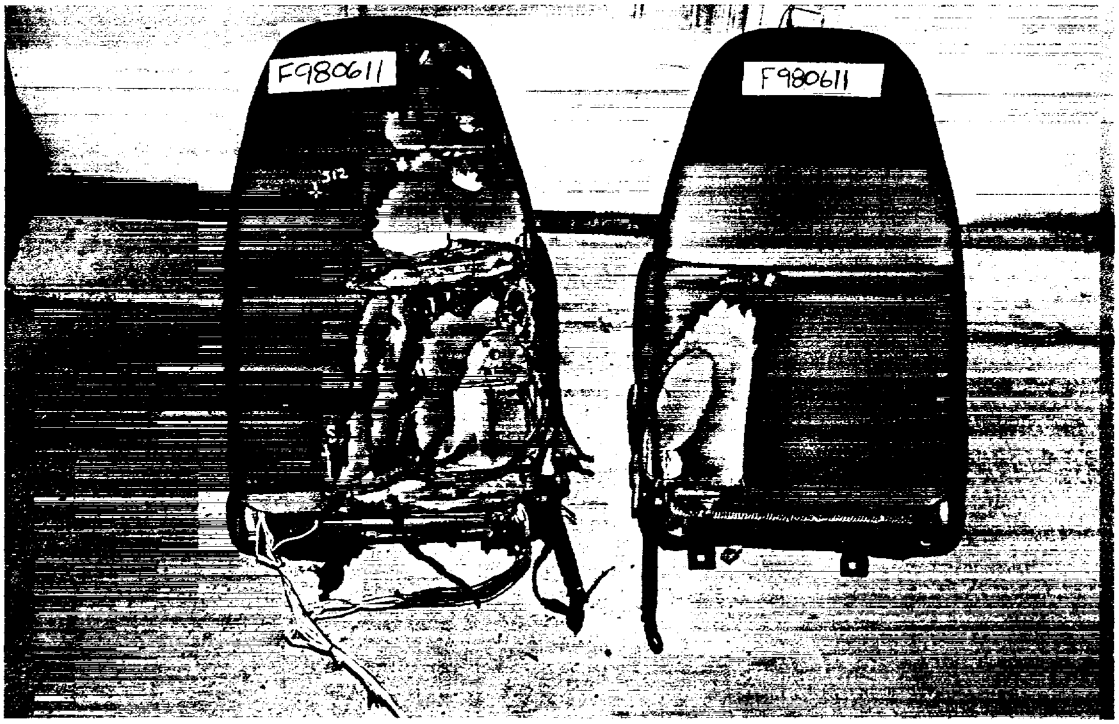

Figure 41. Fire Test F980611. Photograph of the front seats removed from the test vehicle after this test.

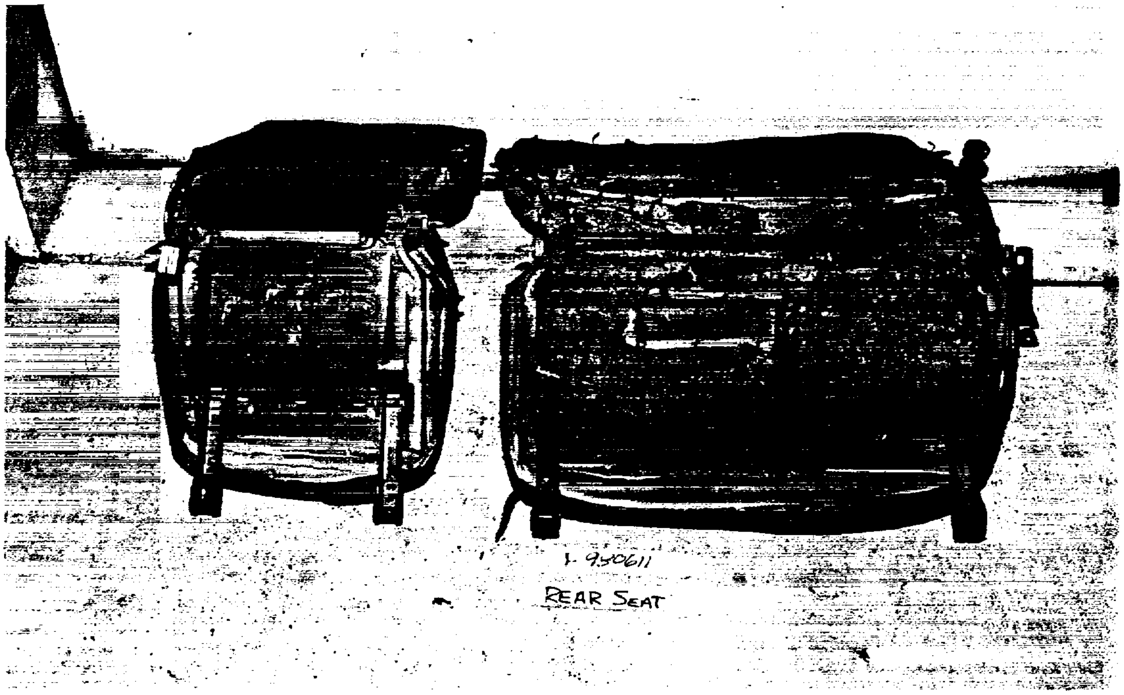

Figure 42. Fire Test F980611. Photograph of the rear seats removed from the test vehicle after this test.

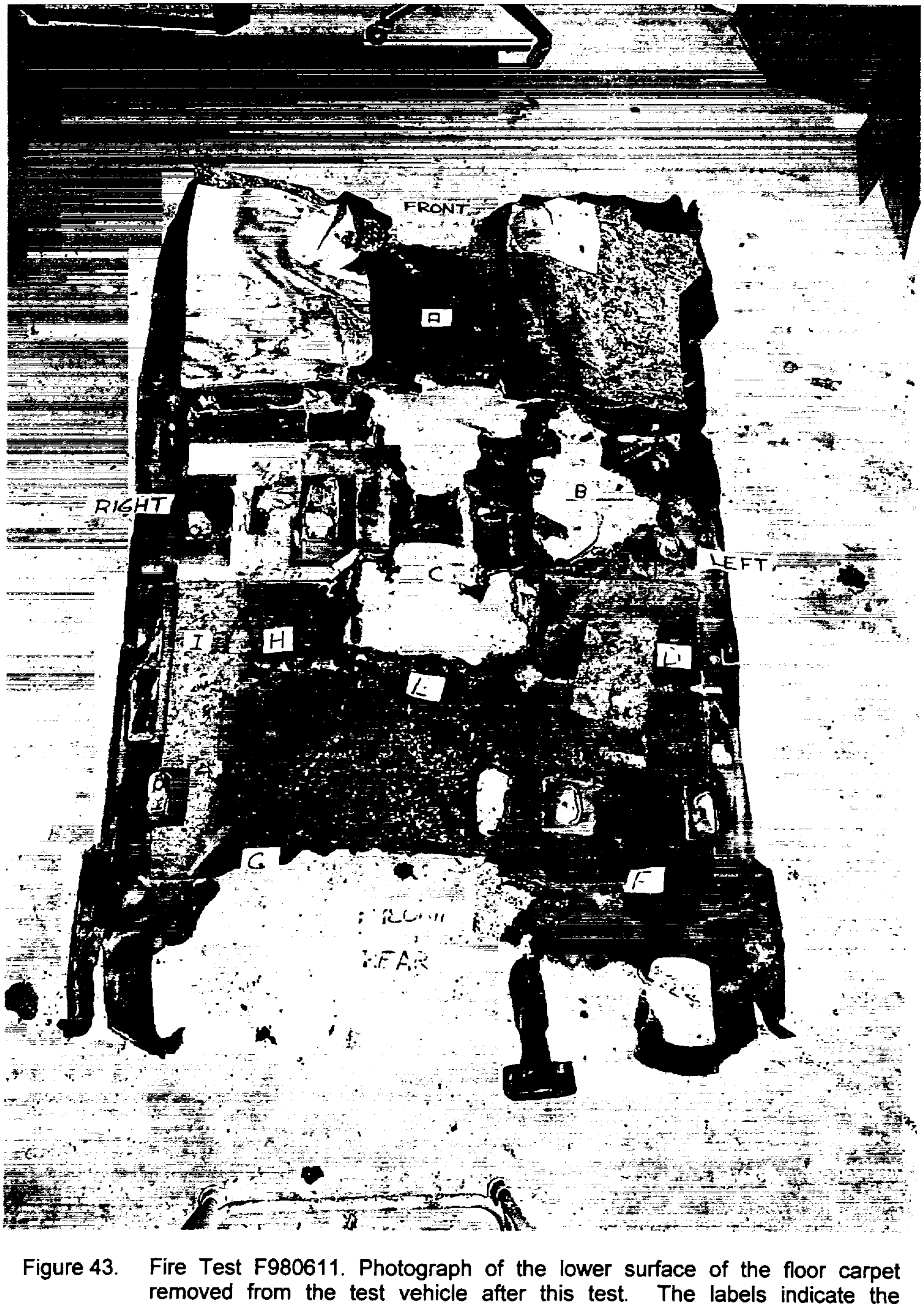

Figure 43. Fire Test F980611. Photograph of the lower surface of the floor carpet removed from the test vehicle after this test. The labels indicate the approximate locations of the shift lever pass-through cover plate (A), electrical pass-throughs under the left front seat (B), and drain holes (C through I) in the floor panel.

Sections of the floor carpet that were over the drive train tunnel, under the left front seat, and under the rear seat on the right side of the vehicle and that did not contain carpet pad ignited and burned during this test. Residue from the floor carpet that had melted during the fire and solidified when the fire was extinguished was adhered to the floor panel in these areas after the floor carpet was removed from the test vehicle (Fig. 24).

5.3 Flame-spread on the Roof Trim Panel

Infrared thermograms for IR6 indicated the presence of smoke and heated gases with temperature > 350°C in the area above the right rear seat between 240 and 245 seconds post-ignition (Fig. 22). Inspection of the test vehicle after this test showed flames burned through two areas of the right rear seat by the time flames inside the passenger compartment were extinguished (Fig. 44).

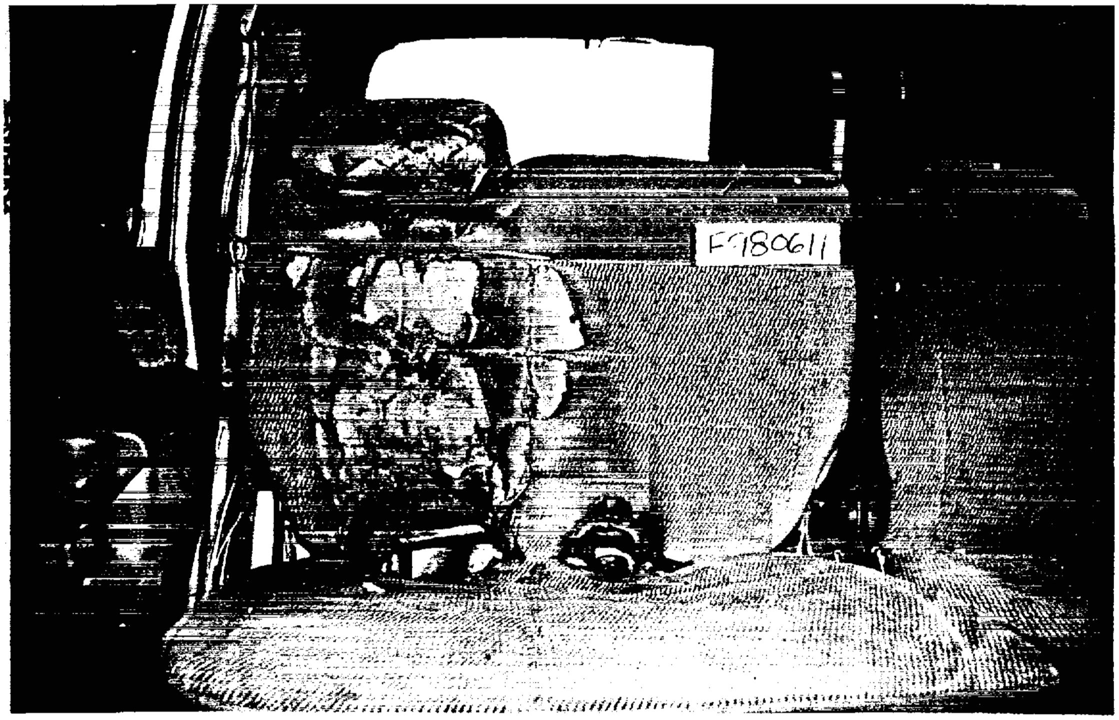

Figure 44. Fire Test F980611. Photograph of the rear seats in the test vehicle after this test.

Figure 45 shows a series of diagrams of the test vehicle with estimated isothermal contour plots of temperature profiles below the headlining panel at 0, 30, 60, 90, 120, 150, 180, 210, 240, and 253 seconds post-ignition.[5] The timing and approximate distribution of flames along the roof trim panel is indicated by isothermal contours with t ≥ 600°C. This analysis indicates that estimated temperatures on the lower surface of the roof trim panel were ≤ 70°C from the time of ignition through 210 seconds post-ignition (Fig. 45). By 240 seconds post-ignition, estimated temperatures were < 200°C on the left side and in the front of the passenger compartment (Fig. 45). By 253 seconds post-ignition, estimated temperatures were > 600°C (Fig. 45) indicating that the fire plume above the right rear seat had reached the lower surface of the roof trim panel above the right rear seat before this test was ended and flames in the passenger compartment were extinguished.

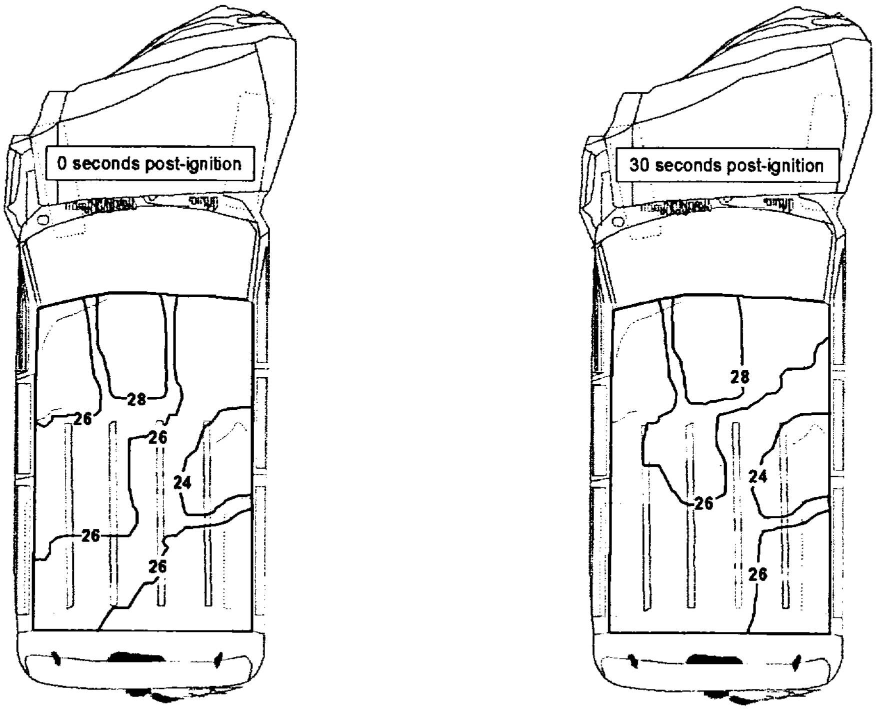

Figure 45. Fire Test F980611. Diagrams showing isothermal contour plots of estimated temperature along the lower surface of the roof trim panel at of the rear compartment floor panel at 0, 30, 60, 90, 120, 150, 180, 210, 240, and 253 seconds post-ignition.

---

[5] Isothermal contours of the temperature below the lower surface of the headlining panel were estimated from the temperature data recorded from Thermocouples R1, R2, R3, R4, R5, R6, R7, R8, R9, R10, and R11using a three-dimensional interpolation algorithm available in SigmaPlot for Windows Version 4.00 [6]. This algorithm used an inverse distance method to interpolate temperature values for points on a uniformly spaced Cartesian grid from the [x,y,t] triple data from these thermocouples. Refer to **APPENDIX C** for the approximate locations of these thermocouples.

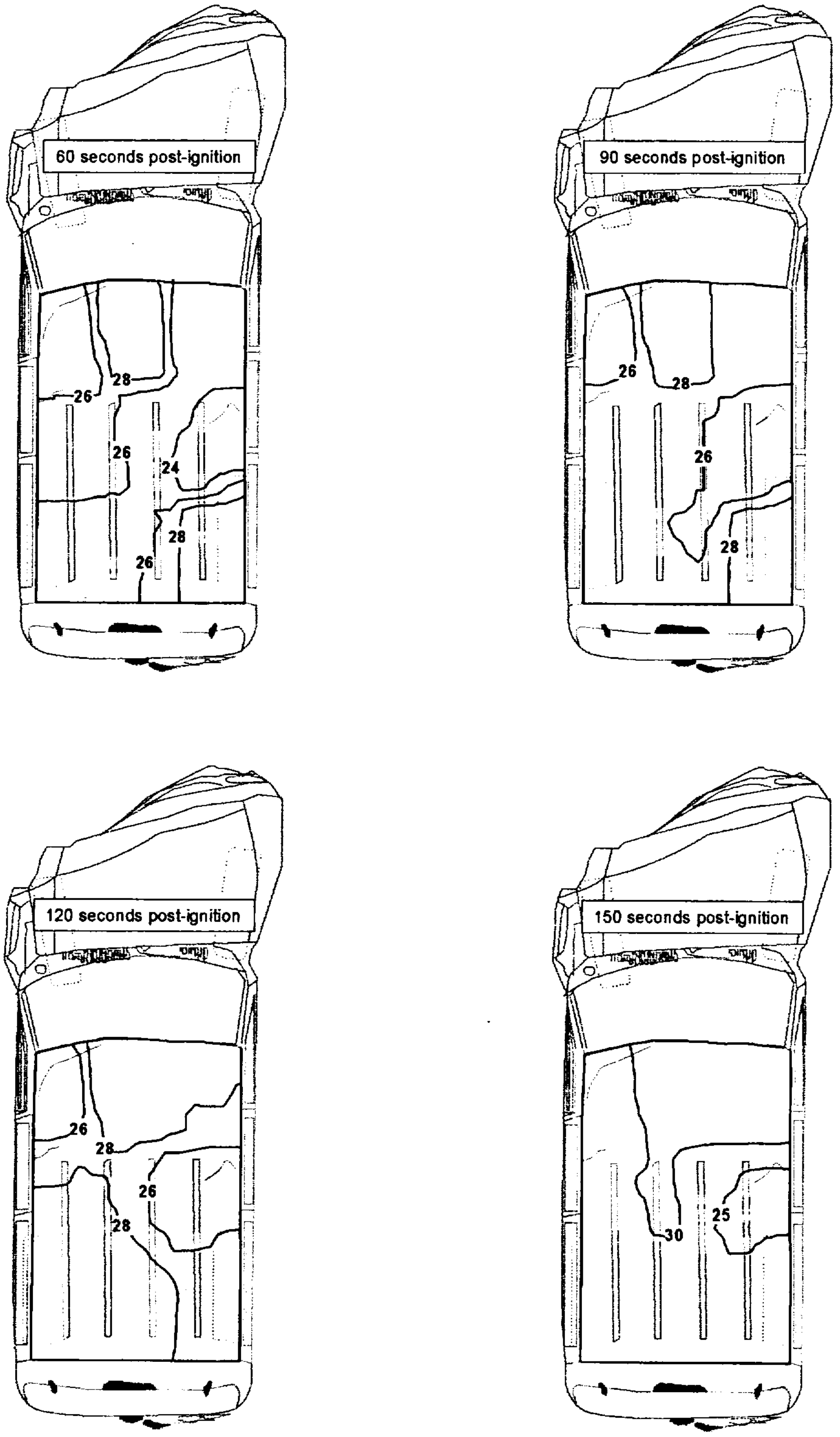

Figure 45, continued. Fire Test F980611. Diagrams showing isothermal contour plots of estimated temperature along the lower surface of the roof trim panel at of the rear compartment floor panel at 0, 30, 60, 90, 120, 150, 180, 210, 240, and 253 seconds post-ignition.

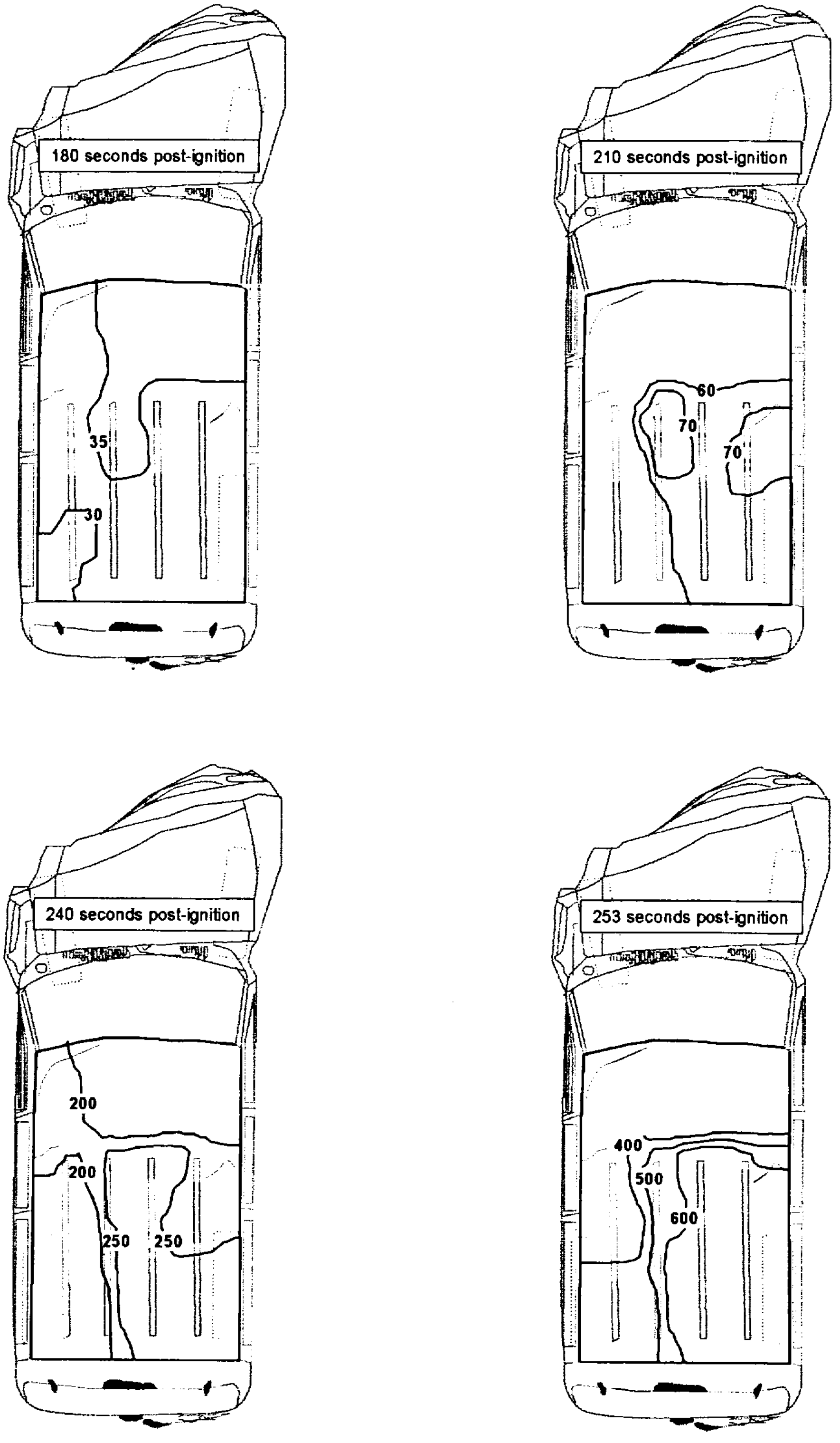

Figure 45, continued. Fire Test F980611. Diagrams showing isothermal contour plots of estimated temperature along the lower surface of the roof trim panel at of the rear compartment floor panel at 0, 30, 60, 90, 120, 150, 180, 210, 240, and 253 seconds post-ignition.

The fabric cover on the lower surface of the roof trim panel was charred above the right rear seat (Fig. 46). The area where estimated temperatures on the roof trim panel exceeded 600°C (Fig. 45) extended further rearward into the rear compartment than the charred area on the roof trim panel (Fig. 46).

Figure 46. Fire Test F980611. Photograph of the roof trim panel removed from the test vehicle after this test.

6 Combustion Conditions

The output of combustion products from a fire depends on the material burning and on the supply of air to the flame. A well-ventilated fire is one in which the air supplied to the flames is sufficient for complete combustion. In partially enclosed spaces, such as an engine compartment or passenger compartment, airflow to the flames may be inadequate for complete combustion. In this case, called a ventilation-controlled or under-ventilated fire, the supply of air limits both the heat released by the fire and oxidation (combustion) of the gaseous fuel in the fire zone. As ventilation decreases, the output of carbon monoxide, hydrocarbons, smoke, and other products of incomplete combustion increase. The chemical composition of these gases depends on the chemical compositions of the materials burning and on the burning conditions, primarily ventilation. For fires in an enclosed space, heated buoyant gases can accumulate below the ceiling or roof of the enclosed space, forming what is called the upper layer. The upper layer can be ignited by flames from burning objects (piloted ignition) or can ignite spontaneously (autoignition) when the temperature of the gases exceeds a minimum threshold temperature (autoignition temperature), which depends on the chemical composition and the fuel/oxygen ratio of the gaseous upper layer. Once ignited, radiation from the burning upper layer transfers heat downward, and may ignite combustible materials below the burning upper layer. Ventilation of the flames affects the chemical composition of the gases produced in a fire.

The equivalence ratio is a quantitative measure of the amount of oxygen consumed during combustion, and is defined as follows:

$$\Phi = \frac{\left[{}^{fuel}\!/_{O_2}\right]_{fire}}{\left[{}^{fuel}\!/_{O_2}\right]_{stoichiometric}}$$

where Φ is the equivalence ratio, $[fuel/O_2]_{fire}$ is the fuel-to-oxygen ratio in the fire, and $[fuel/O_2]_{stoichiometric}$ is the fuel-to-oxygen ratio required for complete (stoichiometric) combustion. Combustion product concentration data, oxygen concentration data, gas temperature data, and airflow data are typically used to calculate a value of the equivalence ratio in laboratory tests [7]. In most instances, the equivalence ratio is not determined for large-scale tests where objects made of different materials may burn in different physical environments. Ventilation and thus the equivalency ratio may be different in each environment. Since it was not possible to isolate and measure the fire products produced by each of the materials burning or to measure airflow into each of the unique environments that existed during this test, the equivalence ratio was not determined here.

Air temperature and gas concentration data collected during this test were used to estimate derived parameters that are related to ventilation. Air temperature and gas concentration data from the Fire Products Collector at the test facility were used to estimate the ratios $[G_{CO}]/[G_{CO2}]$ and $[G_{HC}]/[G_{CO2}]$. Air temperature data from the aspirated thermocouples in the passenger compartment and gas concentration data from the FTIR gas analysis of air in the passenger compartment were used to estimate the ratios $[C_{CO} \times d_{CO}]/[C_{CO2} \times d_{CO2}]$, $[C_{HC} \times d_{HC}]/[C_{CO2} \times d_{CO2}]$, $[C_{CO2} \times d_{CO2}]/[t_{air} \times Cp]$, $[C_{CO} \times d_{CO}]/[t_{air} \times Cp]$, and $[C_{CO2} \times d_{CO2}]/[t_{air} \times Cp]$. Ventilation was assessed by comparing the values of these derived parameters estimated from the test data to reference values obtained during the testing of individual materials in small-scale flammability tests,[15] where the equivalence ratio was measured precisely [7]. The reference parameters used in this comparison include $Y(CO)/Y(CO_2)$, $Y(HC)/Y(CO_2)$, $Y(CO_2)/\Delta H_{CON}$, $Y(CO)/\Delta H_{CON}$, $Y(HC)/\Delta H_{CON}$ (Table 1).

Table 2

Fire Products for Well-ventilated Fires[1,2]

material	$Y(CO)/Y(CO_2)$ (g/g)	$Y(HC)/Y(CO_2)$ (g/g)	$Y(CO_2)/\Delta H_{CON}$ (g/kJ)	$Y(CO)/\Delta H_{CON}$ (g/kJ)	$Y(HC)/\Delta H_{CON}$ (g/kJ)
gasoline[3]	0.011 – 0.014	0.0032 – 0.0039	0.14 – 0.16	0.0021 – 0.0026	0.00058 – 0.00073
poly(ethylene)	0.0087	0.0025	0.13	0.0011	0.00032
poly(propylene)	0.0086	0.0022	0.12	0.0011	0.00027
poly(styrene)	0.026	0.0060	0.21	0.0054	0.00127
polyester	0.05	0.019	0.15	0.0065	0.00185
Nylon	0.018	0.0078	0.13	0.0035	0.00098
Flexible urethane foams	0.006 - 0.027	0.0013 - 0.0033	0.15 - 0.21	0.0012 - 0.0055	0.00023 - 0.00069
Rigid urethane foams	0.015 - 0.046	0.006 - 0.036	0.17 - 0.23	0.0028 - 0.0081	0.00011 - 0.00070

[1] Values reported in Table 2 were calculated from data reported in Table 3-4.11 in reference 9.

[2] $Y(CO)$ is the mass-yield of carbon monoxide (g). $Y(CO_2)$ is the mass-yield of carbon dioxide (g). $Y(HC)$ is the mass-yield of gaseous hydrocarbons (g). $Y(CO_2)/\Delta H_{con} = (C_{CO_2}/c_p\Delta T)(\rho_{CO_2}/\rho_{air})$, $Y(CO)/\Delta H_{con} = (C_{CO}/c_p\Delta T)(\rho_{CO}/\rho_{air})$, and $Y(HC)/\Delta H_{con} = (C_{HC}/c_p\Delta T)(\rho_{HC}/\rho_{air})$. ΔH_{CON} is the convective heat of combustion per unit fuel vaporized (kJ/g). The C_i are the gas-phase concentrations (volume fraction) of carbon dioxide, carbon monoxide, and total hydrocarbons. The ρ_i are the gas-phase densities (g/m^3) of carbon dioxide, carbon monoxide, total hydrocarbons, and air. c_p is the heat capacity of air (kJ/g-K). ΔT is the difference between the gas temperature and the temperature of the ambient air (K).

[3] Values for gasoline were estimated from the data in Table 3-4.11 in reference 7 assuming an aliphatic hydrocarbon content of 60 to 70 % and an aromatic hydrocarbon content of 30 to 40%.

---

[15] Small-scale flammability tests to determine combustion properties of materials were conducted in the Factory Mutual Research Corporation Flammability Apparatus is a small-scale test apparatus (see reference 7).

The values of these parameters in Table 2 were determined for the well-ventilated combustion of poly(ethylene), poly(propylene), poly(styrene), polyester, Nylon, a group of flexible urethane foams, and a group of rigid urethane foams in controlled small-scale laboratory tests.[16]

Analysis of the data from the Fire Products Collector indicates that the production of carbon monoxide relative to carbon dioxide was greater than expected for well-ventilated combustion of gasoline and materials similar to those used in the test vehicle. Figure 47 shows a plot of $[G_{CO}]/[G_{CO2}]$ versus time post-ignition, where G_{CO} and G_{CO2} are the carbon monoxide- and carbon dioxide-release rates measured using the Fire Products Collector (**APPENDIX H**). The ratio $[G_{CO}]/[G_{CO2}]$ is equivalent to $[Y(CO)]/[Y(CO_2)]$ in Table 2.

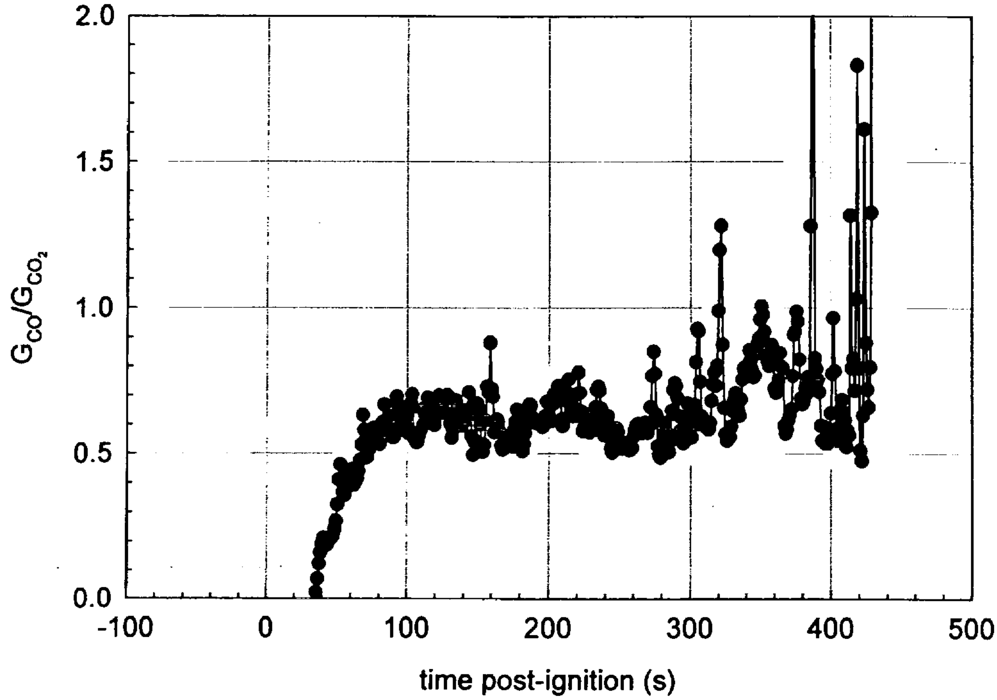

Figure 47. Fire Test F980611. Plots of $[G_{CO}]/[G_{CO2}]$ (—●—) versus time post-ignition determined from the carbon monoxide and carbon dioxide release rates measured by the Fire Products Collector.

Before ignition, $[G_{CO}]/[G_{CO2}]$ was undefined because $G_{CO} = G_{CO2} = 0$. The carbon dioxide- and carbon monoxide-release rates (Plots H2 and H3, respectively) were low during the first 30 to 40

---

[16] The compositions and physical properties such as density, thermal conductivity, and heat capacity of these materials were not specified.

seconds of this test. During this time, small absolute variations in the measured values of G_{CO} and G_{CO2} resulted in the large unrealistic positive and negative variations in the calculated value of $[G_{CO}]/[G_{CO2}]$. Values of $[G_{CO}]/[G_{CO2}]$ before about 35 seconds post-ignition were therefore not plotted in Figure 47.

The data plotted in Figure 47 indicate that the fire in this test was under-ventilated. The value of $[G_{CO}]/[G_{CO2}]$ increased from 35 seconds post-ignition to a pseudo-steady-state value of approximately 0.6 between 100 and 300 seconds post-ignition (Fig. 47). The data in Table 2 indicates that $0.011 < [Y(CO)]/[Y(CO_2)] < 0.014$ for well-ventilated combustion of gasoline, and a value of $[G_{CO}]/[G_{CO2}] > 0.014$ indicates under-ventilated combustion. The value of $[G_{CO}]/[G_{CO2}]$ would have been expected to increase as flames spread to polymeric materials in the test vehicle. It was not possible to determine the exact timing of ignition of individual materials in the test vehicle during this test or the relative amounts of carbon dioxide and carbon monoxide produced by each material, including gasoline, that was burning. The data in Table 2 indicate that $0.006 < [Y(CO)]/[Y(CO_2)] < 0.05$ for well-ventilated combustion of materials similar to those used in the test vehicle, and a value of $[G_{CO}]/[G_{CO2}] > 0.05$ indicates under-ventilated combustion. Thus, values of $0.5 < [G_{CO}]/[G_{CO2}] < 0.7$ from 100 to 300 seconds post-ignition indicate under-ventilated combustion predominated for this test (Fig. 47).

As the test progressed, the fire on the cement board surface under the test vehicle diminished, and the burning gasoline appeared to be localized in the fuel tank skid plate (**Section 4**). The clearance between the lower surface of the fuel tank and the skid plate was less than 1 in. Flames emanating from the fuel tank skid plate appeared to spread outward into the drive train tunnel and into the spaces between exhaust system heat shields and the floor panel on the right side the test vehicle. The results in Figure 47 suggest that airflow into these confined spaces resulted in under-ventilated combustion of gasoline vapor. As combustible materials in the test vehicle were heated by flames form burning gasoline, these materials would have undergone thermal decomposition before starting to burn. Thermal decomposition of these materials in air would have yielded a mixture of incomplete oxidation products, including carbon monoxide, resulting in values of $[G_{CO}]/[G_{CO2}]$ greater than those expected for well-ventilated combustion.

A similar analysis of air temperature and gas concentration data from the passenger compartment is shown in Figures 48 through 52. Air temperature and gas concentration data from the passenger compartment were used to determine $[C_{CO} \times d_{CO}]/[C_{CO2} \times d_{CO2}]$, $[C_{HC} \times d_{HC}]/[C_{CO2} \times d_{CO2}]$, $[C_{CO2} \times d_{CO2}]/[t_{air} \times Cp]$, $[C_{CO} \times d_{CO}]/[t_{air} \times Cp]$, and $[C_{HC} \times d_{HC}]/[t_{air} \times Cp]$. In these formulas, C_j is the gas-phase concentration of species j, d_j is the density of species j, t_{air} is the air temperature, and C_p is the heat capacity of air. The product $[C_j \times d_j]$ equals the mass-concentration of species j in passenger compartment. The concentrations of the gaseous combustion products (C_j) were determined by Fourier Transform Infrared Spectrometry (**APPENDIX I**). Air temperature data from the aspirated thermocouple assemblies in the passenger compartment (**APPENDIX D**) was used to determine t_{air}. The ratios $[C_{CO} \times d_{CO}]/[C_{CO2} \times d_{CO2}]$, $[C_{HC} \times d_{HC}]/[C_{CO2} \times d_{CO2}]$, $[C_{CO2} \times d_{CO2}]/[t_{air} \times Cp]$, $[C_{CO} \times d_{CO}]/[t_{air} \times Cp]$, and $[C_{HC} \times d_{HC}]/[t_{air} \times Cp]$ are equivalent to $[Y(CO)]/[Y(CO_2)]$, $[Y(HC)]/[Y(CO_2)]$, $Y(CO_2)/\Delta H_{CON}$, $Y(CO)/\Delta H_{CON}$, and $Y(HC)/\Delta H_{CON}$, respectively, in Table 2.

The concentrations of carbon dioxide, carbon monoxide, and hydrocarbons in the passenger compartment of the test vehicle started to increase between 120 and 150 seconds post-ignition (**APPENDIX H**). The air temperature recorded from the aspirated thermocouples located at the lower surface of the headlining panel started to increase between 100 and 120 seconds post-ignition (APPENDIX D). Values of $[C_{CO} \times d_{CO}]/[C_{CO2} \times d_{CO2}]$ and $[C_{HC} \times d_{HC}]/[C_{CO2} \times d_{CO2}]$ increased sharply at this time to $0.09 <$ of $[C_{CO} \times d_{CO}]/[C_{CO2} \times d_{CO2}] < 0.12$ and $0.04 < [C_{HC} \times d_{HC}]/[C_{CO2} \times d_{CO2}] < 0.05$ (Fig.'s 48 and 49). These values were greater than the respective reference values for well-ventilated combustion of shown in Table 2.

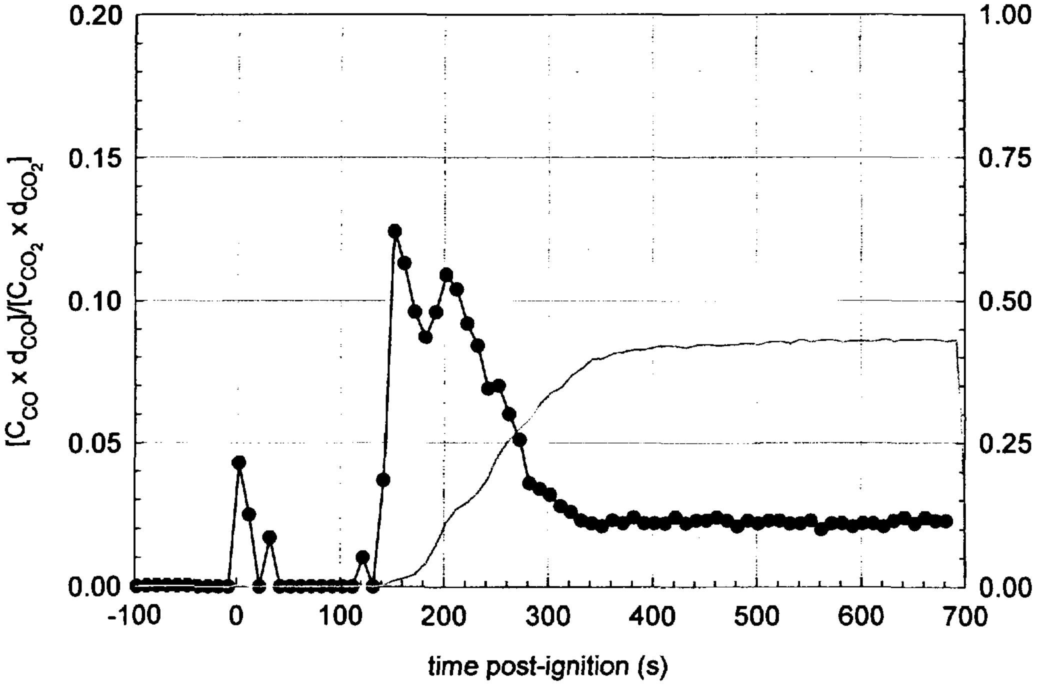

Figure 48. Fire Test F980611. Plots of $[C_{CO} \times d_{CO}]/[C_{CO2} \times d_{CO2}]$ (–●–, left axis) and the concentration of carbon monoxide (—, right axis) in the passenger compartment.

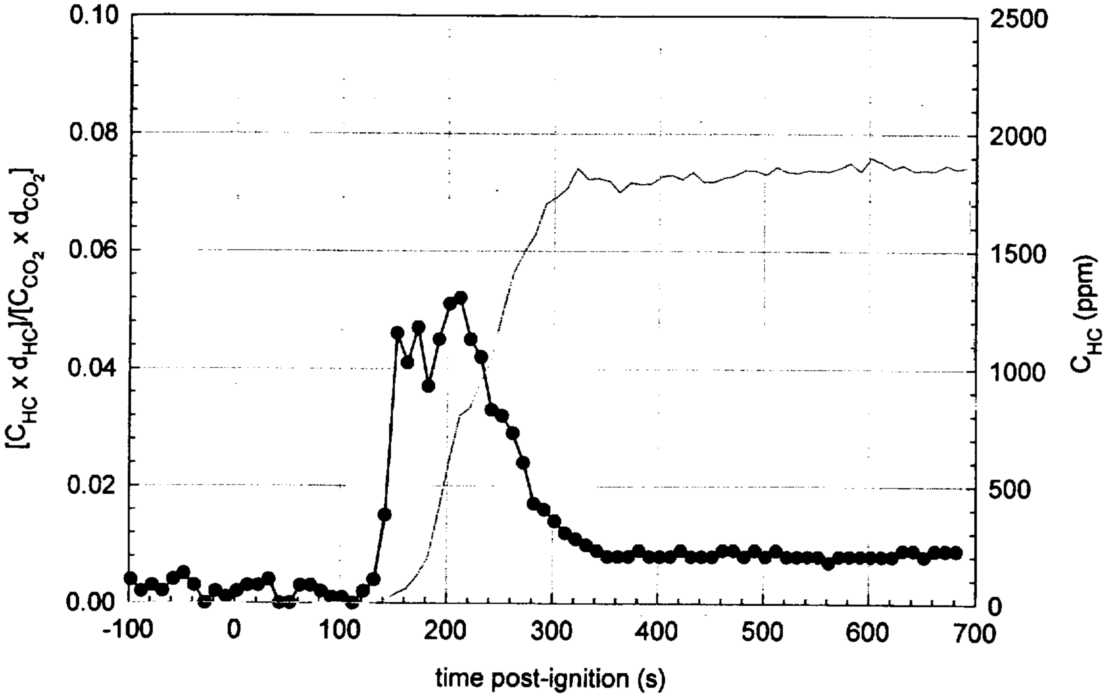

Figure 49. Fire Test F980611. Plots of $[C_{HC} \times d_{HC}]/[C_{CO2} \times d_{CO2}]$ (–●–, left axis) and the concentration of total hydrocarbons (—, right axis) in the passenger compartment.

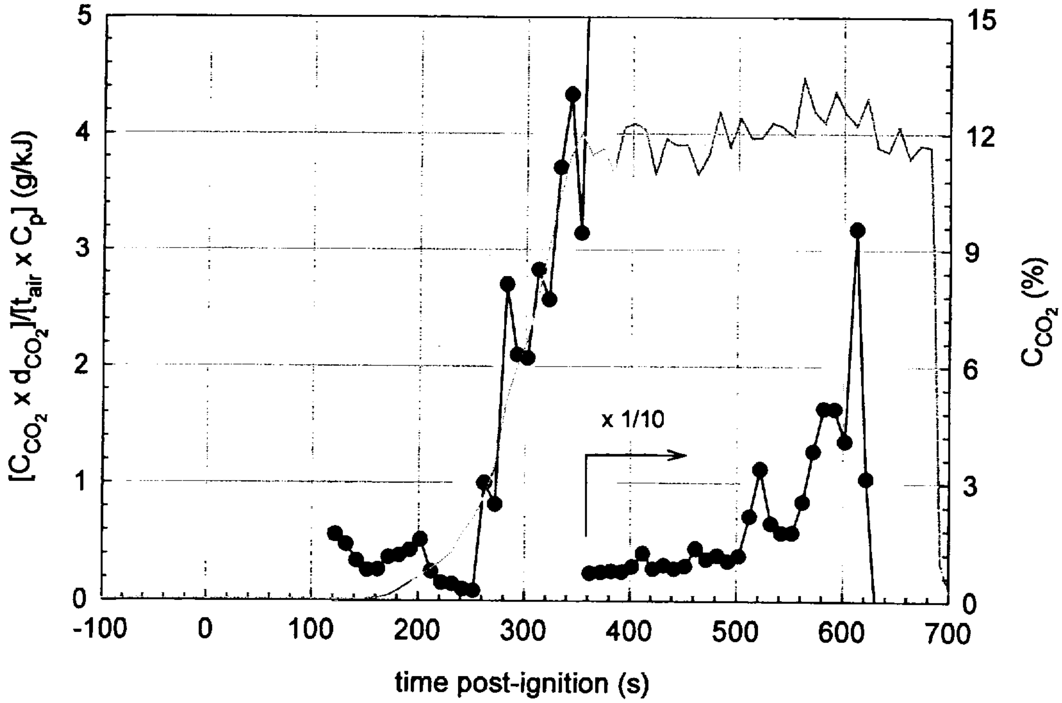

Figure 50. Fire Test F980611. Plots of $[C_{CO2} \times d_{CO2}]/[t_{air} \times Cp]$ (–●–, left axis) and the concentration of carbon dioxide (—, right axis) in the passenger compartment.

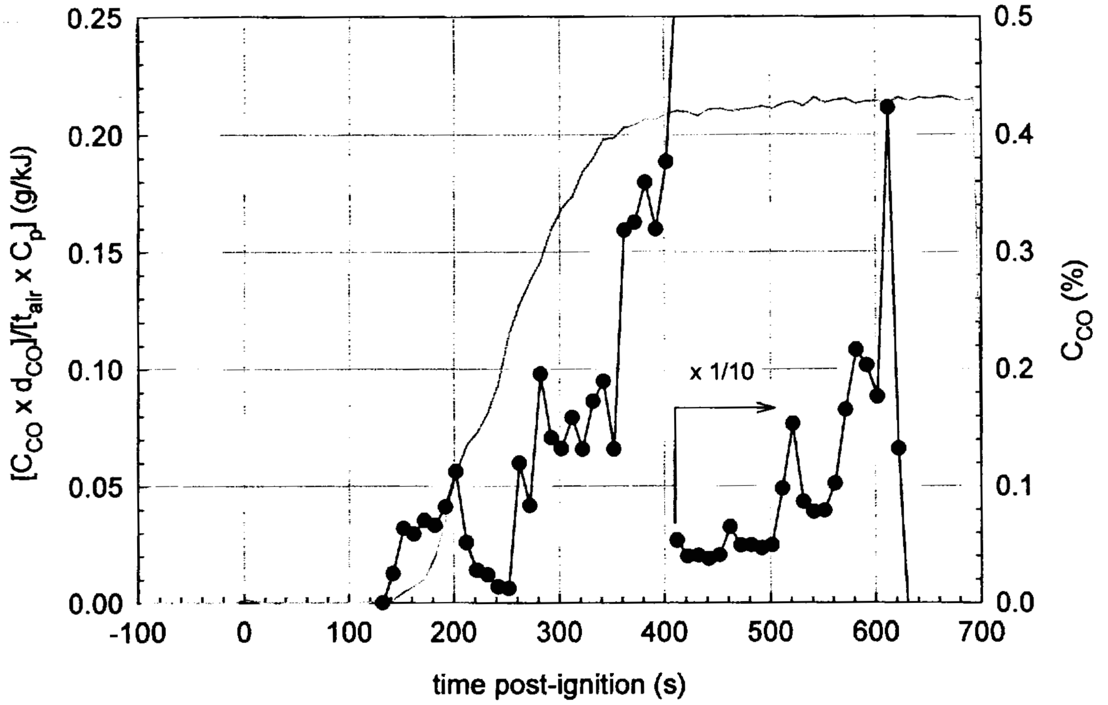

Figure 51. Fire Test F980611. Plots of $[C_{CO} \times d_{CO}]/[t_{air} \times Cp]$ (–●–, left axis) and the concentration of carbon monoxide (—, right axis) in the passenger compartment.

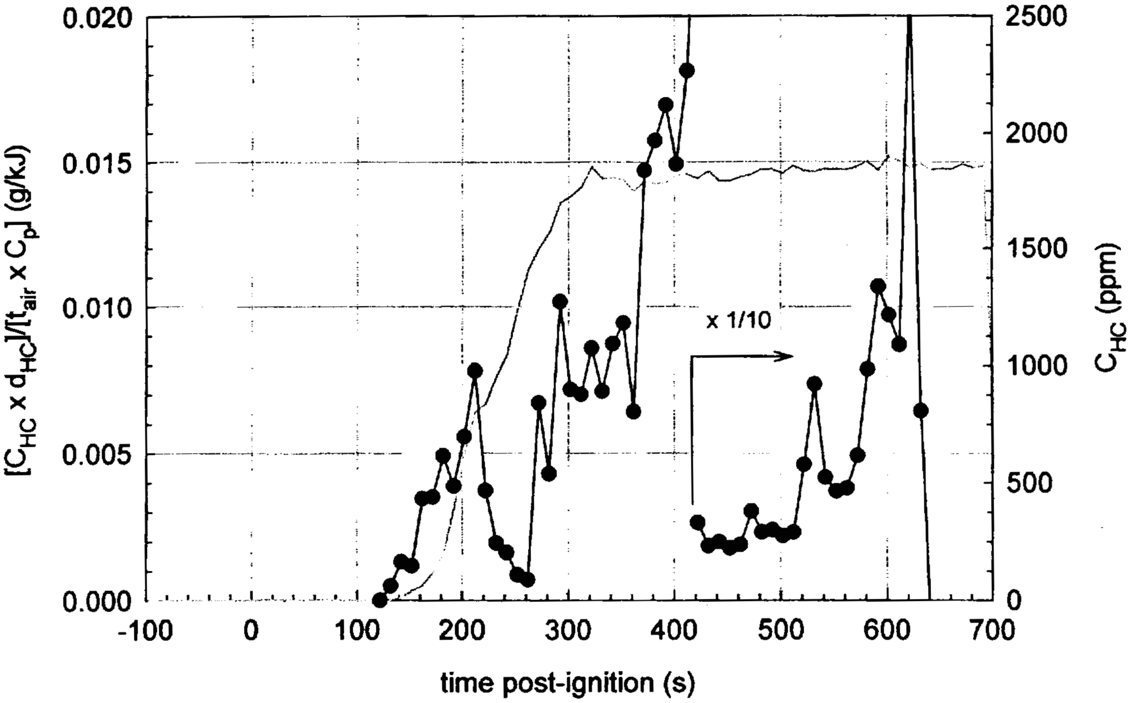

Figure 52. Fire Test F980611. Plots of $[C_{HC} \times d_{HC}]/[t_{air} \times Cp]$ (–●–, left axis) and the concentration of hydrocarbons (—, right axis) in the passenger compartment.

Values of $[C_{CO} \times d_{CO}]/[C_{CO2} \times d_{CO2}]$ and $[C_{HC} \times d_{HC}]/[C_{CO2} \times d_{CO2}]$ after about 200 seconds post-ignition (Fig.'s 48 and 49), asymptotically approaching values of 0.020 – 0.025 and 0.08 – 0.09, respectively.

Plots of $[C_{CO2} \times d_{CO2}]/[t_{air} \times Cp]$, $[C_{CO} \times d_{CO}]/[t_{air} \times Cp]$, and $[C_{HC} \times d_{HC}]/[t_{air} \times Cp]$ start at about 120 seconds post-ignition, when temperatures recorded from the aspirated thermocouples at the height of the FTIR gas sampling inlet (t_{air}) started to increase (Fig.'s 50 through 52). Values of $[C_{CO2} \times d_{CO2}]/[t_{air} \times Cp]$, $[C_{CO} \times d_{CO}]/[t_{air} \times Cp]$, and $[C_{HC} \times d_{HC}]/[t_{air} \times Cp]$ generally increased after 120 seconds post-ignition, peaking at $[C_{CO2} \times d_{CO2}]/[t_{air} \times Cp] = 0.52$, $[C_{CO} \times d_{CO}]/[t_{air} \times Cp] = 0.056$, and $[C_{HC} \times d_{HC}]/[t_{air} \times Cp] = 0.0078$ between 200 and 210 seconds post-ignition (Fig.'s 50 through 52). Values of $[C_{CO2} \times d_{CO2}]/[t_{air} \times Cp]$, $[C_{CO} \times d_{CO}]/[t_{air} \times Cp]$, and $[C_{HC} \times d_{HC}]/[t_{air} \times Cp]$ decreased, approaching values expected for well-ventilated combustion (Table 2) between about 210 and 255 seconds post-ignition (Fig.'s 50 through 52).

These trends in $[C_{CO} \times d_{CO}]/[C_{CO2} \times d_{CO2}]$, $[C_{HC} \times d_{HC}]/[C_{CO2} \times d_{CO2}]$, $[C_{CO2} \times d_{CO2}]/[t_{air} \times Cp]$, $[C_{CO} \times d_{CO}]/[t_{air} \times Cp]$, and $[C_{HC} \times d_{HC}]/[t_{air} \times Cp]$ appear to have been related to transition from pyrolysis to flaming combustion of materials in the passenger compartment. Initially, components in the passenger compartment such as the floor carpet and foam pads in the seat cushions were heated by conduction through the floor panel or, in the case of the foam pad in the left front seat cushion, directly by flames from the burning gasoline under the test vehicle. This heating resulted in thermal decomposition of the constituent materials in these components, producing more carbon monoxide (CO) and unburned hydrocarbons (HC), and less carbon dioxide (CO_2) than predicted for well-ventilated combustion. The convective heat release in the passenger compartment also would have been less than expected for well-ventilated combustion. As these materials ignited, the rates of production of carbon monoxide and unburned hydrocarbons would have decreased, while the rate of production of carbon monoxide and the convective heat release in the passenger compartment would have increased.

7 Estimation of Skin Temperature Profiles from Measured Heat Flux Data, Fractional Equivalent Dose Parameters from Measured Gas Concentration Data, and Thermal Damage to the Respiratory Tract from Measured Air Temperature Data

The mathematical model "BURNSIM: A Burn Hazard Assessment Model" [8] was used to estimate the time and depth of burns to exposed skin. The inputs to this model were heat fluxes derived from the directional flame thermometer measurements and air temperatures measured using the aspirated thermocouple probe.

Two models were used to estimate the potential for toxicity from exposure to the combustion gases measured in the passenger compartment. The Federal Aviation Administration (FAA) Combined Hazard Survival Model [9] was used to estimate the time to incapacitation and the time to lethality. A model described by Purser [10] also was used to estimate the time to incapacitation. Both models estimate the risk from exposure to hot air, reduced oxygen, carbon monoxide, carbon dioxide, hydrogen cyanide, hydrogen chloride, hydrogen fluoride, hydrogen bromide, acrolein, and nitrogen dioxide. Both models also account for the physiological effect of carbon dioxide-induced hyperventilation, which increases the respiratory uptake.

7.1 The BURNSIM Model

The computer model BURNSIM was the analytical tool chosen to estimate skin temperature depth profiles from the heat flux data in **APPENDIX G**. The BURNSIM model divides the skin into a series of ten layers, with a uniform thickness of 0.2 mm per layer. The top layer was divided into 8 layers each with a uniform thickness of 0.025 mm to better account for the non-instantaneous heat transfer from the epidermal surface into the first layer.

Skin Model of BURNSIM

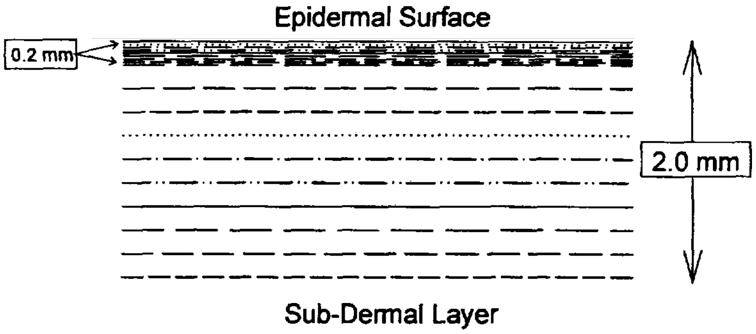

The BURNSIM analysis used here incorporated the following assumptions to estimate skin temperature profiles. The absorbtivity of exposed skin was assumed to be 0.60 (i.e., the skin absorbs 60% of the radiation incident upon the epidermal surface). The absorbtivity of surface hair was assumed to be 0.05 (i.e., surface hair absorbs 5% of the incident radiation before it reached the skin). Exposed skin was assumed to absorb 100% of the measured convective heat flux to its surface. The temperature of each layer was estimated as a function of the time of exposure to an external heat flux. A portion of the absorbed heat is removed from the skin by the circulatory system. Thermal damage to a layer of skin exceeds the capacity of the physiological repair processes when the temperature of that layer exceeds 45°C.

In estimating skin temperature, the analysis presented in this paper using BURNSIM did not account for the presence of facial or head hair, or clothing covering the skin, all of which may block direct heat transfer to the skin. This analysis also did not account for variations in skin thickness among individuals, or variations in skin thickness at different parts of the body on the same individual. For example, skin thickness can vary from 1 to 5 mm with body location. This analysis also did not account for effect of skin pigmentation on absorbtivity. In using the radiative and convective heat flux estimates shown in **APPENDIX G** to estimate skin temperature profiles, this analysis assumed that the location and orientation of the skin was identical to that of the HFT/RAD transducer assemblies used to measure heat flux. Small changes in position or angle of the surface can result in large differences between in the incident heat flux to the surface (see below). Based on the currently available information and data, the accuracy of the estimated skin temperature depth profiles in humans exposed to heat flux levels from fire such as measured in this test obtained using BURNSIM has not been determined.

7.1.1 Estimation of Skin Temperature Profiles using BURNSIM

The absorbed heat flux at each of the HFT/RAD assembly locations was estimated from the data recorded from HFT/RAD 10 through HFT/RAD 15. Estimates of absorbed heat flux obtained by analysis of the data recorded from these transducers were input into the BURNSIM model to estimate skin temperature profiles for exposed skin at these locations. The BURNSIM calculations were performed using data recorded between 0 and 300 seconds post-ignition. The resulting estimated temperature profiles are shown in Figures 53 through 58.

This BURNSIM analysis of the HFT/RAD data indicated that estimated skin temperature profiles increased between 200 and 250 seconds post-ignition (Fig. 53 through 58). The timing and magnitude of increases in the estimated skin temperature profiles calculated from the recorded convective and radiative heat flux data, which was dependent on the location and orientation of the HFT/RAD assemblies in the test vehicle. For example, HFT/RAD assemblies 10, 11, and 12 were located above the left front seat cushion and HFT/RAD assemblies 13, 14, and 15 were located above the left rear seat cushion (**APPENDIX E**).

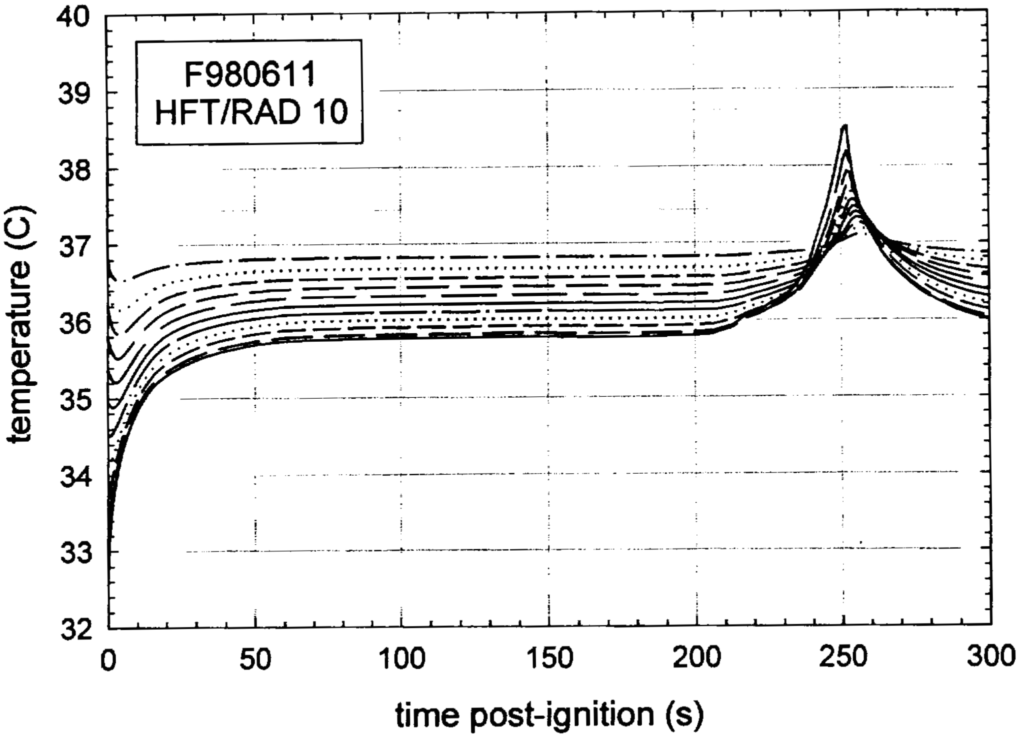

Figure 53. Fire Test F980611. Skin temperature profiles estimated from heat flux data recorded from HFT/RAD Assembly 10 (**APPENDIX E**, Plots E3 and E4).

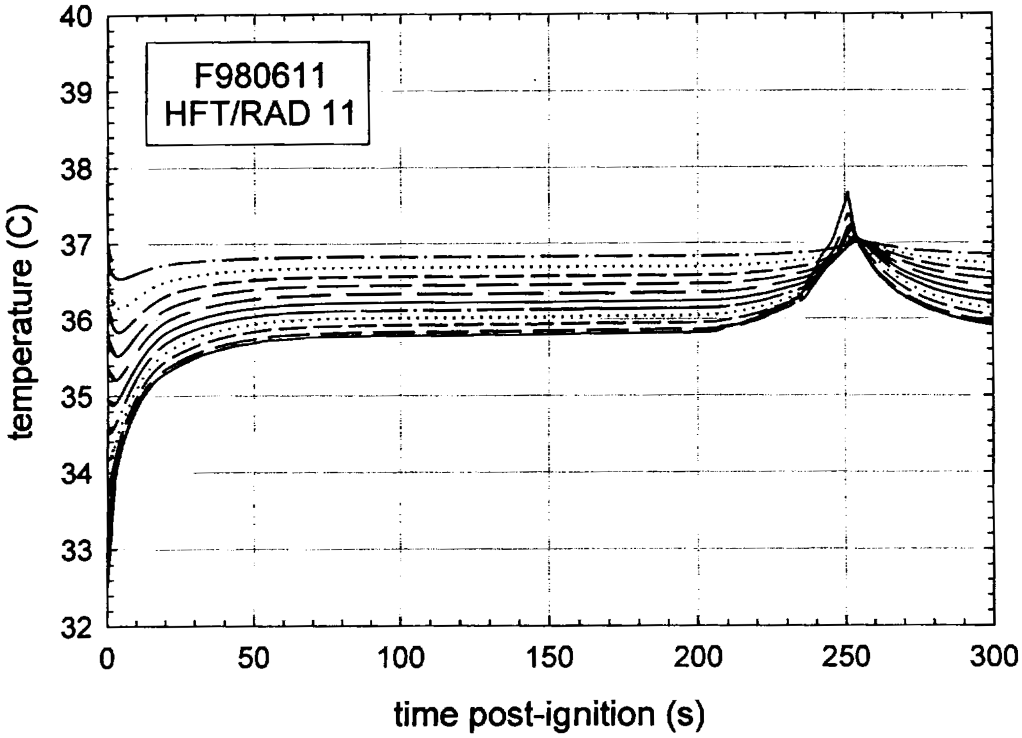

Figure 54. Fire Test F980611. Skin temperature profiles estimated from data recorded from HFT/RAD Assembly 11 (**APPENDIX E**, Plots E5 and E6).

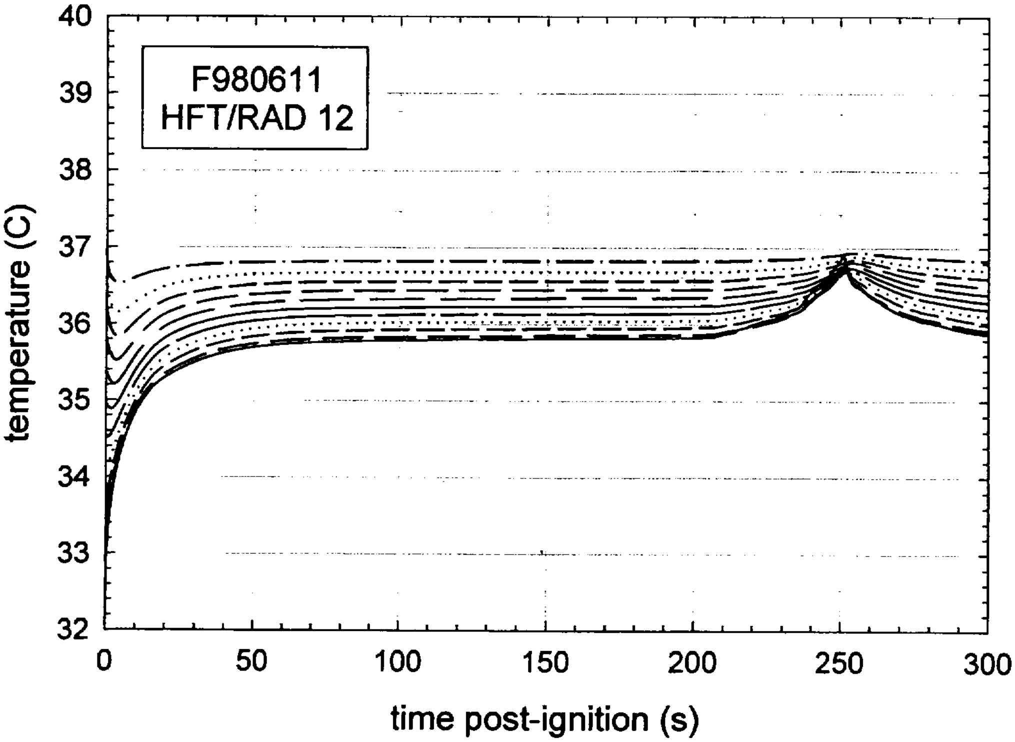

Figure 55. Fire Test F980611. Skin temperature profiles estimated from data recorded from HFT/RAD Assembly 12 (**APPENDIX E**, Plots E7 and E8).

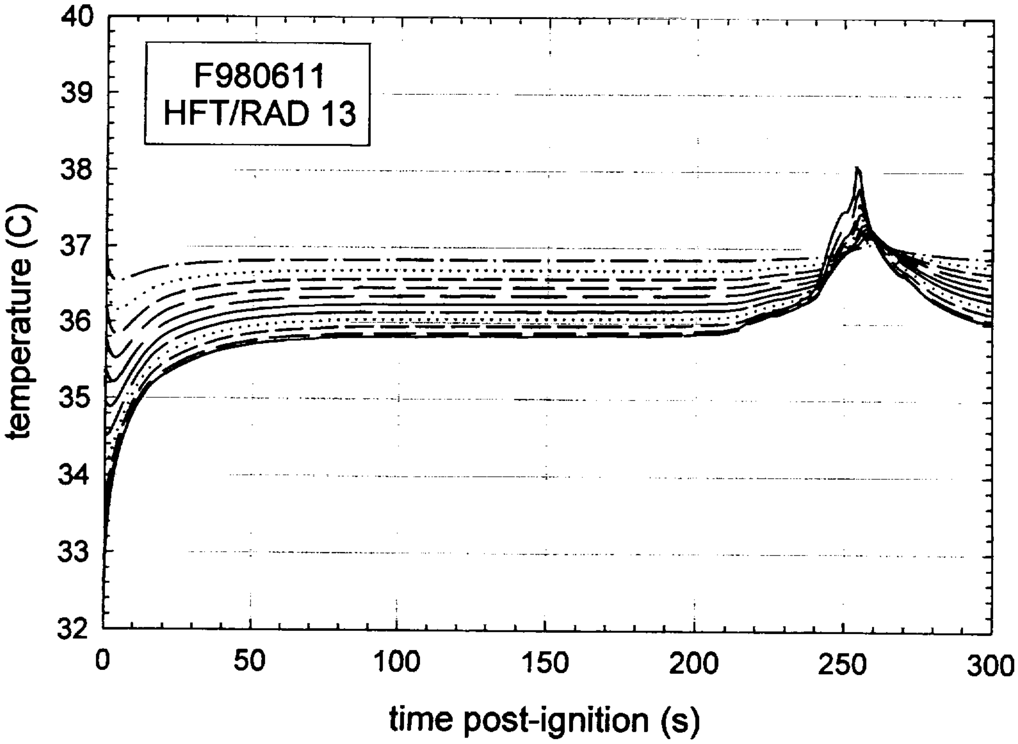

Figure 56. Fire Test F980611. Skin temperature profiles estimated from data recorded from HFT/RAD Assembly 13 (**APPENDIX E**, Plots E9 and E10).

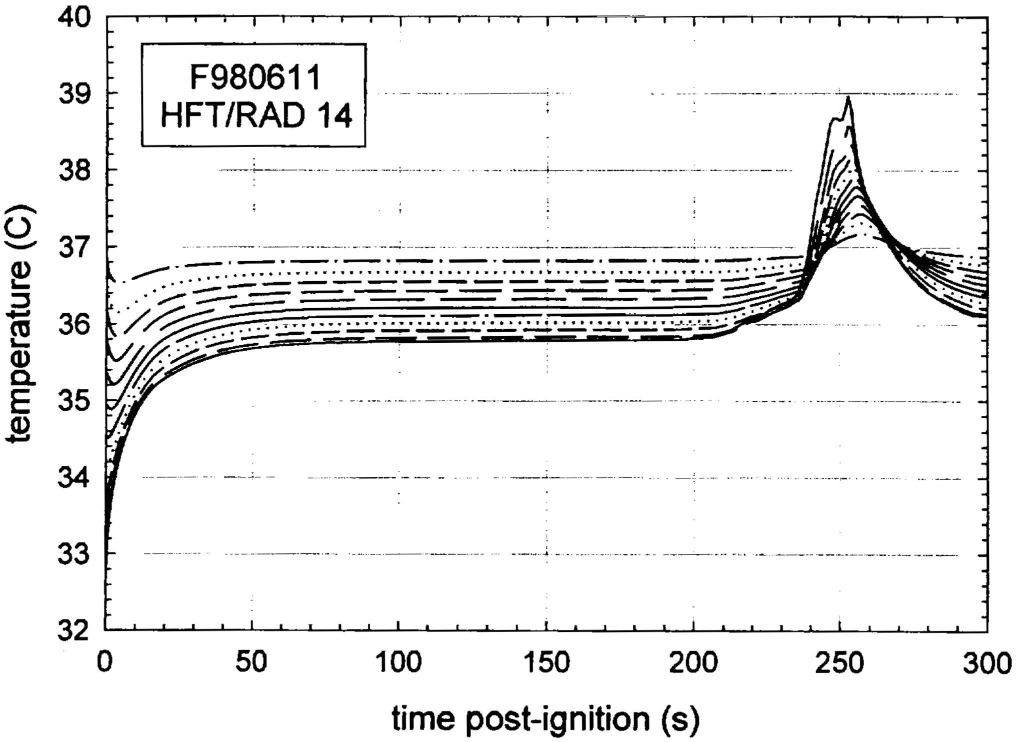

Figure 57. Fire Test F980611. Skin temperature profiles estimated from data recorded from HFT/RAD Assembly 14 (**APPENDIX E**, Plots E11 and E12).

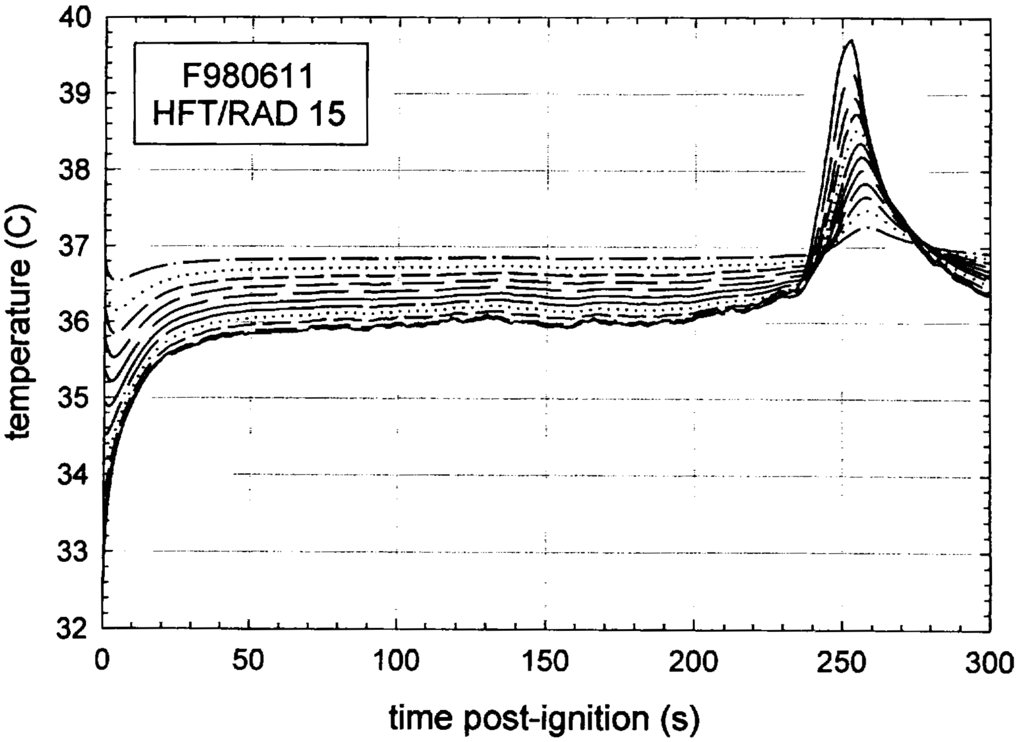

Figure 58. Fire Test F980611. Skin temperature profiles estimated from data recorded from HFT/RAD Assembly 15 (**APPENDIX E**, Plots E13 and E14).

The transducer surfaces in HTF/RAD10, HTF/RAD11, and HFT/RAD12 were oriented upward, to the left, and downward toward the foot area in front of the left front seat, respectively (**APPENDIX E**). The transducer surfaces in HTF/RAD13, HFT/RAD14, and HFT/RAD15 were oriented to the left, upward, and forward, respectively (**APPENDIX E**). Skin temperature profiles estimated using data recorded from HFT/RAD10, HFT/RAD11, and HFT/RAD12 showed a maximum estimated epidermal temperatures of 38.5°C at 252 seconds post-ignition (Fig. 53), 37.6°C at 251 seconds post-ignition (Fig. 54), and 36.9°C at 251 seconds post-ignition (Fig. 55). Skin temperature profiles estimated using data recorded from HFT/RAD13, HFT/RAD14, and HFT/RAD15 showed a maximum estimated epidermal temperatures of 38.1°C at 254 seconds post-ignition (Fig. 56), 39.0°C at 253 seconds post-ignition (Fig. 57), and 39.7°C at 253 seconds post-ignition (Fig. 58).

7.2 The FAA Combined Hazard Survival Model and Purser's Model of Combustion Gas Toxicity

The FAA Combined Hazard Survival Model and Purser's model utilize the concept of a Fractional Effective Dose [FED] to estimate the cumulative effects of exposure to a mixture of gases produced by burning materials. For exposure to a single gas with an unchanging concentration in air, the Fractional Effective Dose for Incapacitation [FED(I)] is defined as the product of the gas-phase concentration and the time of exposure (C × t) normalized to the concentration-time product that results in incapacitation of 50% of an exposed population [8, 9]. Similarly, the Fractional Effective Dose for lethality [FED(L)] is defined as the product of the gas-phase concentration and the time of exposure normalized to the concentration-time product that results in the death of 50% of an exposed population [see references in 8 and 9]. The estimates of FED(I) and FED(L) obtained using the FAA Combined Hazard Survival Model or Purser's model of combustion gas toxicity and presented in this report cannot be used to predict precisely when the gas concentrations measured in this test would have resulted in incapacitating narcosis or death for a vehicle occupant. Whether exposure to these gases results in toxicity depends on a number of complex physical and physiological variables.

Some of the physical variables include the exact chemical composition of the gaseous mixture, the concentration of each component of the gaseous mixture, and the time of exposure. Exposure to these gases in a burning vehicle can be highly variable, and depend on factors such as elevation in the passenger compartment and airflow through the passenger compartment. As mentioned in the previous section, combustion gases are hotter than the ambient air and form an upper-layer. As both heat and mass are conserved in a fire, the existence of a steep vertical air-temperature gradient implies the existence of similarly steep vertical concentration gradients for gaseous combustion products accumulating in the passenger compartment. The location of the head and nose in the passenger compartment will effect the exposure concentration. An occupant whose head was located below the level where gases were measured, such as an occupant bent over in the seat, would have been exposed to lower concentrations of combustion gases than those shown in **APPENDIX H**. Airflow through the passenger compartment will dilute or remove these gases.

Uncertainties in the responses of humans exposed to these gases also complicate the determination of when and whether toxicity occurs. The mathematical equations for the calculation of FED(I) and FED(L) were derived by analysis of data from controlled experiments in which different species of laboratory animals were exposed to a range of concentrations of each gas. In using data from these laboratory animal experiments to define FED(I) and FED(L), both models implicitly assume that humans respond the same as laboratory animals to exposure to these gases – an assumption that is largely untested and may not be accurate. For example, except for incapacitation from exposure to carbon dioxide, none of the model predictions using either the FAA Combined Hazard Survival Model or Purser's model have been validated for humans. That is, the accuracy of FED(I) and FED(L) in predicting human responses to exposure to the combustion gases measured in this test has not been determined. Consequently, there is a high degree of uncertainty as to the effect exposure to these levels of combustion gases would actually have on a human vehicle occupant. In addition, neither of these models accounts for variation in individual responses to these gases nor the effect of trauma suffered during the crash on an occupant's response to these gases.

The equations presented in both the FAA Combined Hazard Survival Model and in Purser's model divide the exposure into one-minute intervals when the concentration of the gaseous species changes with time. In this test, Fourier Transform Infrared spectra were obtained at seven-second intervals to characterize the changing gas concentrations observed in the passenger compartment. The equations presented in the FAA Combined Hazard Survival Model and in Purser's model were modified to account for the faster sampling times used in this test. These modified equations are shown below and were used to derive the estimated of FED(I) and FED(L) shown in **SECTION 7.2.1.**

Carbon dioxide-induced hyperventilation can increase the respiratory uptake of airborn combustion products. The FAA Combined Hazard Survival Model uses a multiplication factor to account for the increased respiratory uptake of gaseous combustion products because of exposure to elevated levels of carbon dioxide [V_{CO2}]:

$$V_{CO_2} = \frac{\exp(1.9086 + 0.2496 \times C_{CO_2})}{6.8} \qquad (1)$$

where the units of C_{CO2} are %. This equation was not modified for the analysis presented in **SECTION 7.2.1**.

The Fractional Effective Doses for Incapacitation from exposure to carbon dioxide, carbon monoxide, hydrogen chloride, hydrogen cyanide and decreased oxygen were calculated using the following equations modified to account for sampling intervals of less than 1 minute:

$$FED(I)_{CO_2} = \left(\frac{t}{60}\right) \times \sum \left\{ \frac{1}{2193.8 - (311.6 \times C_{CO_2})} \right\} \qquad (2)$$

when $5.5 \le C_{CO2} \le 7.0\%$,

$$FED(I)_{CO_2} = \left(\frac{t}{60}\right) \times \sum \left\{ \frac{1}{\exp(6.1623 - (0.5189 \times C_{CO_2}))} \right\} \qquad (3)$$

when $C_{CO2} > 7.0\%$,

$$FED(I)_{CO} = \left(\frac{t}{60}\right) \times \left(\frac{1}{3.4250}\right) \times \sum \{V_{CO_2} \times C_{CO}\} \qquad (4)$$

when $V_{CO2} \times C_{CO} > 0.01\%$,

$$FED(I)_{HCl} = \left(\frac{t}{60}\right) \times \sum \left\{ \frac{1}{3 + \dfrac{336{,}000}{(V_{CO_2} \times C_{HCl}) - 300}} \right\} \qquad (5)$$

when $V_{CO2} \times C_{HCl} > 300$ ppm;

$$FED(I)_{HCN} = \left(\frac{t}{60}\right) \times \left(\frac{1}{564}\right) \times \sum \{(V_{CO_2} \times C_{HCN}) - 63\} \qquad (6)$$

when $V_{CO2} \times C_{HCN} > 63$ ppm; and

$$FED(I)_{O_2} = \left(\frac{t}{60}\right) \times \sum \left\{ \frac{1}{\exp\left(8.55 - \left(0.511 \times \left(20.9 - C_{O_2}\right)\right)\right)} \right\} \quad (7)$$

when $C_{O2} < 11\%$. The value of t in these equations was the time in seconds between acquisition of FTIR spectra. The overall Fractional Effective Dose for Incapacitation was calculated by summing the terms in equations 2 through 7:

$$FED(I)_{TOTAL} = FED(I)_{CO_2} + FED(I)_{CO} + FED(I)_{HCl} + FED(I)_{HCN} + FED(I)_{O_2} \quad (8)$$

The Fractional Effective Doses for Lethality from exposure to carbon monoxide and hydrogen cyanide were calculated using the following equations modified to account for sampling intervals of less than 1 minute:

$$FED(L)_{CO} = \left(\frac{t}{60}\right) \times \sum \left\{ \frac{1}{\exp\left(5.85 - \left(0.00037 \times V_{CO_2} \times C_{CO}\right)\right)} \right\} \quad (9)$$

when $2000 \leq V_{CO2} \times C_{CO} \leq 9000$ ppm,

$$FED(L)_{CO} = \left(\frac{t}{60}\right) \times \sum \left\{ \frac{1}{0.4 + \left(\frac{58{,}000}{V_{CO_2} \times C_{CO}}\right)} \right\} \quad (10)$$

when $V_{CO2} \times C_{CO} > 9000$ ppm, and

$$FED(L)_{HCN} = \left(\frac{t}{60}\right) \times \left(\frac{1}{2586}\right) \times \sum \left\{ \left(V_{CO_2} \times C_{HCN}\right) - 43.2 \right\} \quad (11)$$

when $V_{CO2} \times C_{HCN} > 43.2$ ppm;

The overall Fractional Effective Dose for Lethality was calculated by summing the terms in equations 8 through 10:

$$FED(L)_{TOTAL} = FED(L)_{CO} + FED(L)_{HCN} \quad (12)$$

The model described by Purser also uses a multiplication factor to account for the enhanced respiratory uptake of toxic gases because of exposure to elevated levels of carbon dioxide:

$$V_{CO_2} = \frac{\exp\left(1.9086 + \left(0.2496 \times C_{CO_2}\right)\right)}{6.8} \tag{13}$$

The Fractional Effective Doses for Incapacitation from exposure to carbon monoxide and hydrogen cyanide were calculated using the following equations modified to account for sampling intervals of less than 1 minute:

$$FED(I)_{CO_2} = \left(\frac{t}{60}\right) \times \sum \left\{ \frac{1}{\exp\left(6.1623 - \left(0.5189 \times C_{CO_2}\right)\right)} \right\} \tag{14}$$

when $C_{CO2} > 5\%$,

$$FED(I)_{CO} = \left(\frac{t}{60}\right) \times V_{CO_2} \times \sum \left\{ \frac{0.00082925 \times C_{CO}}{30} \right\} \tag{15}$$

where the units of C_{CO} are ppm,

$$FED(I)_{HCN} = \left(\frac{t}{60}\right) \times V_{CO_2} \times \sum \left\{ \frac{4.4}{185 - C_{HCN}} \right\} \tag{16}$$

when $80 \leq C_{HCN} \leq 180$ ppm,

$$FED(I)_{HCN} = \left(\frac{t}{60}\right) \times V_{CO_2} \times \sum \left\{ \frac{1}{\exp\left(5.396 - \left(0.023 \times C_{HCN}\right)\right)} \right\} \tag{17}$$

when $C_{HCN} > 180$ ppm; and

$$FED(I)_{O_2} = \left(\frac{t}{60}\right) \times \sum \left\{ \frac{1}{\exp\left(8.13 - \left(0.54 \times \left(20.9 - C_{O_2}\right)\right)\right)} \right\} \tag{18}$$

when $C_{O2} < 11.3\%$.

As in the FAA model, the value of t in these equations was the time in seconds between acquisition of FTIR spectra. The overall Fractional Effective Dose for Incapacitation was calculated by summing the terms in equations 14 through 18:

$$FED(I)_{TOTAL} = FED(I)_{CO_2} + FED(I)_{CO} + FED(I)_{HCN} + FED(I)_{O_2}$$

(19)

Both the FAA Combined Hazard Survival model and Purser's model predict that 50% of an exposed population would experience incapacitating narcosis (*i.e.*, an occupant loses consciousness and would be unable to exit a vehicle without assistance) when $\mathrm{FED(I)}_{\mathrm{TOTAL}} = 1.0$. Similarly, both of these models predict that 50% of an exposed population would die when $\mathrm{FED(L)}_{\mathrm{TOTAL}} \geq 1.0$.

7.2.1 Estimation of Fractional Equivalent Dose Parameters

The analysis presented in this report included estimates of FED(I) and FED(L) for carbon dioxide, carbon monoxide, hydrogen chloride, and hydrogen cyanide using the FAA Combined Hazard Survival Model and Purser's model for assessment of the toxicity of combustion products. The other gaseous species included in the FAA Combined Hazard Model and Purser's model were not measured during this test; therefore, values of FED(I) or FED(L) were not estimated for these gases. Figures 59 through 62 show plots of $\mathrm{FED(I)}_{\mathrm{co2}}$, $\mathrm{FED(I)}_{\mathrm{co}}$, $\mathrm{FED(I)}_{\mathrm{HCN}}$, and $\mathrm{FED(I)}_{\mathrm{HCL}}$ computed using the FAA Combined Hazard Survival Model and Purser's model for assessment of the toxicity of combustion products.

Plots of the $\mathrm{FED(I)}_{\mathrm{co2}}$ parameters estimated using the FAA Combined Hazard Model and Purser's model are shown in Figure 59. Both models yielded estimates of $\mathrm{FED(I)}_{\mathrm{TOTAL}} > 0$ by 300 seconds post-ignition, when the concentration of carbon dioxide was between 5 and 6%. Both models yielded estimates of $\mathrm{FED(I)}_{\mathrm{co2}} > 1$ between 390 and 400 seconds post-ignition. The estimates of $\mathrm{FED(I)}_{\mathrm{co2}}$ reached maximum values of about 6.5 by 7050 seconds post-ignition (Fig. 59).

Plots of the $\mathrm{FED(I)}_{\mathrm{co}}$ parameters estimated using both models are shown in Figure 60. The equations presented in the Purser model for computation of $\mathrm{FED(I)}_{\mathrm{co}}$ include a term for respiratory minute volume. Minute volumes corresponding to respiration during rest (8.5 L/min) and light activity (25 L/min) were used in these calculations [9]. Purser's model also accounts for the effect of exposure to carbon dioxide on respiratory rate.

The FAA Combined Survival Hazard Model computes only one estimate of $\mathrm{FED(I)}_{\mathrm{co}}$, which accounts for the effect of exposure to carbon dioxide on respiratory rate [8]. Both models yielded estimates of $\mathrm{FED(I)}_{\mathrm{co}} > 0$ at about 160 seconds post-ignition. The estimates of $\mathrm{FED(I)}_{\mathrm{co}}$ derived using the FAA model and Purser's model with a respiratory minute volume of 25 L/min became greater than 1 between 340 and 350 seconds post-ignition, and reached values of about 15.2and 14.5, respectively, at 700 seconds post-ignition.

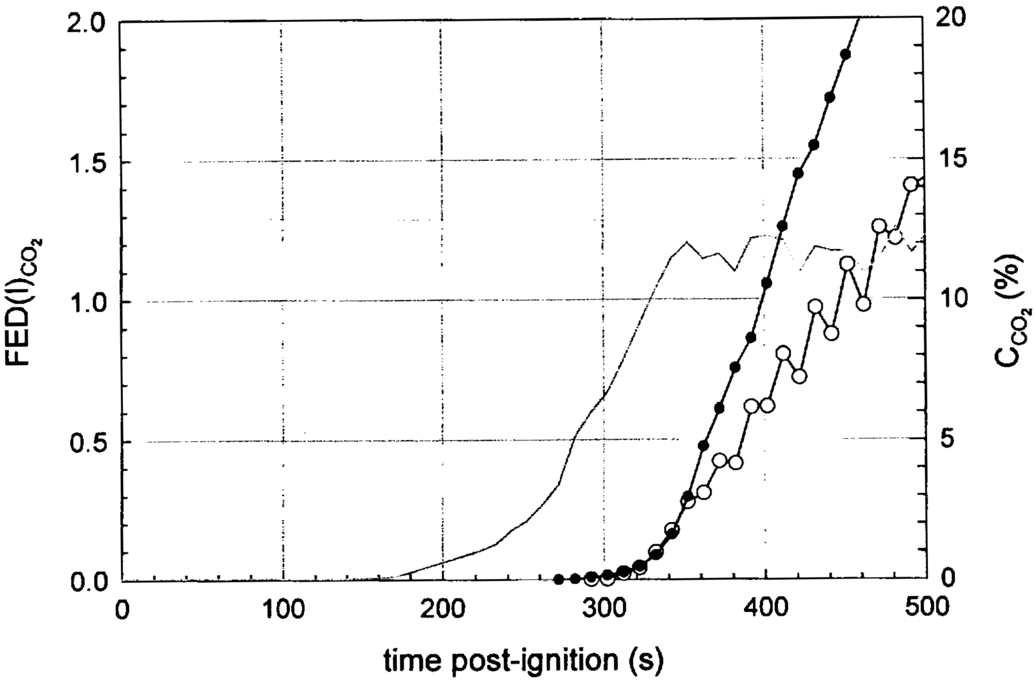

Figure 59. Fire Test F980611. Plots of $FED(I)_{CO2}$ versus time post-ignition: FAA Combined Hazard Survival Model (—○—); and Purser's model (—●—). A plot of C_{CO2} (——) is included for reference.

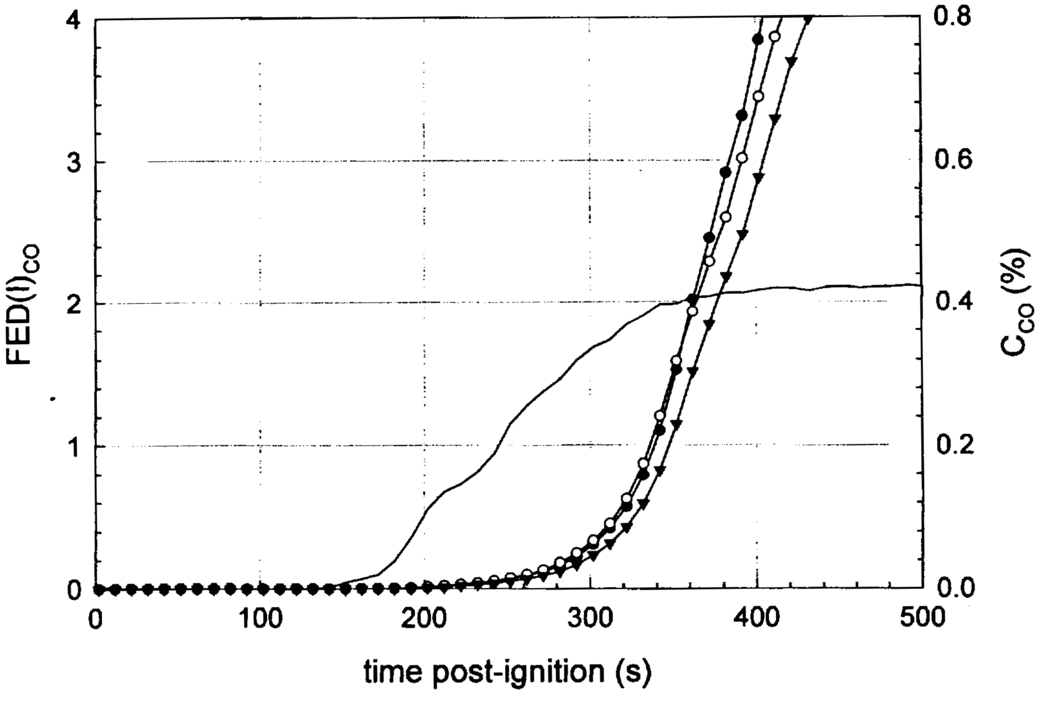

Figure 60. Fire Test F980611. Plots of estimates of $FED(I)_{CO}$ versus time post-ignition computed using the FAA Combined Hazard Survival Model (—○—), the Purser model with a respiratory minute volume of 8.5 L/min (—▼—), and the Purser model with a respiratory minute volume of 25 L/min (—●—). A plot of C_{CO} (——) is included for reference.

The estimate of $FED(I)_{co}$ derived using Purser's model with a respiratory minute volume of 8.5 L/min became greater than 1 between 330 and 340 seconds post-ignition, and reached a value of approximately 19.4 at 700 seconds post-ignition.

Plots of the $FED(I)_{HCN}$ parameters estimated using both models are shown in Figure 61. Both the FAA Combined Survival Hazard Model and Purser's model employ a threshold concentrations to determine when to start computing $FED(I)_{HCN}$ (refer to equations 6 and 14, respectively). The estimates of $FED(I)_{HCN}$ using the FAA model started at 262 seconds post-ignition, became greater than 1 between 222 and 232 seconds post-ignition, and reached a maximum value of about 30.4 at 692 seconds post-ignition. The estimates of $FED(I)_{HCN}$ using Purser's model started at 302 seconds post-ignition, became greater than 1 between 362 and 372 seconds post-ignition, and reached a maximum value of about 13.8 at 712 seconds post-ignition.

The concentration of hydrogen chloride in the passenger compartment was less than the threshold for computation of FED(I) and FED(L). Therefore, $FED(I)_{HCL}$ was not computed (Fig. 62).

Plots of the $FED(I)_{TOTAL}$ parameters estimated using both models are shown in Figure 61. The FAA Combined Survival Hazard Model yielded $FED(I)_{TOTAL} > 1$ after about 310 seconds post-ignition, where $FED(I)_{CO2}$ accounted for 5.5% of $FED(I)_{TOTAL}$, $FED(I)_{CO}$ accounted for 48.0% of $FED(I)_{TOTAL}$, and $FED(I)_{HCN}$ accounted for 46.5 % of $FED(I)_{TOTAL}$. The estimated $FED(I)_{TOTAL}$ reached a value of 52 at 700 seconds post-ignition. $FED(I)_{CO2}$ accounted for 12.5% of $FED(I)_{TOTAL}$, $FED(I)_{CO}$ accounted for 29.1% of $FED(I)_{TOTAL}$, and $FED(I)_{HCN}$ accounted for 58.3 % of $FED(I)_{TOTAL}$ at this time.

Purser's model yielded $FED(I)_{TOTAL} > 1$ between 320 and 340 seconds post-ignition using respiratory minute volumes of 8.5 L/min and 25 L/min in the calculations. With a respiratory minute volume of 8.5 L/min, $FED(I)_{CO2}$ accounted for 10.8% of $FED(I)_{TOTAL}$, $FED(I)_{CO}$ accounted for 55.4% of $FED(I)_{TOTAL}$, and $FED(I)_{HCN}$ accounted for 33.8% of $FED(I)_{TOTAL}$. With a respiratory minute volume of 25 L/min, $FED(I)_{CO2}$ accounted for 7.3% of $FED(I)_{TOTAL}$, $FED(I)_{CO}$ accounted for 67.3% of $FED(I)_{TOTAL}$, and $FED(I)_{HCN}$ accounted for 30.5% of $FED(I)_{TOTAL}$. The estimated $FED(I)_{TOTAL}$ reached a value of 34.9 at 700 seconds post-ignition ignition using respiratory minute volumes of 8.5 L/min. $FED(I)_{CO2}$ accounted for 18.8% of $FED(I)_{TOTAL}$, $FED(I)_{CO}$ accounted for 41.7% of $FED(I)_{TOTAL}$, and $FED(I)_{HCN}$ accounted for 39.6% of $FED(I)_{TOTAL}$. The estimated $FED(I)_{TOTAL}$ reached a value of 39.8 at 700 seconds post-ignition ignition using respiratory minute volumes of 25 L/min. $FED(I)_{CO2}$ accounted for 16.5% of $FED(I)_{TOTAL}$, $FED(I)_{CO}$ accounted for 48.7% of $FED(I)_{TOTAL}$, and $FED(I)_{HCN}$ accounted for 34.8% of $FED(I)_{TOTAL}$.

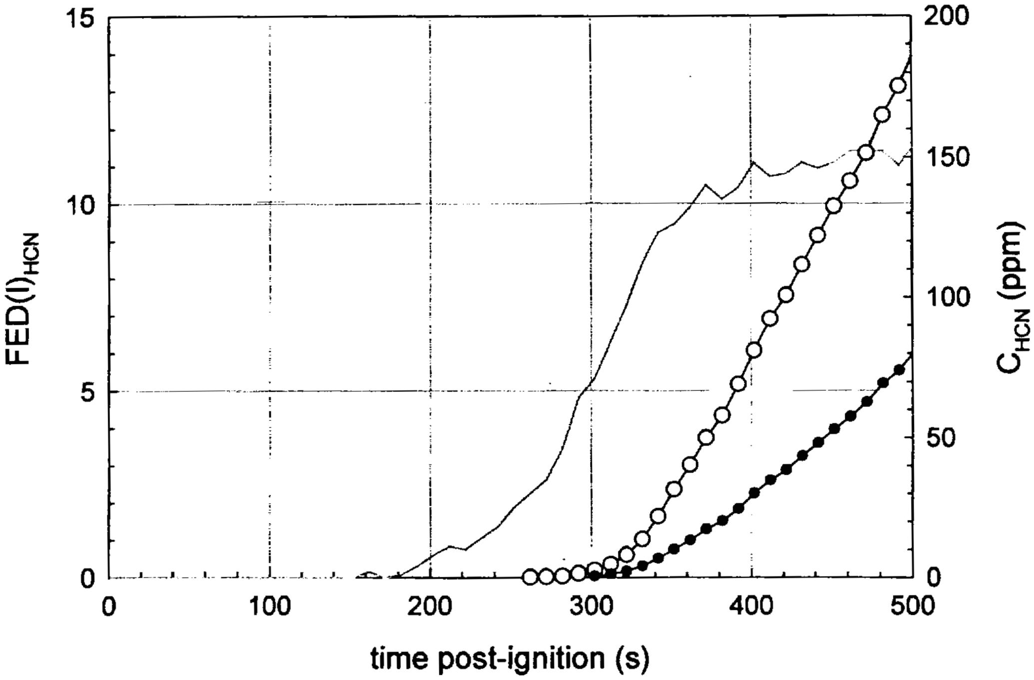

Figure 61. Fire Test F980611. Plots of $FED(I)_{HCN}$ versus time post-ignition: FAA Combined Hazard Survival Model (—○—); and Purser's model (—●—). A plot of C_{HCN} (——) is included for reference.

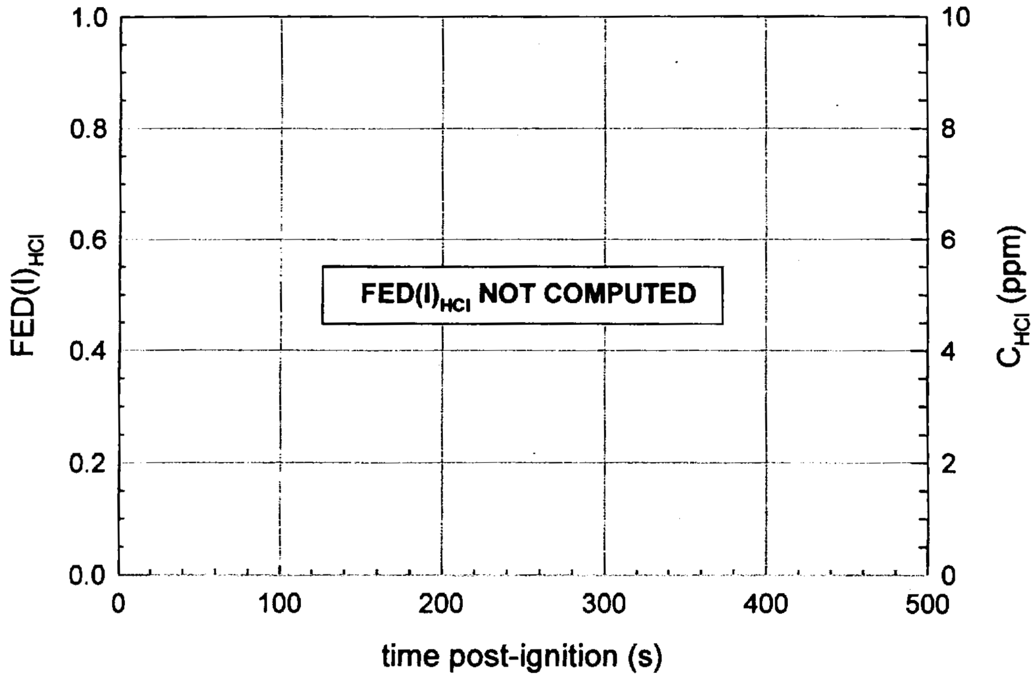

Figure 62. Fire Test F980611. $FED(I)_{HCL}$ were not calculated because C_{HCL} was less than the threshold concentration for calculation of $FED(I)_{HCL}$.

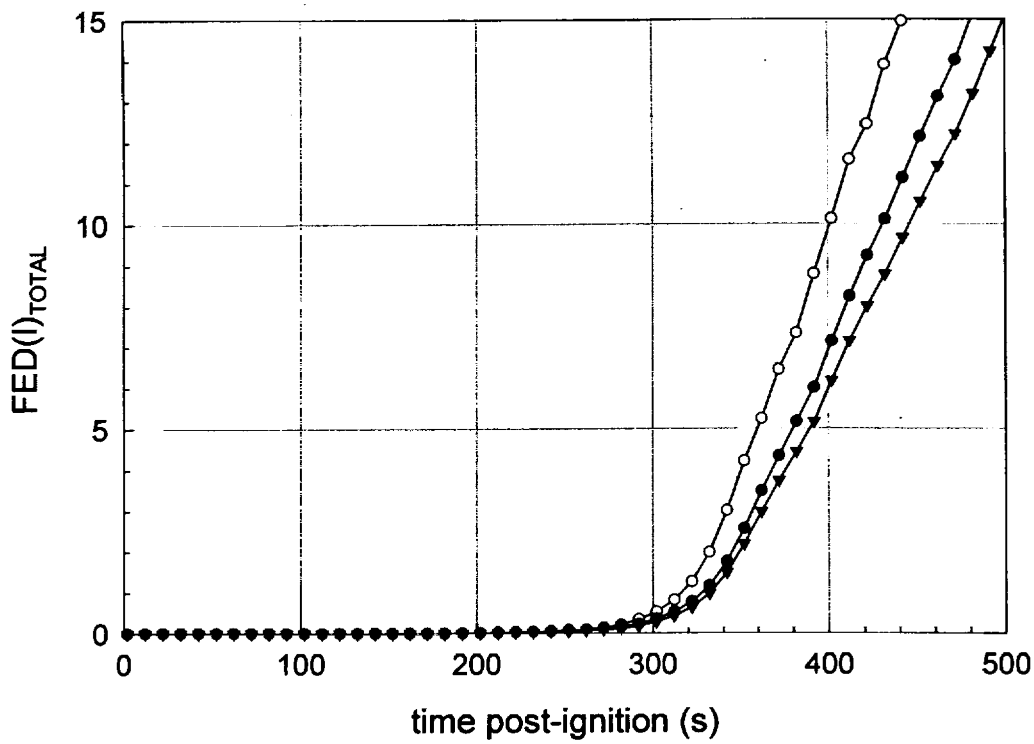

Figure 63. Fire Test F980611. Plots of $FED(I)_{TOTAL}$ versus time post-ignition: FAA Combined Hazard Survival Model (–○–); Purser's model with RMV = 8.5 L/min (–▼–); and Purser's model with RMV = 25 L/min (–●–).

Figure 64 shows plots of $FED(L)_{CO}$, $FED(L)_{HCN}$, and $FED(L)_{TOTAL}$ computed using the FAA Combined Survival Hazard Model. These calculations yielded and $FED(L)_{TOTAL} > 1$ after 360 seconds post-ignition. $FED(L)_{CO}$ accounted for 52.3% of $FED(L)_{TOTAL}$ and $FED(L)_{HCN}$ accounted for 47.7% of $FED(L)_{TOTAL}$. The estimated $FED(L)_{TOTAL}$ reached a value of 11.3 at 700 seconds post-ignition ignition. $FED(L)_{CO}$ accounted for 40.7% of $FED(L)_{TOTAL}$ and $FED(L)_{HCN}$ accounted for 59.3% of $FED(L)_{TOTAL}$.

The estimates of FED(I) and FED(L) obtained using the FAA Combined Hazard Survival Model and Purser's model of combustion gas toxicity can not predict precisely when the gas concentrations measured in this test would have resulted in incapacitating narcosis or death. This is especially true for prediction of lethality, where the mathematical relationships in these models were derived from experiments using laboratory animals or accidental, uncontrolled human exposures [8, 9]. Variation in susceptibility to these hazards among the human population also will contribute to the uncertainty in these predictions.

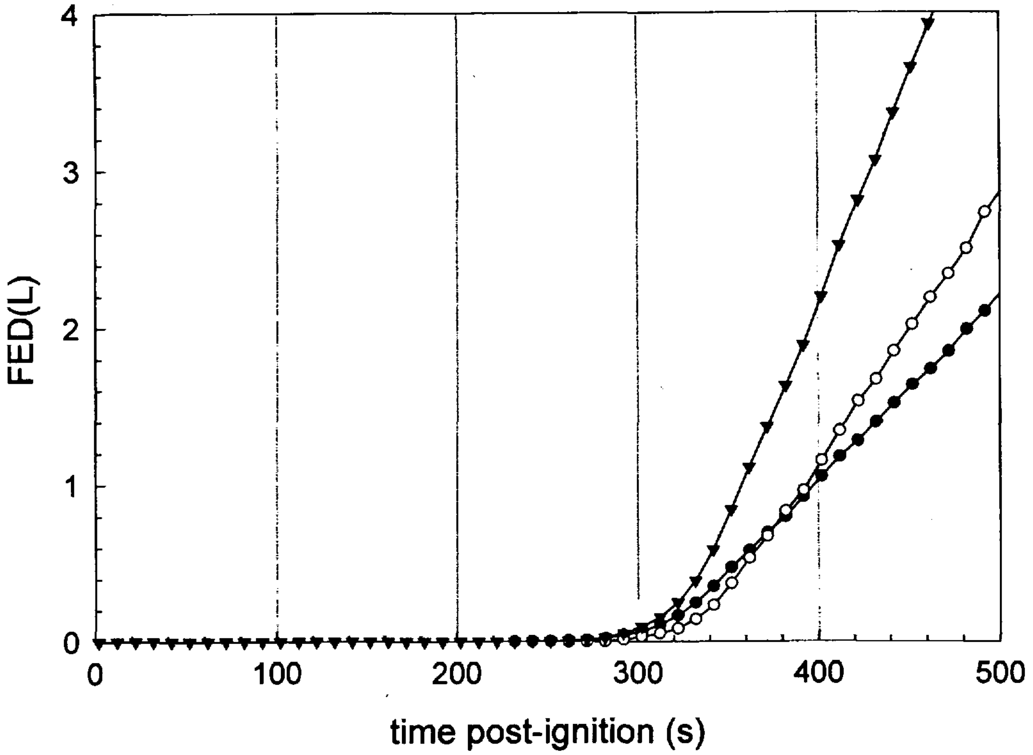

Figure 64. Fire Test F980611. Plots of $FED(L)_{CO}$ (-●-), $FED(L)_{HCN}$ (-○-), and $FED(L)_{TOTAL}$ (-▼-) versus time post-ignition computed using the FAA Combined Hazard Survival Model Fire.

In addition, the effect of trauma caused by the crash on an occupant's tolerance to these toxic gases is impossible to quantify.

Another variable that may affect an occupant's susceptibility to the combustion products is the location of the head. The data from the aspirated thermocouples indicated that a steep air-temperature gradient developed in the front of the passenger compartment during this test (see below). As both heat and mass are conserved in a fire, the existence of a steep vertical air-temperature gradient implies the existence of a similarly steep vertical concentration gradient for combustion products accumulating in the passenger compartment. The inlet to the gas sampling tube in the passenger compartment was in the breathing zone of that of a six-foot tall adult male sitting upright in either the driver's or front passenger's seat. An occupant whose head was located below the level where gases were sampled would have been exposed to lower concentrations of combustion gases that those shown in **APPENDIX H**. And, the estimated values of FED(I) and FED(L) for this occupant would have been lower than those shown in Figures 59 through 64.

7.3 Estimation of Burn-Injury to the Respiratory Tract

Figures 65 shows plots of temperature data recorded from the aspirated thermocouples in the passenger compartment of the test vehicle (**APPENDIX D**). The aspirated thermocouple [robe was located between the front seat backs and measured air temperature at 6 heights in the passenger compartment.

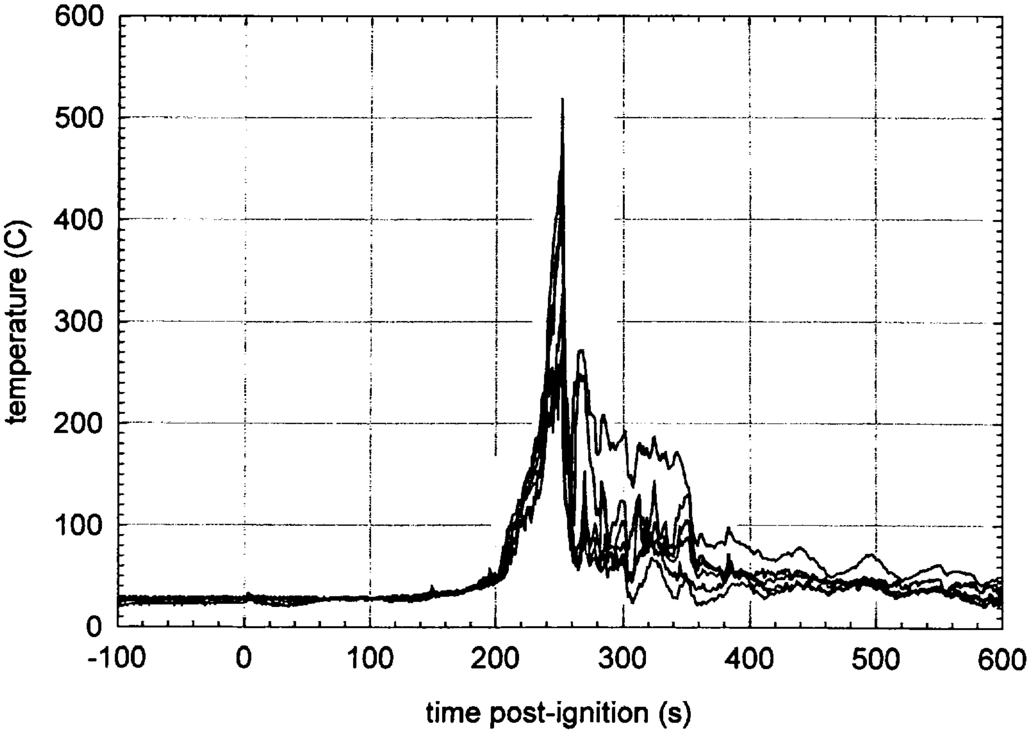

Figure 65. Fire Test F980611. Plots of temperature data recorded from the aspirated thermocouples in the passenger compartment of the test vehicle.

A maximum air temperature of 518°C was recorded from the thermocouple located approximately 7.6 cm below the roof trim panel at 252 seconds post-ignition (Fig. 65). The air temperature decreased approximately 8°C/cm below the roof trim panel at the location of the aspirated thermocouple probe. Temperatures recorded from the aspirated thermocouples decreased after flames in the passenger compartment were extinguished starting at 252 seconds post-ignition (Fig. 65).

It is not possible to estimate the potential for burn injury to the respiratory tract caused by inhalation of hot air by relying solely on air temperature data. Water and particulate produced by the fire increase the heat capacity of the air. The concentrations of these species in the inhaled air have been shown to affect both the severity and depth of burn injury in the respiratory system [see references in 10]. Neither the water- nor the particulate-concentrations of air in the passenger compartment were measured in this test. Purser states that a robust quantitative relationship between the temperature, water-content, and particulate-content of inhaled air and subsequent burn injury to respiratory airways has not been established [10]. A few controlled animal studies indicate that inhalation of steam at 100°C caused burns to the larynx and trachea similar to those produced by inhalation of dry air at 350°C or flames at 500°C [see references in 10]. In these controlled animal studies, death was not immediate, but resulted from obstructive edema in the burned airways a few to twenty-four hours after the exposure. As the concentration of water vapor in the air sampled from the passenger compartment was not measured during this test, the potential for burn injury to the respiratory airways from inhalation of hot gas cannot be determined accurately from the air temperature data shown.

ACKNOWLEDGEMENTS

Dr. Thomas Ohlemiller and Thomas Cleary of the Building and Fire Research Laboratory, National Institute of Standards and Technology were responsible for video taping this fire test, and provided an initial analysis of the test data for fire propagation. Dr. Archibald Tewarson of Factory Mutual Research Corporation provided the data from the Fire Products Collector at the test facility that was collected during this test.

REFERENCES

1. Jack L. Jensen and Jeffrey Santrock. Evaluation of Motor Vehicle Fire Initiation and Propagation. Part 1: Vehicle Crash Test and Fire Propagation Test Program. Submitted to the National Highway Transportation Safety Administration pursuant to the Settlement Agreement between General Motors and the Department of Transportation. Submitted July 31, 1997.

2. Jack L. Jensen and Jeffrey Santrock. Evaluation of Motor Vehicle Fire Initiation and Propagation. Part 8: Crash Tests on a Sport-Utility-Vehicle. Submitted to the National Highway Transportation Safety Administration pursuant to the Settlement Agreement between General Motors and the Department of Transportation. February 15, 2001.

3. Federal Safety Standards. Motor Vehicle Safety Standard No. 214 Side Impact Protection - Passenger Cars, Trucks, Buses & Multipurpose Passenger Vehicles with GVWR of 10,000 Pounds or Less. 60FR57838-39 (November 22, 1995).

4. NFPA 325 - Guide to Fire Hazard Properties of Flammable Liquids, Gases, and Volatile Solids. National Fire Protection Association, Quincy, MA 02269-9101. 1994 Edition.

5. Jeffrey Santrock. Project B.10 – Study of Flammability of Materials. Identification of the Base Polymers in Selected Components and Parts from a 1997 Ford Explorer by Pyrolysis / Gas Chromatography / Mass Spectroscopy and Attenuated Total Reflectance / Fourier Transform Infrared Spectroscopy. Submitted to the National Highway Transportation Safety Administration pursuant to the Settlement Agreement between General Motors and the Department of Transportation. Submitted DATE.

6. SigmaPlot® 4.0 for Windows®, SPSS Inc., 444 North Michigan Avenue, Chicago, IL 60611. Copyright © 1997 by SPSS Inc..

7. Archibald Tewarson. "Generation of Heat and Chemical Compounds in Fires" Section 3/Chapter 4, SFPE Handbook of Fire Protection Engineering, 2nd Edition, 1995, pp. 3:53-124.

8. F. S. Knox III, Dena Bonetti, and Chris Perry. User's Manual for BRNSIM/BURNSIM: A Burn Hazard Assessment Model. United States Army Aeromedical Research Laboratory Report No. 93-13. Fort Rucker, Alabama 36362-5292. February 1993.

9. L. C. Speitel. Toxicity Assessment of Combined Gases and Development of a Survival Model. DOT/FAA/AR-95-5. July 1995.

10. David A. Purser. "Toxicity Assessment of Combustion Products" Section 2/Chapter 8, SFPE Handbook of Fire Protection Engineering, 2nd Edition, 1995, pp. 2:85-146

APPENDIX A
PREPARATION OF THE FUEL TANK IN THE TEST VEHICLE

The flow rate of fluid from the hole in the inboard front side of the fuel tank was measured after the crash test. For this measurement, the fuel tank was removed from the test vehicle and strapped to a tilt-table and leveled. The fuel pump assembly was removed to equalize the pressure inside the tank with atmospheric pressure. Body-putty was used to construct a dam around the hole to direct all fluid flowing from the hole into a single container (Figure A1). The hole was plugged and Stoddard solvent (approximately 25 gallons) was added to the tank until the liquid level reached the bottom of the filler tube inside the tank.

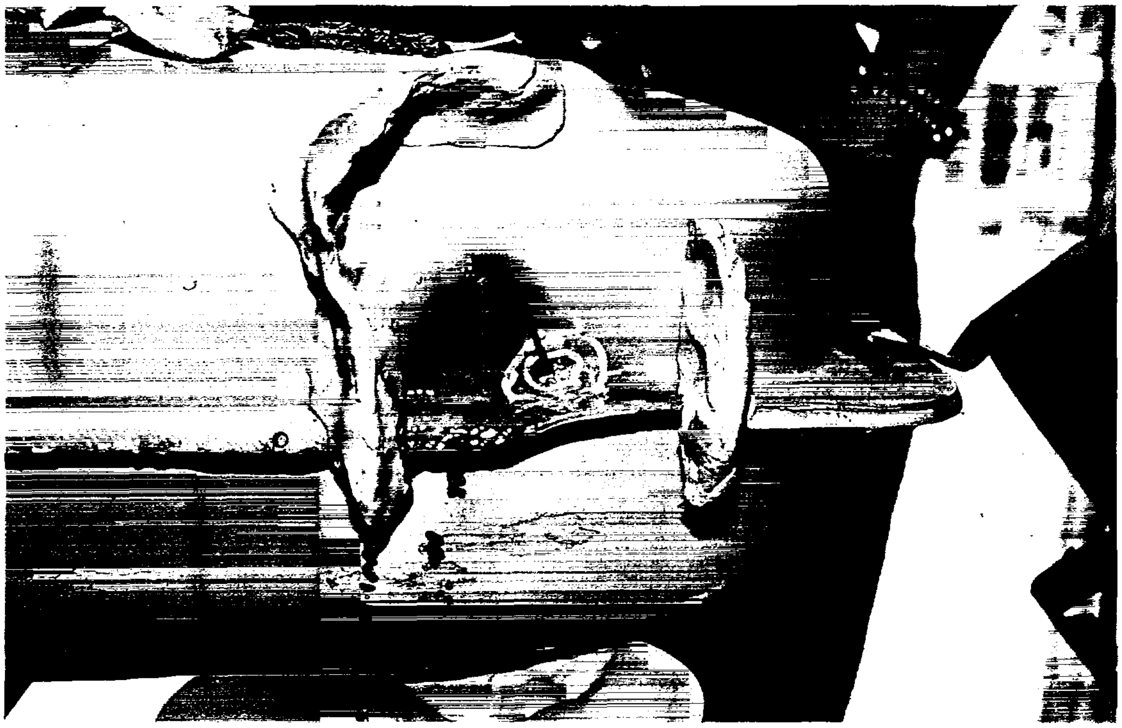

Figure A1. Fire Test F980611. Photograph of Stoddard solvent flowing from the hole in the fuel tank removed from the test vehicle after the crash test.

The plug was removed and fluid was collected for one- and five-minute intervals. A beaker with a capacity of 500 mL and 50 mL graduations was used to measure the fluid volume collected during the one-minute intervals. A beaker with a capacity of 5 L and 500 mL graduations was used to measure the volume of fluid collected during the five-minute intervals. Triplicate measurements were made at each time interval. The volume of fluid collected during each measurement is shown in Table A1.

Table A1

Leak-rate from Ford Explorer Fuel Tank
Crash Test C11687

Collection Interval (min)	Fluid Volume (cm^3)	Flow-Rate (cm^3/min)
1	290	290
1	295	295
1	290	290
5	1400	280
5	1400	280
5	1400	280

The average flow-rate measured during the 1-minute intervals was 292 cm^3/min. The average flow-rate measured during the 5-minute intervals was 280 cm^3/min. The difference in flow-rates measured during the one- and five-minute intervals was attributed to uncertainty in the measurement of fluid volumes, caused by differences in the readability of the scales on the beakers used to measure the volumes of the fluid collected. The readability of the scale of the 500 mL beaker was ± 5 mL, whereas the readability of the scale of the 5 L beaker was ± 100 mL.

To prepare the test vehicle for this fire test, a service parts fuel tank was purchased from a Ford dealership. An 1/8 in. clearance hole was drilled in the side wall of this fuel tank in the approximate location of the hole in the fuel tank removed from the crash tested vehicle. Stainless steel tubing (1/8 in. o.d.) was installed in the fuel tank as shown in Figure A2. The outlet of the tubing was silver-soldered to the tank and bent to produce dispersion and drip patterns on the side of the tank (Fig. A2) similar to the dispersion and drip patterns observed on the fuel tank removed from the crash tested vehicle (Fig. A1). A plastic shield was removed from the front of the original fuel tank in the crash tested vehicle and installed on the modified service parts fuel tank. The modified service parts fuel tank and original fuel tank skin plate from the crash tested vehicle were installed in the test vehicle for this fire test. The tubing added to the service parts fuel tank was routed through the fuel pump assembly port, forward and to the right along the underside of the floor panel, and the inlet of the tubing was clamped to the left outer fender panel just rearward of the right front wheelhouse. A valve and fitting were attached to the tubing inlet for connection to the fuel delivery system for the fire test.

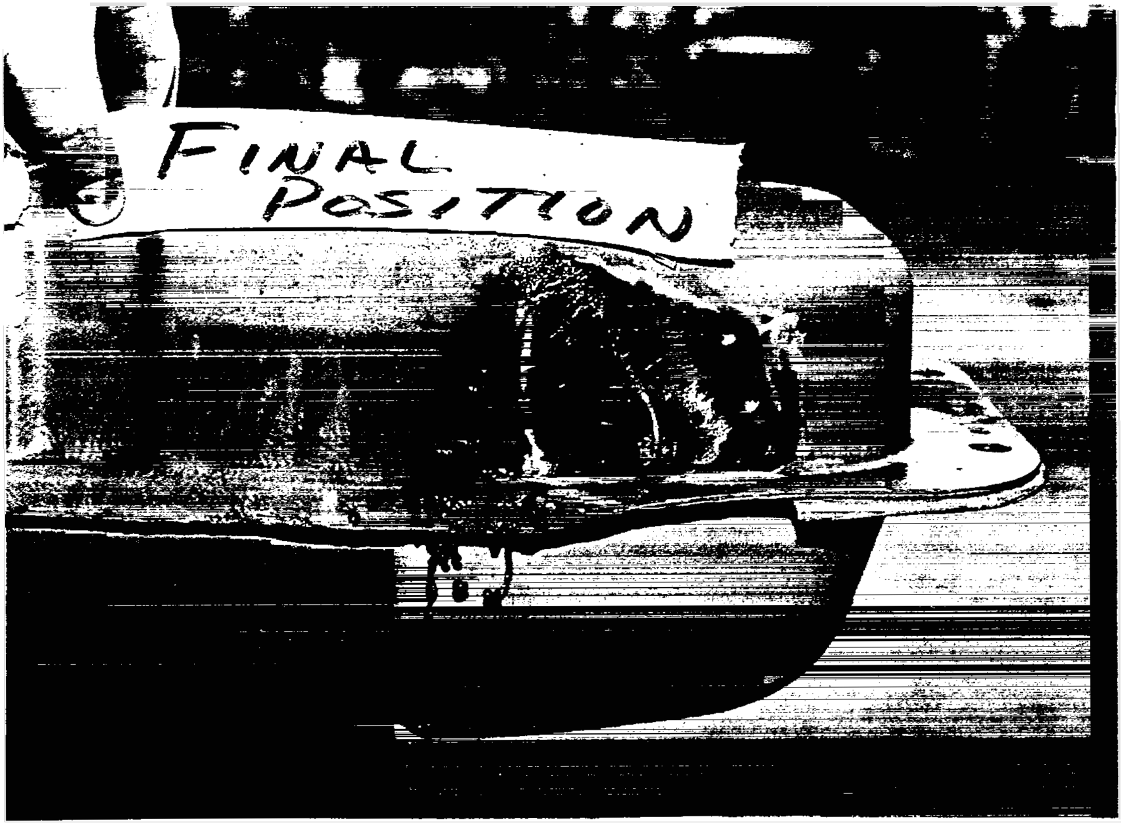

Figure A2. Fire Test F980611. Photograph of Stoddard solvent flowing the stainless steel tubing installed in the service parts fuel tank.

APPENDIX B
VIDEO CAMERA SET-UP

Scientific and technical personnel from the Building and Fire Research Laboratory, National Institute of Standards and Technology were primarily responsible for obtaining a video record of this test. Ten video cameras were used in this test. Figure B1 shows the approximate locations of the video cameras relative to the test vehicle during this test.

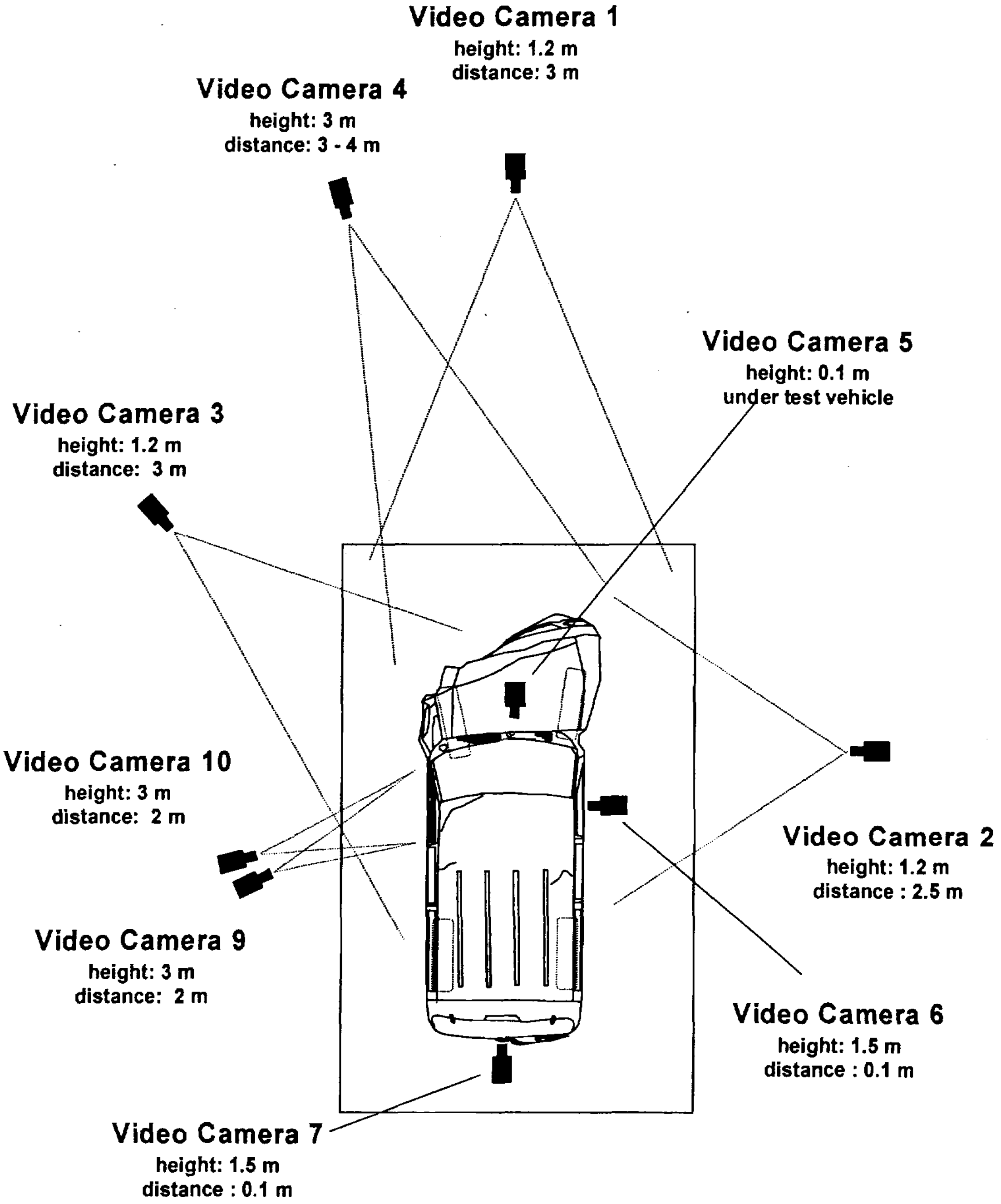

Figure B1. Fire Test F980611. Diagram showing the approximate locations of the video cameras during this test. Distances in this figure are not to scale in this diagram.

Camera 1 was a Hi-8 camcorder mounted on a tripod. It had a field-of-view that included the full height and width of the front of the test vehicle. Camera 2 was a Hi-8 camcorder mounted on a tripod. It had a field-of-view that included the right side of the test vehicle from about the rear door to beyond the front bumper fascia. Camera 3 was a Hi-8 camcorder mounted on a tripod. It had a field-of-view that included the left side of the test vehicle from about the front of the fender to the rear door. Camera 4 was a Hi-8 camcorder mounted on a tower fixture approximately 3 to 4 m above the test vehicle. Its field-of-view included the front of the test vehicle. Camera 5 was a CCD camera located under the engine compartment of the test vehicle. Its field of view included a section of the front of the floor panel. Camera 6 was a CCD camera located on the front passenger's seat. It's field of view steering wheel, deployed driver's airbag, driver's seat, and the driver's door. Camera 7 was a CCD camera located in the rear of the test vehicle and facing forward. It's field of view included the section of the passenger compartment forward of this camera. Camera 8 malfunctioned before this test. No video was recorded for this test. The location of Camera 8 is not shown in figure A1. Camera 9 was Hi-8 camcorder mounted on a tripod with a light filter attached to the lens and focused through the window in the drivers door onto the driver's seat cushion. The video from this camera was not used in the analysis of this test. Camera 10 was Hi-8 camcorder mounted on a tripod and focused through the window in the drivers door onto the driver's seat cushion.

All video cameras were started before the test. A microphone on each camera recorded the air horn, which signaled the start of the gasoline flow, ignition of the gasoline, and the end of the test.

Quartz-halogen floodlights were used to illuminate the exterior of the vehicle. The level of illumination provided by these lamps was insufficient to balance the intensity of light reflecting from the vehicle surfaces with the brightness of the flames. To compensate for this imbalance, the light sensitivity adjustments on the Hi-8 camcorders were set to the manual position so that the apparent brightness of the vehicle surfaces did not change as the fire developed. As a result, the flames were overexposed, causing them to appear more opaque than they actually were.

APPENDIX C
INFRARED THERMOGRAPHY

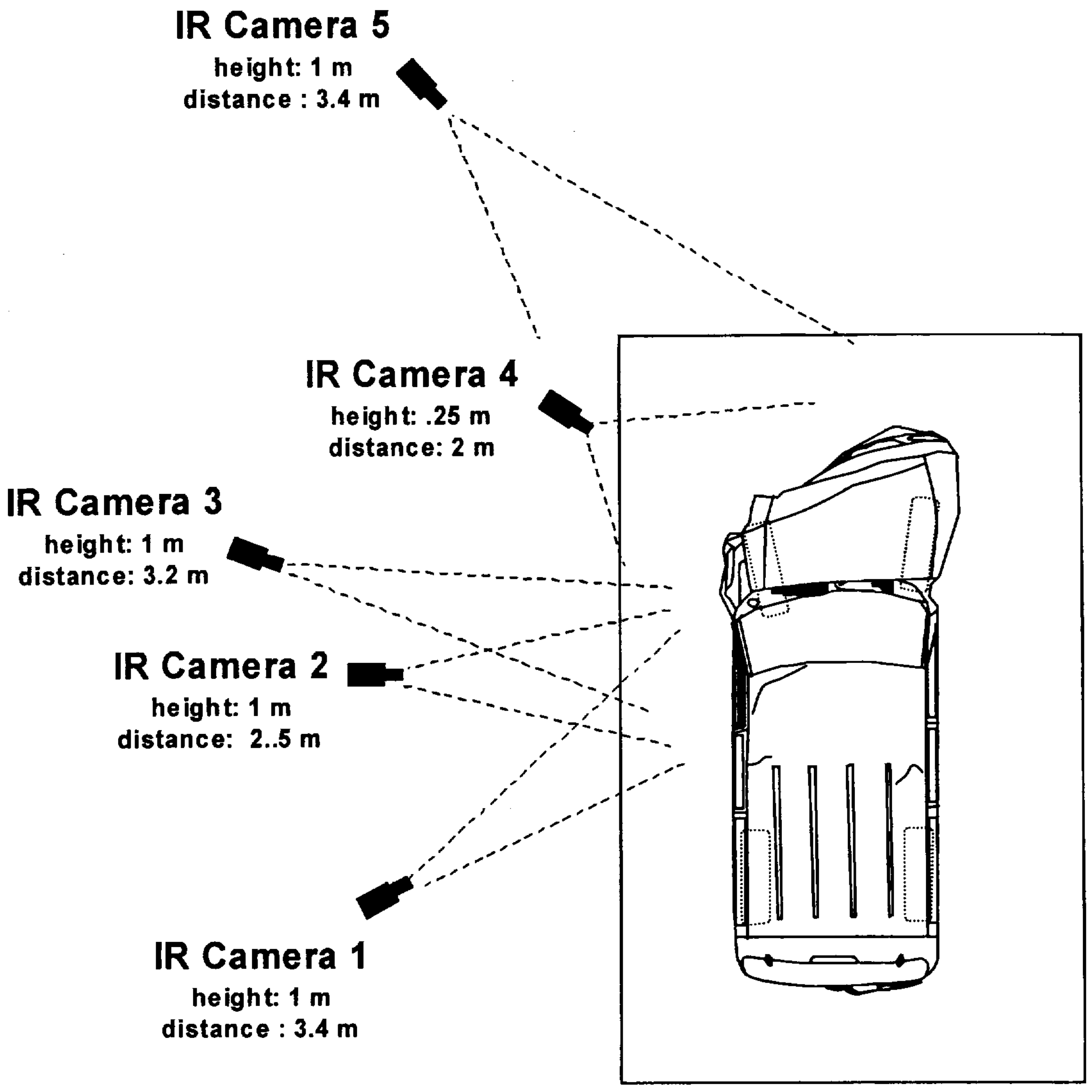

Figure C1. Fire Test F980611. Diagram showing the approximate locations of infrared cameras around the test vehicle during this test. Distances in this diagram are approximate and not drawn to scale in this diagram.

C.2 Data Analysis

Thermal imaging systems measure infrared radiation within a certain spectral band and must be calibrated to convert radiant intensity in that spectral band to temperature. Due to variations in system response, every system has to be calibrated. Calibration curves for the basic thermal imaging radiometers are measured at the factory and stored in read-only memory or in analysis software programs. Additional calibrations are needed for the optical filters. These calibrations are stored in the analysis software programs. Since thermal imaging radiometers are AC coupled devices, they measure differences in thermal radiation. To get absolute temperatures, there must be a reference to provide DC restoration. In these instruments, the reference is an internal blackbody reference source that is viewed periodically by the detector.

The general radiometric equation was used to convert radiant energy to temperature:

$$I = [E_t \times F(T_t)] + [(1 - E_t) \times F(T_b)] - [E_r \times F(T_r)] - [(1 - E_r) \times F(T_b)] \tag{C1}$$

Where I is the difference in radiance between the target and a reference surface; E_t is the emittance of the target surface, generally unknown; E_r is the emittance of the reference surface, T_t is the temperature of the target surface; T_b is the temperature of background surfaces (i.e., ambient temperature), or other emitters such as flames reflected from the target; T_r is the temperature of the reference surface; $F(T_t)$ is the radiance from an ideal emitting surface (i.e., black body) at the temperature of the target surface (T_t); $F(T_r)$ is the radiance from an ideal emitting surface at the temperature of the reference (T_r); and $F(T_b)$ is the radiance from the background relative to the radiance value from the reference surface when $E_r = 1$. Factors other than temperature determine the emittance of an object. These factors include the type of material, the texture of the surface, the wavelength of the detector, and the view-angle. In determining temperatures from the radiant energy from an object, the operator can set the emittance of an unknown target surface to a value of between .01 and 1.0.

Radiant intensity measured by the thermal imaging system is converted to a gray-scale value. An 8 bit system provides gray scale values from 0 to 255 for the radiant energy at each pixel in the instantaneous field of view. A 12 bit system provides gray scale values from 0 to 4095. As the radiometer scans the image, each pixel is assigned a gray scale value, and the gray scale image is stored either in a computer memory or onto videotape. When stored in computer memory, a single frame (1 thermogram) can contain up to 68,000 pixels (discrete measurements) with an assigned 8 bit or 12 bit value. Videotape provides a temporal resolution of 30 frames per second. Depending on the thermal range of the thermal imaging radiometer, a temperature value was assigned to each pixel using either the factory calibration curves accompanying each instrument, or calibration curves stored in IR analysis software.

Separation of the apparent temperatures of various surfaces on and inside a burning vehicle from the captured data is not a trivial task. The data represent a complex combination of emitted infrared energy from those surfaces as well as reflected infrared energy from the flames, and reflected infrared energy from high intensity lights used to illuminate the vehicle for visual data capture. In addition, the flames themselves were emitting infrared radiation due to their sooty content, some part of which was captured by the infrared thermal imaging systems. Also, some of the infrared radiation being emitted by the vehicle surfaces had to pass through flames containing soot from incomplete combustion of synthetic polymers or through clear (clean) flames where more complete combustion was occurring, and/or a combination of both types of flames. In all of these cases, gases in the flame absorbed some of the infrared radiation emitted by objects behind the flame.

The following steps were taken to minimize the impact of unwanted infrared radiation being captured by the thermal imaging systems.

- Anti-reflection tapes, paint, and glazes were applied to highly reflective surfaces on the test vehicle to minimize interference from reflections of the video floor and spot lights on the test vehicle.
- The thermal imaging systems were located in the shadows of the vehicle to block the video lights from shining directly into the radiometer.
- In some cases, flame filters (3.9 μm) were used in an attempt to screen out a portion of the infrared radiation from flames.

Despite these precautions, accurate surface temperatures could not be determined for areas of the vehicle blocked by intense flame. As a result, only surface temperatures determined to be reliable by the IR analysts are reported here. In some cases, specialized data analysis techniques were used to obtain reliable surface temperatures from areas in close proximity to, but not shielded by flame. Where possible, temperature data were reported from areas that lie in the shadow of the flames, which comes from highly emissive surfaces not affected by the flame radiation, and/or is deemed reliable based on the experience of the analysts. Data from nearby thermocouples were compared to IR temperature readings for a more comprehensive analysis.

During the data analysis, the videotapes were reviewed frame-by-frame to observe the burn sequence. The analyst captured images from selected frames on a video board. The image was processed to produce a digitized gray scale value for each element in the pixel matrix utilizing the camera settings automatically documented between video frames on the videotape during data acquisition. Thermograms were produced from the digitized image matrix using a commercial software package (Thermogram Pro V1.3, sold by Inframetrics, Inc., Billerica, MA). This software utilized the NIST traceable calibration tables supplied by the manufacturer with each thermal imaging system.

APPENDIX D
THERMOCOUPLE DATA

The thermocouples used in this test were type-N thermocouples fabricated by Medtherm Corporation (Huntsville, AL). Each thermocouple consisted of an ungrounded thermocouple junction (30 AWG thermocouple wire) enclosed in an Inconel 600 sheath insulated with magnesium oxide (o.d. = 0.040 in. (1 mm), length = 50 ft. (15.2 m)). A transition was made through a stress-relief bushing to a duplex thermocouple extension cable (24 AWG) with fiberglass insulation and a stainless steel over-braid (length = 1 ft. (0.28 m)). Each thermocouple wire terminated in a grounded, compensated Type-N thermocouple plug. The thermocouples were connected to the data acquisition system using Type-N thermocouple extension cables (length = 50 ft. (15.2 m)).

The data acquisition system consisted of a PC (75 MHz Pentium Processor, 16 MB RAM, an 814 MB hard disk, and a 16-bit, Model BG45-AP5CP, ACER Inc., Taiwan R. O. C.) with a 100 kHz I/O board with 16 analog input channels (DaqBoard 200A, IOTech, Inc., Cleveland, OH). Thermocouple multiplex expansion cards (DBK-19, IOTech, Inc., Cleveland, OH) were used for data acquisition from the thermocouples. The expansion cards were mounted in an electronics cabinet and hard-wired to a panel containing compensated Type-N thermocouple jacks.

To reduce electronic noise on the thermocouples, the ground leads from each thermocouple jack was connected to the electronic chassis ground of the thermocouple mutliplex extension cards. The vehicle chassis was connected to the electronic chassis ground by a large-gauge cable. The electronic chassis ground was connected to an isolated earth ground.

The data acquisition software (DASYLab, Daten System Technik GmbH, Mönchengladbach, Germany) was configured to sample each channel at a rate of 10 Hz and store the data in 10-point block averages.

Figures D1 through D10 show the approximate locations of thermocouples in the test vehicle. Plots D1 through D119 show plots of the temperature data recorded from these thermocouples during this test.

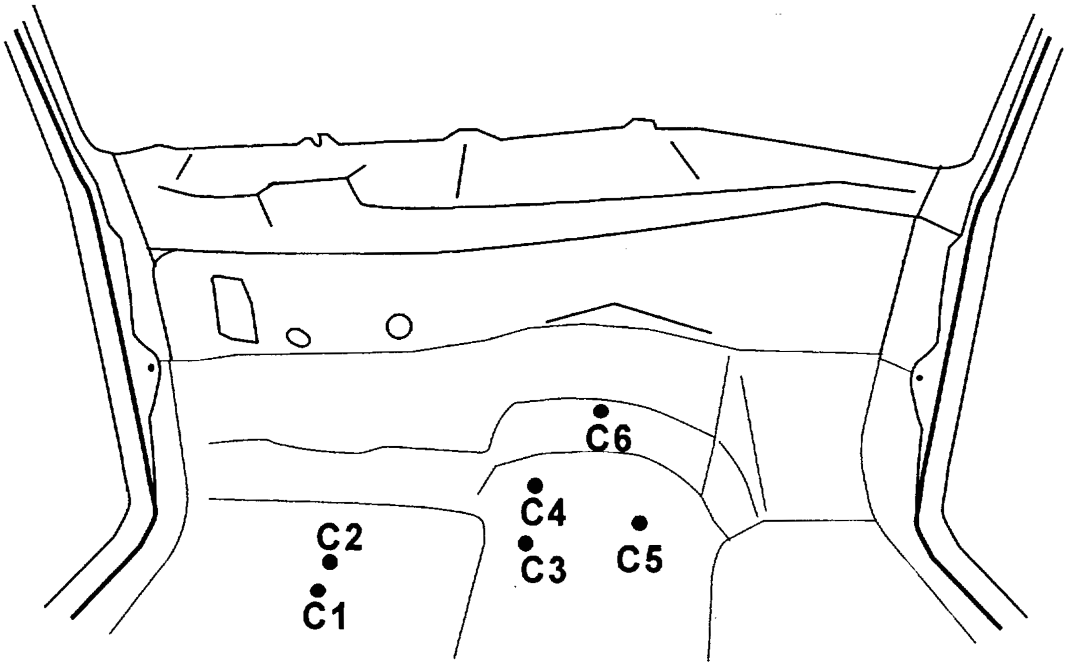

Figure D1. Fire Test F980611. Diagram showing the approximate locations of thermocouples on the carpet in the front of test vehicle. Thermocouples C1 and C2 were located on the upper surface of the carpet above the electrical pass-through in the floor pan under the driver's seat. Thermocouples C3, C4, C5, and C6 were located on the upper surface of the carpet over the front of drive line tunnel.

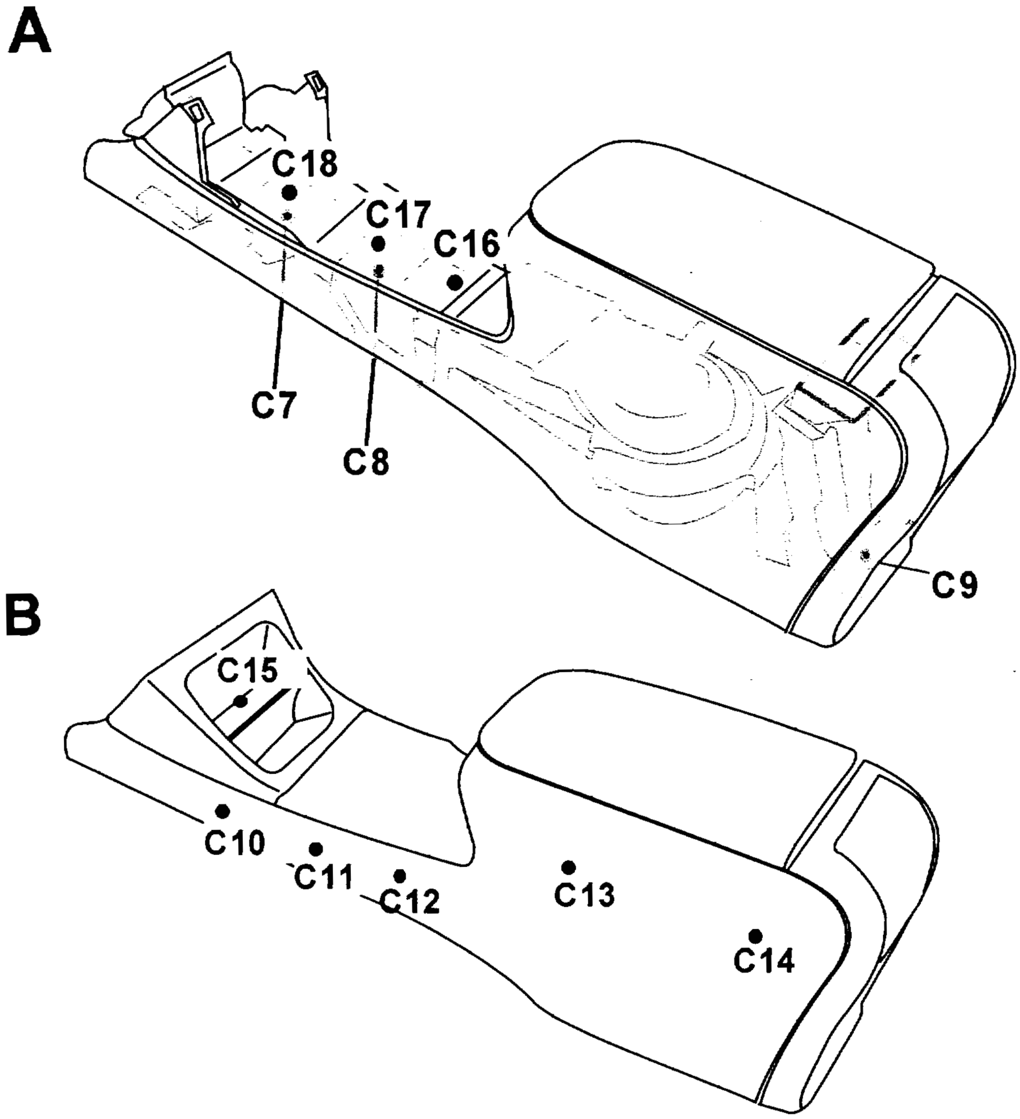

Figure D2. Fire Test F980611. Diagram showing the approximate locations of thermocouples on the center console in the test vehicle. DIAGRAM A. Thermocouples C7, C8, and C9 were located on the bottom surface of the heater duct for the rear seat. Thermocouples C16, C17, and C18 were located inside and approximately 1 cm from the top surface of the heater duct for the rear seat. DIAGRAM B. Thermocouples C10, C11, C12, C13, and C14 were located on the exterior surface of left side of the center console. Thermocouple C15 was inside the center console centered laterally above the rear heater duct and behind accessory tray.

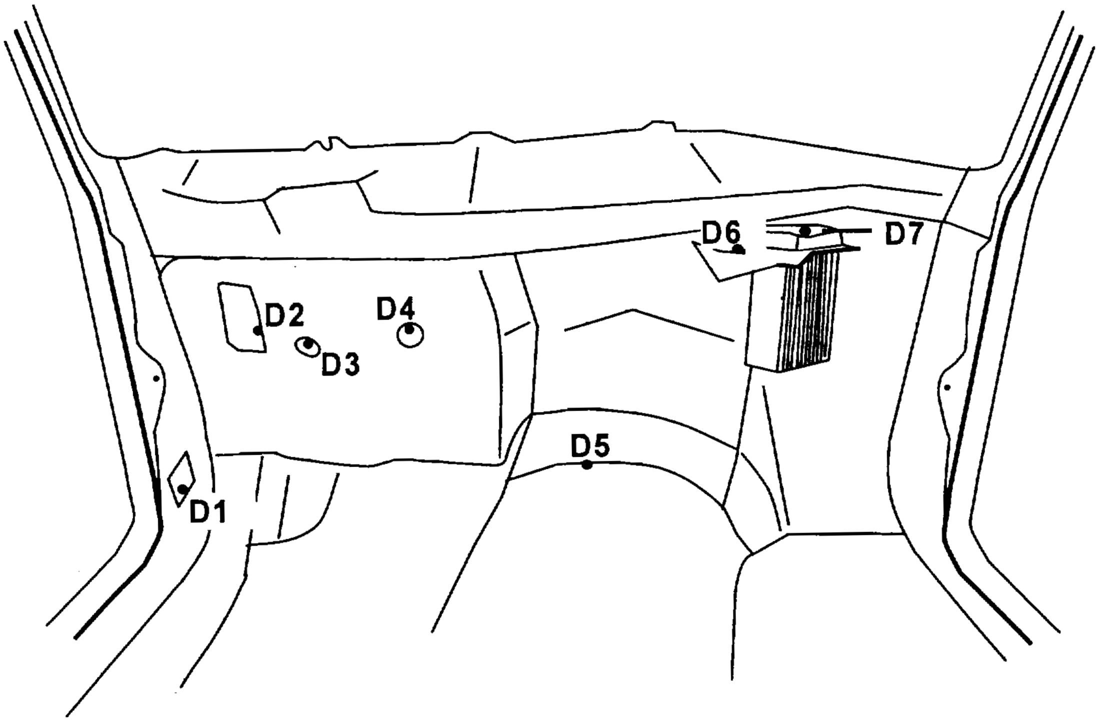

Figure D3. Fire Test F980611. Diagram showing the approximate locations of thermocouples in the test vehicle. Thermocouple D1 was located adjacent to an electrical pass-through inside the driver's side hinge pillar. Thermocouple D2 was located at the wire harness pass-through in the dash panel. Thermocouple D3 was located at the transmission shift cable pass-through in the dash panel. Thermocouple D4 was located at the steering column pass-through in the dash panel. Thermocouple, D5, was located at a seam opening on top of the drive line tunnel. Thermocouple D6 was located behind the heater core inside the HVAC module. Thermocouple D7 was located inside the HVAC module behind the upper right corner of the heater core.

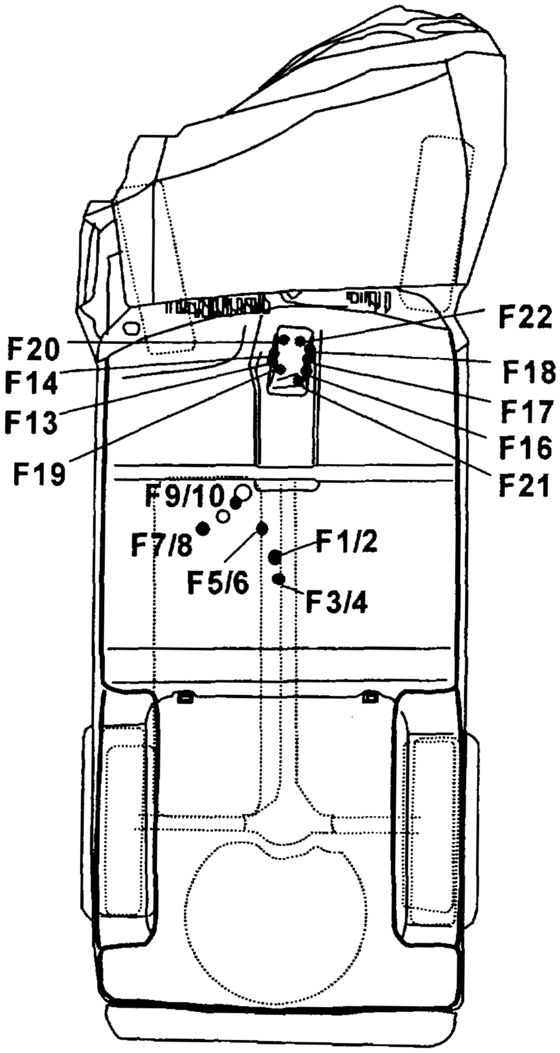

Figure D4. Fire Test F980611. Diagram showing the approximate locations of thermocouples on the floor pan of the test vehicle. Thermocouple F3, F5, F7 and F9 were located approximately 1 cm below the lower surface of the floor pan. Thermocouples F2, F4, F6, F8, and F10 were attached to the upper surface of the floor pan with thermally conducting ceramic cement. Thermocouples F13, F14, F16, F17, and F18 were located in an opening between the manual transmission shift lever pass-through cover plate on top of drive line tunnel and the floor pan. Thermocouple F19, F20, F21 and F22 were located approximately 1 cm below the lower surface of the manual transmission shift lever pass-through cover plate.

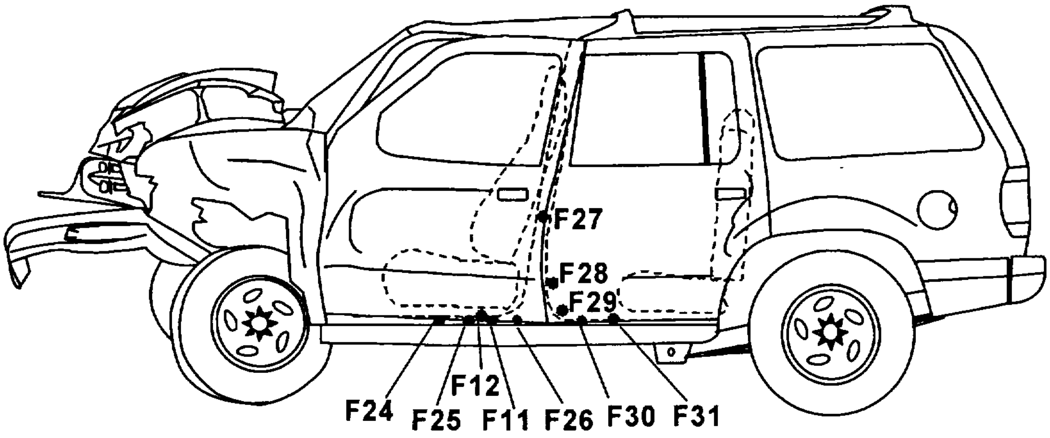

Figure D5. Fire Test F980611. Diagram showing the approximate locations of thermocouples on the test vehicle. Thermocouple F12 was located in a seam opening between the floor pan and rocker panel below the driver's door. Thermocouples F11, F24, F25, and F26 were located on the surface of the driver's side front door scuff plate. Thermocouple F27 was located in the driver's side "B" pillar adjacent to an electrical pass-through. Thermocouple F28, F29 and F30 were located on the 'B' pillar underneath the rear door weather-strip extending approximately 1 cm into the space between the "B"pillar and the rear door. Thermocouple F31 was located on the surface of the left rear door scuff plate approximately 1 cm outboard of the rear door weather-strip.

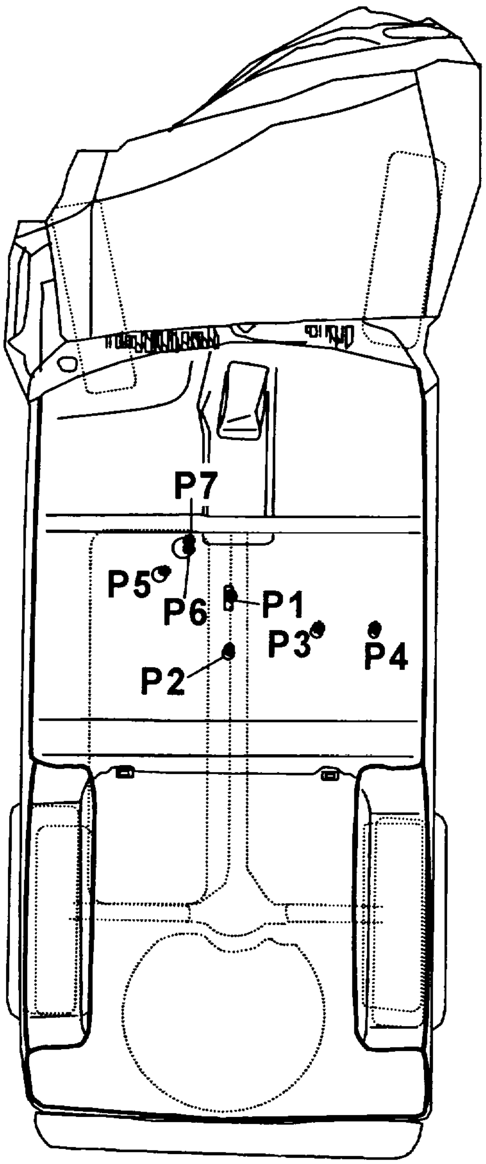

Figure D6. Fire Test F980611. Diagram showing the approximate locations of thermocouples on drain hole plugs and electrical pass-through openings in the floor panel of the test vehicle. Thermocouples P1, P2, P3, and P4 were located on the upper surfaces of floor pan drain hole plugs. Thermocouple P5 was located on the upper surface of electrical pass-through closure. Thermocouples P6 and P7 were located in the opening of an electrical pass-through in the floor pan, extending into the opening approximately 1 cm.

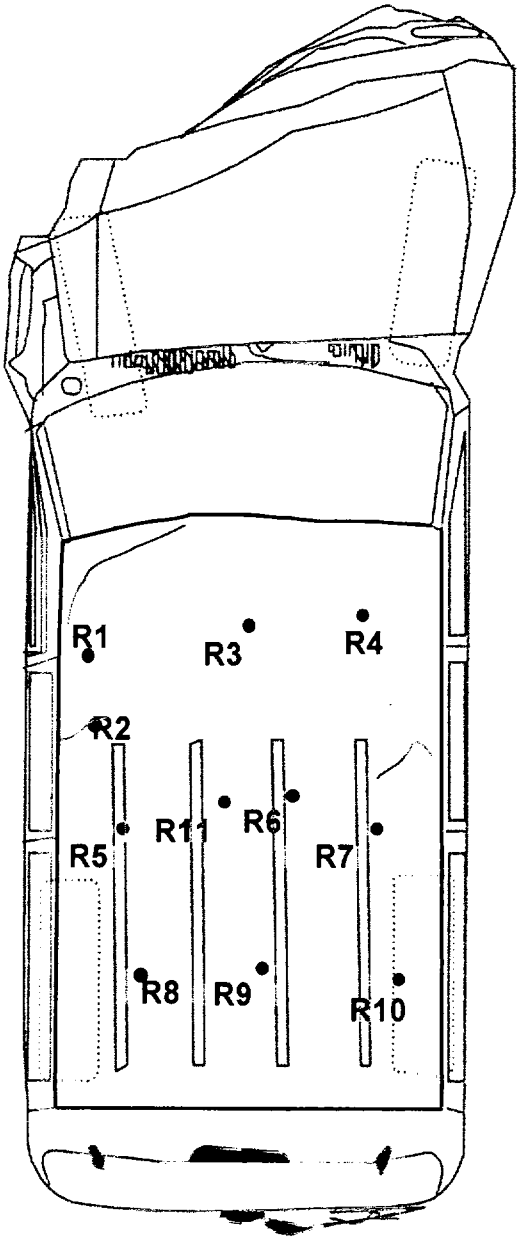

Figure D7. Fire Test F980611. Diagram showing the approximate locations of thermocouples on the roof in the test vehicle. Thermocouples R1 through R11 were located approximately 1 cm below the lower surface of the headlining panel.

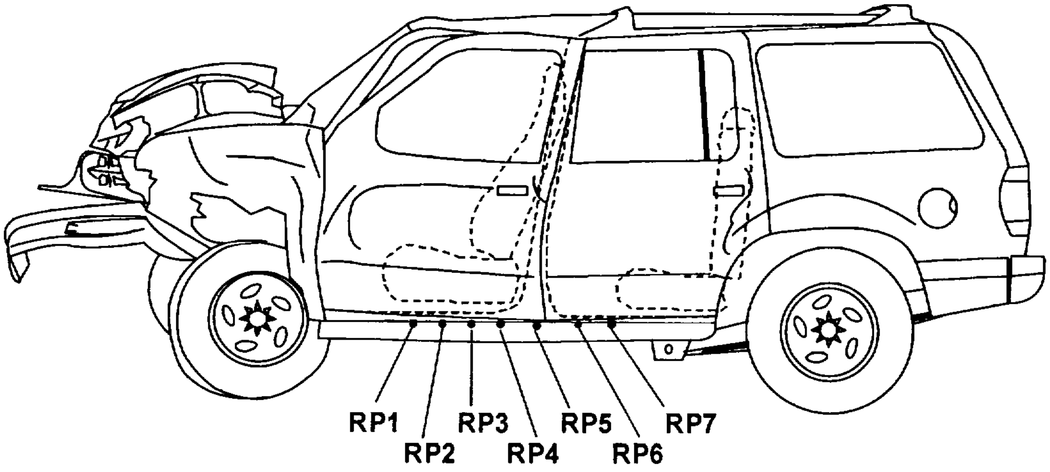

Figure D8. Fire Test F980611. Diagram showing the approximate locations of thermocouples on the rocker panel on the test vehicle. Thermocouples RP1 through RP7 were located on the surface of the rocker panel, in the gap between the door and the rocker panel.

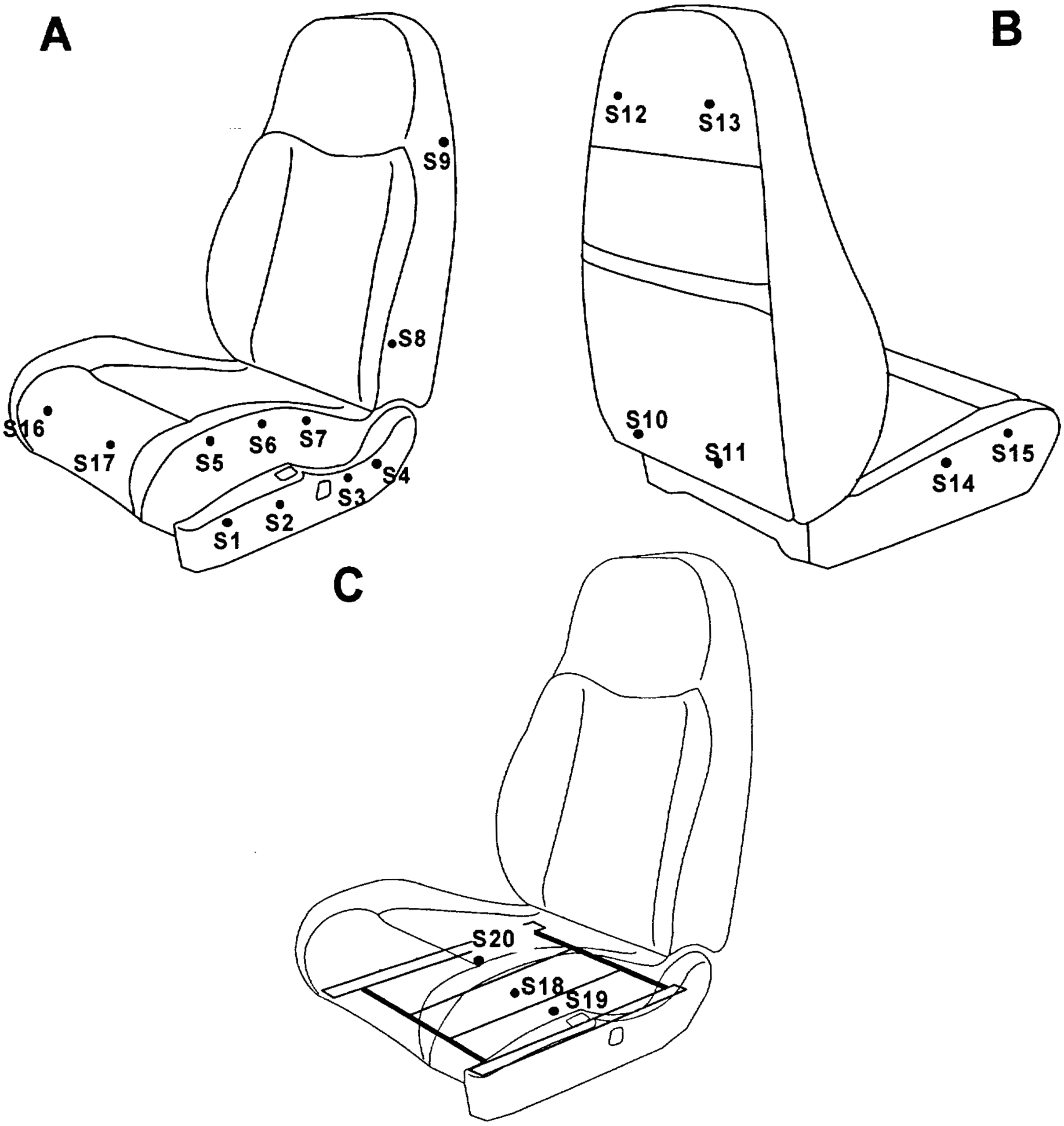

Figure D9. Fire Test F980611. Diagrams are showing the approximate locations of thermocouples on the left front seat in the test vehicle. Thermocouples S1 through S4 were located on the outer surface of the front seat cushion side cover. Thermocouples S5 through S7 were located on the exterior surface of the cover on the left side of the seat bottom. Thermocouples S8 and S9 were located on exterior surface of the cover on the left side of the seat back. Thermocouples S10 through S13 were located on exterior surface of the cover on the rear of the seat back. Thermocouples S16 and S17 were located on exterior surface of the cover on the front of the seat bottom. Thermocouples S18, S19, and S20 were located on the on lower surface of the seat frame.

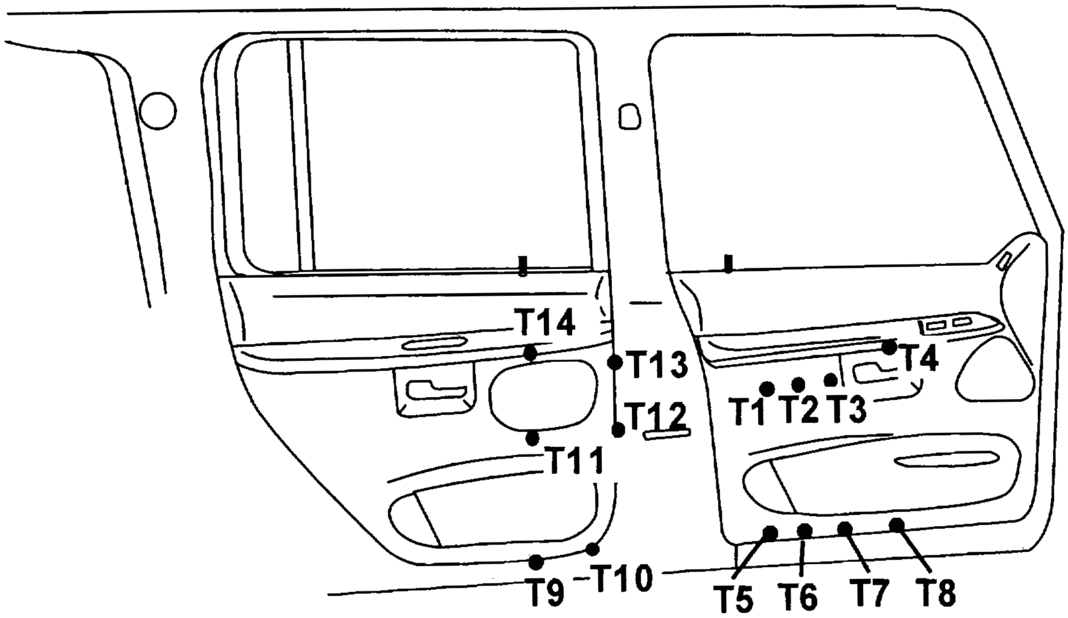

Figure D10. Fire Test F980609. Diagram showing the approximate locations of thermocouples on a section of the left front and rear door in the test vehicle. Thermocouples T1 through T8 were located on the exposed surface of the left front door interior trim panel. Thermocouples T9 through T14 were located on the exposed surface of the left rear door interior trim panel.

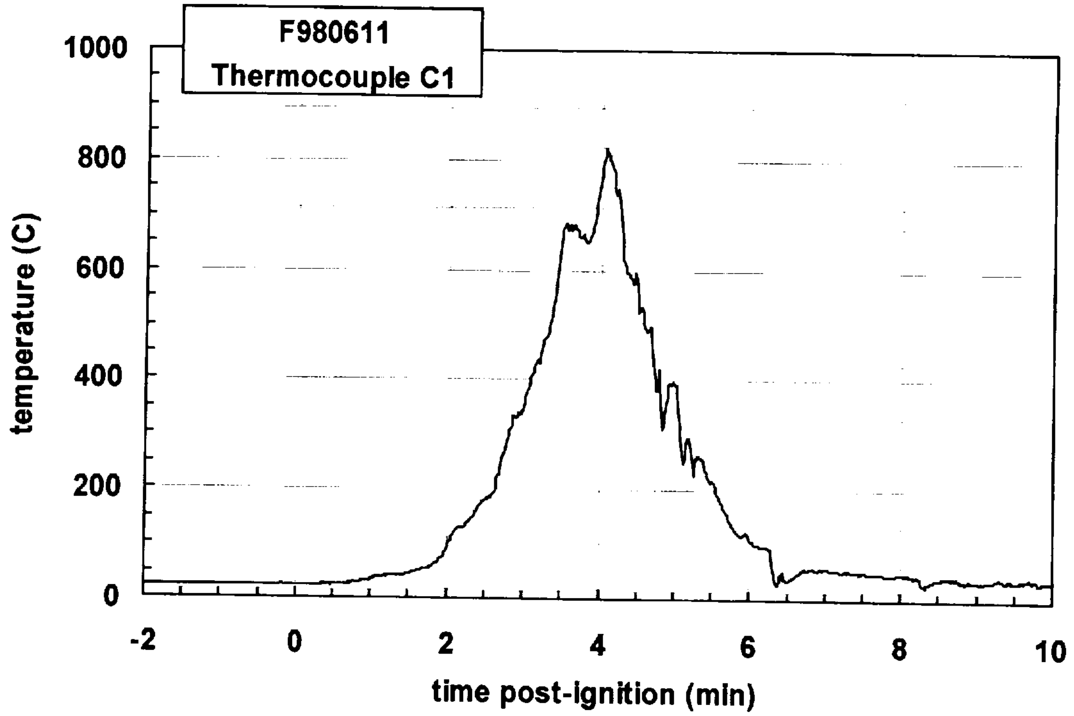

Plot D1. Fire Test F980611. Data plot from thermocouple C1.

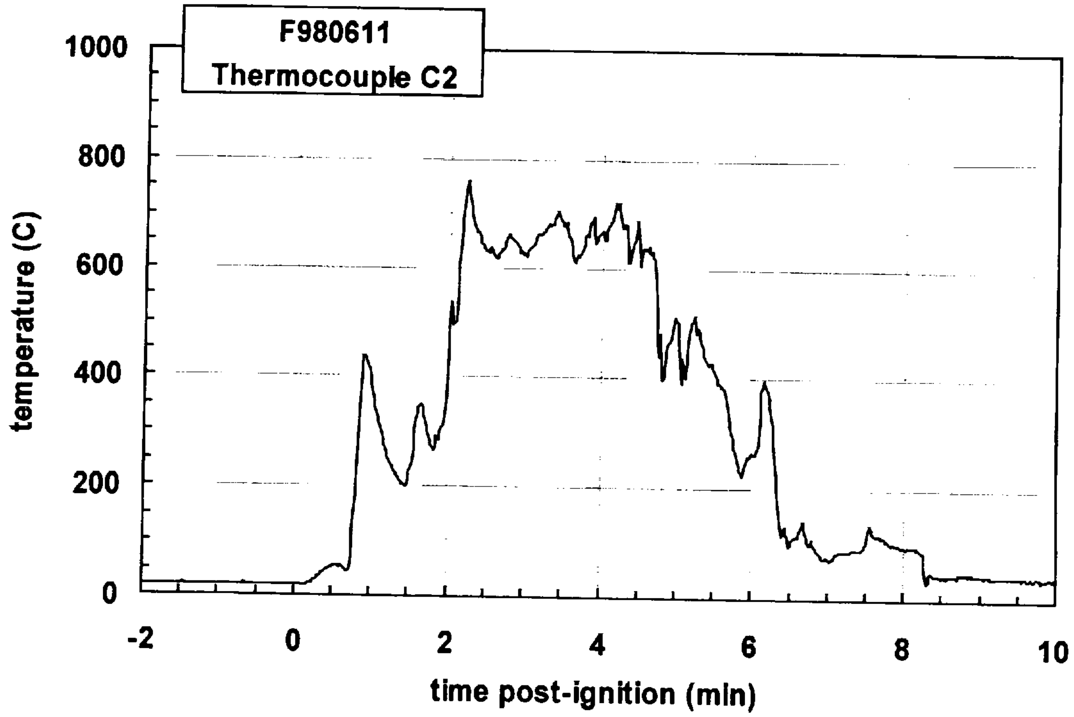

Plot D2. Fire Test F980611. Data plot from thermocouple C2.

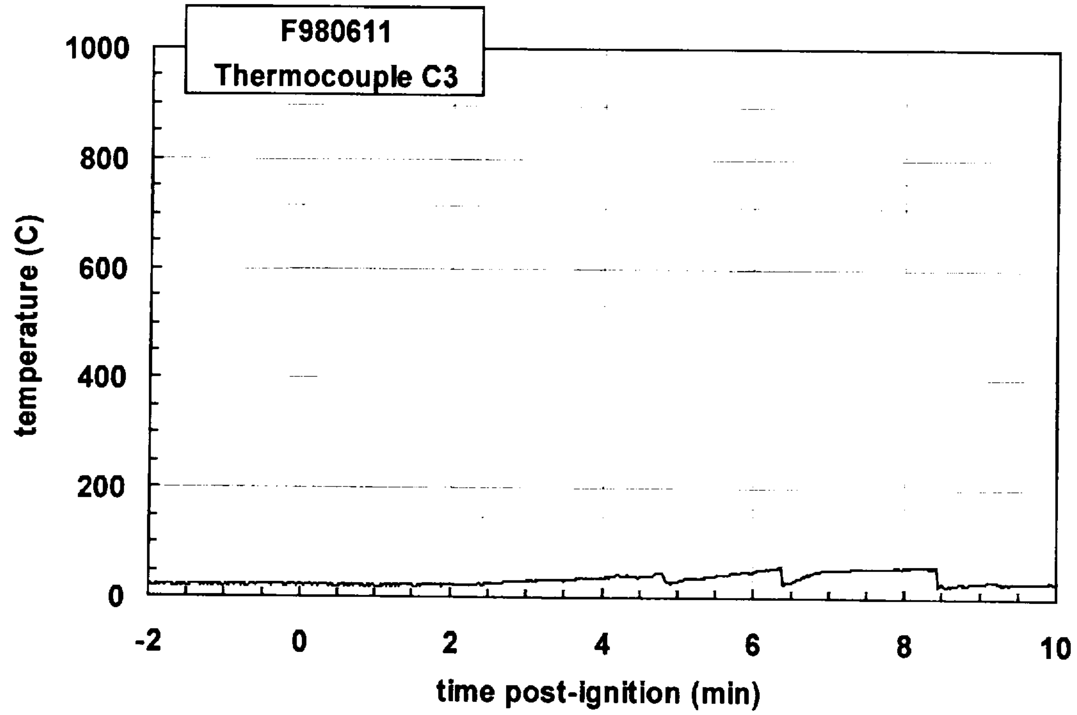

Plot D3. Fire Test F980611. Data plot from thermocouple C3.

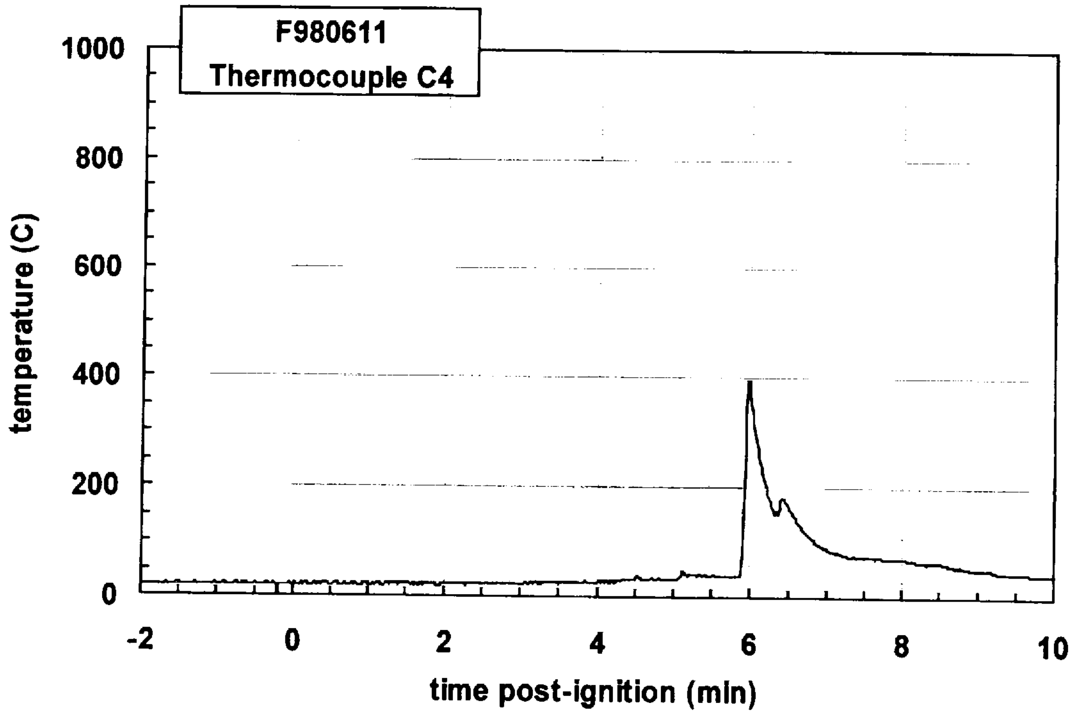

Plot D4. Fire Test F980611. Data plot from thermocouple C4.

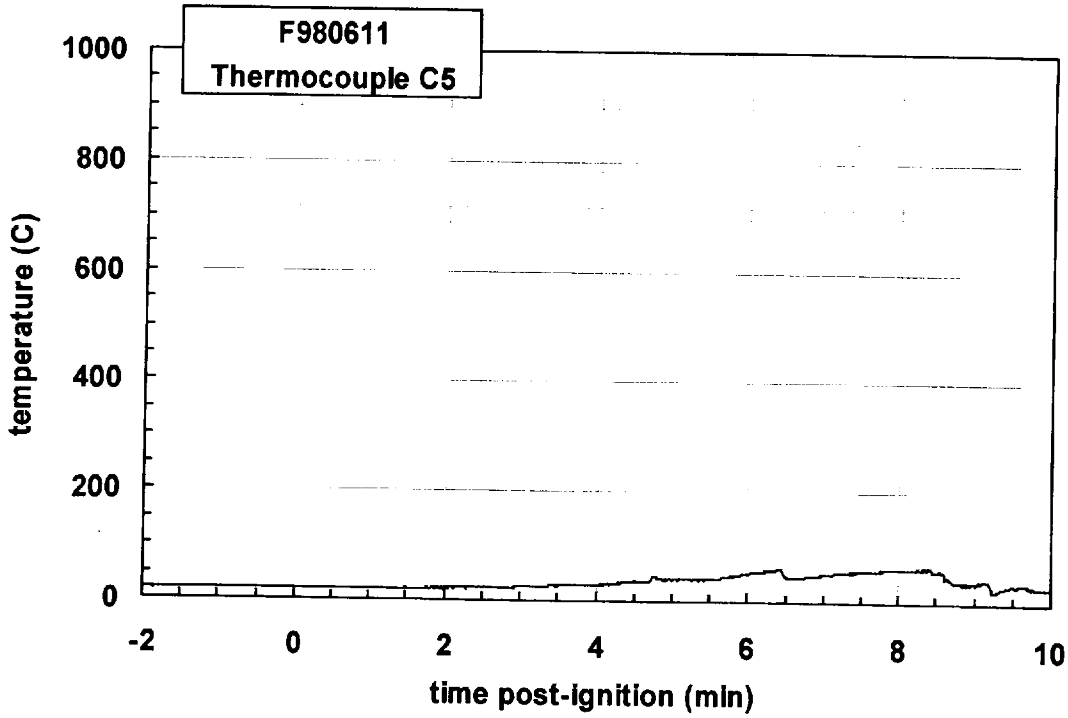

Plot D5. Fire Test F980611. Data plot from thermocouple C5.

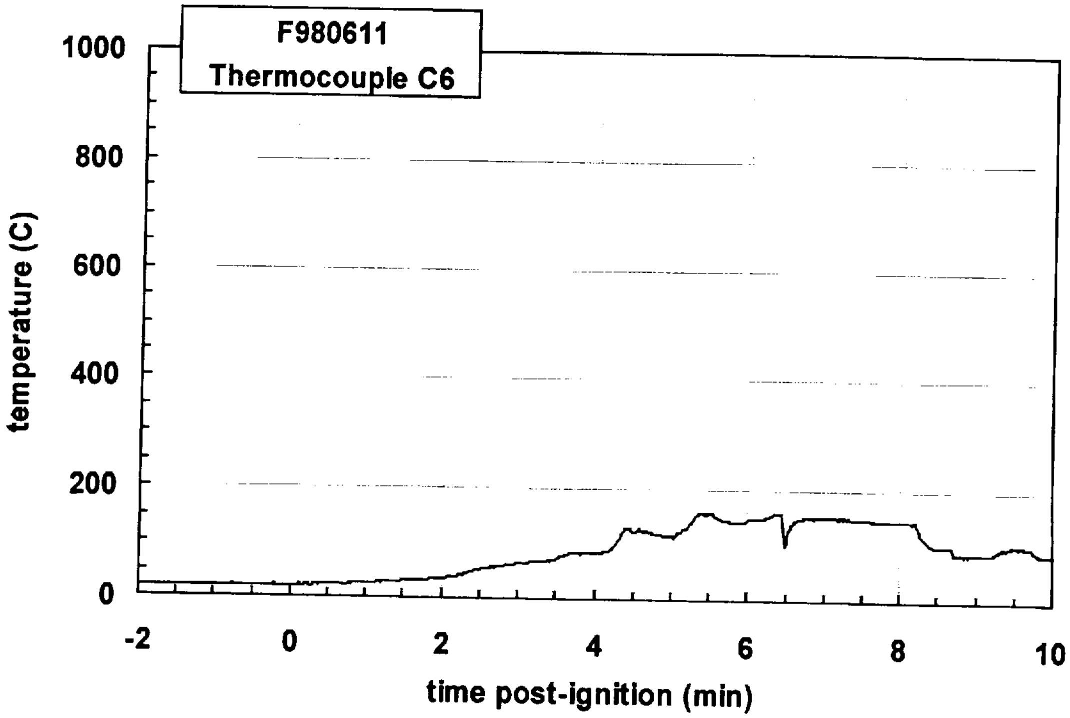

Plot D6. Fire Test F980611. Data plot from thermocouple C6.

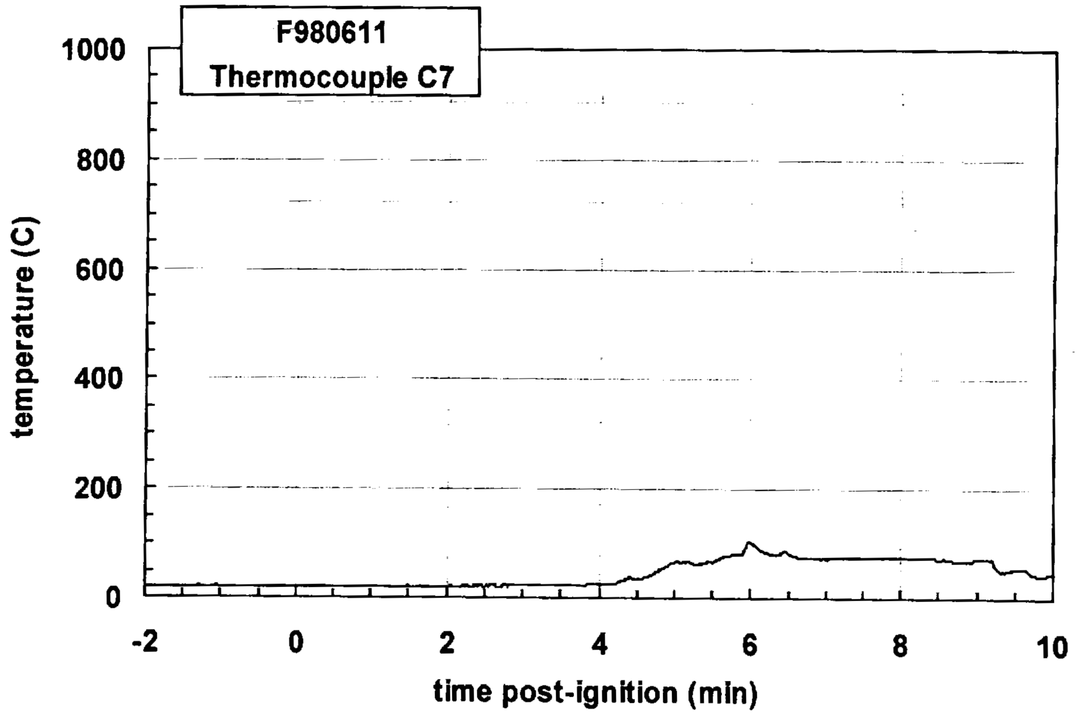

Plot D7. Fire Test F980611. Data plot from thermocouple C7.

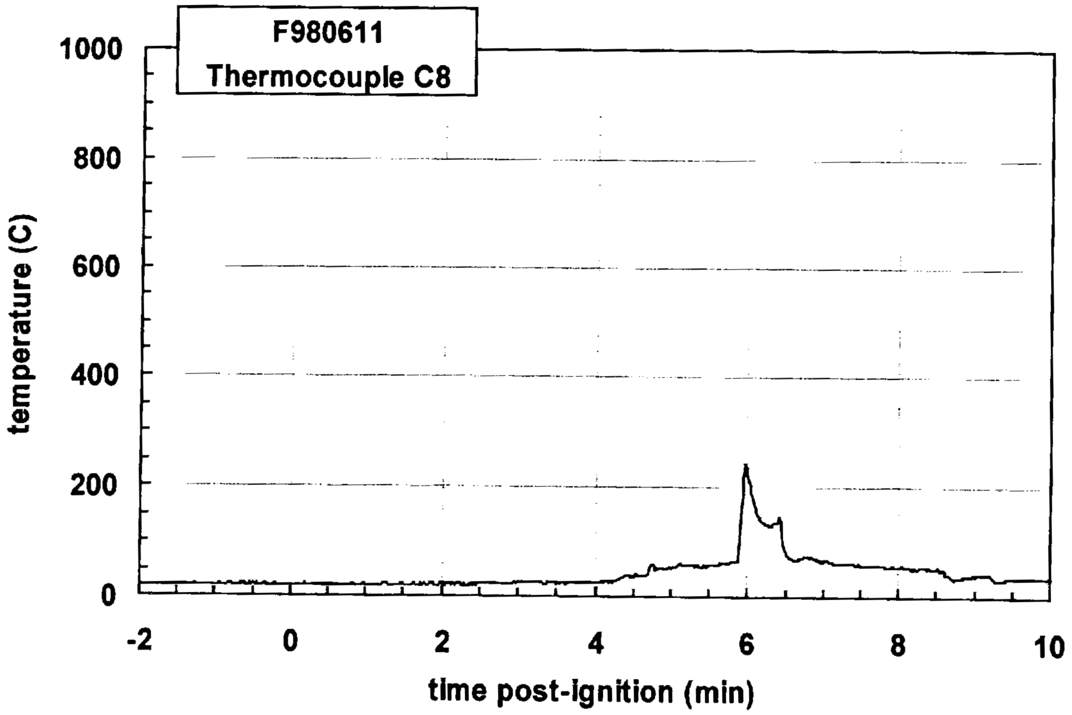

Plot D8. Fire Test F980611. Data plot from thermocouple C8.

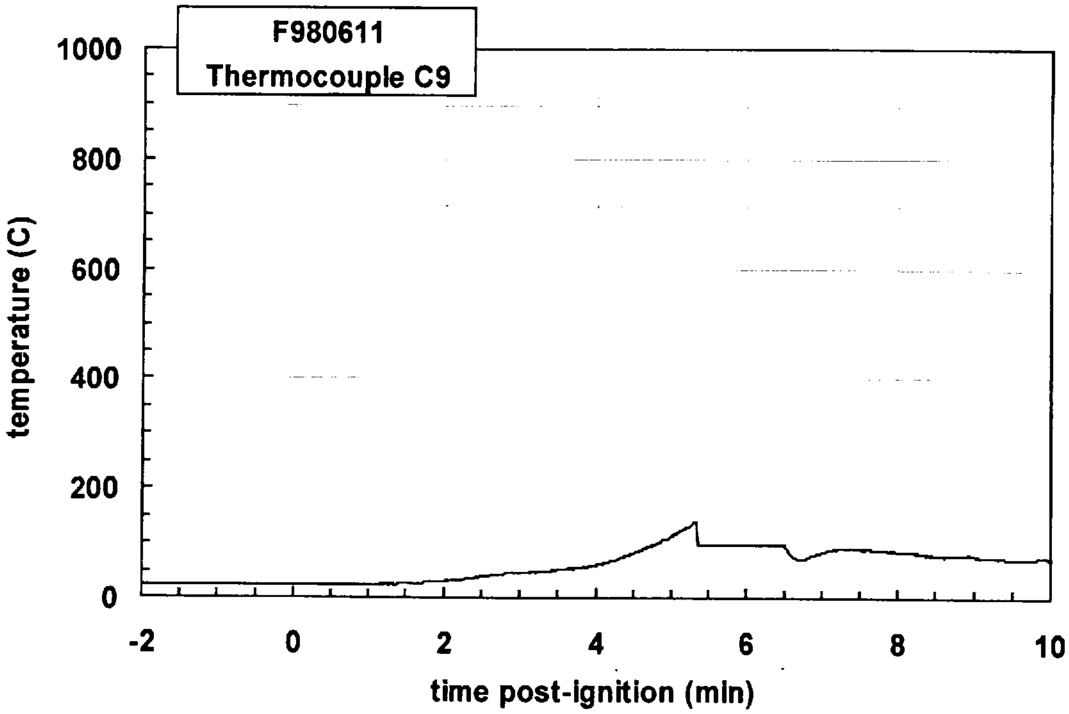

Plot D9. Fire Test F980611. Data plot from thermocouple C9.

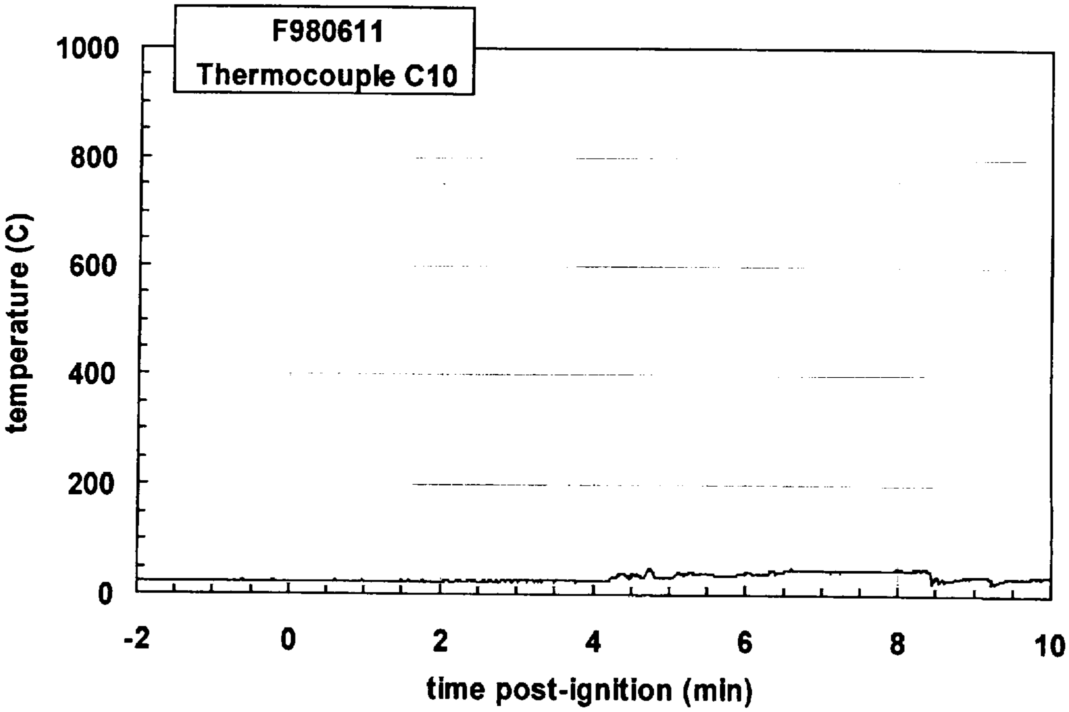

Plot D10. Fire Test F980611. Data plot from thermocouple C10.

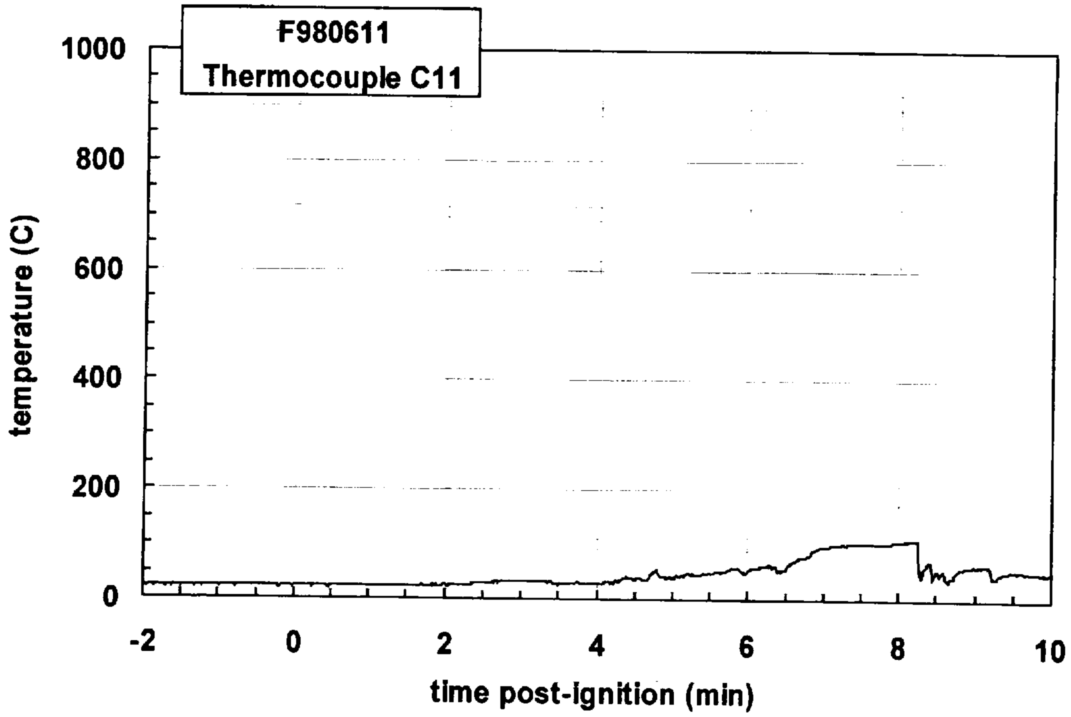

Plot D11. Fire Test F980611. Data plot from thermocouple C11.

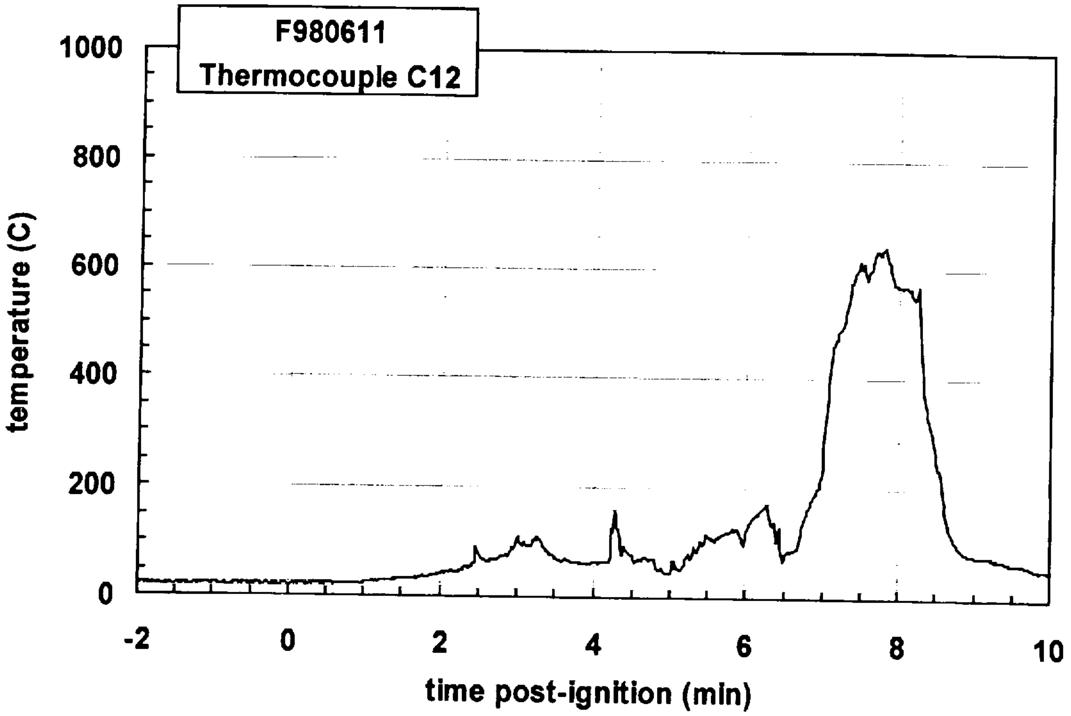

Plot D12. Fire Test F980611. Data plot from thermocouple C12.

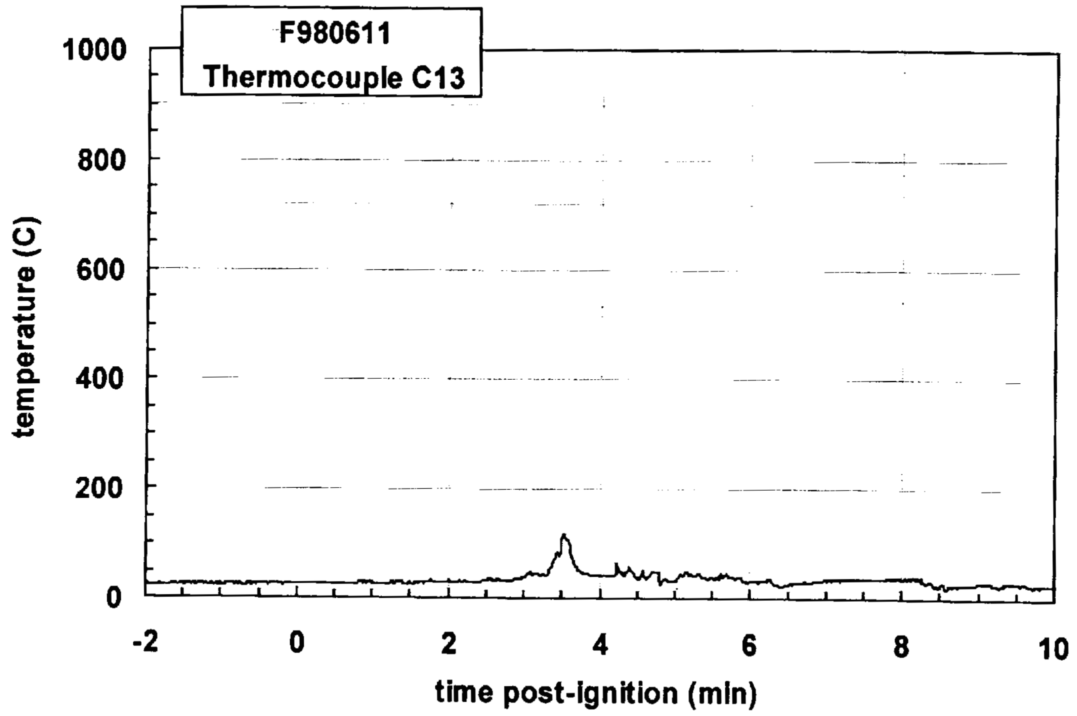

Plot D13. Fire Test F980611. Data plot from thermocouple C13.

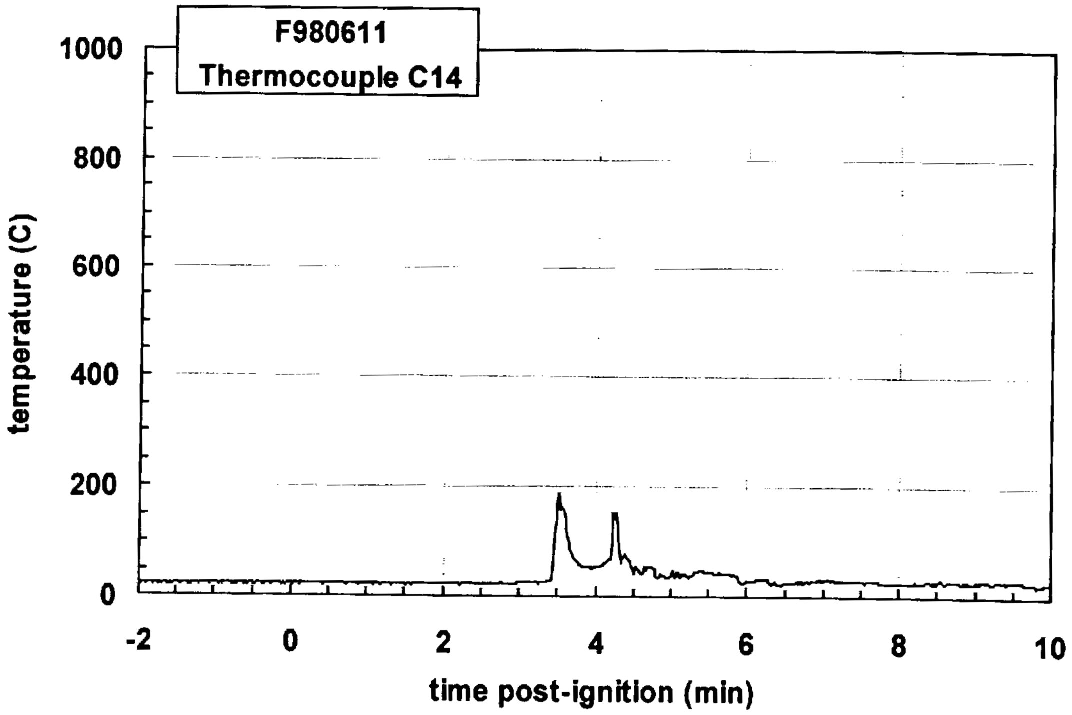

Plot D14. Fire Test F980611. Data plot from thermocouple C14.

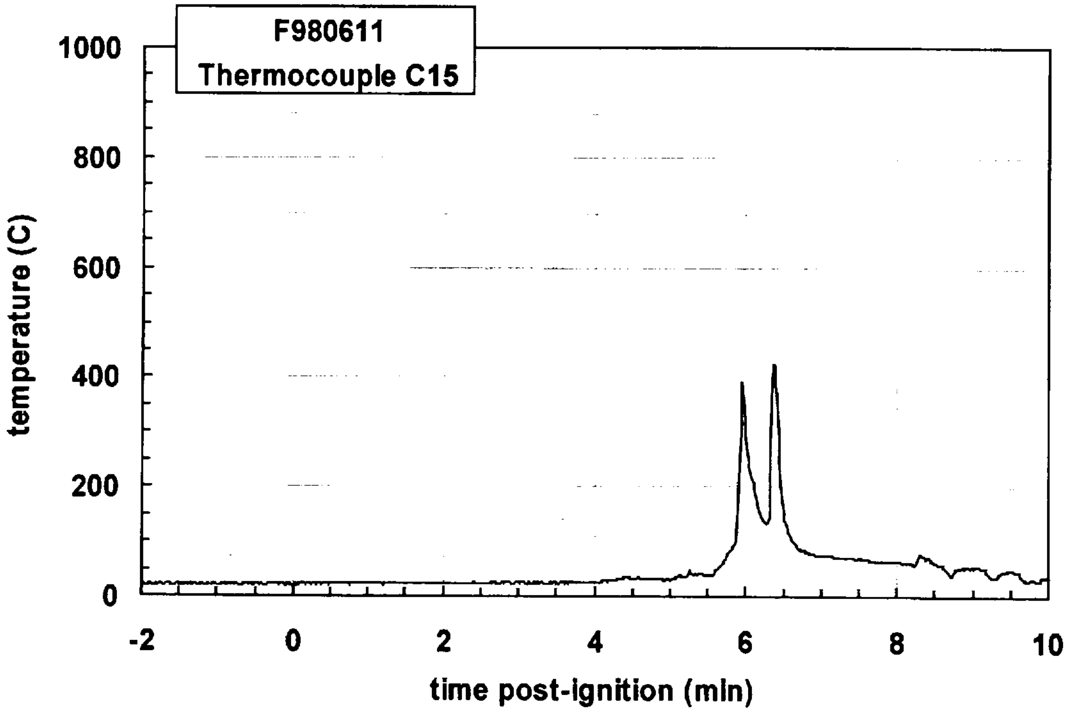

Plot D15. Fire Test F980611. Data plot from thermocouple C15.

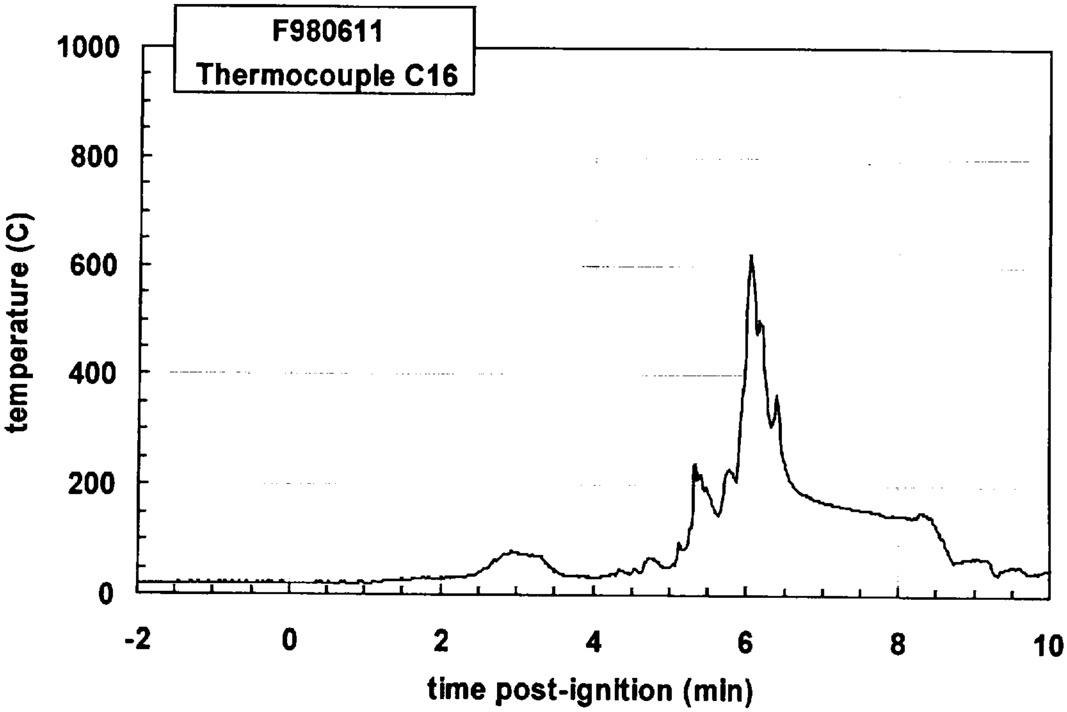

Plot D16. Fire Test F980611. Data plot from thermocouple C16.

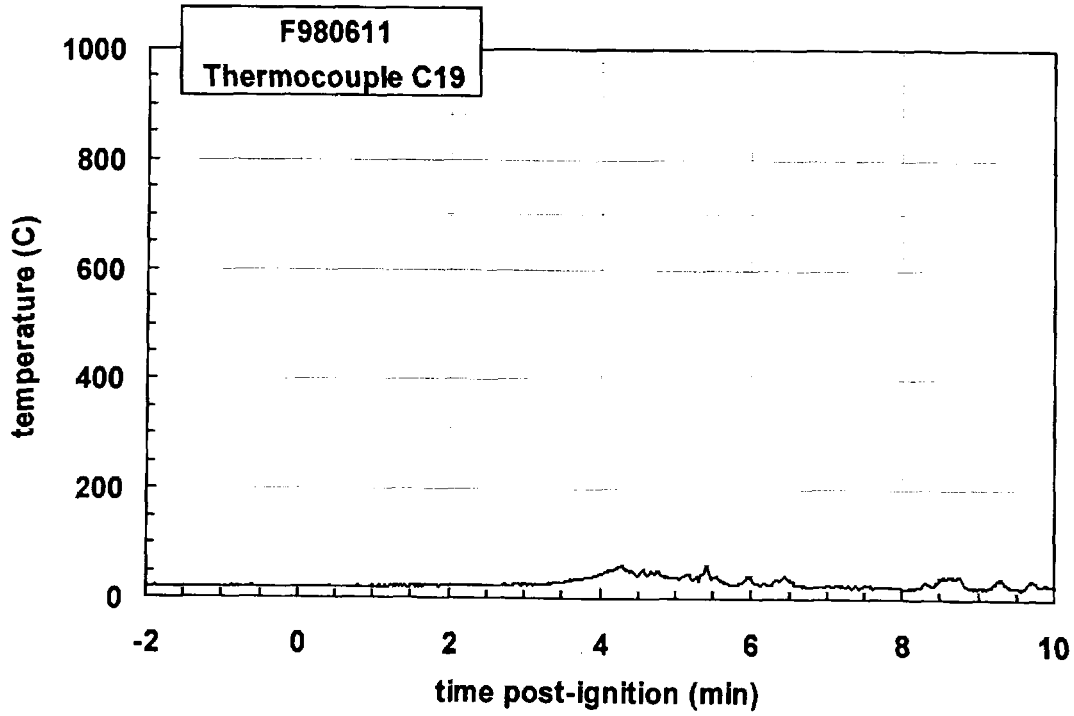

Plot D19. Fire Test F980611. Data plot from thermocouple C19.

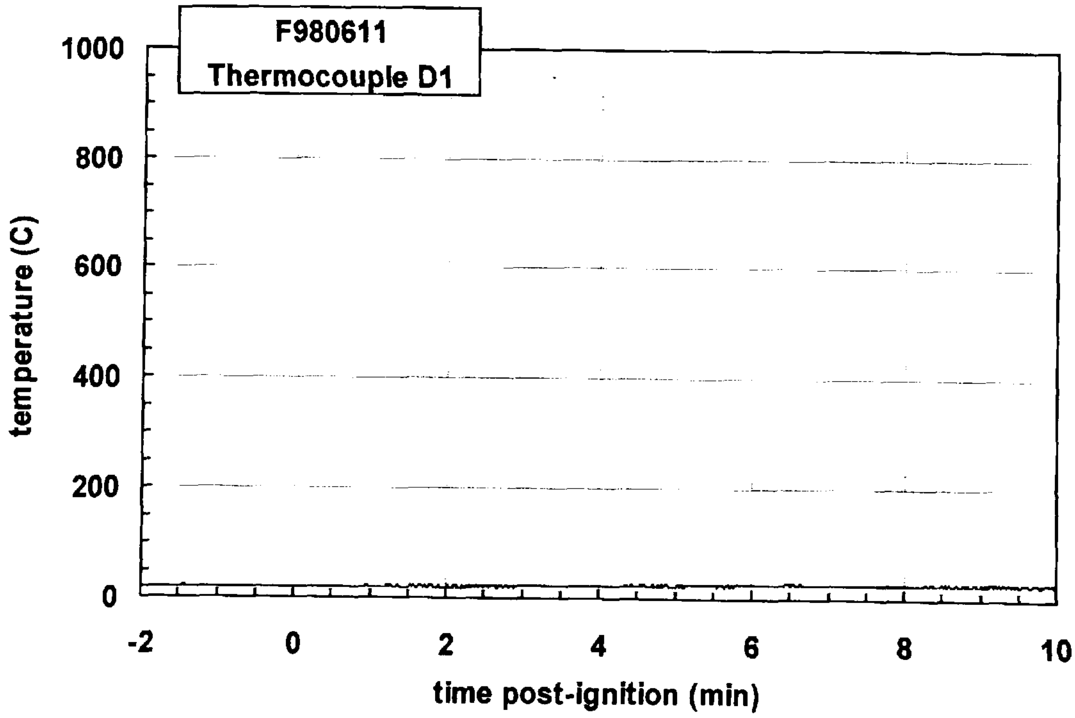

Plot D20. Fire Test F980611. Data plot from thermocouple D1.

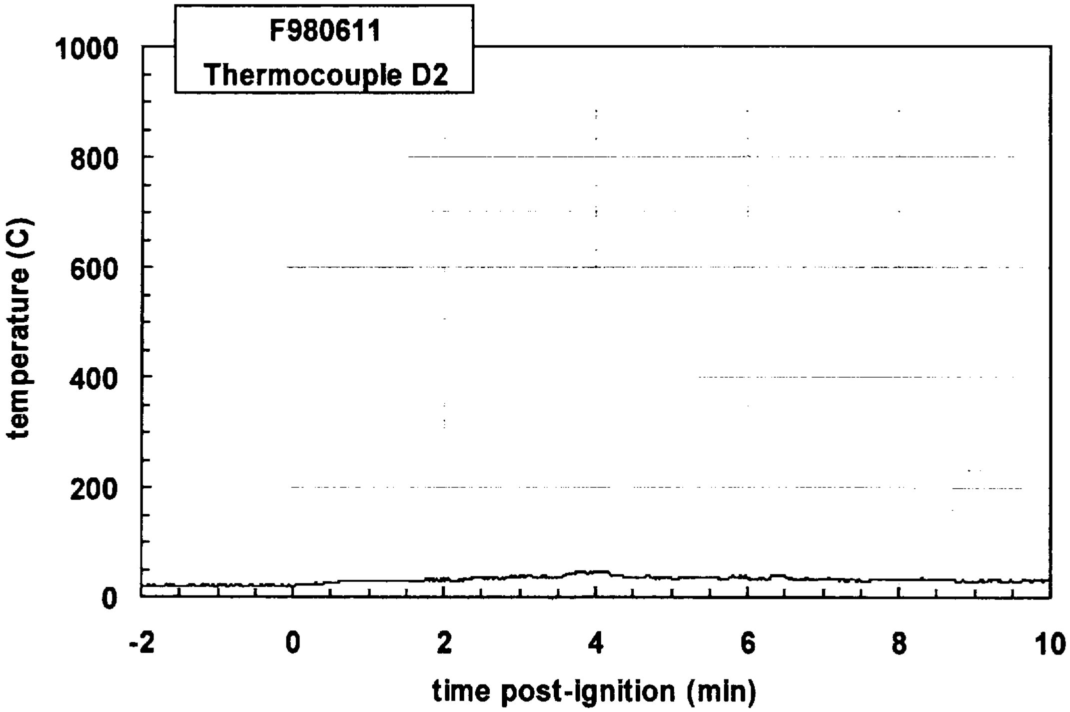

Plot D21. Fire Test F980611. Data plot from thermocouple D2.

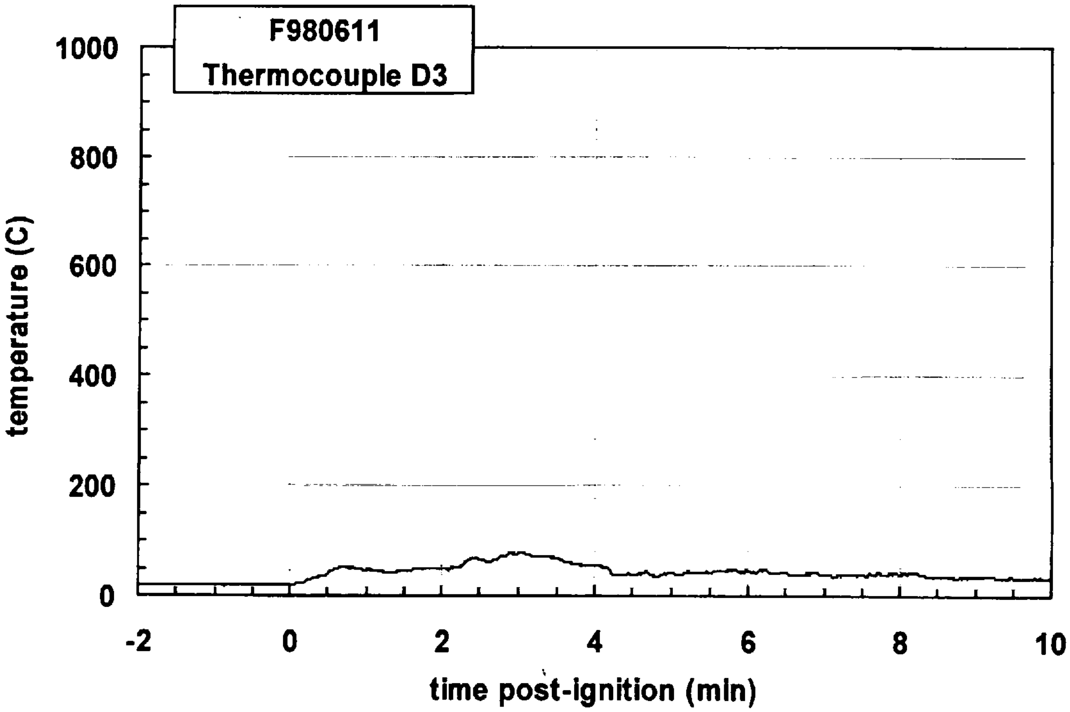

Plot D22. Fire Test F980611. Data plot from thermocouple D3.

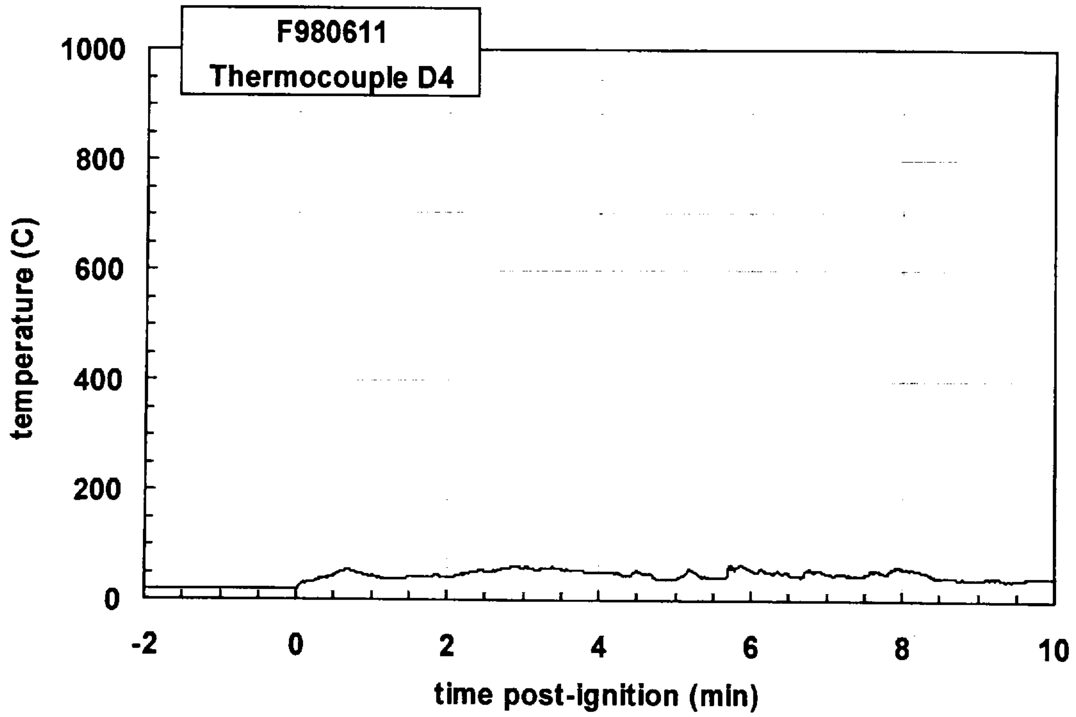

Plot D23. Fire Test F980611. Data plot from thermocouple D4.

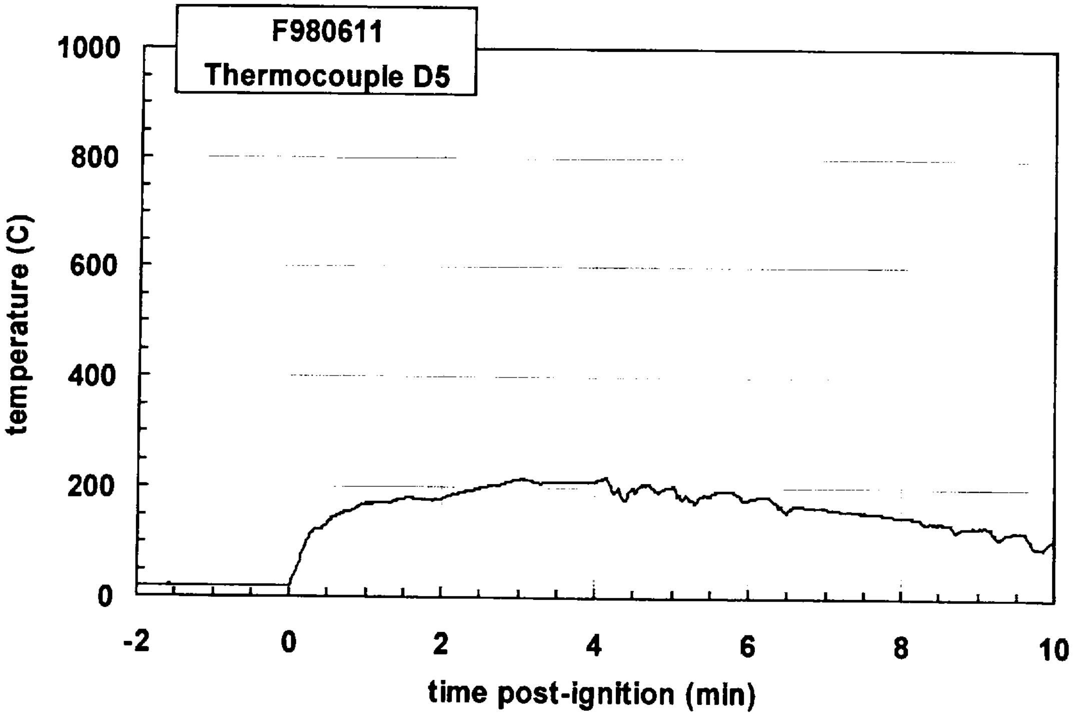

Plot D24. Fire Test F980611. Data plot from thermocouple D5.

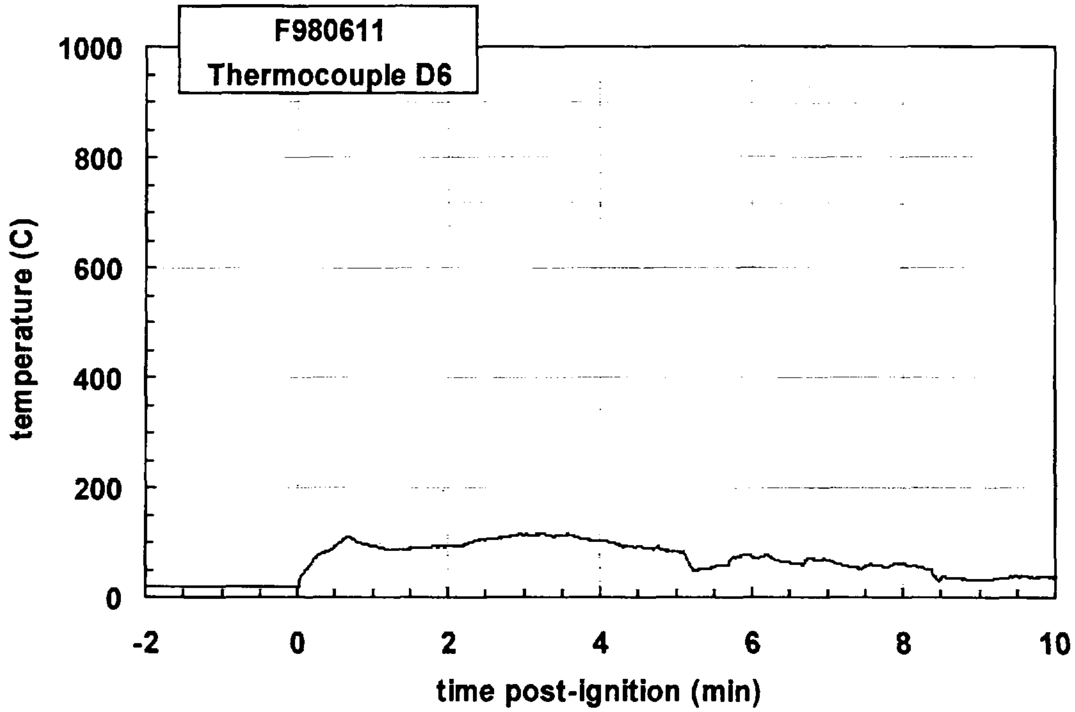

Plot D25. Fire Test F980611. Data plot from thermocouple D6.

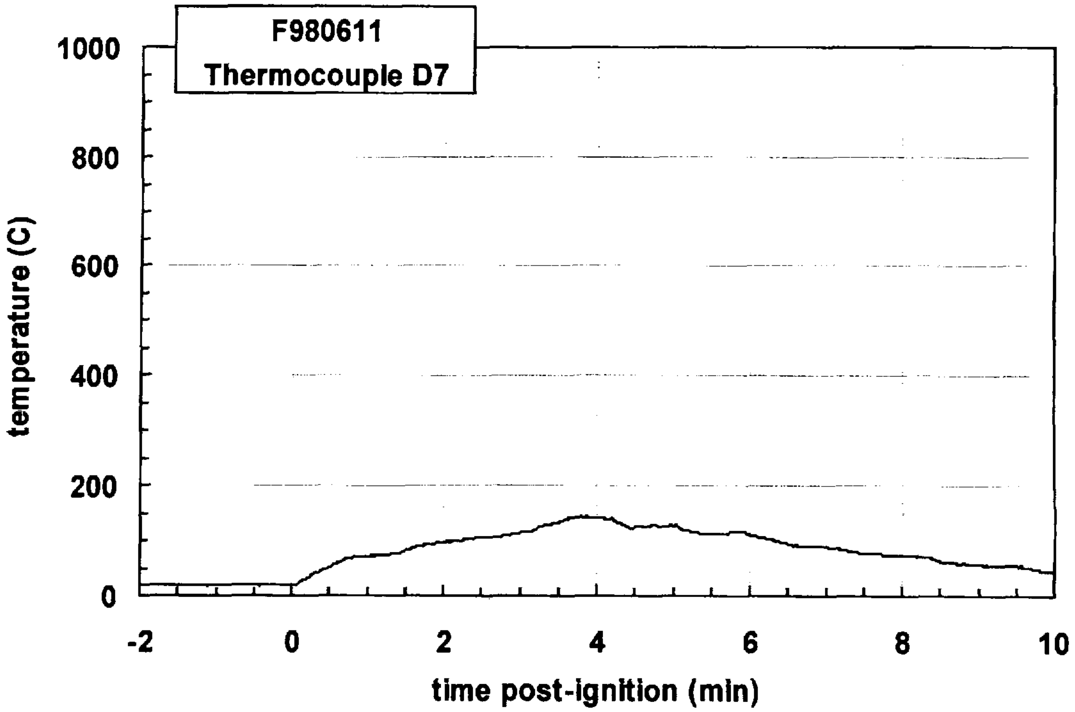

Plot D26. Fire Test F980611. Data plot from thermocouple D7.

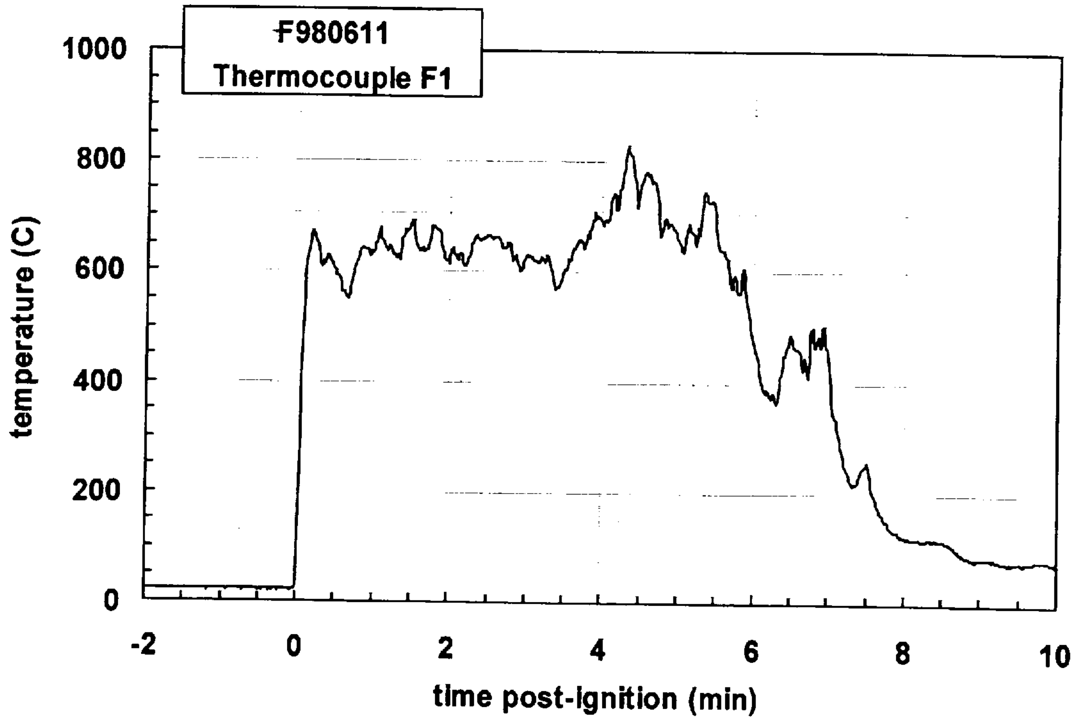

Plot D27. Fire Test F980611. Data plot from thermocouple F1.

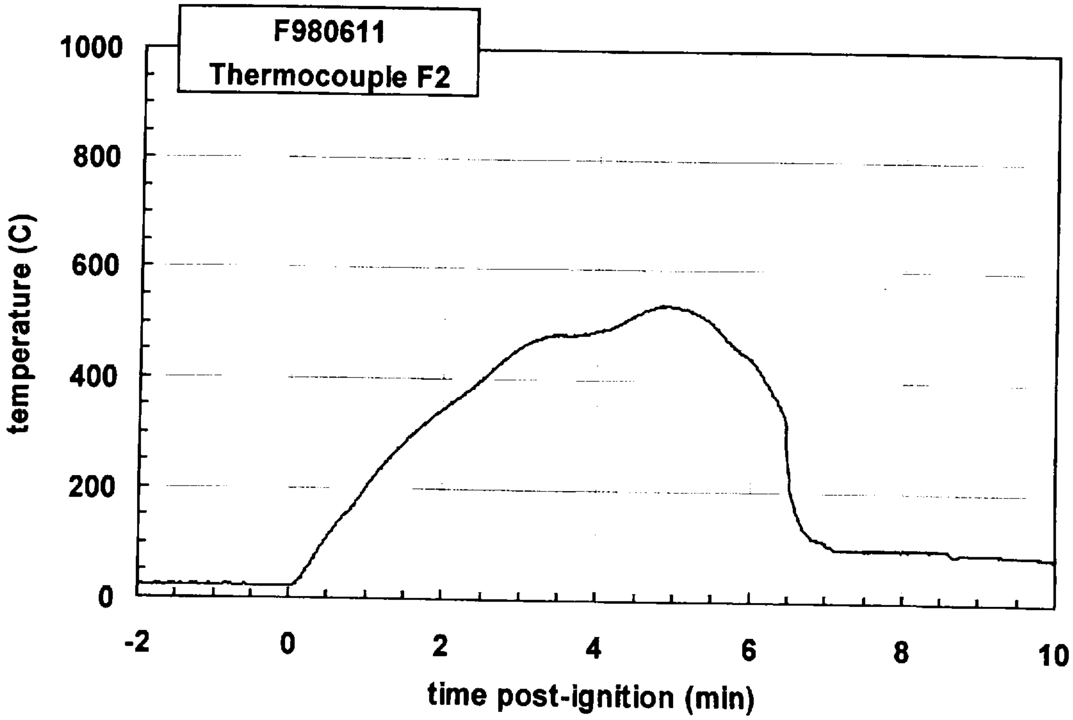

Plot D28. Fire Test F980611. Data plot from thermocouple F2.

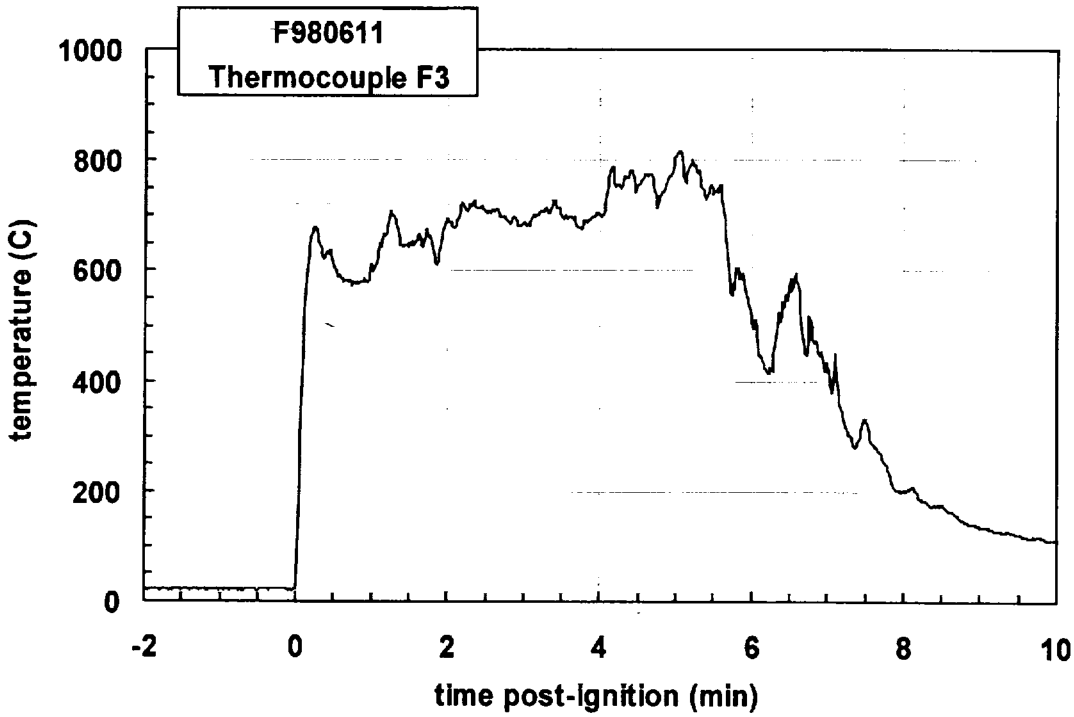

Plot D29. Fire Test F980611. Data plot from thermocouple F3.

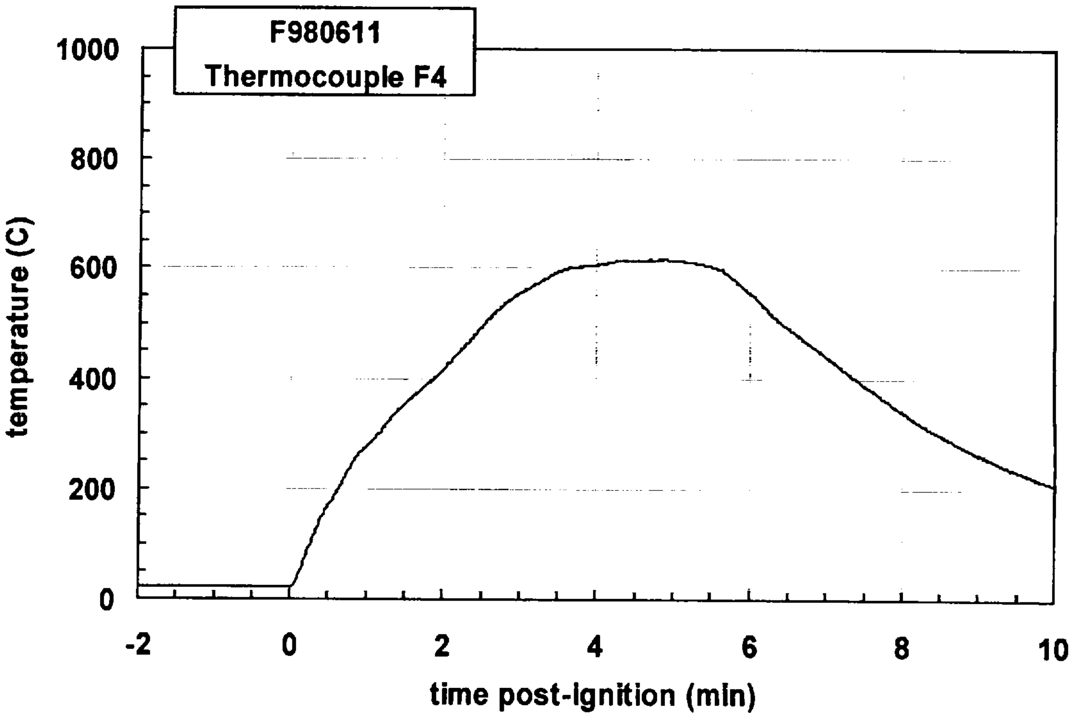

Plot D30. Fire Test F980611. Data plot from thermocouple F4.

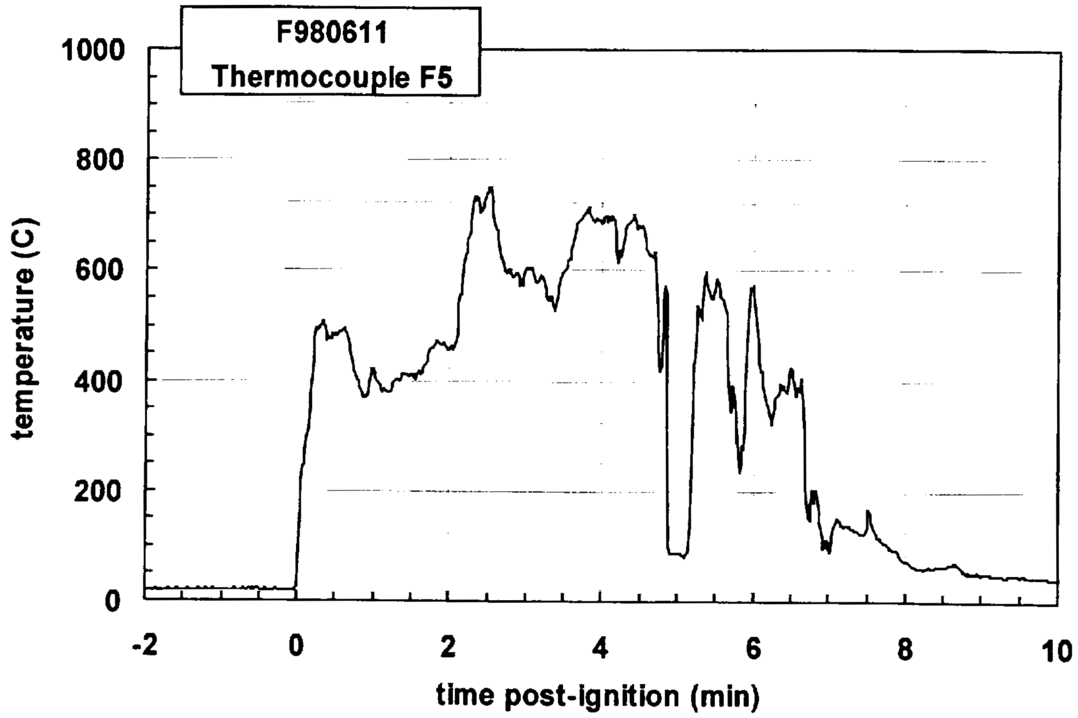

Plot D31. Fire Test F980611. Data plot from thermocouple F5.

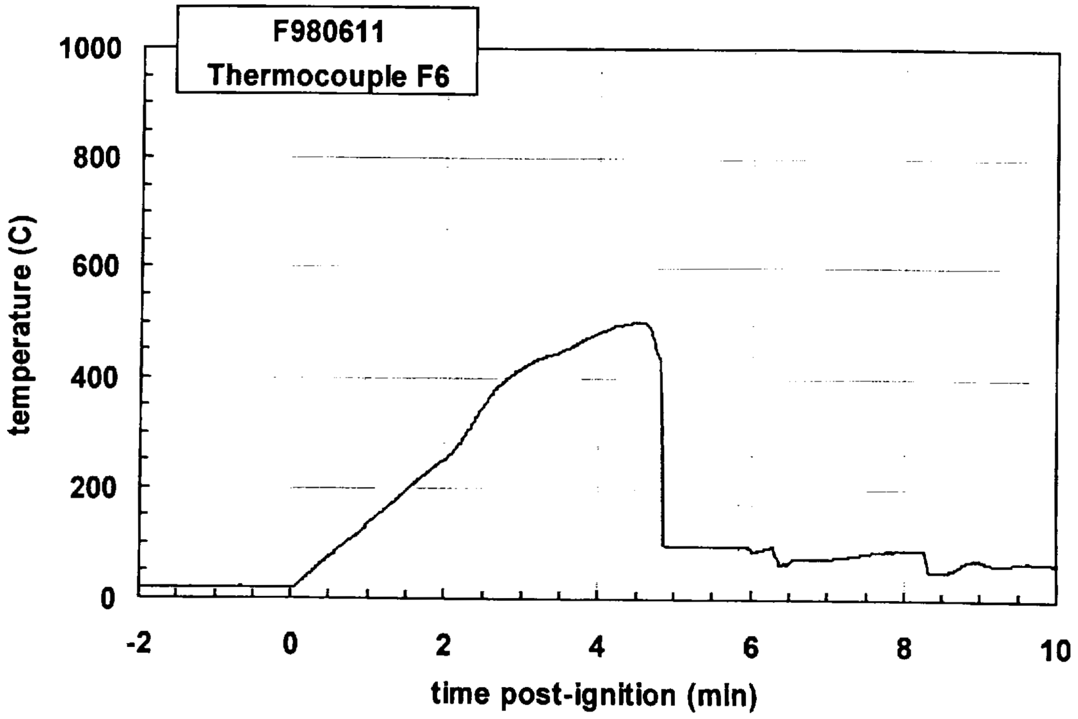

Plot D32. Fire Test F980611. Data plot from thermocouple F6.

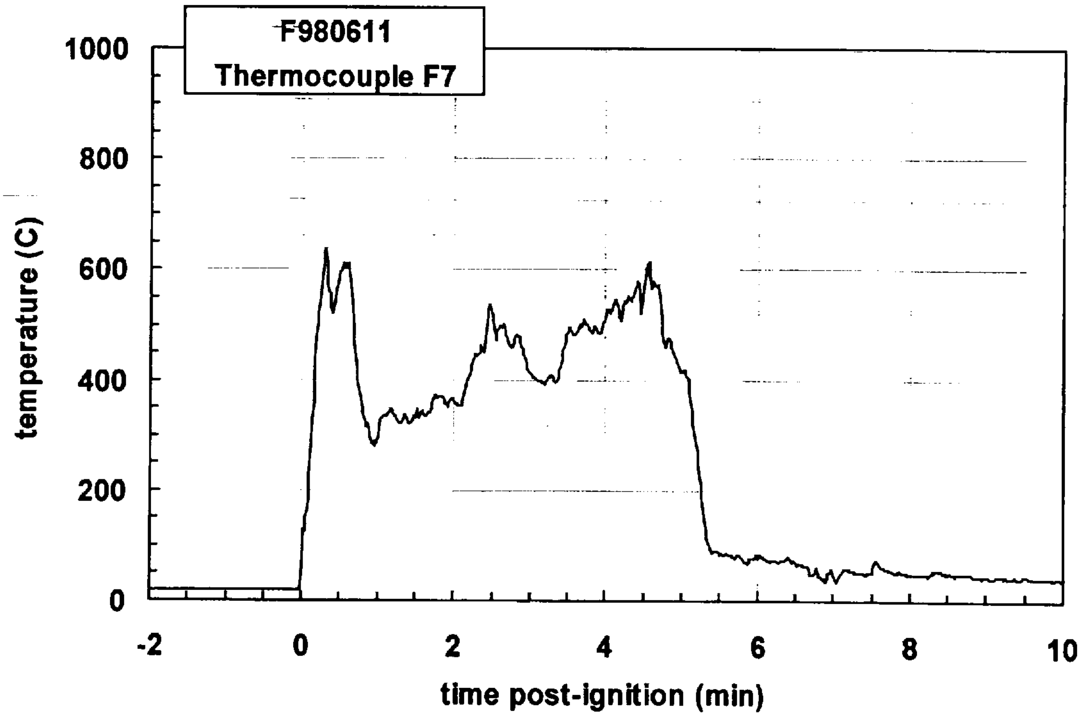

Plot D33. Fire Test F980611. Data plot from thermocouple F7.

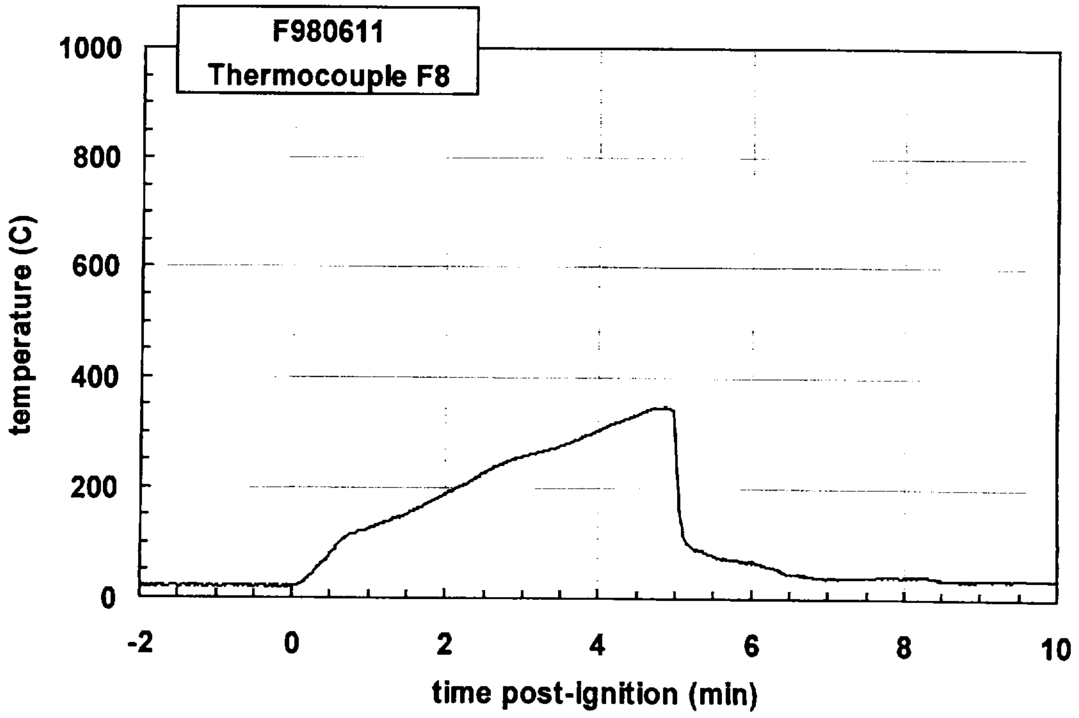

Plot D34. Fire Test F980611. Data plot from thermocouple F8.

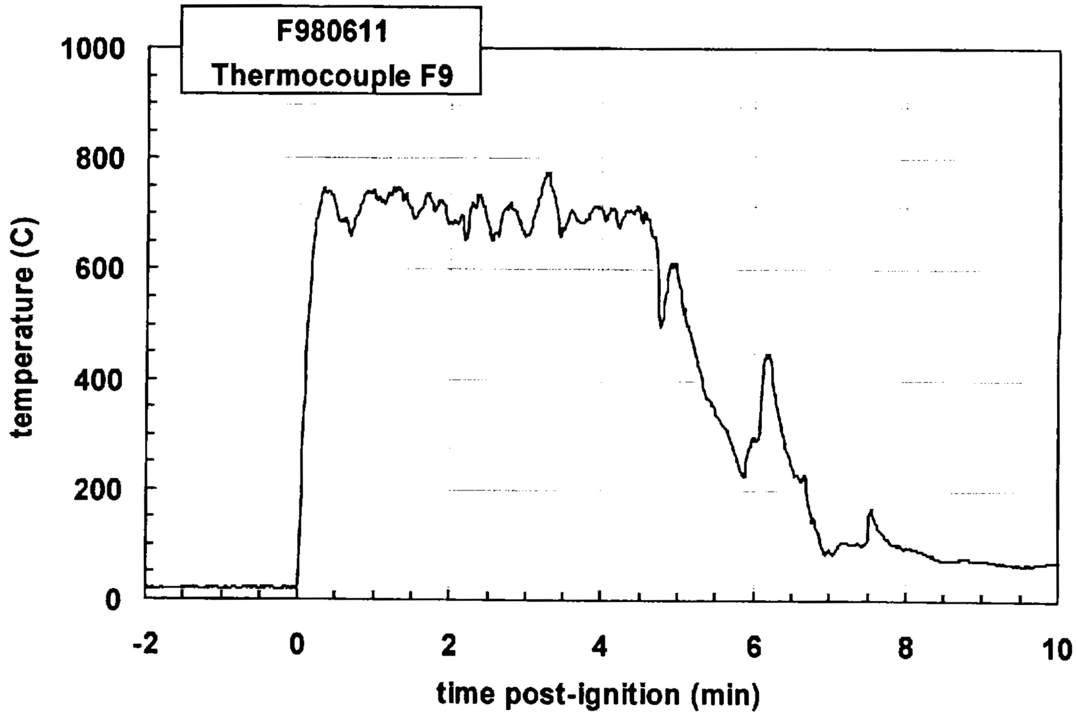

Plot D35. Fire Test F980611. Data plot from thermocouple F9.

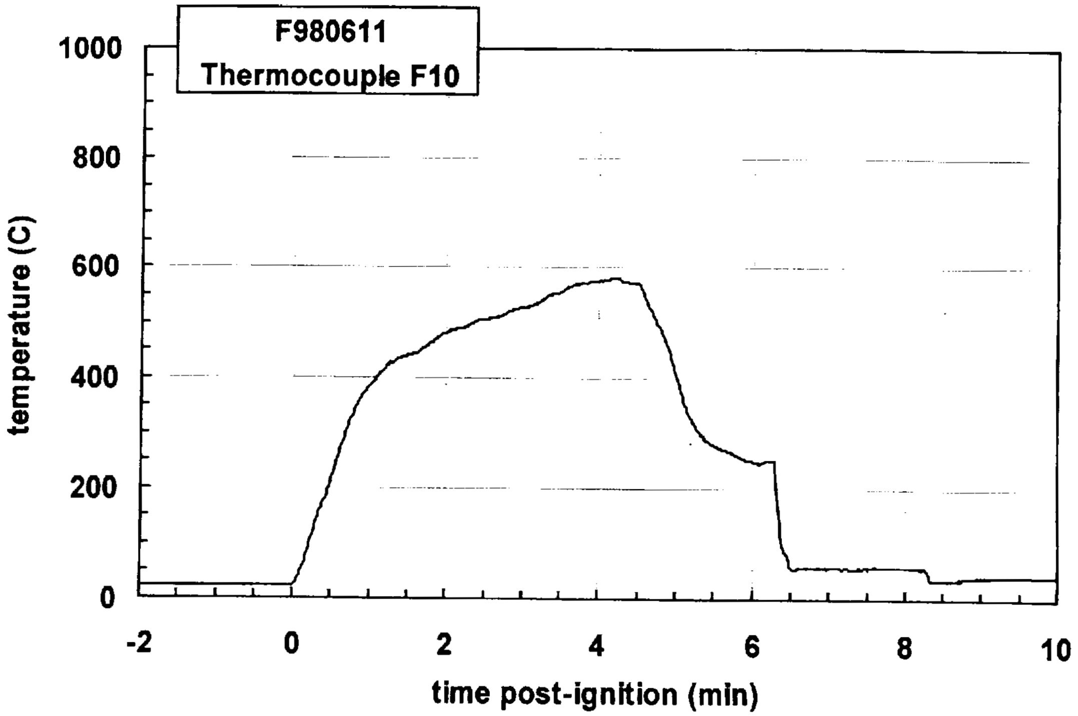

Plot D36. Fire Test F980611. Data plot from thermocouple F10.

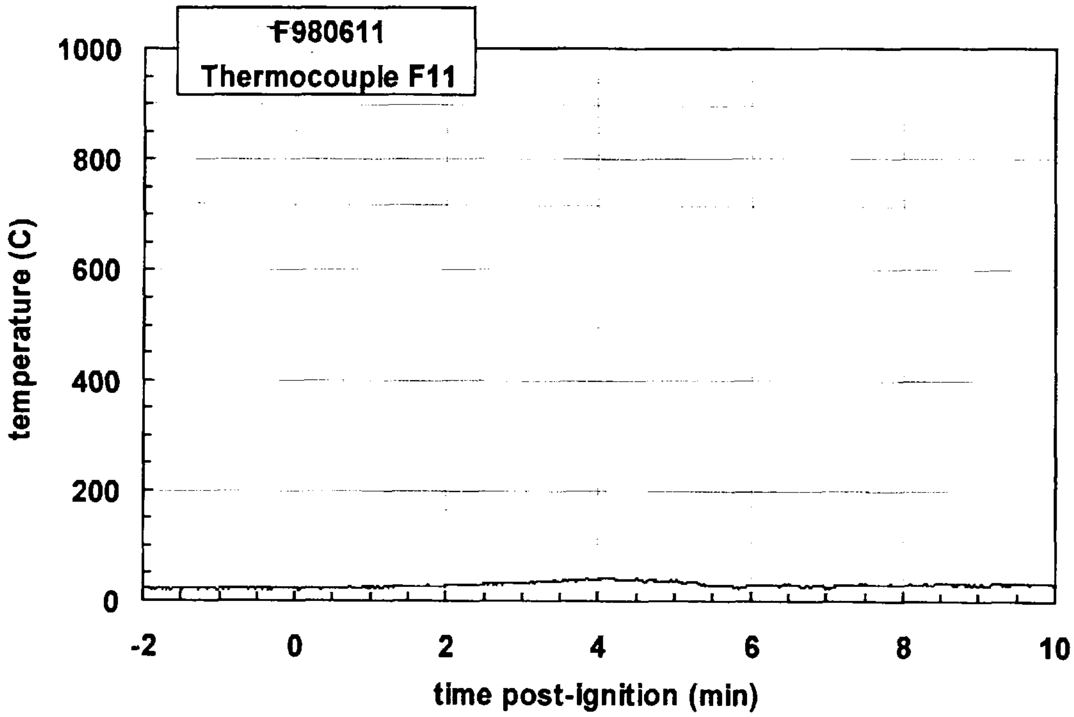

Plot D37. Fire Test F980611. Data plot from thermocouple F11.

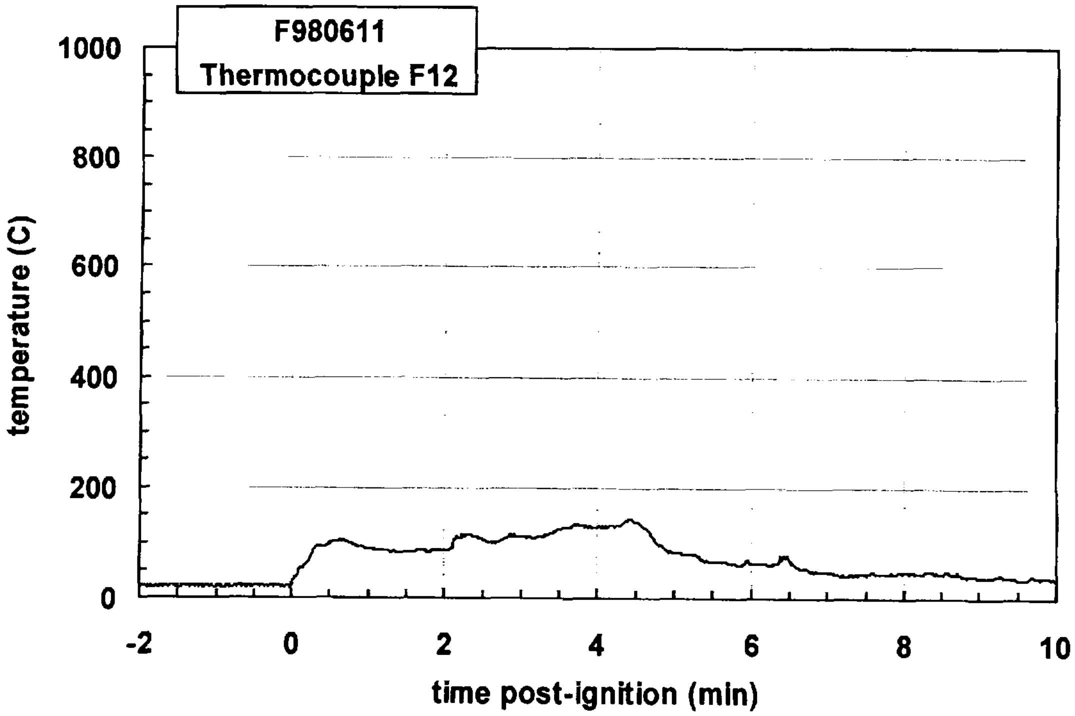

Plot D38. Fire Test F980611. Data plot from thermocouple F12.

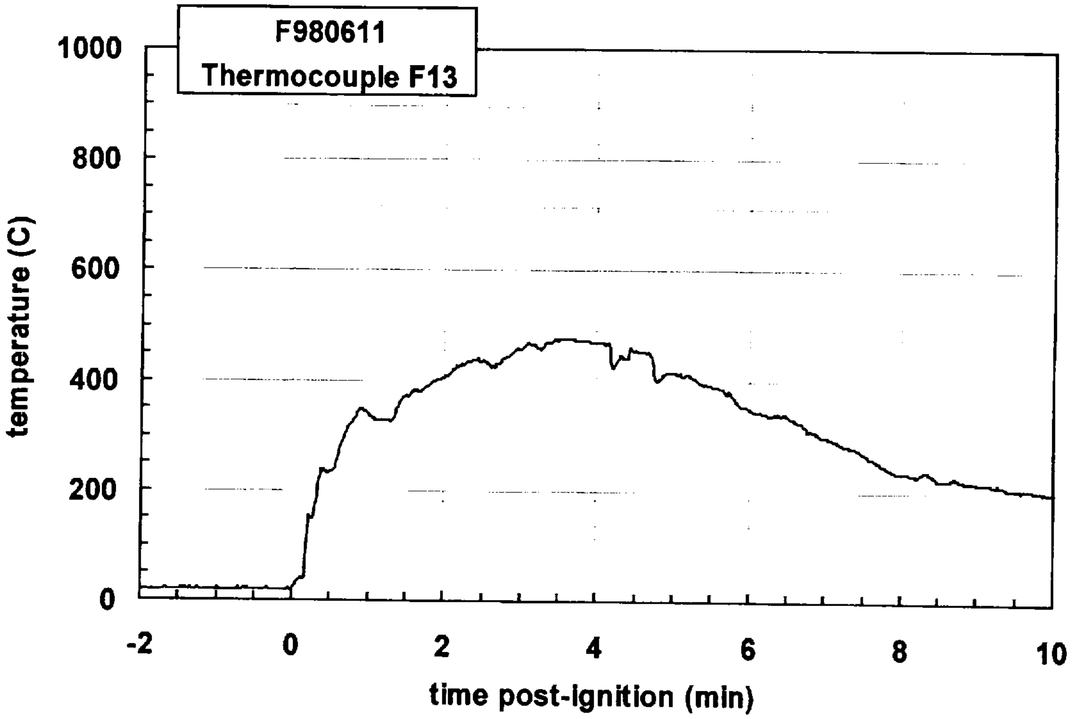

Plot D39. Fire Test F980611. Data plot from thermocouple F13.

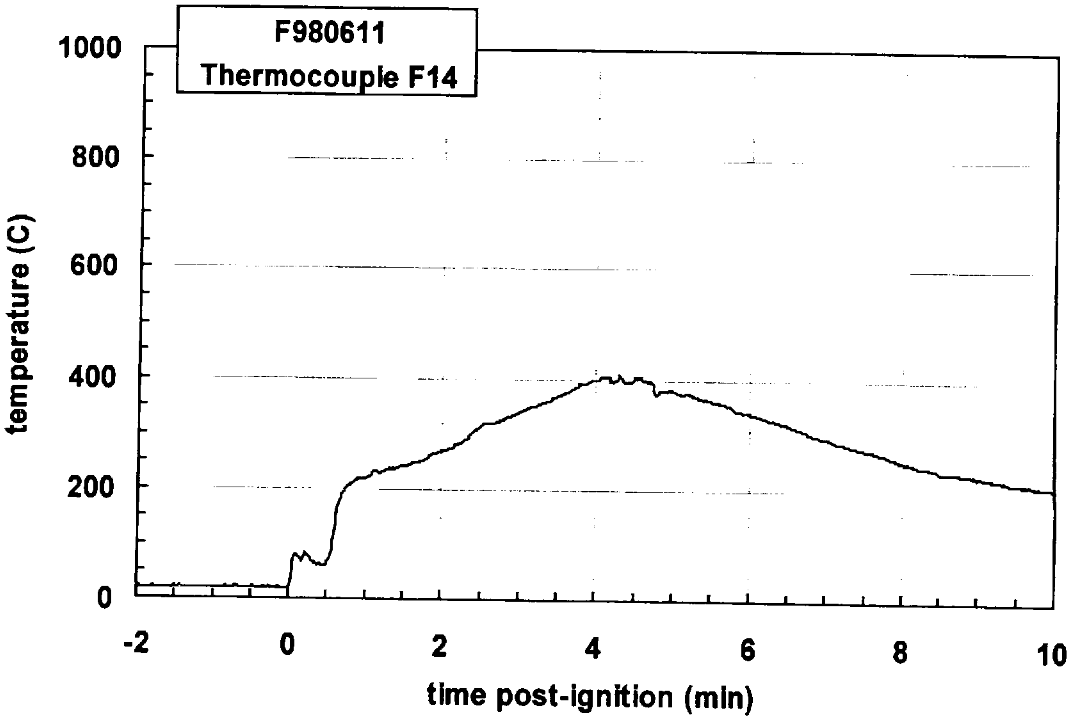

Plot D40. Fire Test F980611. Data plot from thermocouple F14.

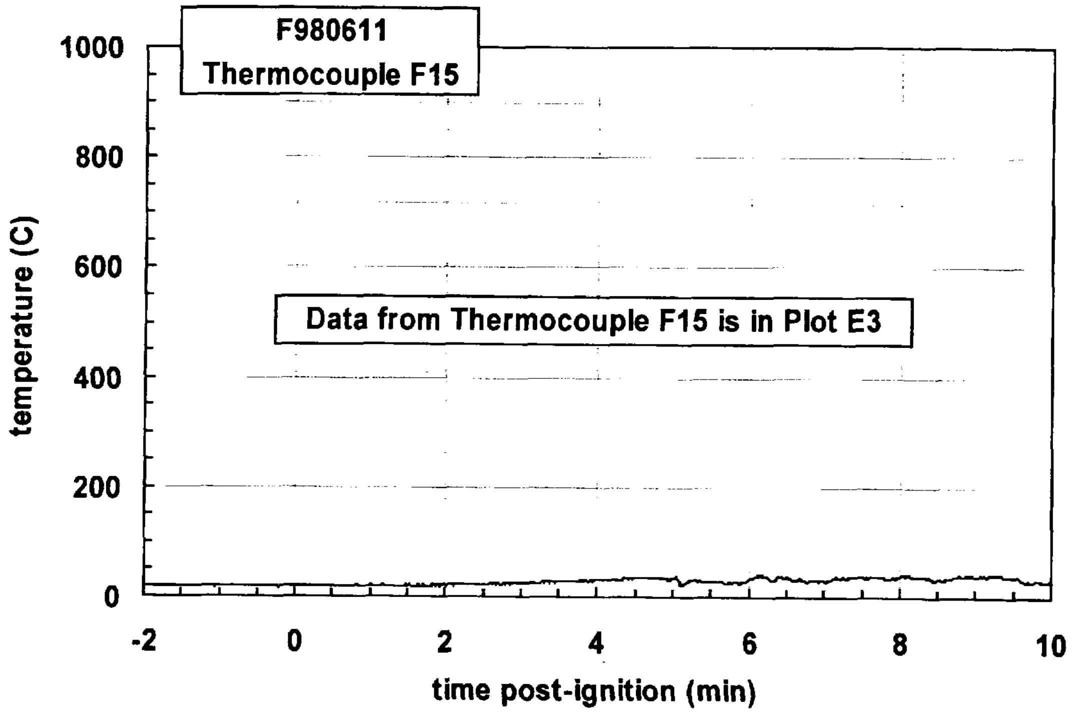

Plot D41. Fire Test F980611. Data plot from thermocouple F15.

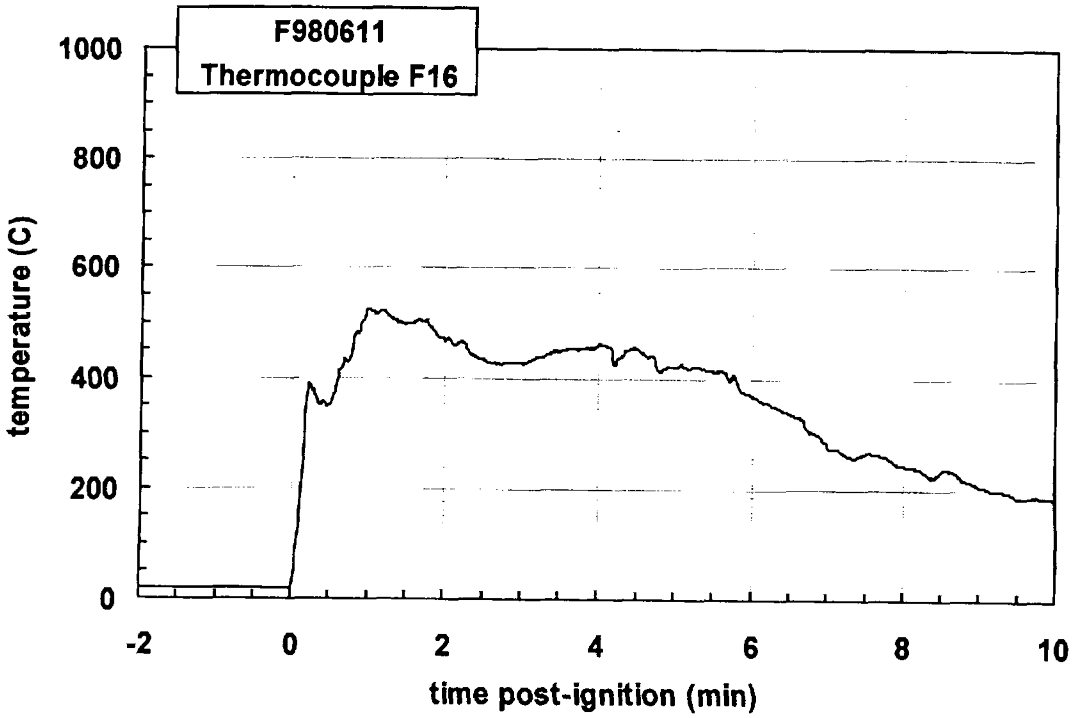

Plot D42. Fire Test F980611. Data plot from thermocouple F16.

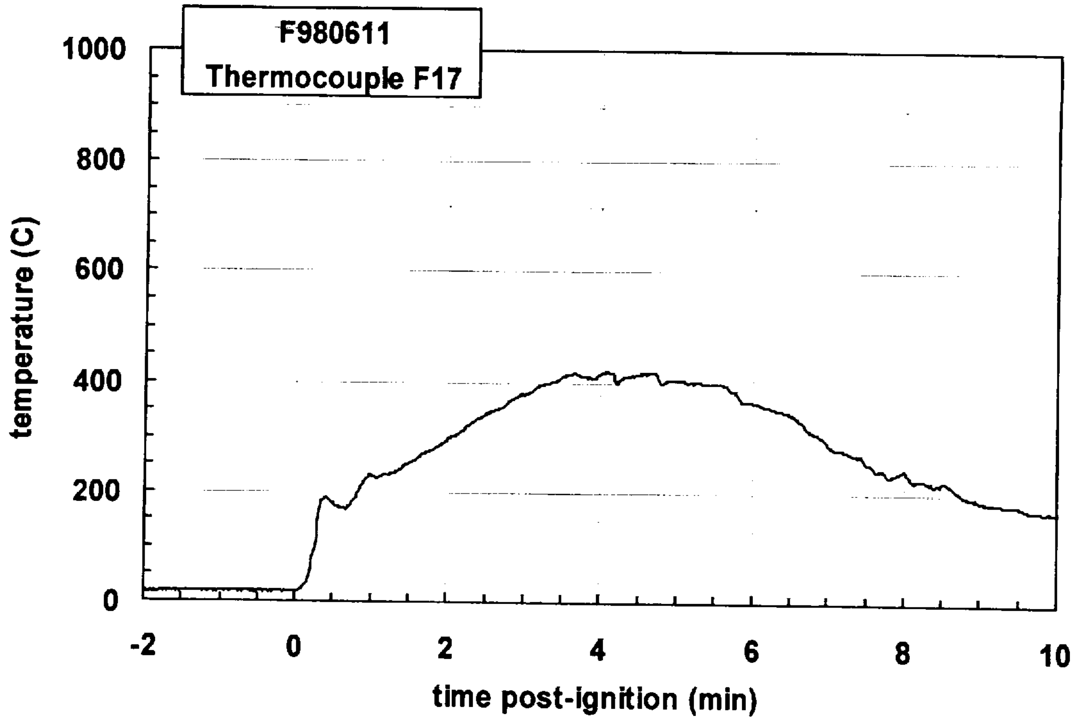

Plot D43. Fire Test F980611. Data plot from thermocouple F17.

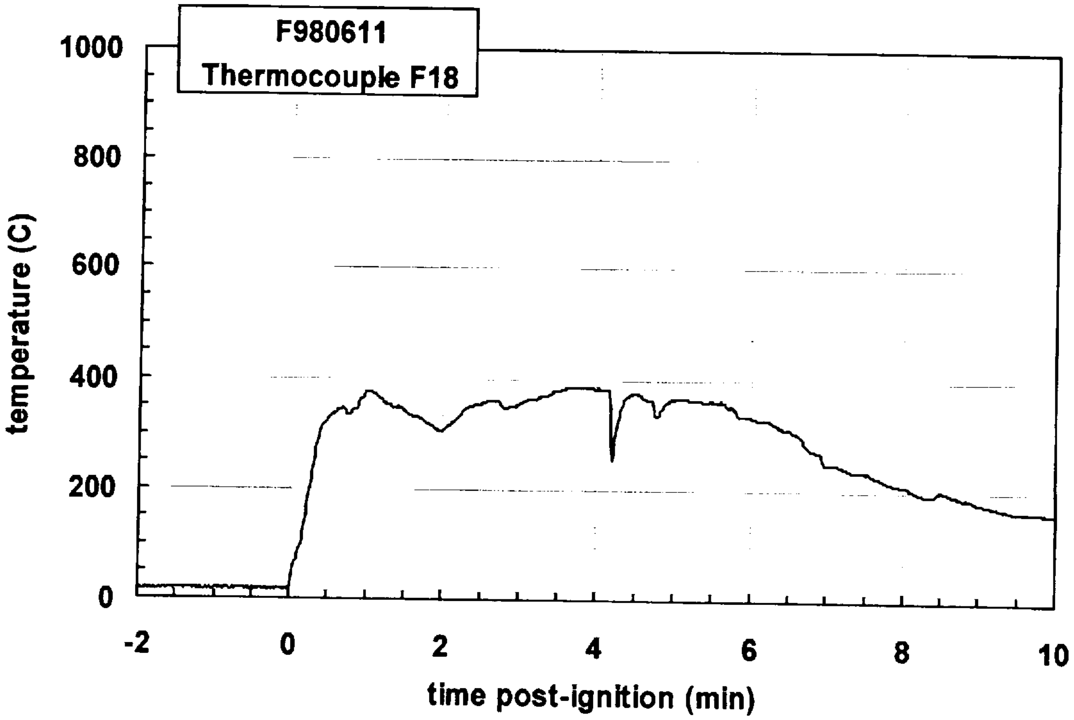

Plot D44. Fire Test F980611. Data plot from thermocouple F18.

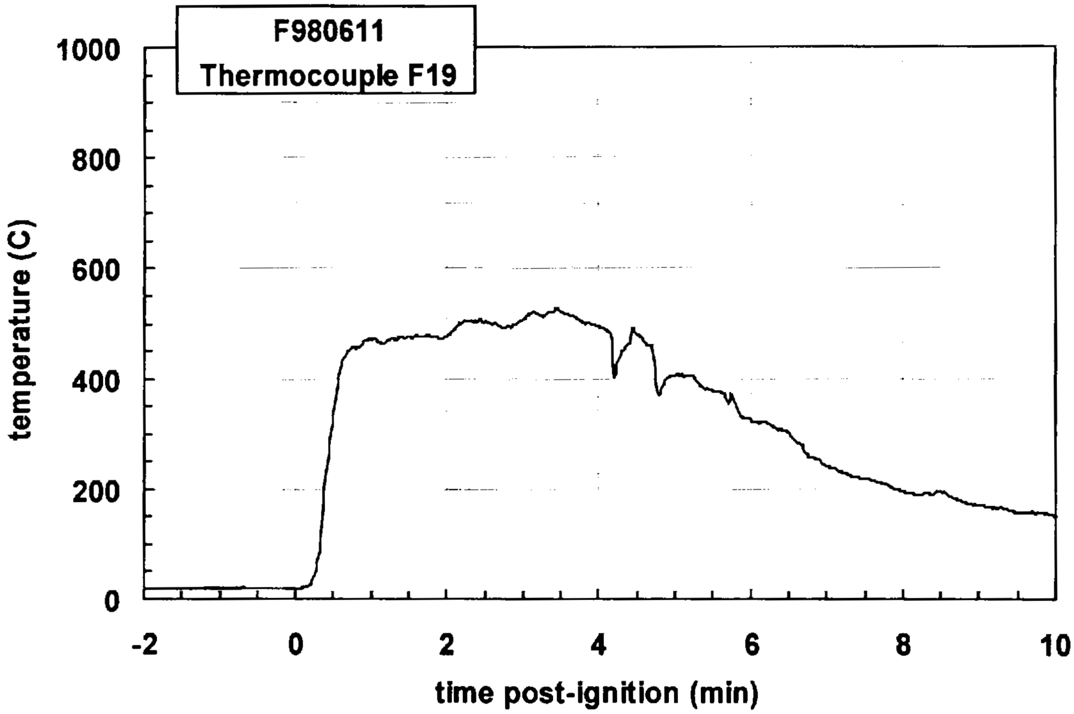

Plot D45. Fire Test F980611. Data plot from thermocouple F19.

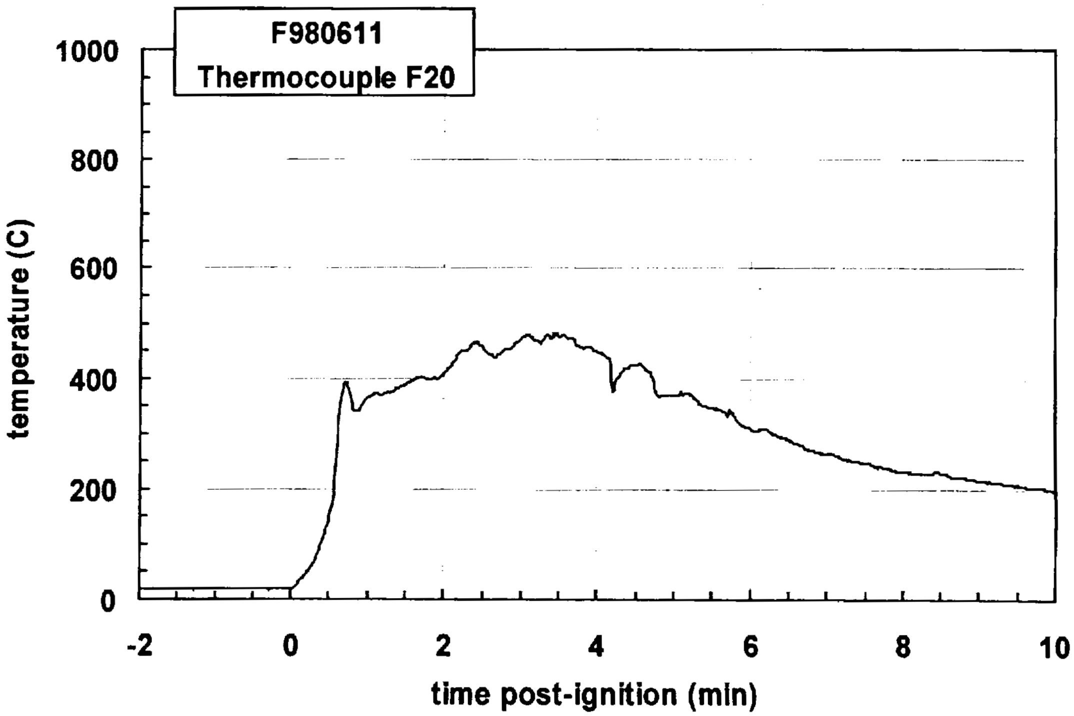

Plot D46. Fire Test F980611. Data plot from thermocouple F20.

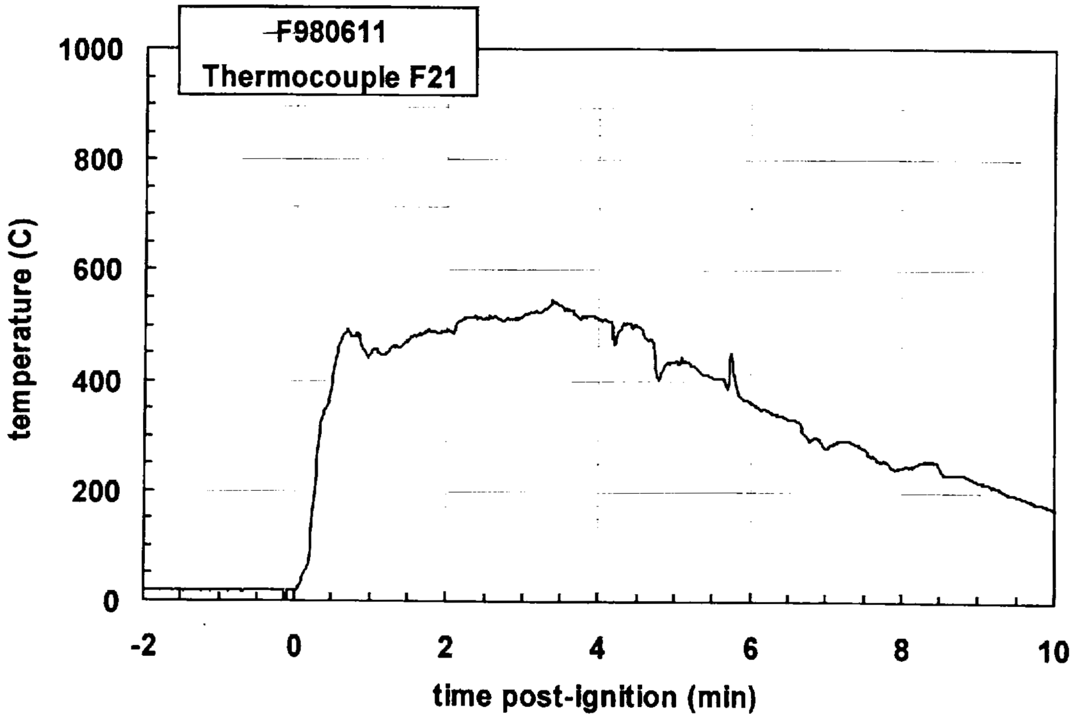

Plot D47. Fire Test F980611. Data plot from thermocouple F21.

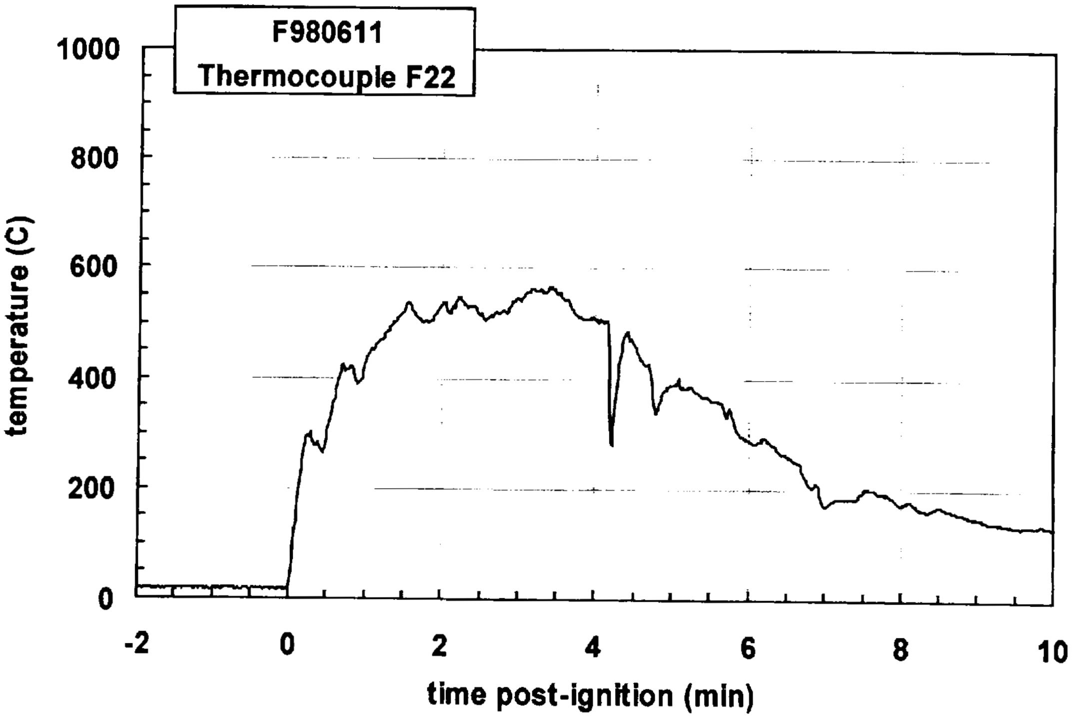

Plot D48. Fire Test F980611. Data plot from thermocouple F22.

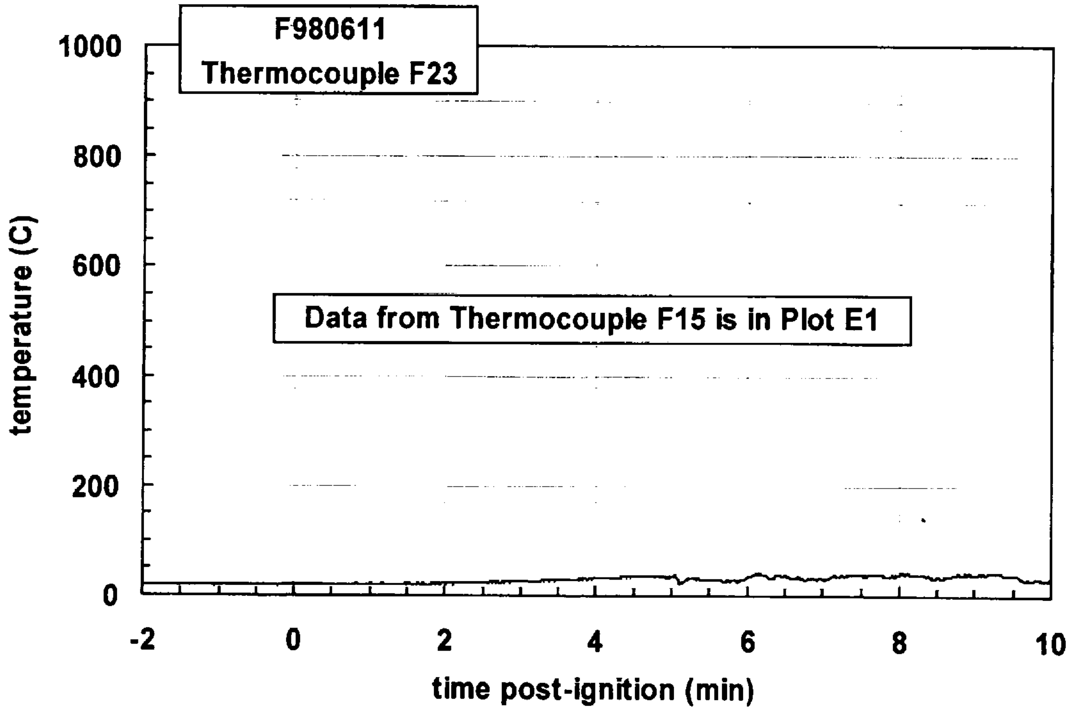

Plot D49. Fire Test F980611. Data plot from thermocouple F23.

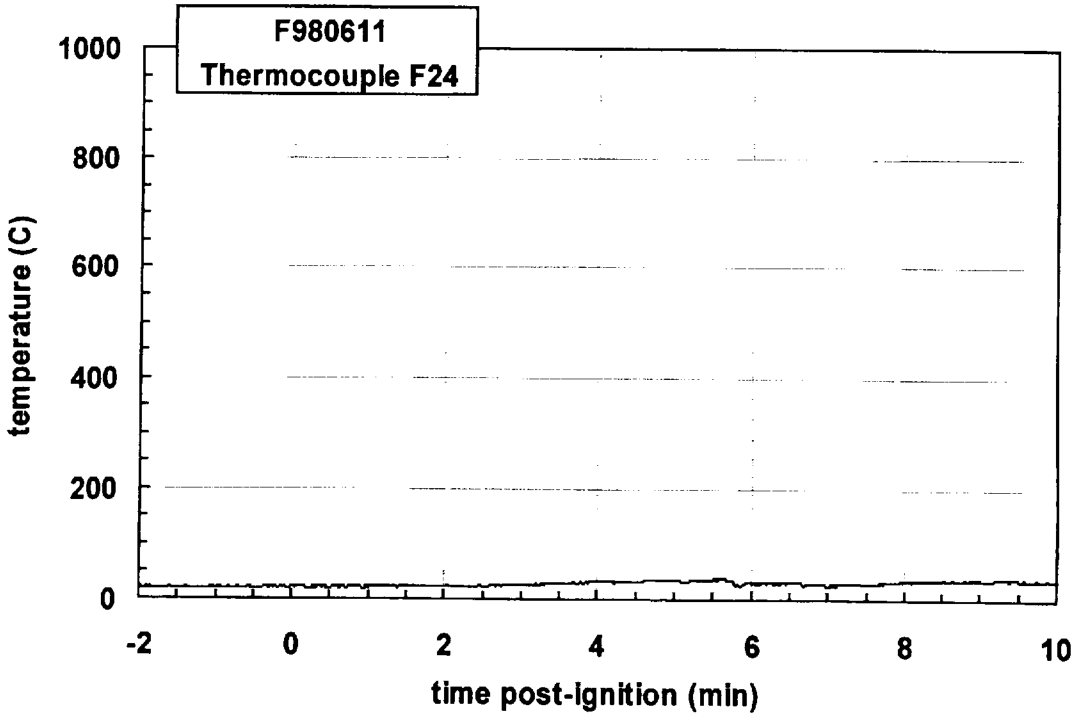

Plot D50. Fire Test F980611. Data plot from thermocouple F24.

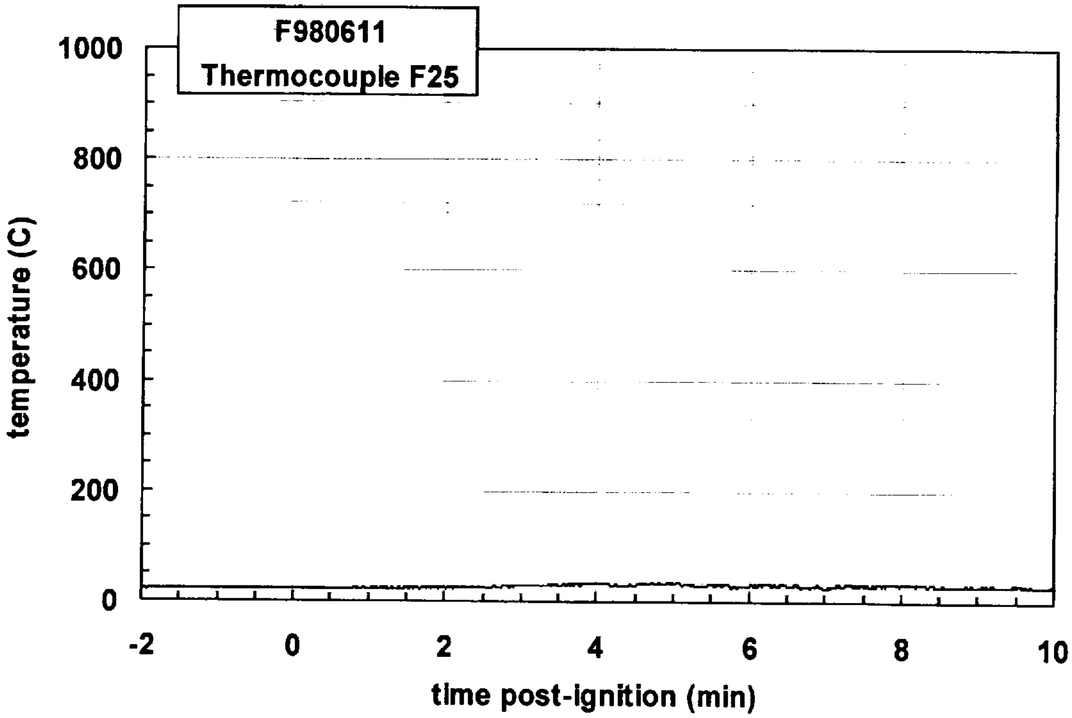

Plot D51. Fire Test F980611. Data plot from thermocouple F25.

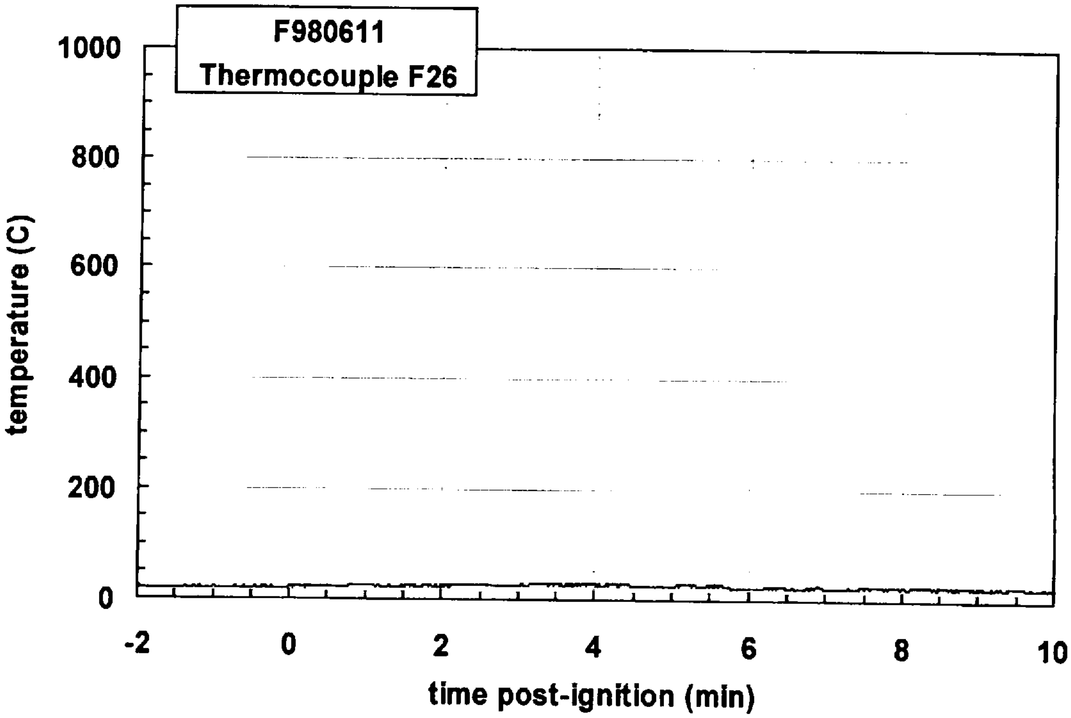

Plot D52. Fire Test F980611. Data plot from thermocouple F26.

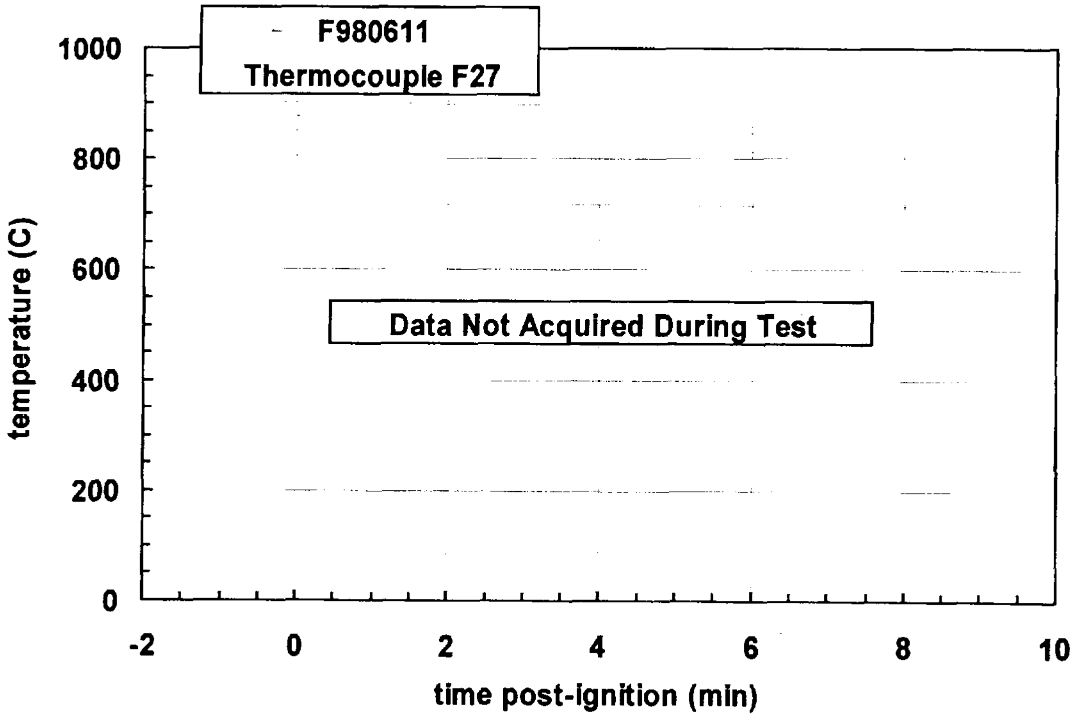

Plot D53. Fire Test F980611. Data plot from thermocouple F27.

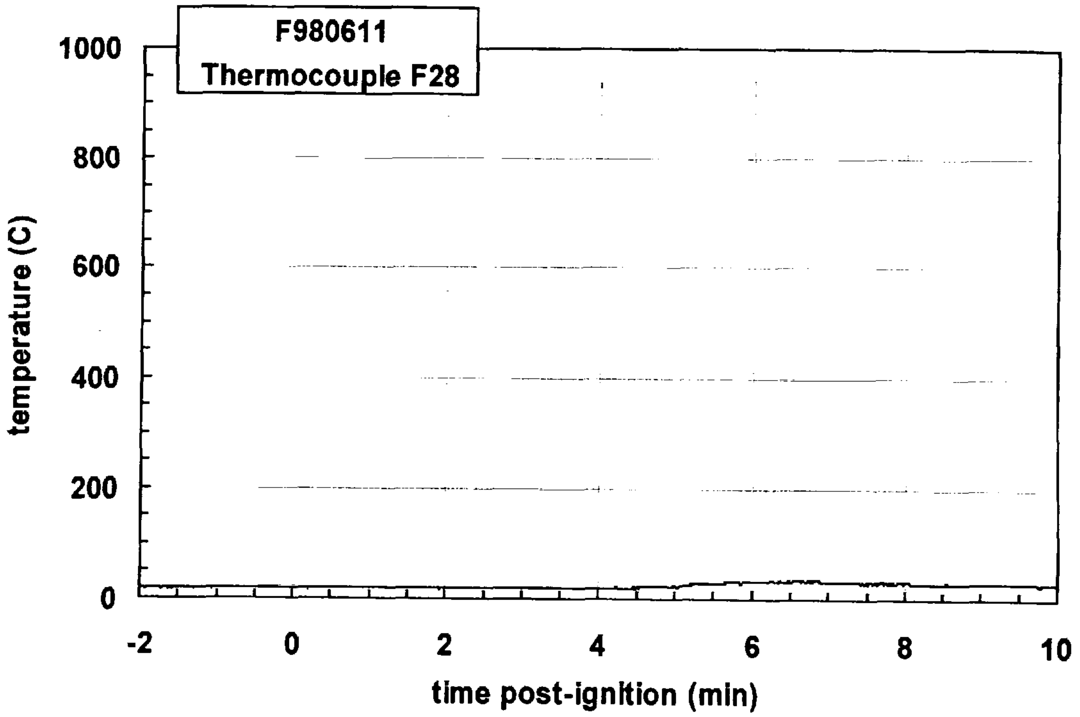

Plot D54. Fire Test F980611. Data plot from thermocouple F28.

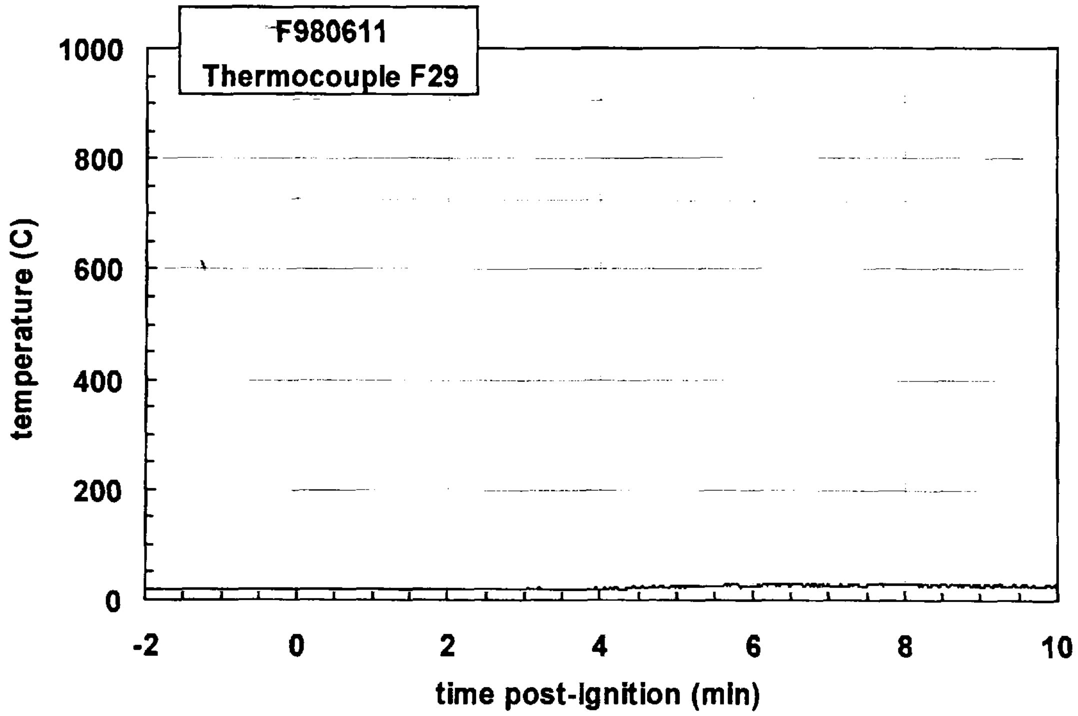

Plot D55. Fire Test F980611. Data plot from thermocouple F29.

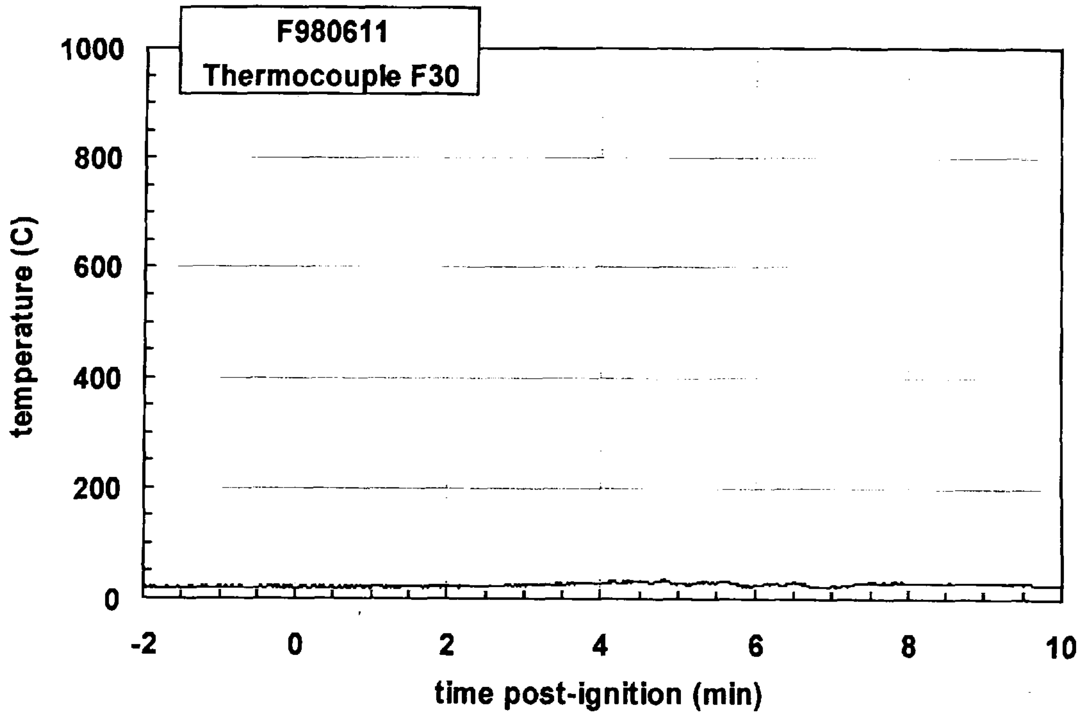

Plot D56. Fire Test F980611. Data plot from thermocouple F30.

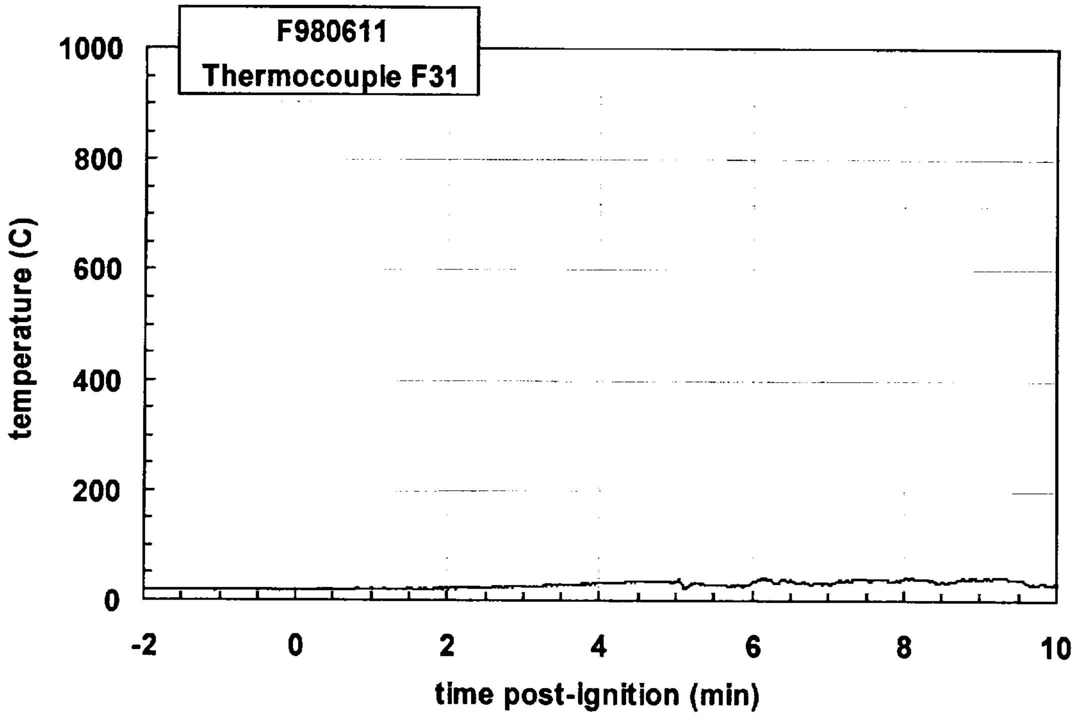

Plot D57. Fire Test F980611. Data plot from thermocouple F31.

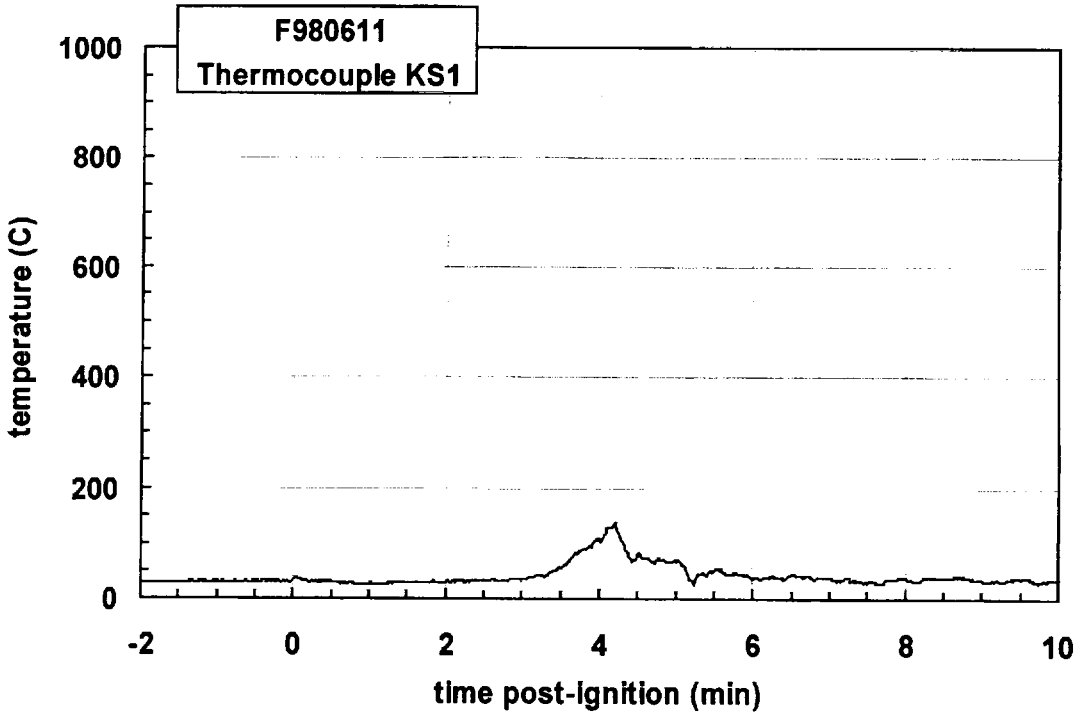

Plot D58. Fire Test F980611. Data plot from thermocouple KS1.

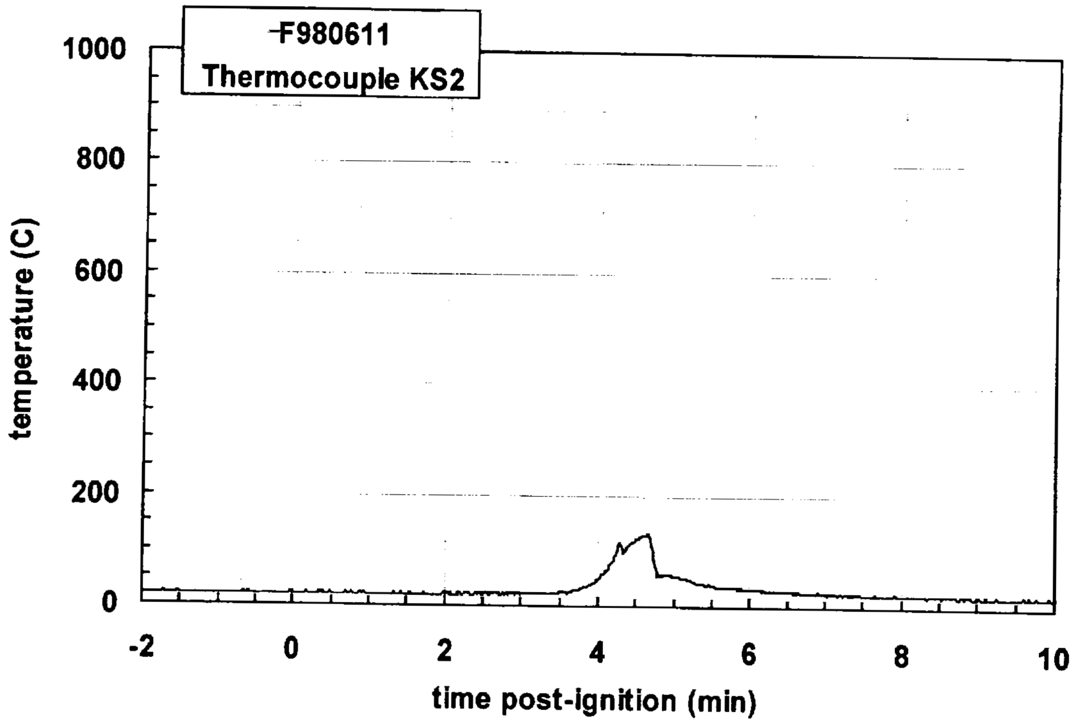

Plot D59. Fire Test F980611. Data plot from thermocouple KS2.

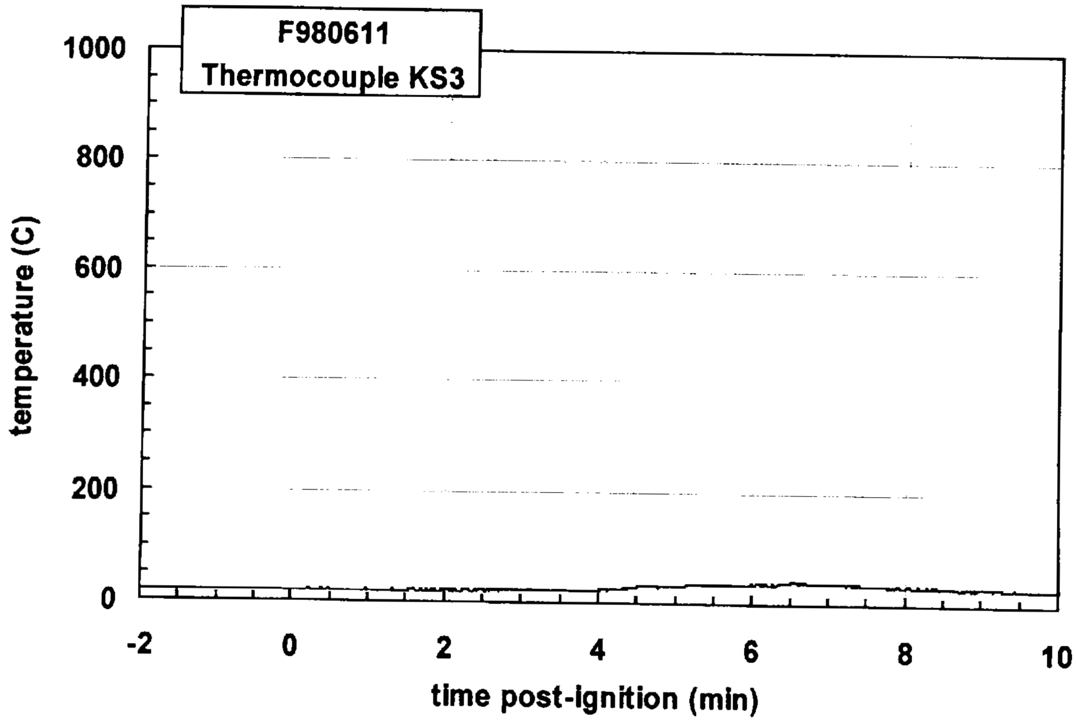

Plot D60. Fire Test F980611. Data plot from thermocouple KS3.

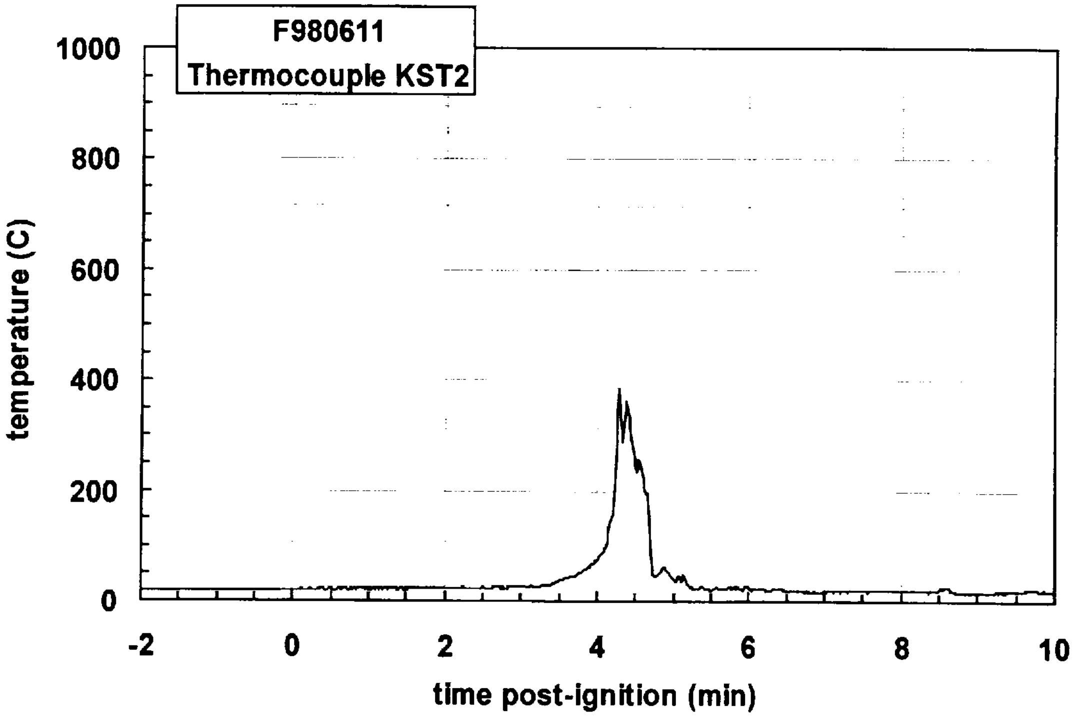

Plot D61. Fire Test F980611. Data plot from thermocouple KST2.

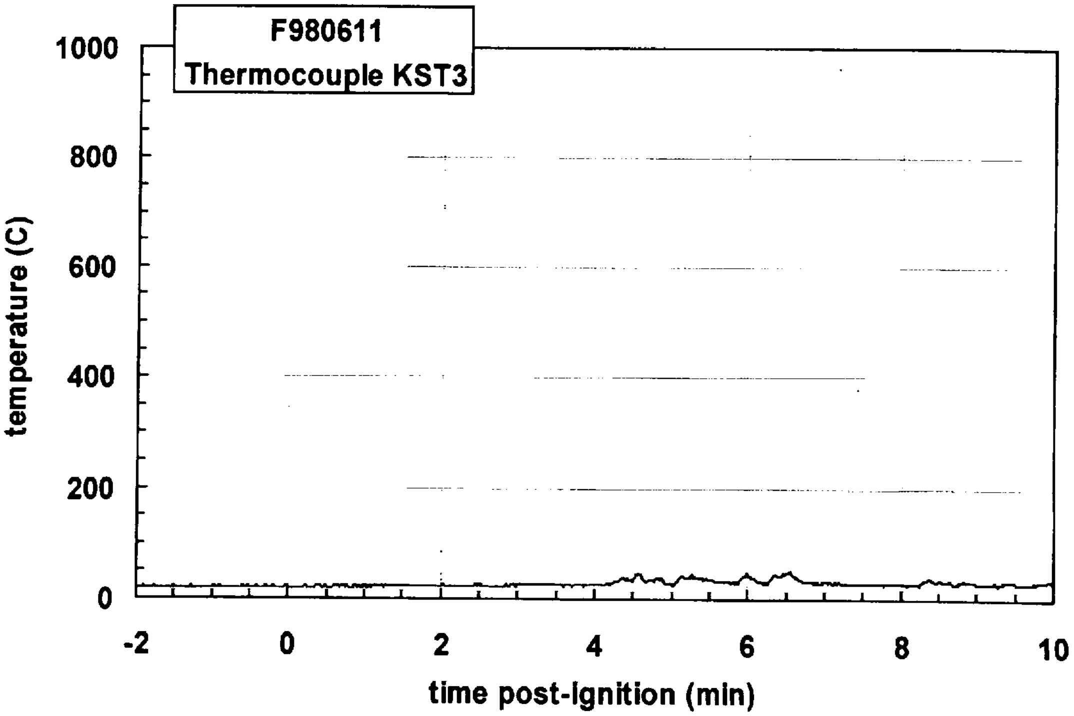

Plot D62. Fire Test F980611. Data plot from thermocouple KST3.

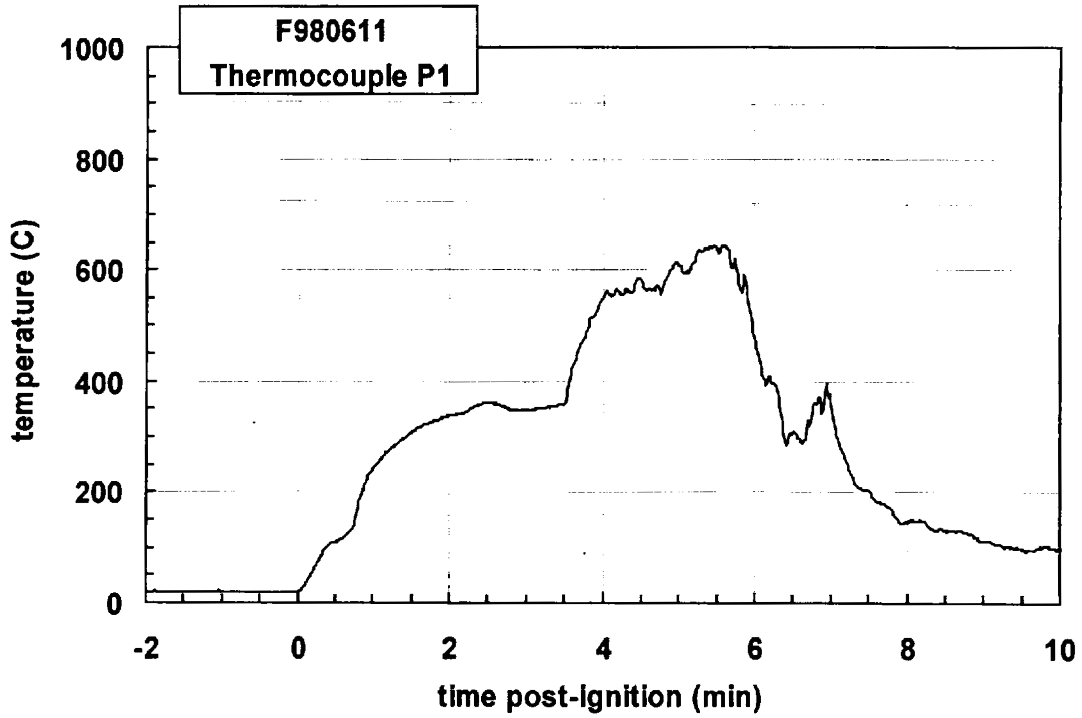

Plot D63. Fire Test F980611. Data plot from thermocouple P1.

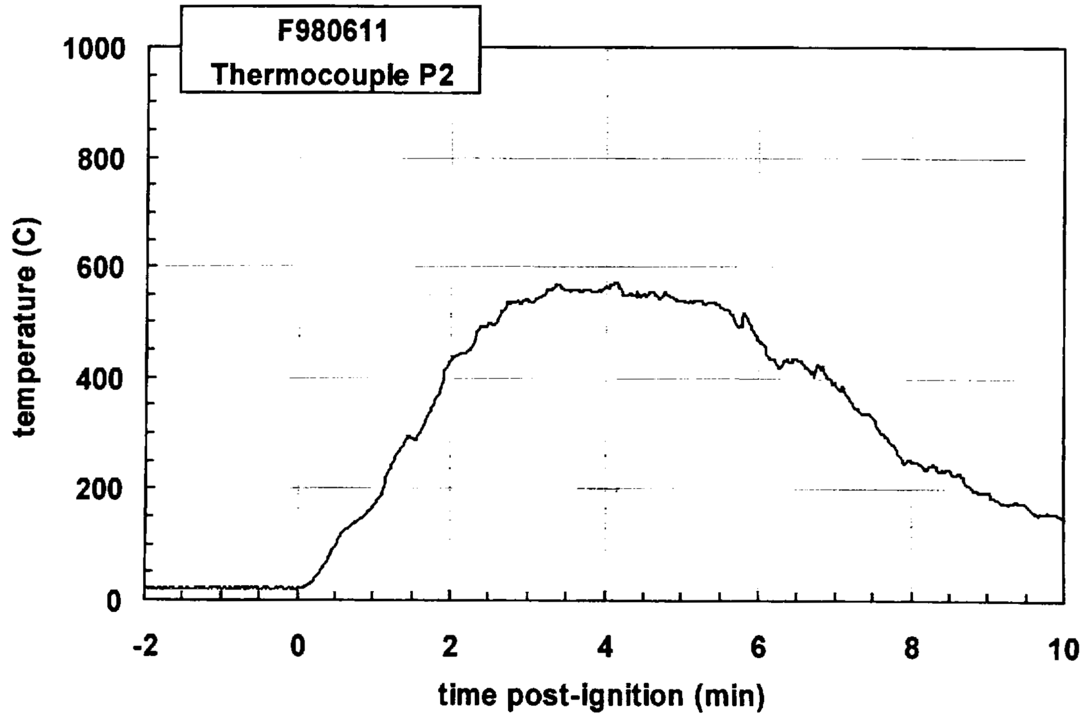

Plot D64. Fire Test F980611. Data plot from thermocouple P2.

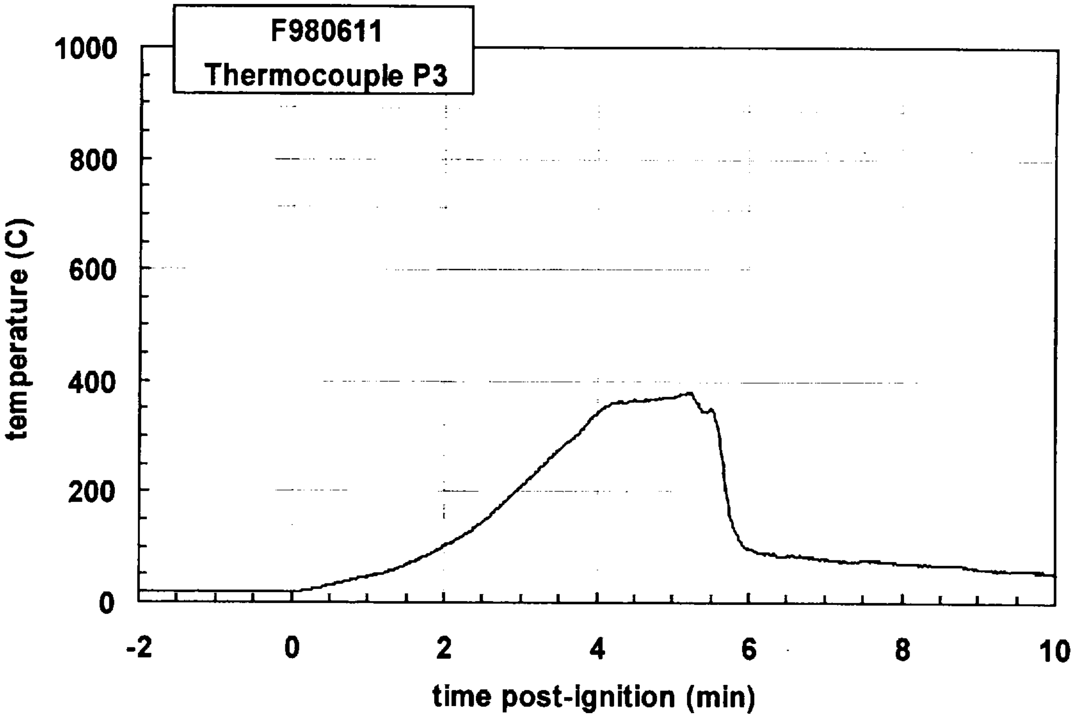

Plot D65. Fire Test F980611. Data plot from thermocouple P3.

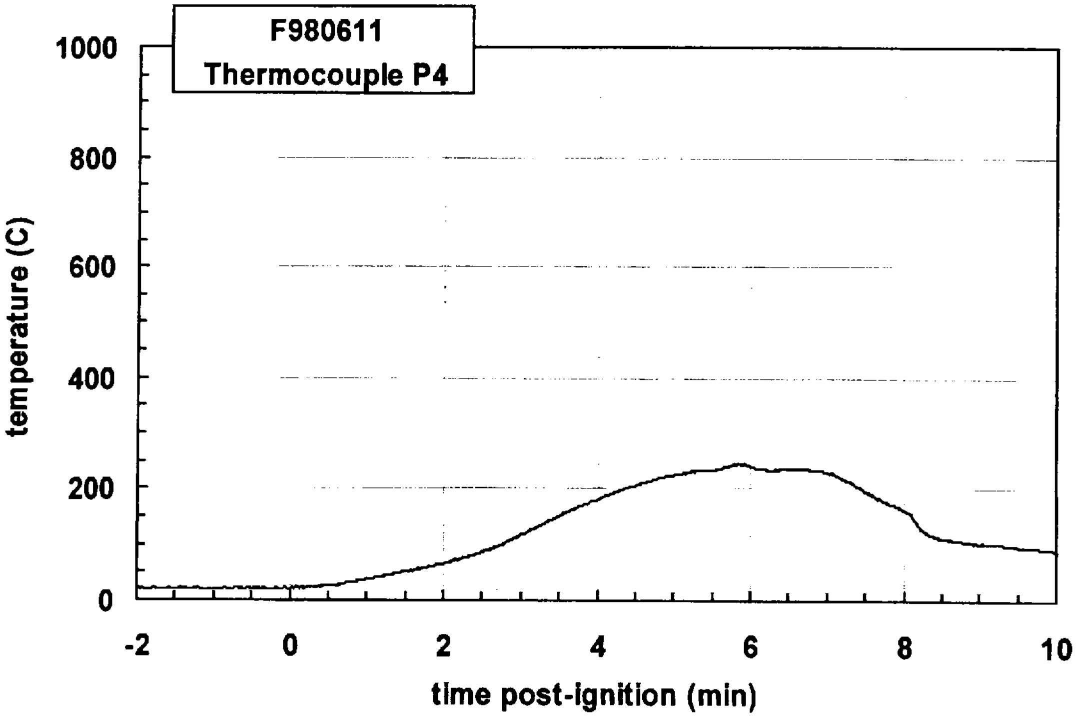

Plot D66. Fire Test F980611. Data plot from thermocouple P4.

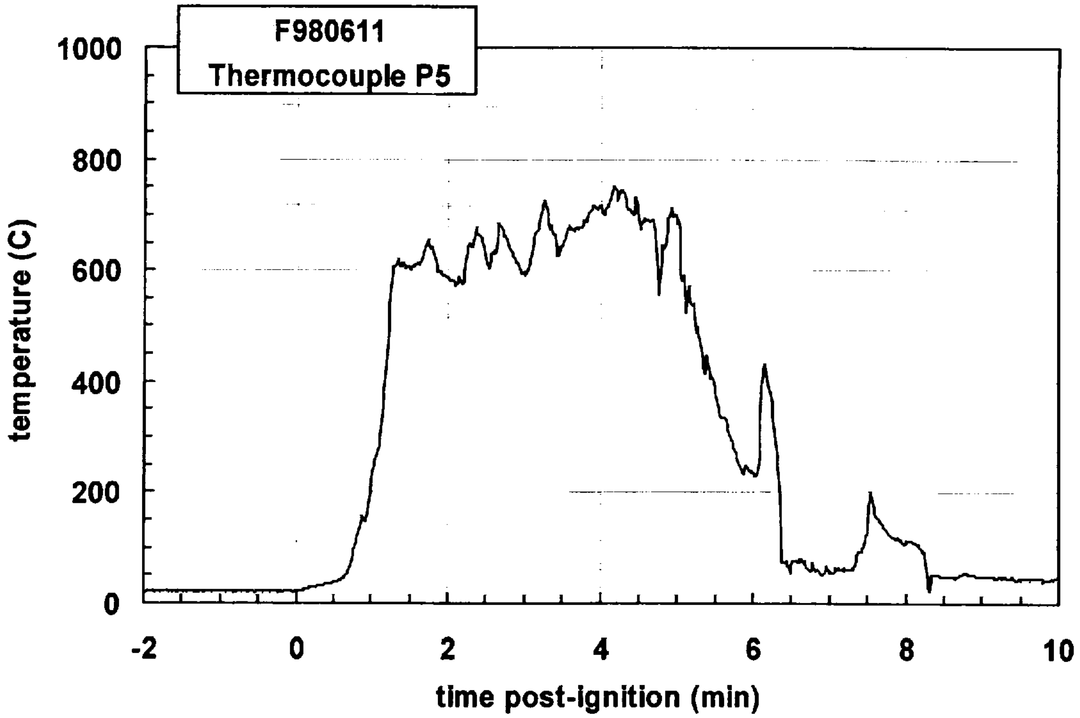

Plot D67. Fire Test F980611. Data plot from thermocouple P5.

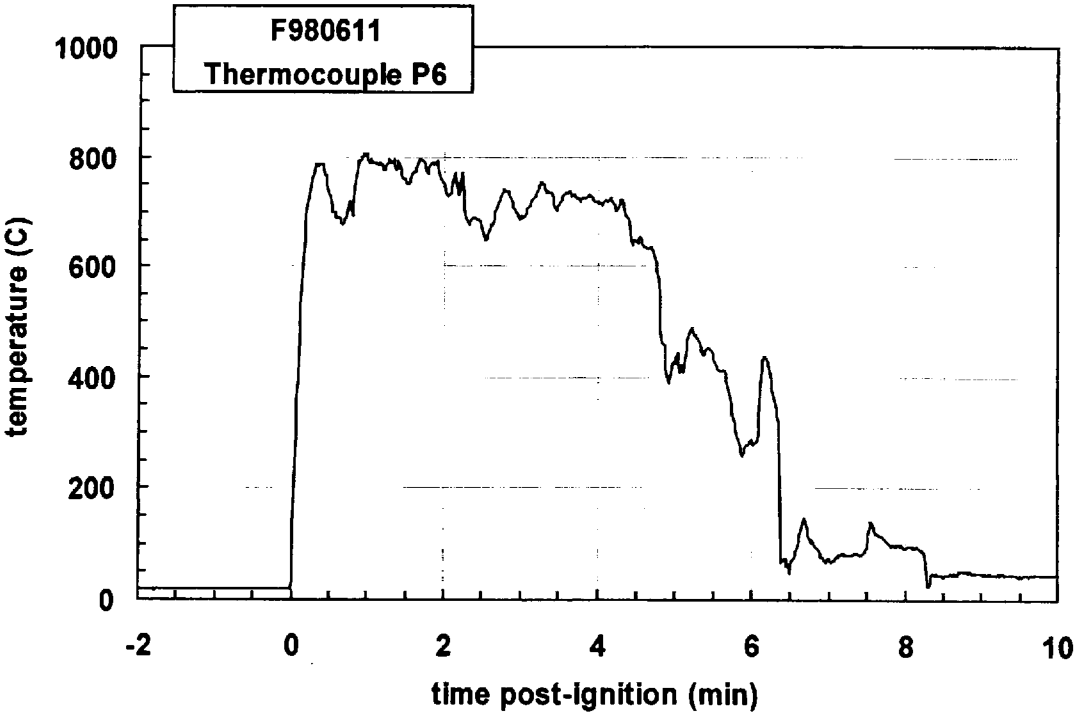

Plot D68. Fire Test F980611. Data plot from thermocouple P6.

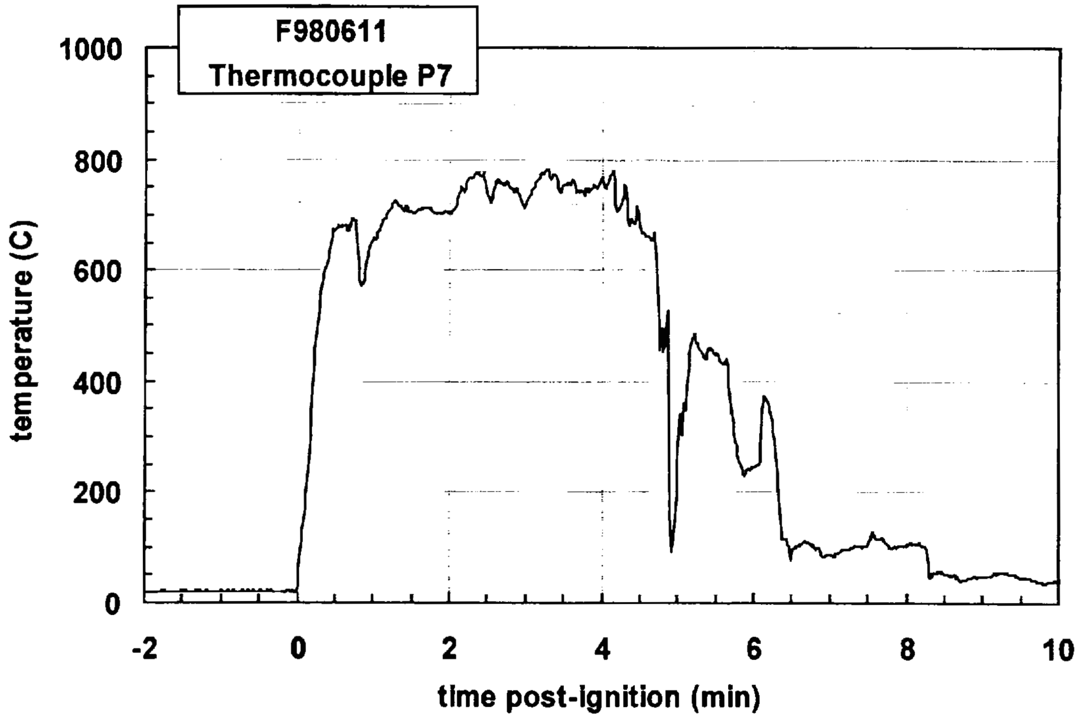

Plot D69. Fire Test F980611. Data plot from thermocouple P7.

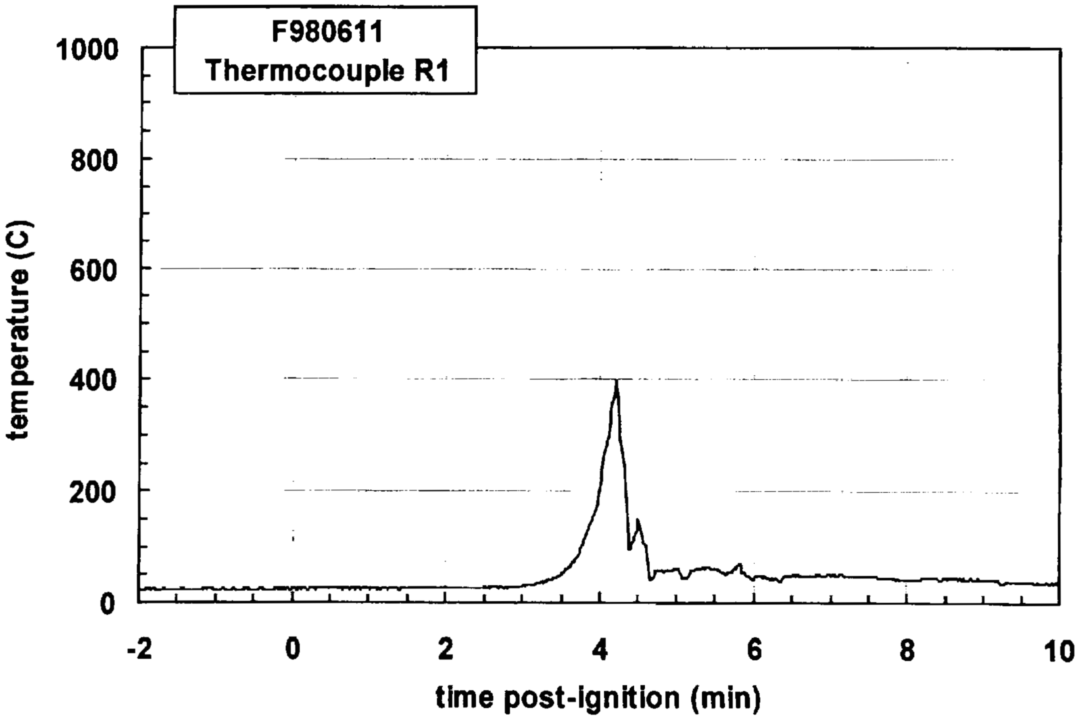

Plot D70. Fire Test F980611. Data plot from thermocouple R1.

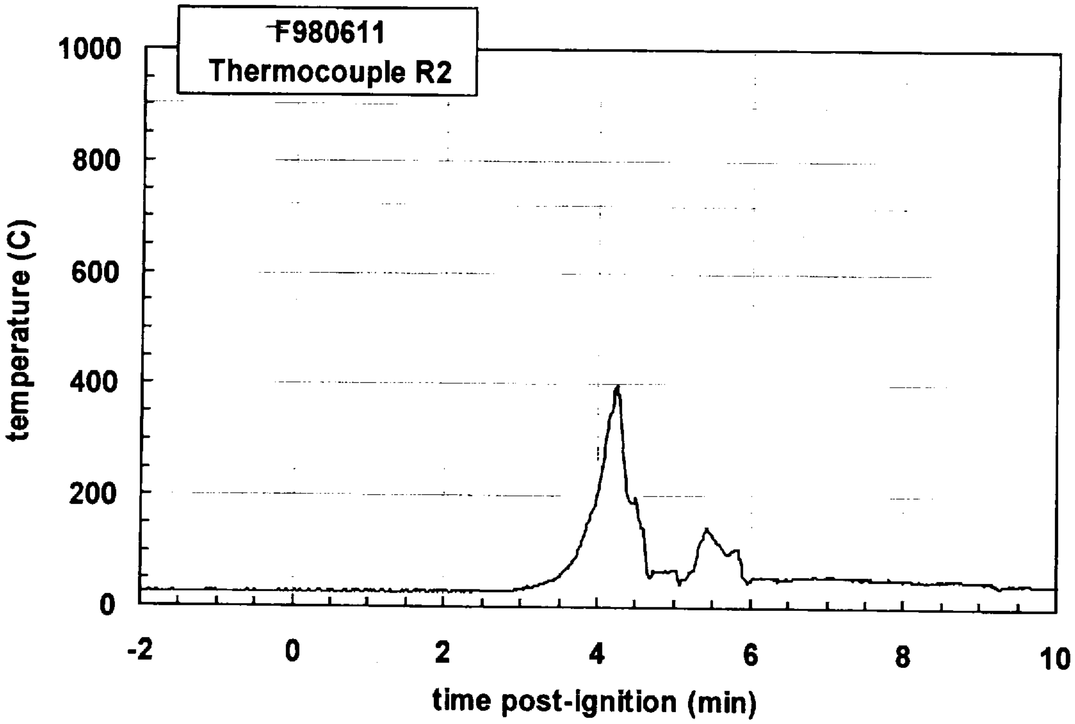

Plot D71. Fire Test F980611. Data plot from thermocouple R2.

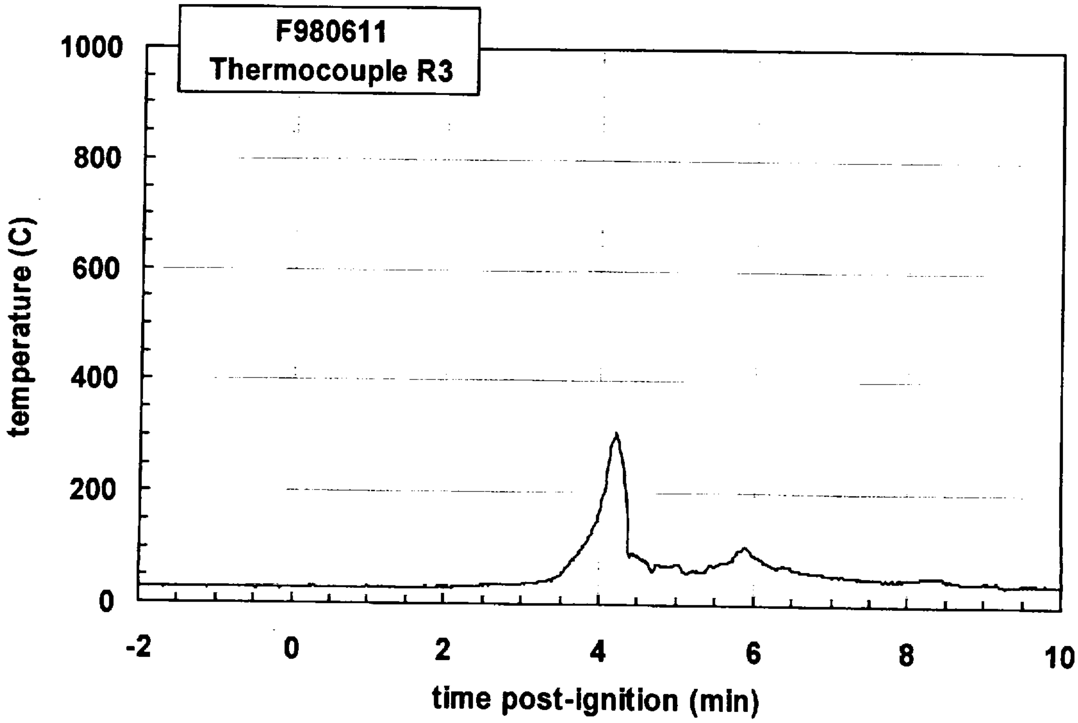

Plot D72. Fire Test F980611. Data plot from thermocouple R3.

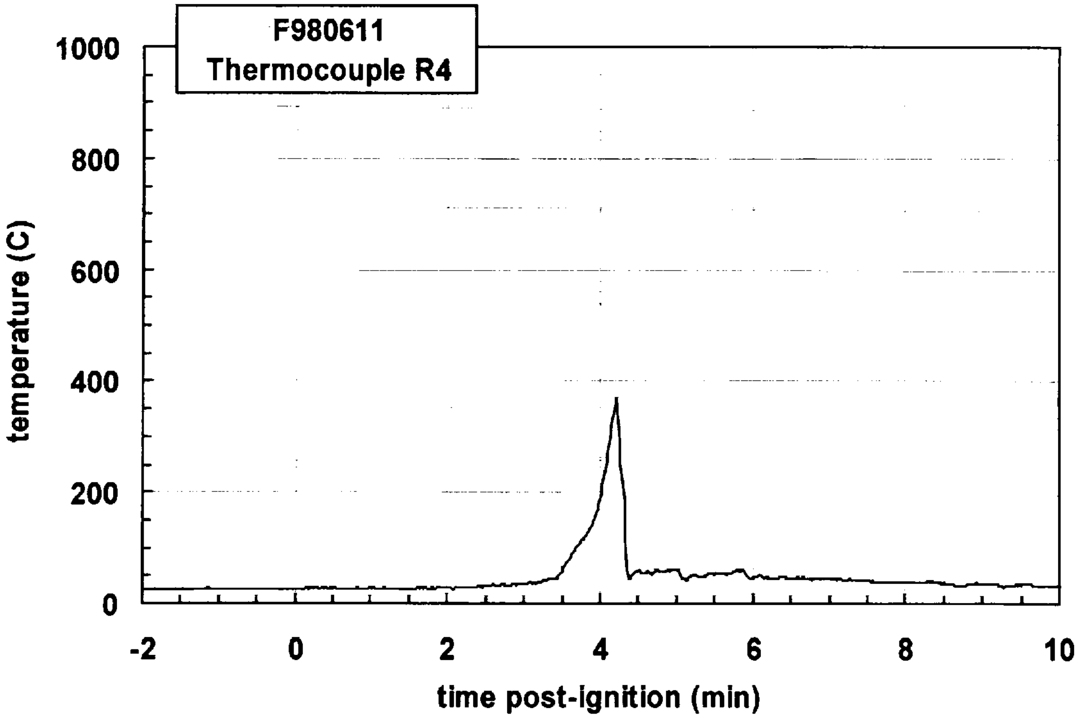

Plot D73. Fire Test F980611. Data plot from thermocouple R4.

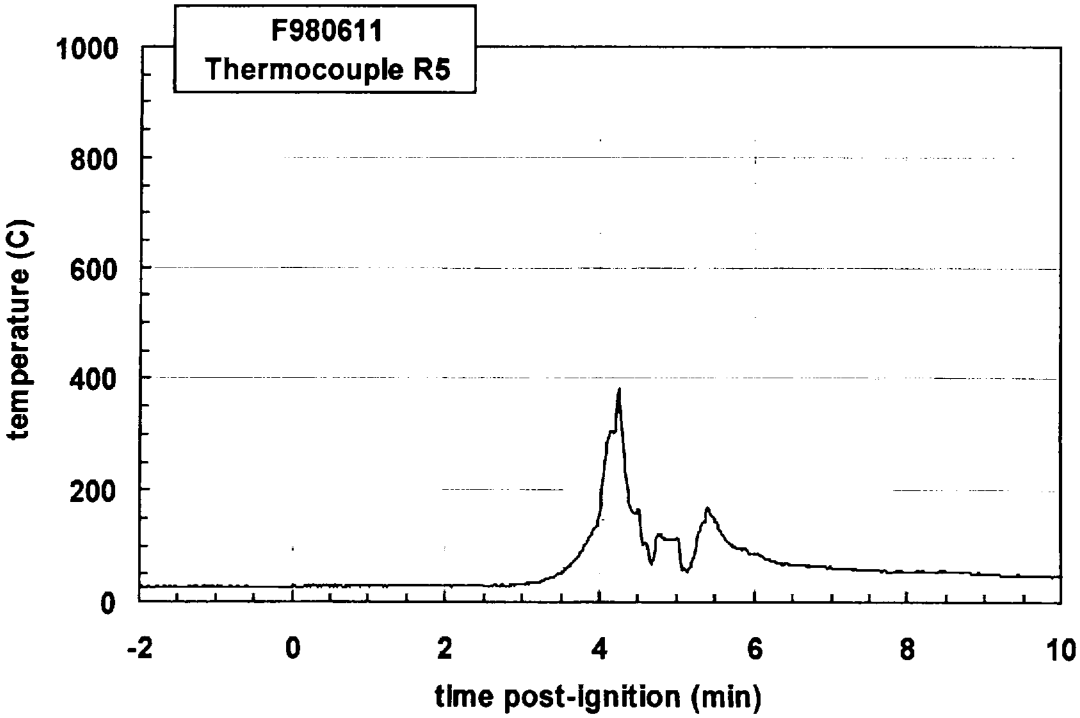

Plot D74. Fire Test F980611. Data plot from thermocouple R5.

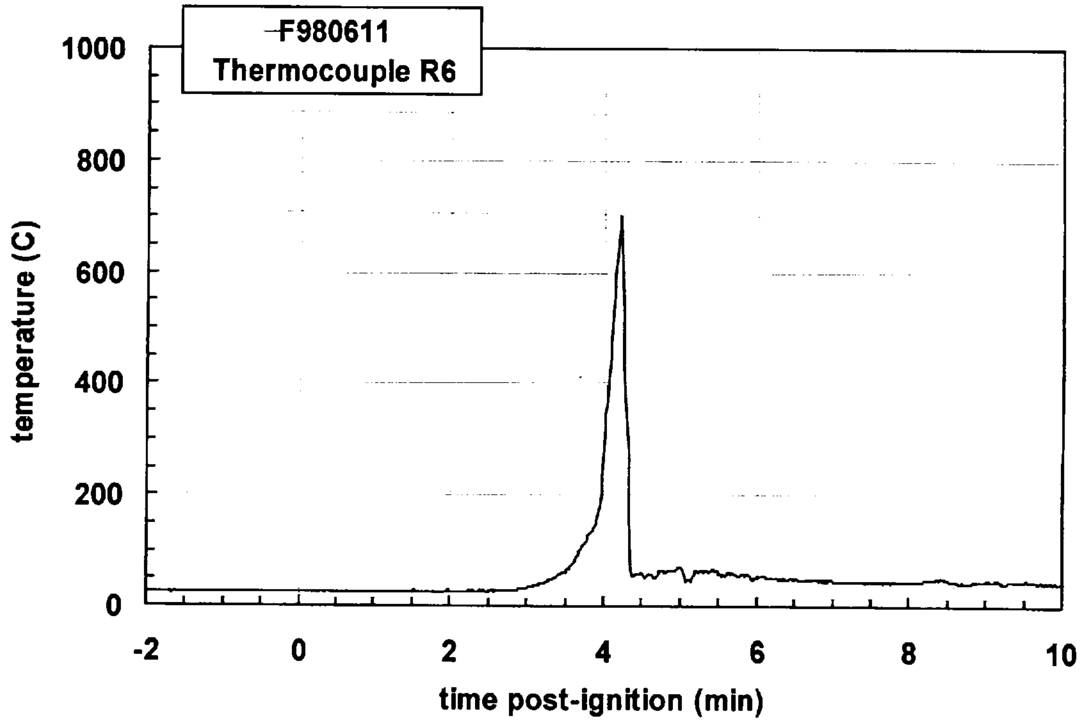

Plot D75. Fire Test F980611. Data plot from thermocouple R6.

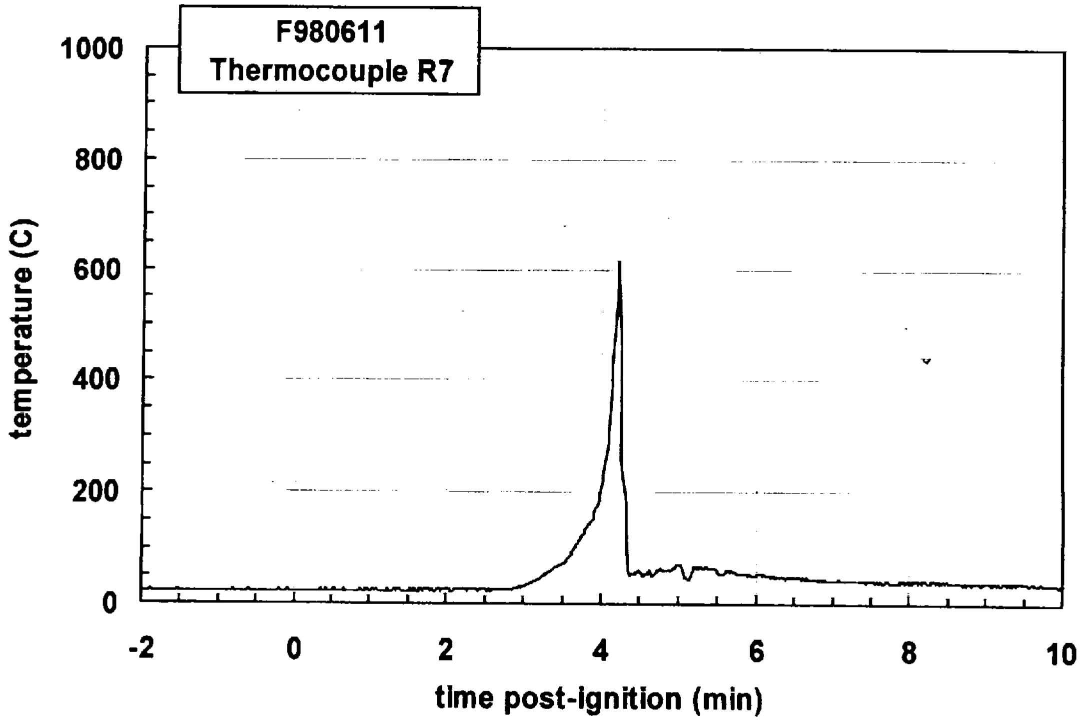

Plot D76. Fire Test F980611. Data plot from thermocouple R7.

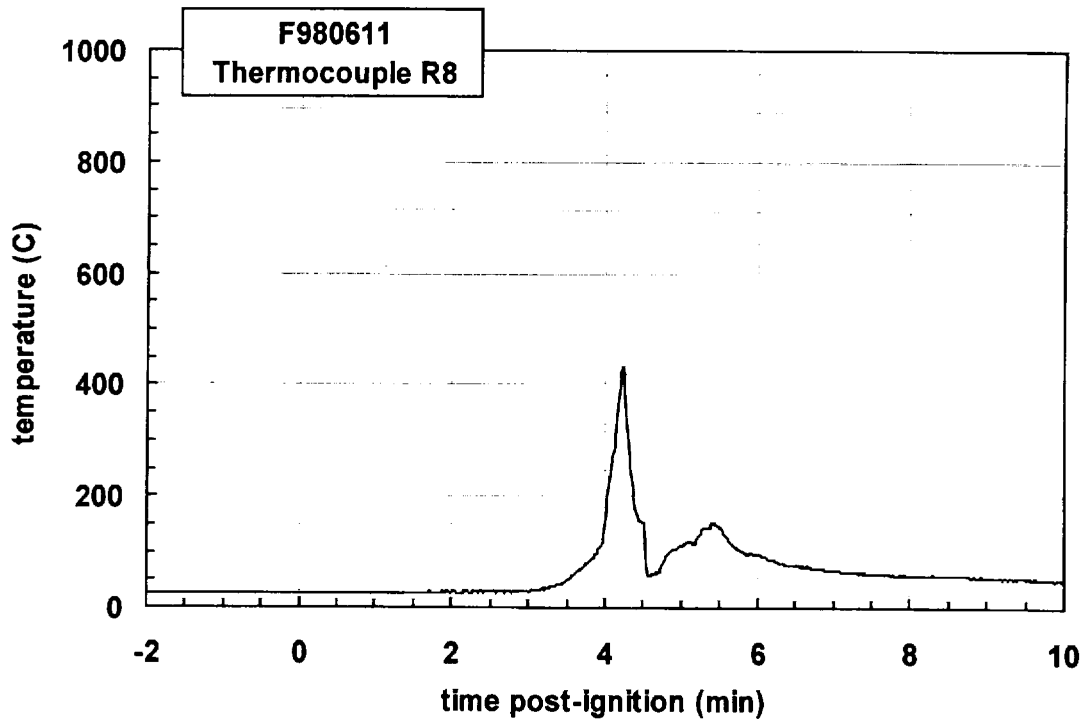

Plot D77. Fire Test F980611. Data plot from thermocouple R8.

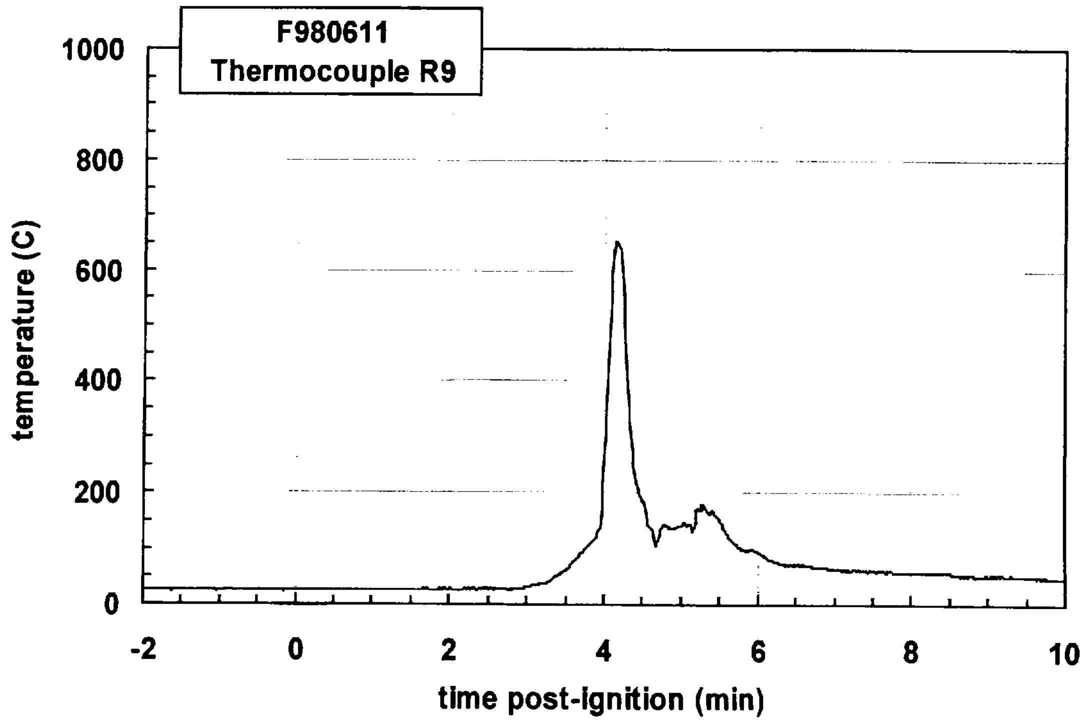

Plot D78. Fire Test F980611. Data plot from thermocouple R9.

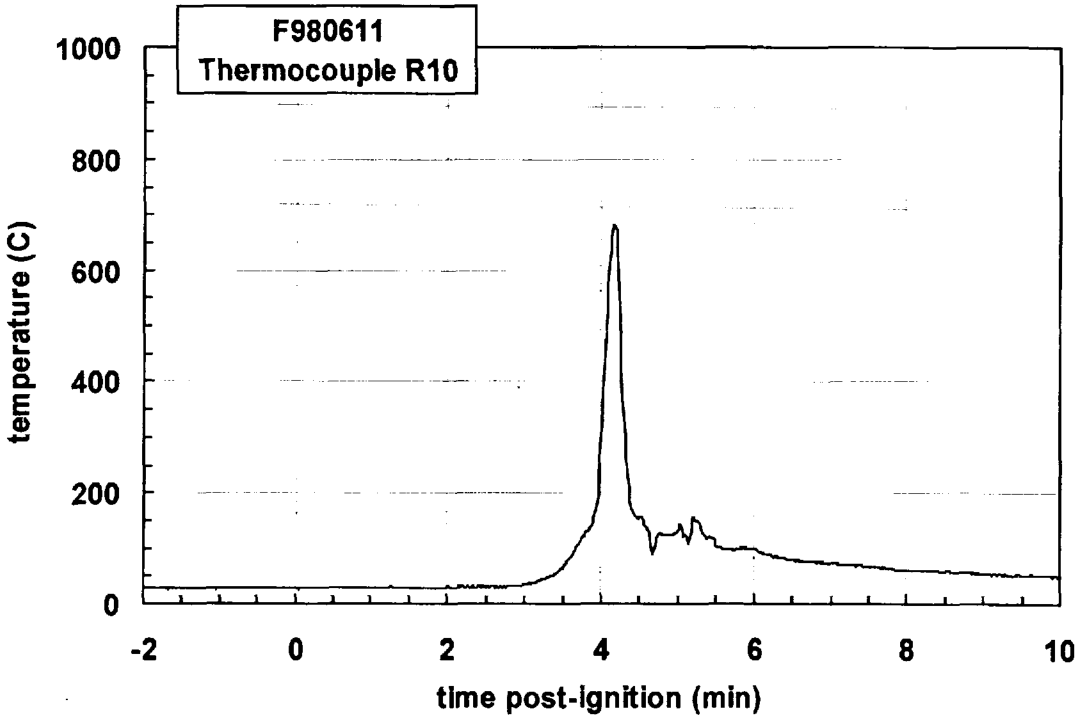

Plot D79. Fire Test F980611. Data plot from thermocouple R10.

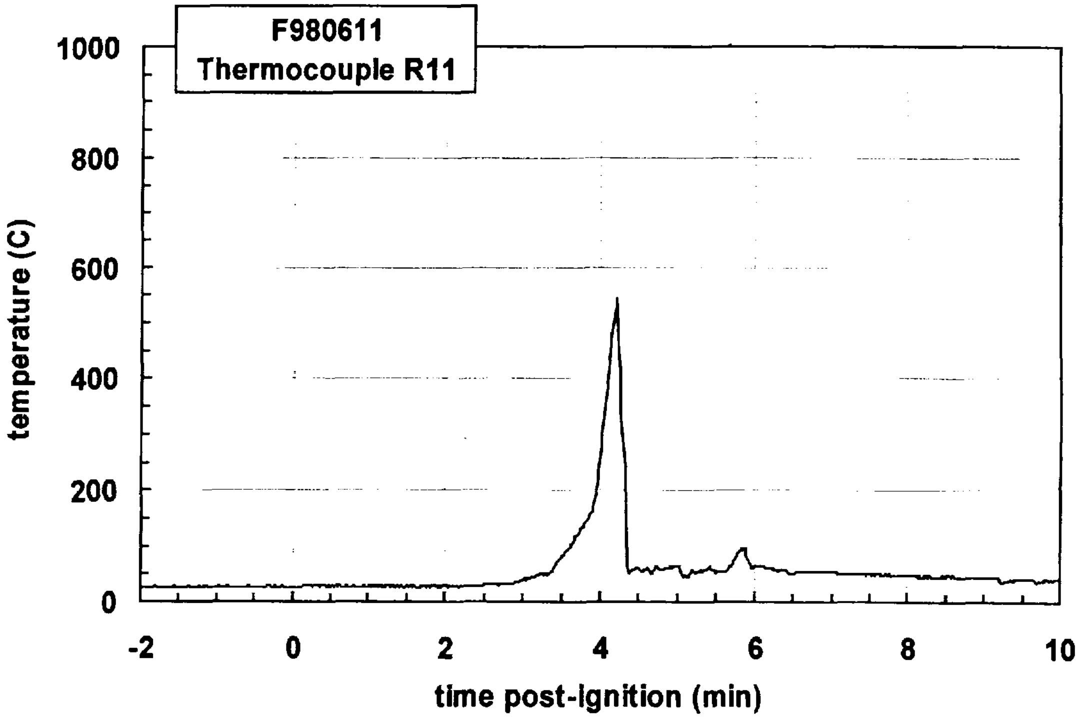

Plot D80. Fire Test F980611. Data plot from thermocouple R11.

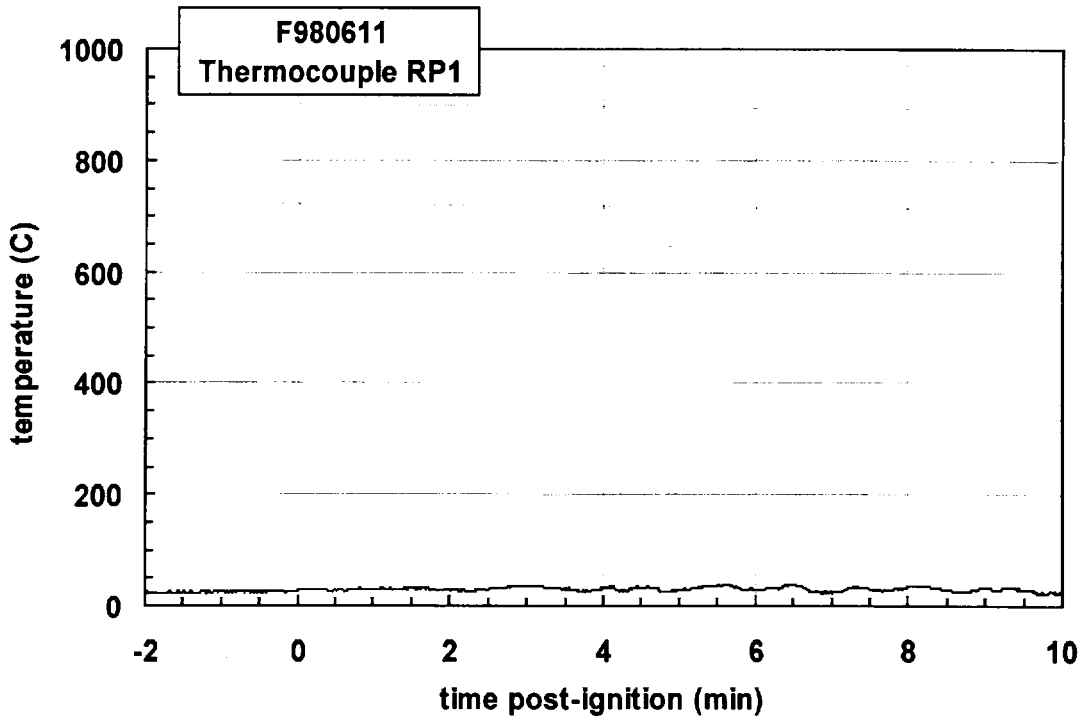

Plot D81. Fire Test F980611. Data plot from thermocouple RP1.

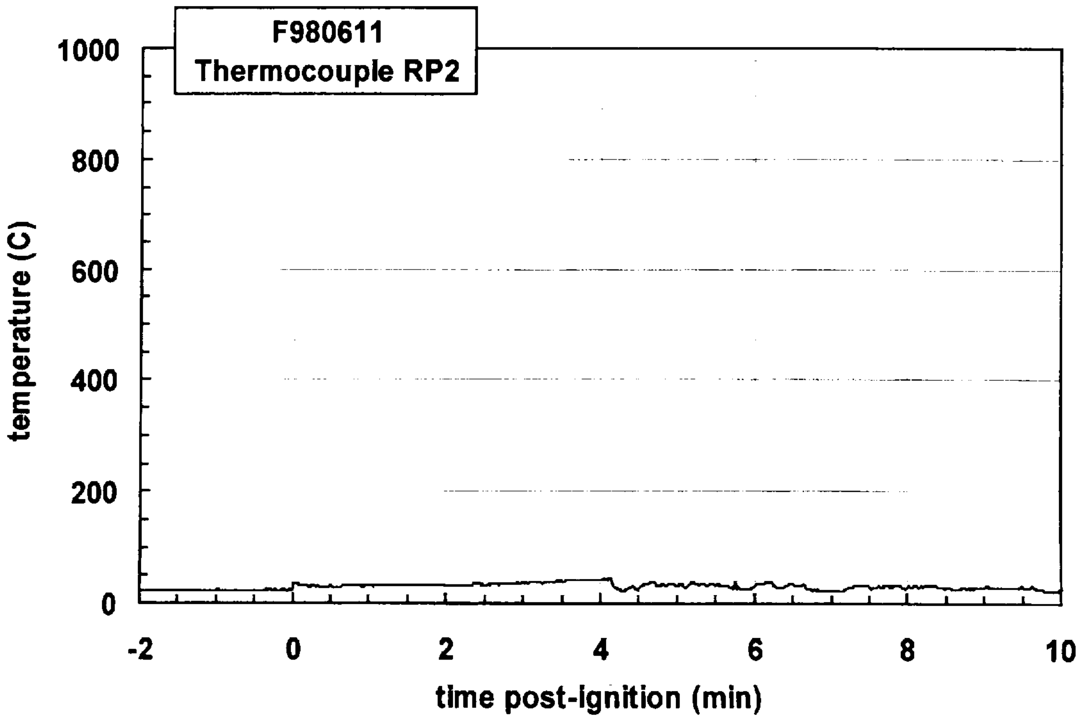

Plot D82. Fire Test F9806011. Data plot from thermocouple RP2.

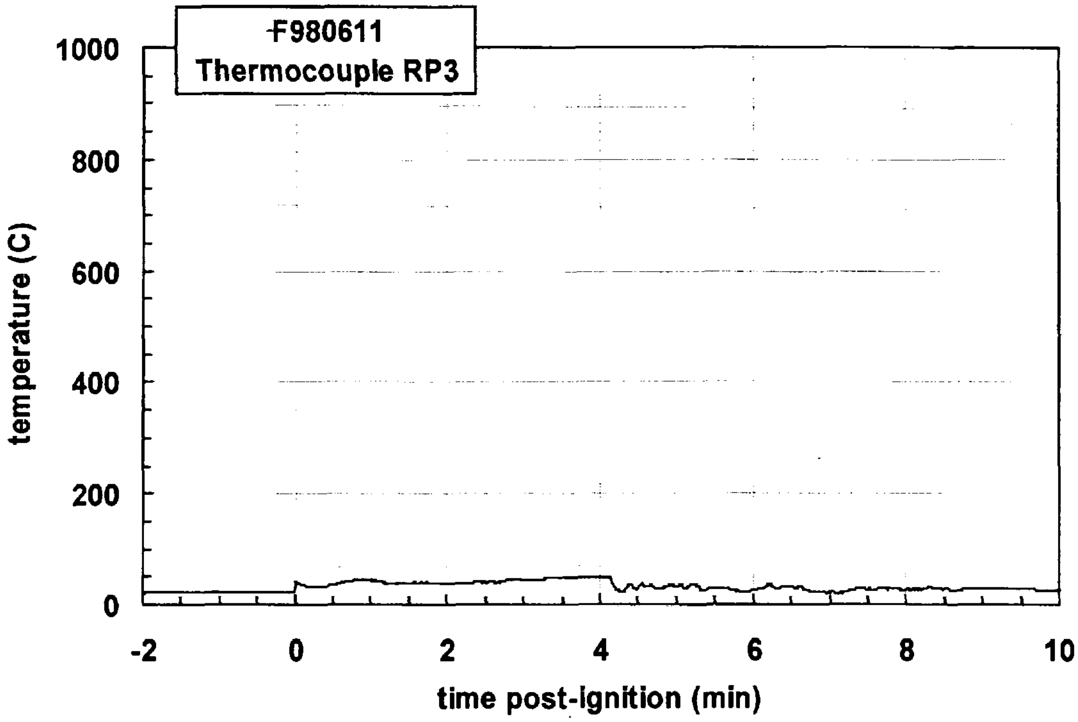

Plot D83. Fire Test F980611. Data plot from thermocouple RP3.

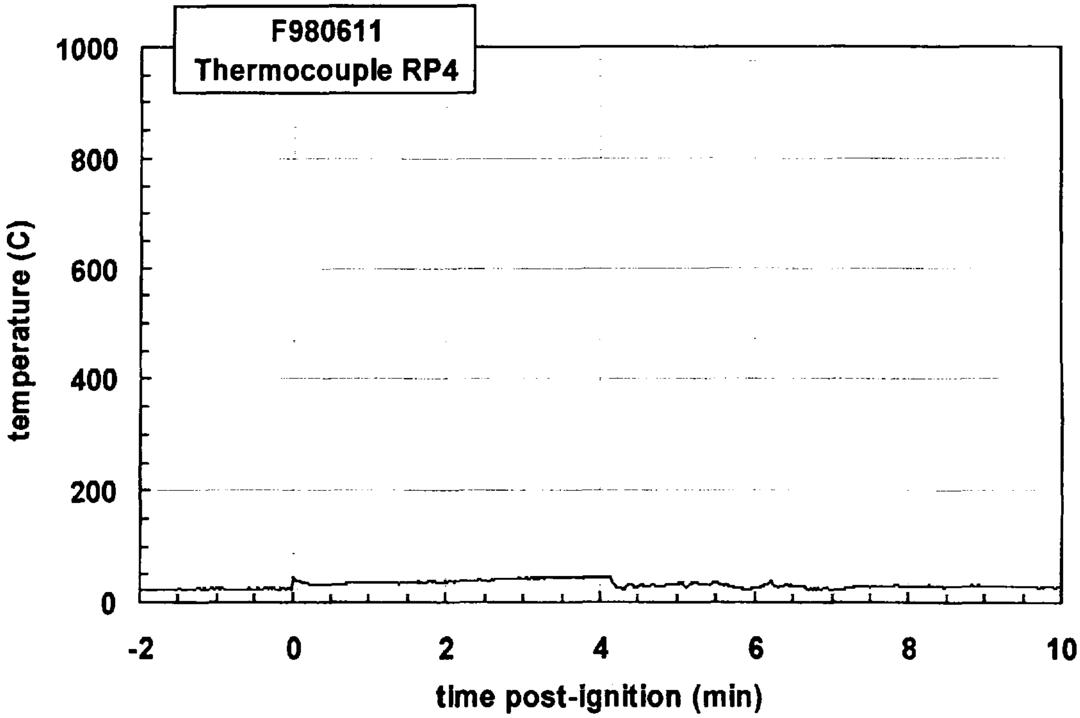

Plot D84. Fire Test F980611. Data plot from thermocouple RP4.

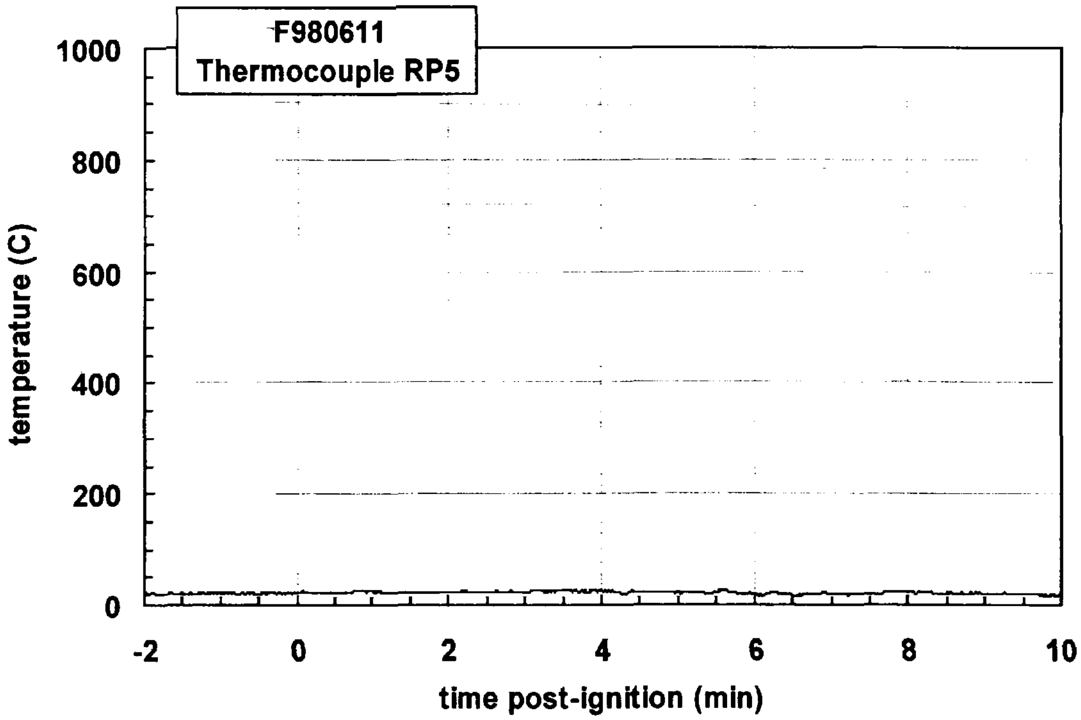

Plot D85. Fire Test F980611. Data plot from thermocouple RP5.

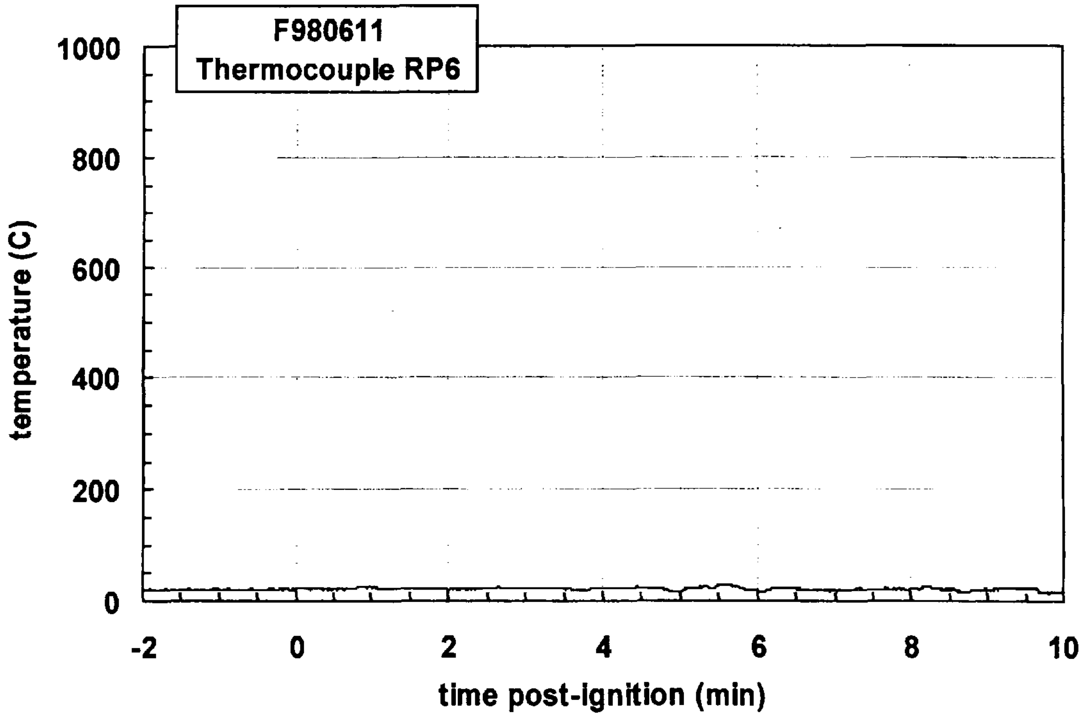

Plot D86. Fire Test F980611. Data plot from thermocouple RP6.

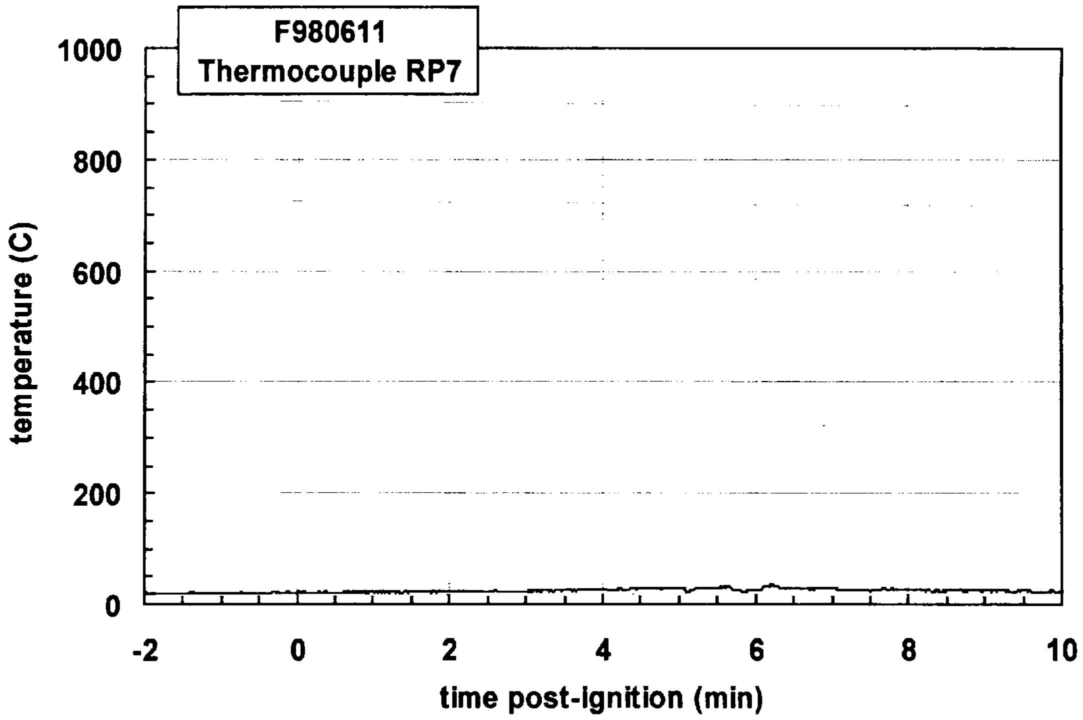

Plot D87. Fire Test F980611. Data plot from thermocouple RP7.

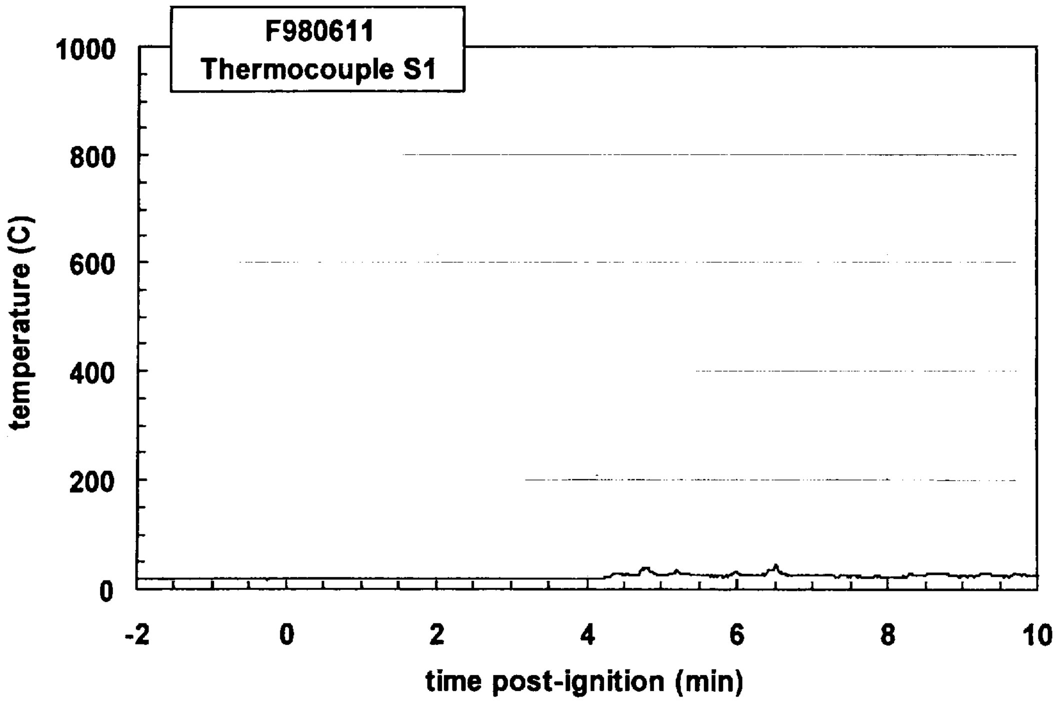

Plot D88. Fire Test F980611. Data plot from thermocouple S1.

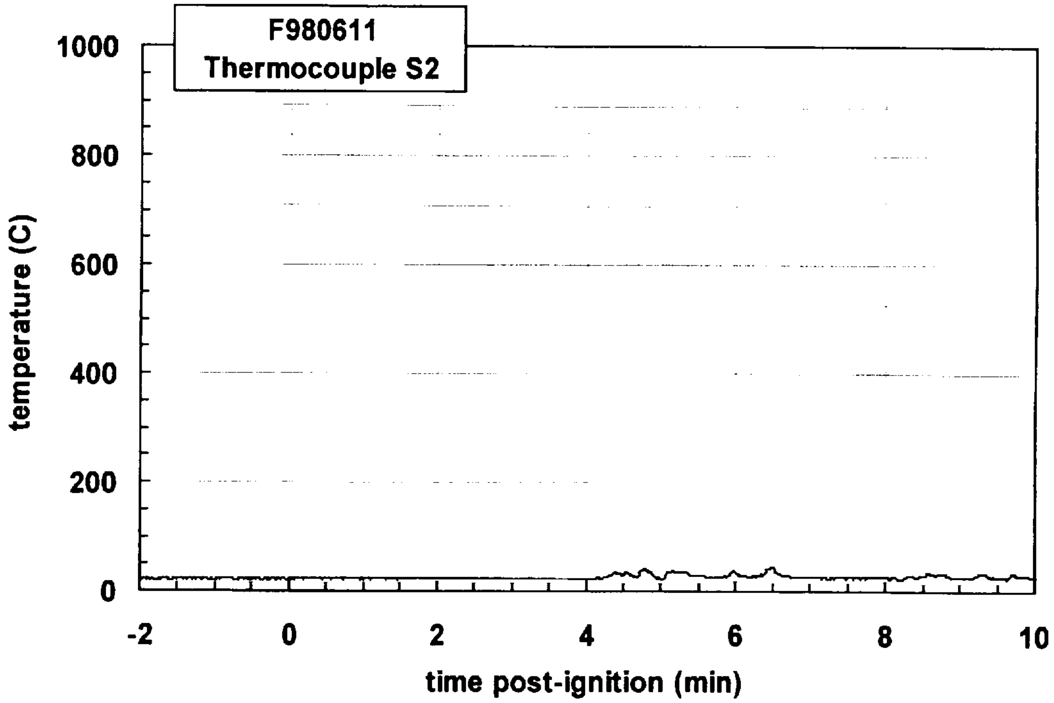

Plot D89. Fire Test F980611. Data plot from thermocouple S2.

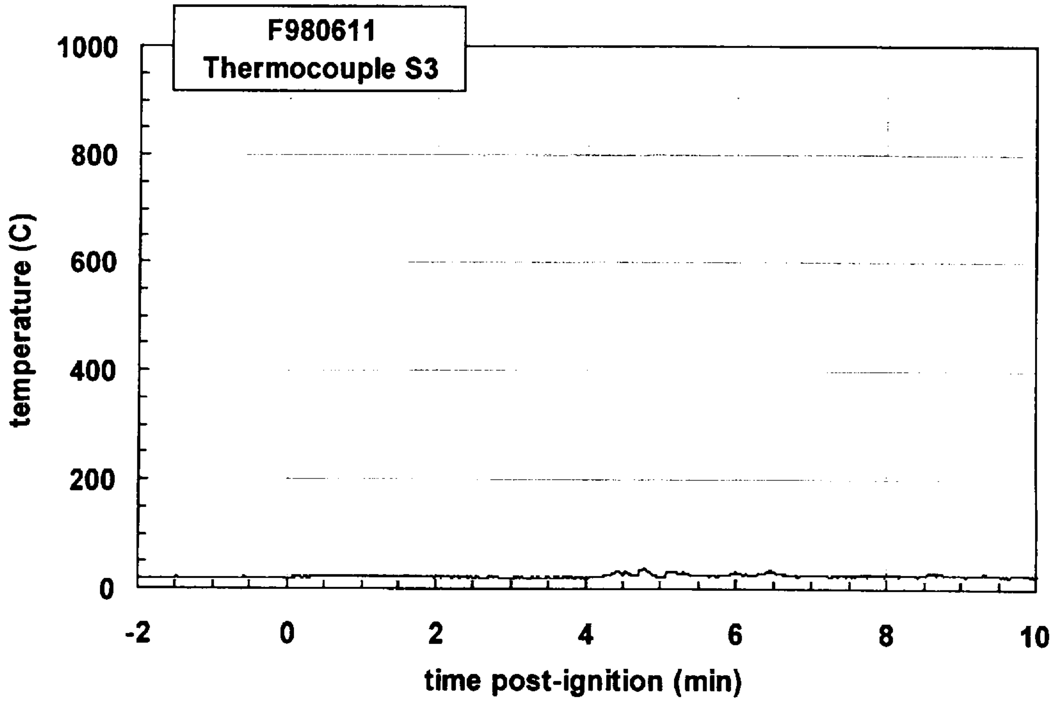

Plot D90. Fire Test F980611. Data plot from thermocouple S3.

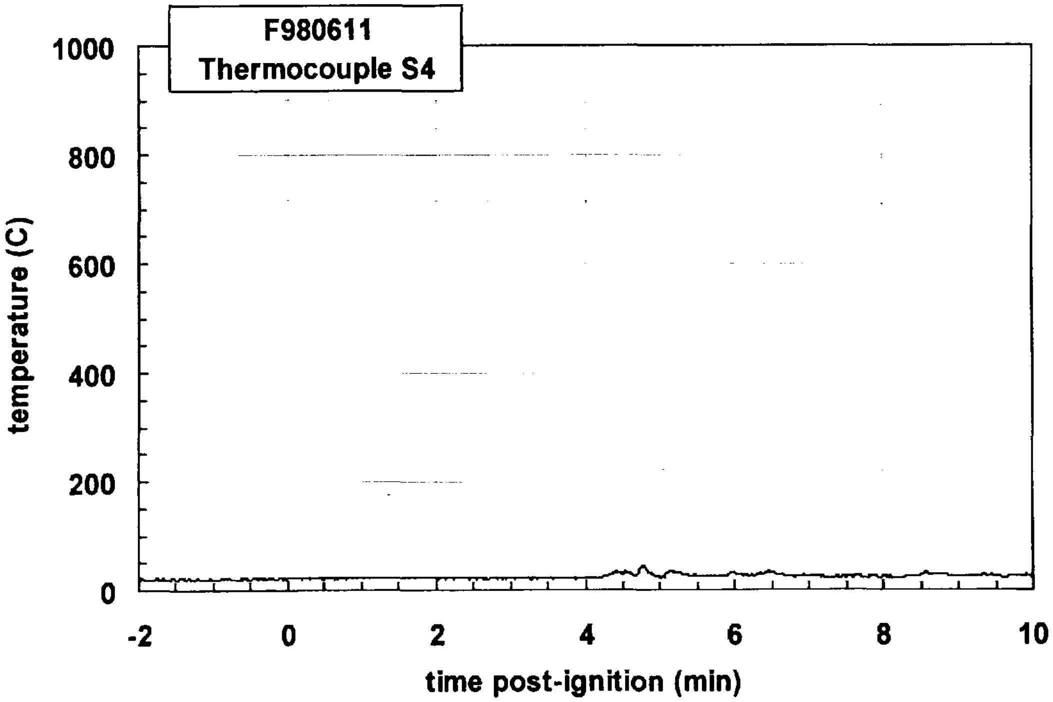

Plot D91. Fire Test F980611. Data plot from thermocouple S4.

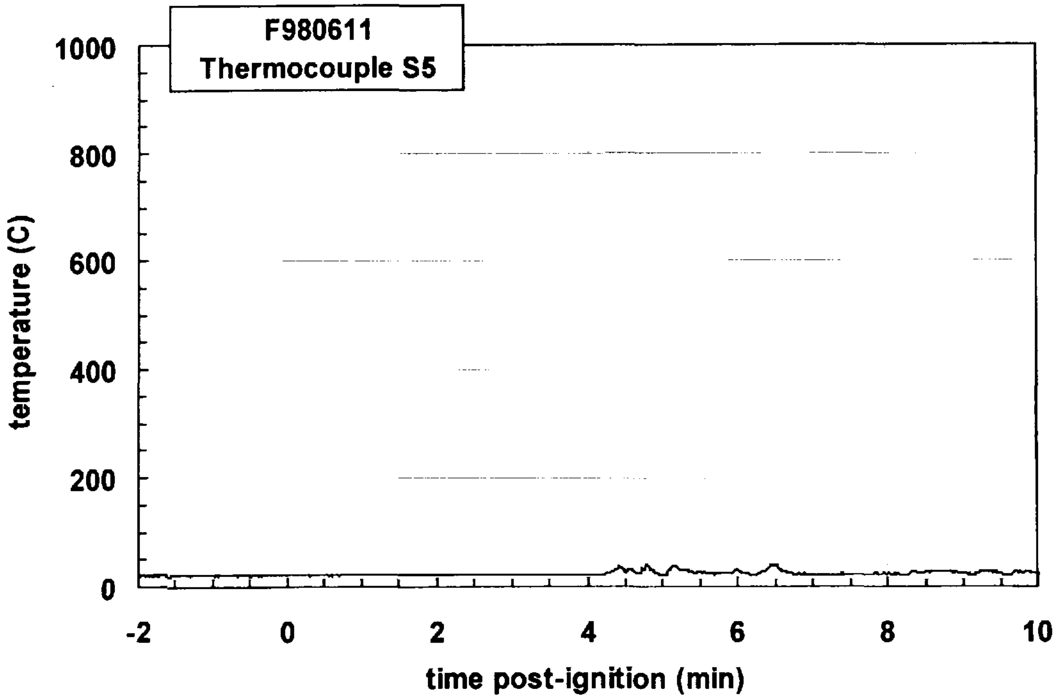

Plot D92. Fire Test F980611. Data plot from thermocouple S5.

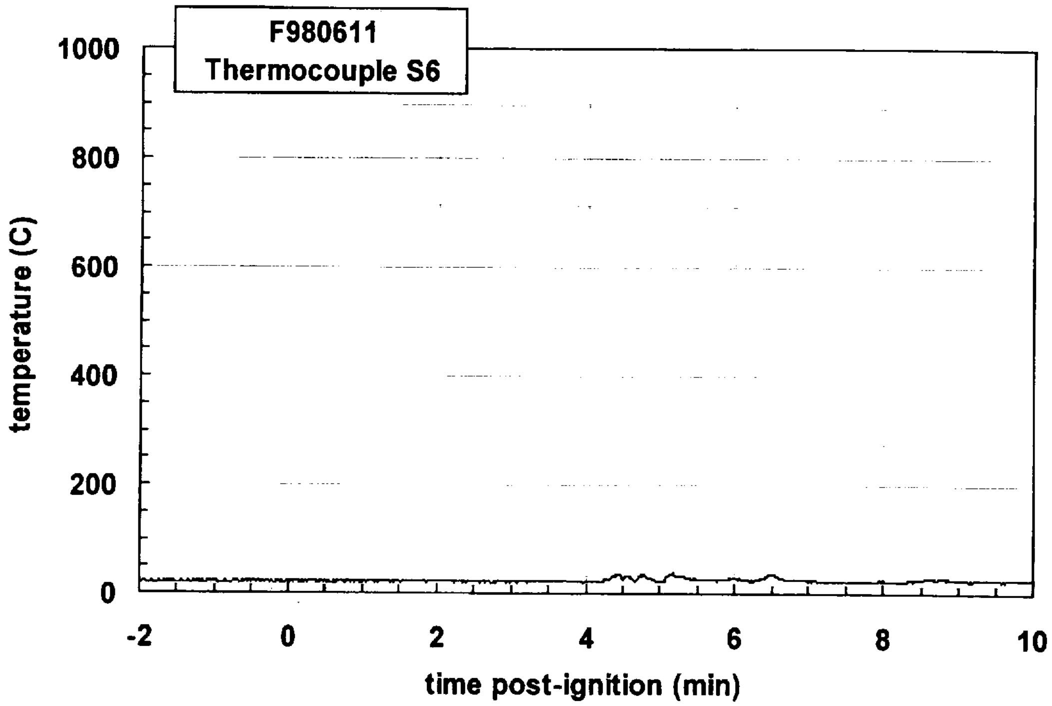

Plot D93. Fire Test F980611. Data plot from thermocouple S6.

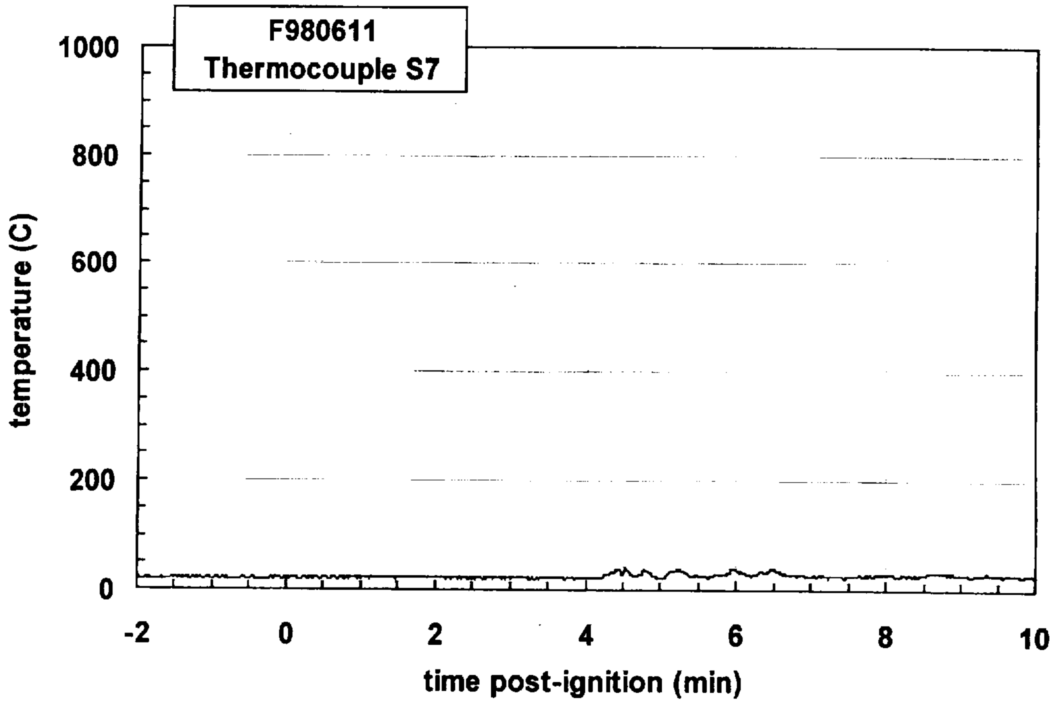

Plot D94. Fire Test F980611. Data plot from thermocouple S7.

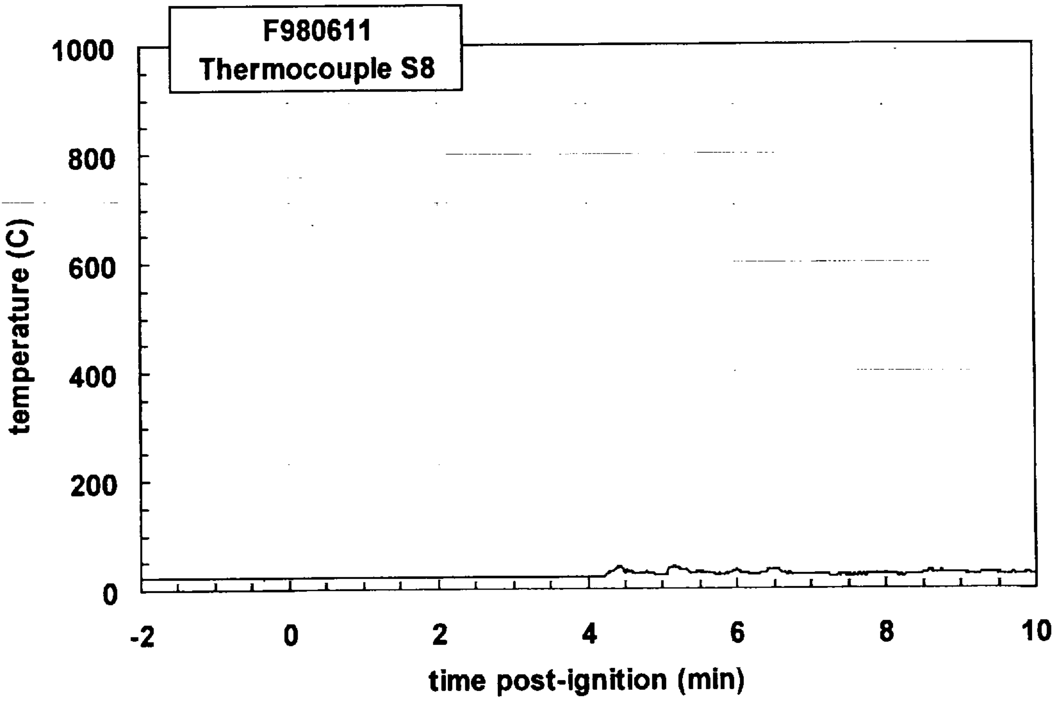

Plot D95. Fire Test F980611. Data plot from thermocouple S8.

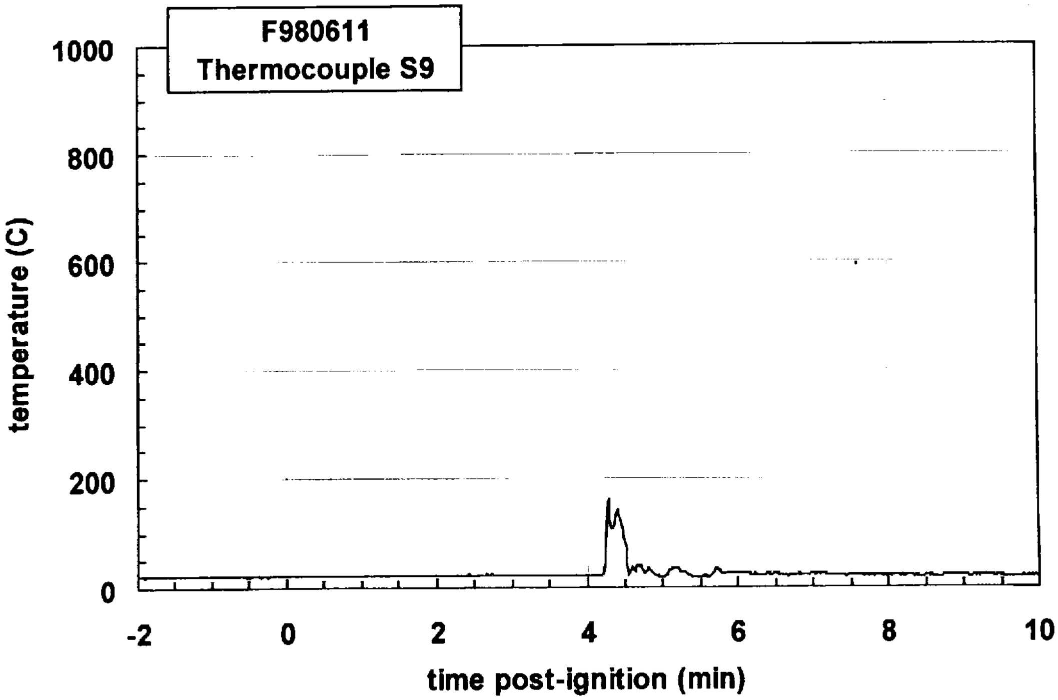

Plot D96. Fire Test F980611. Data plot from thermocouple S9.

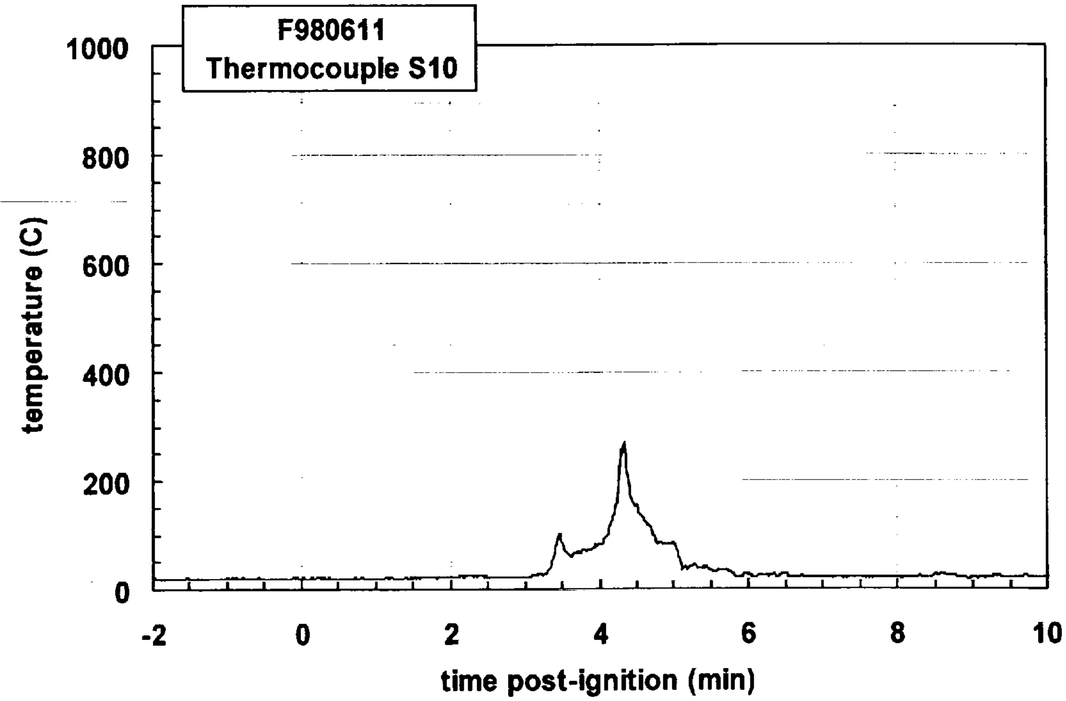

Plot D97. Fire Test F980611. Data plot from thermocouple S10.

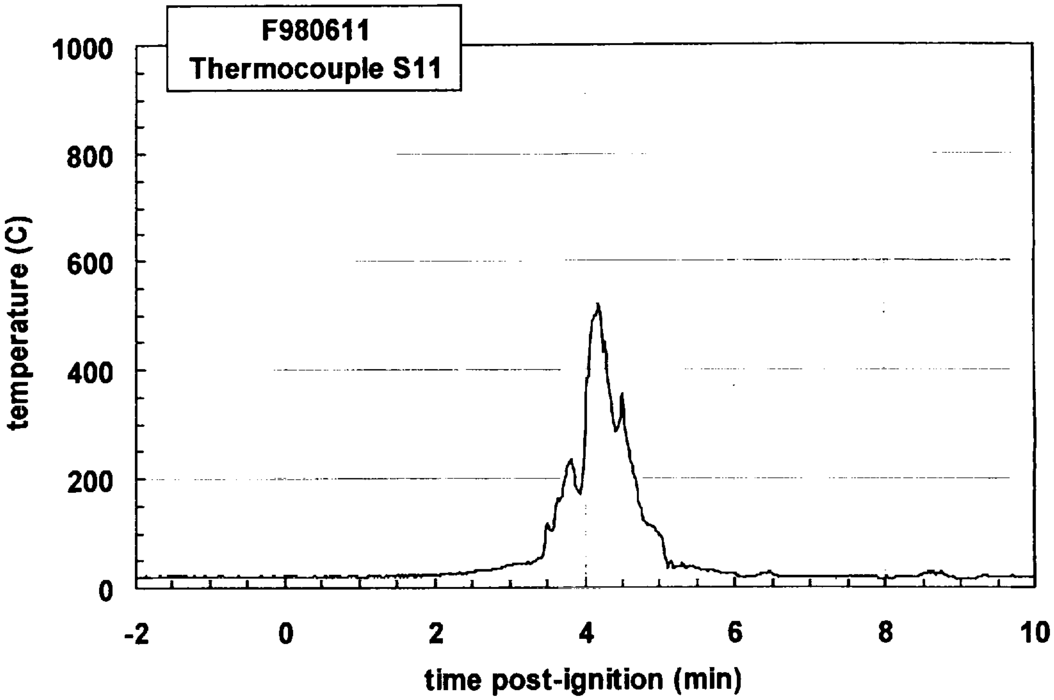

Plot D98. Fire Test F980611. Data plot from thermocouple S11.

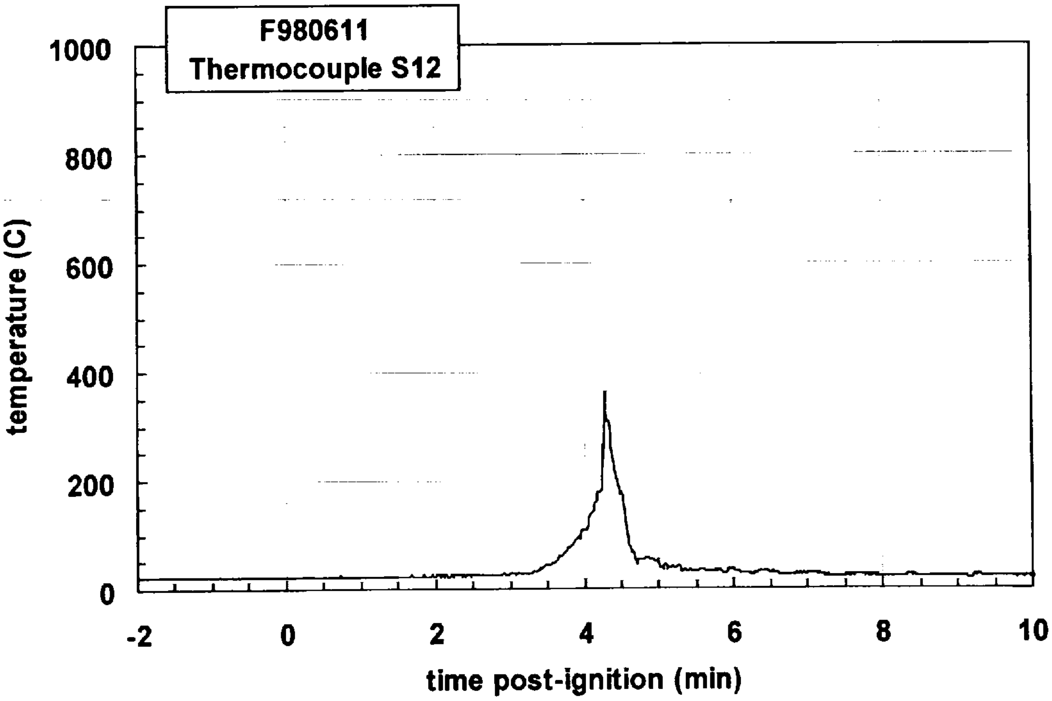

Plot D99. Fire Test F980611. Data plot from thermocouple S12.

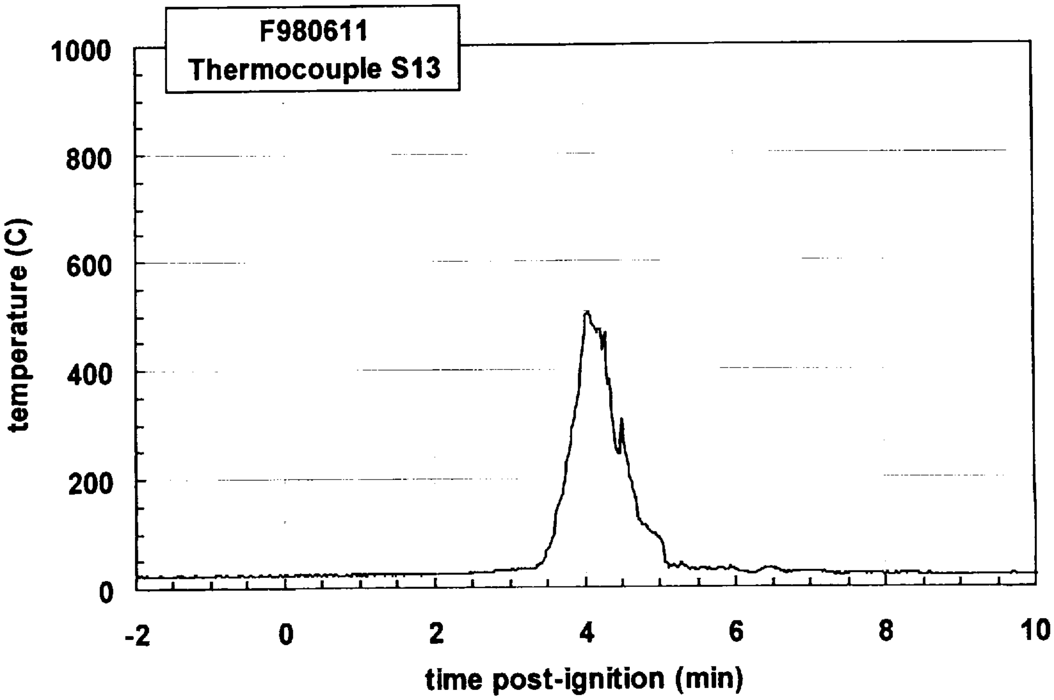

Plot 100. Fire Test F980611. Data plot from thermocouple S13.

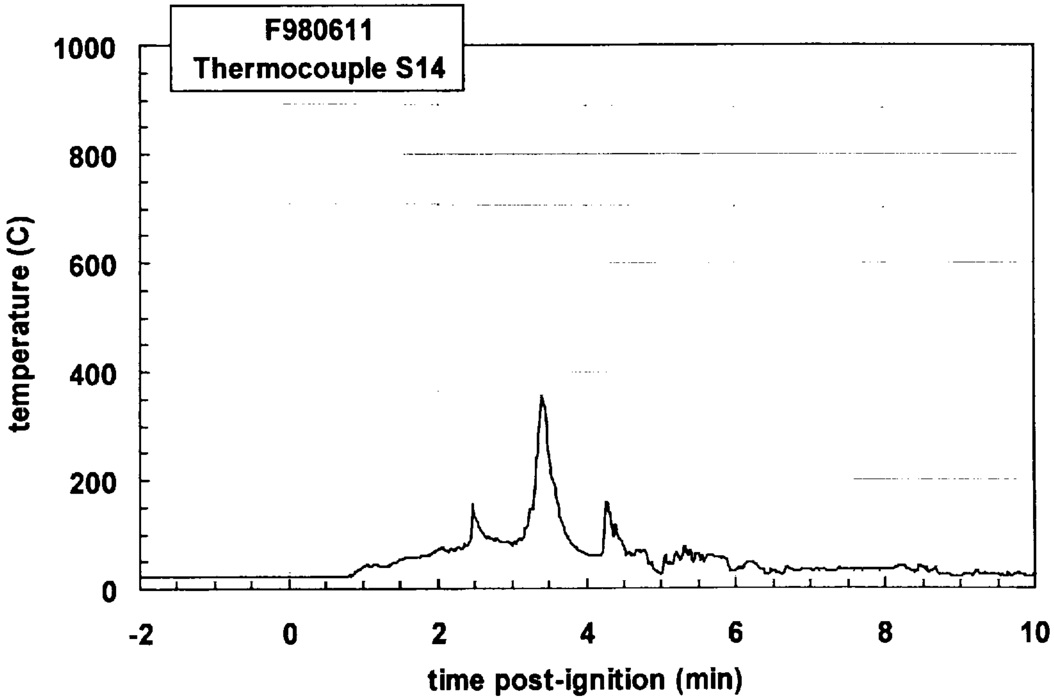

Plot D101. Fire Test F980611. Data plot from thermocouple S14.

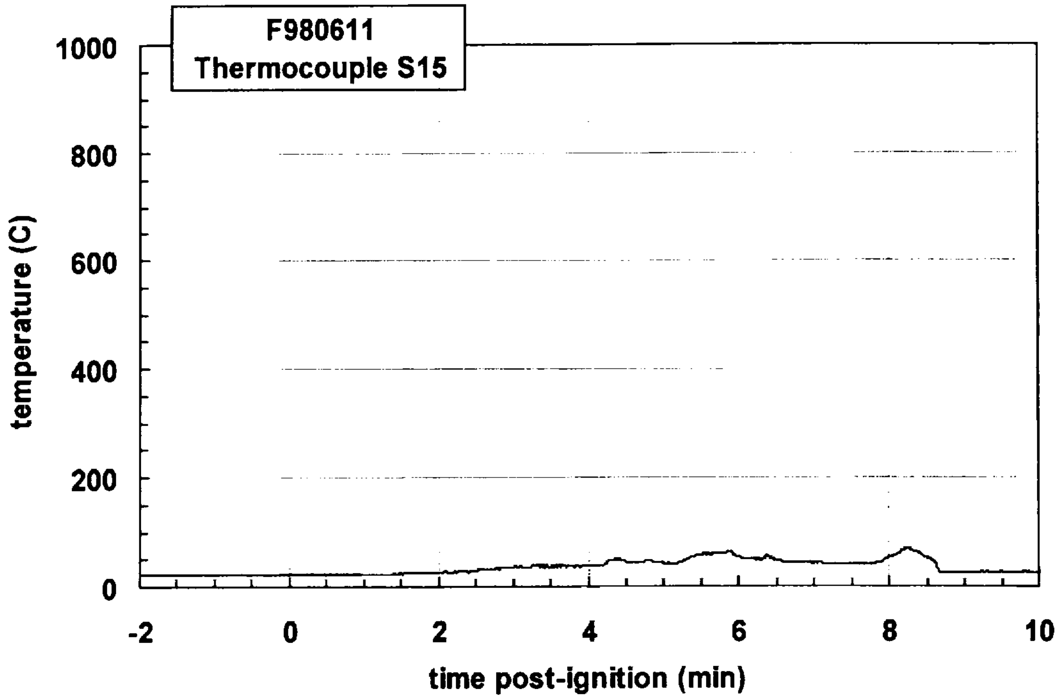

Plot D102. Fire Test F980611. Data plot from thermocouple S15.

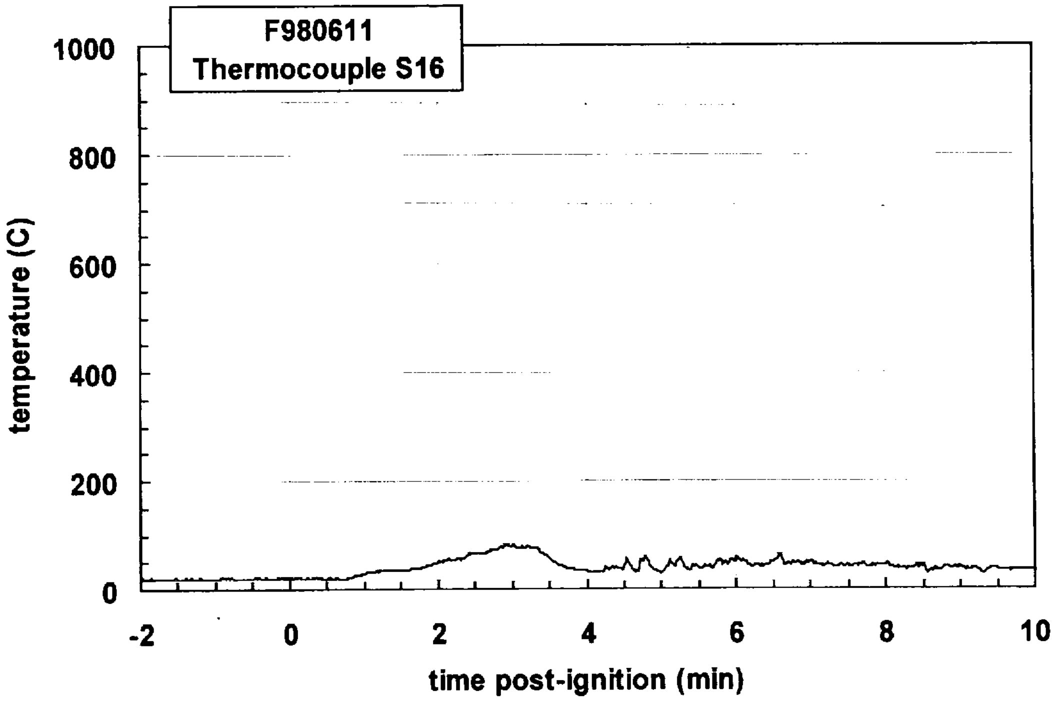

Plot D103. Fire Test F980611. Data plot from thermocouple S16.

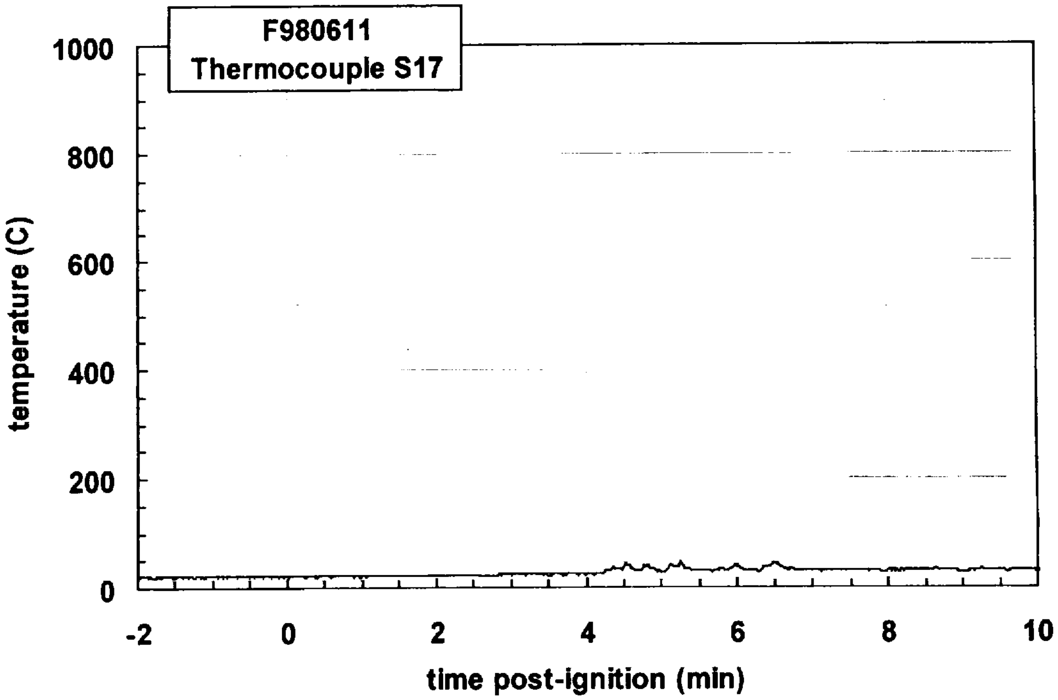

Plot D104. Fire Test F980611. Data plot from thermocouple S17.

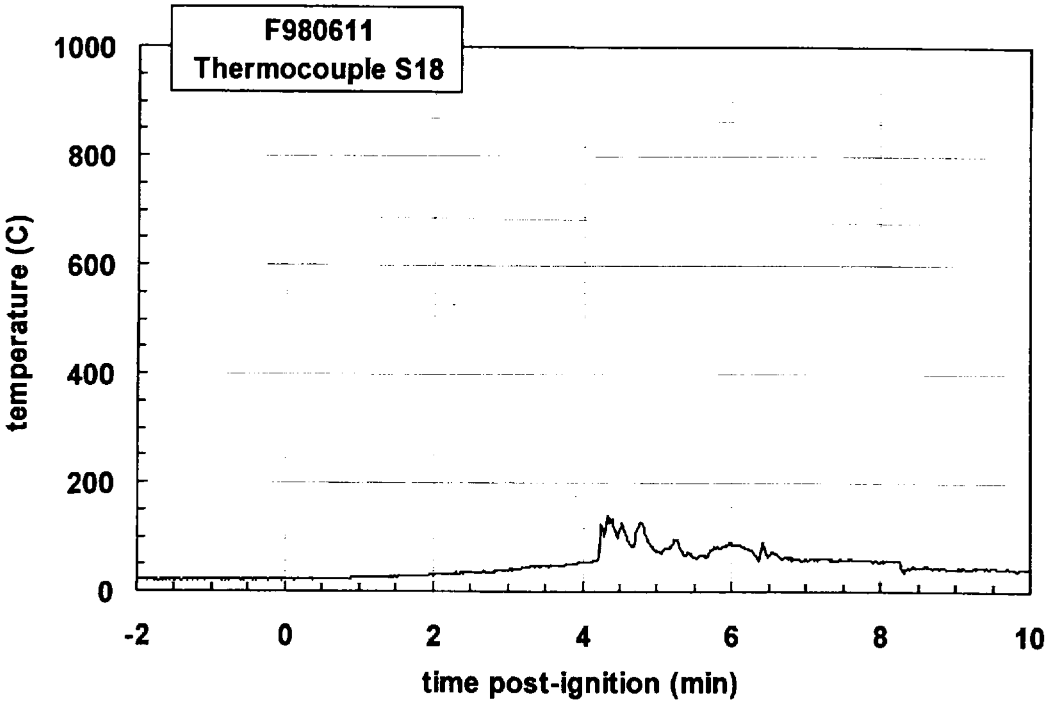

Plot D105. Fire Test F980611. Data plot from thermocouple S18.

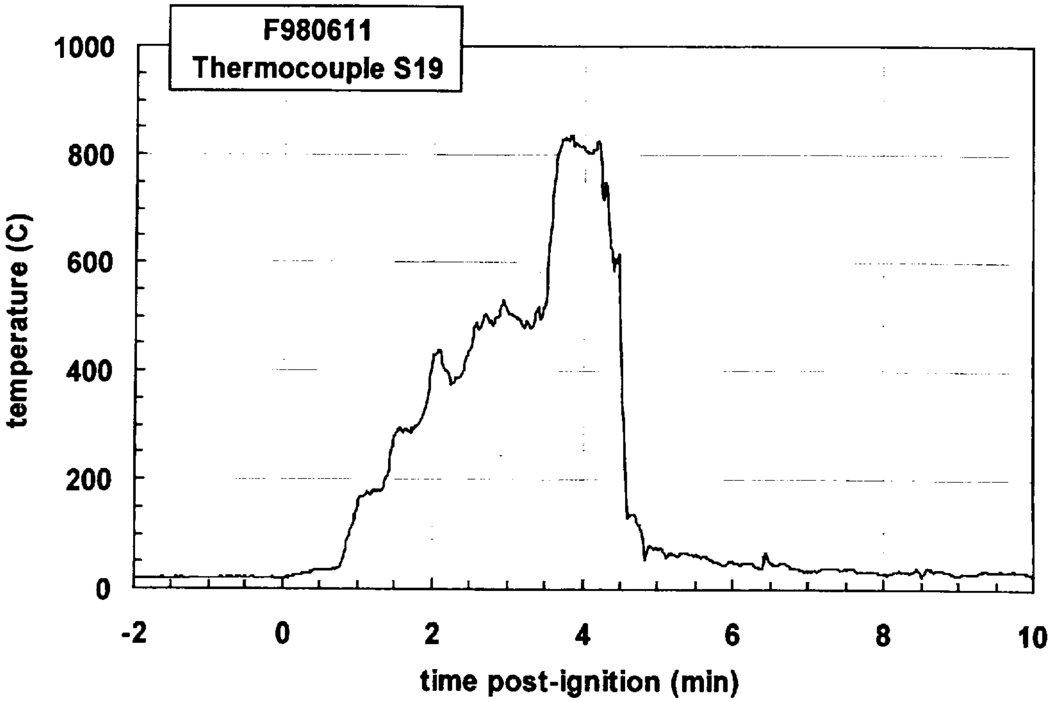

Plot D16. Fire Test F980611. Data plot from thermocouple S19.

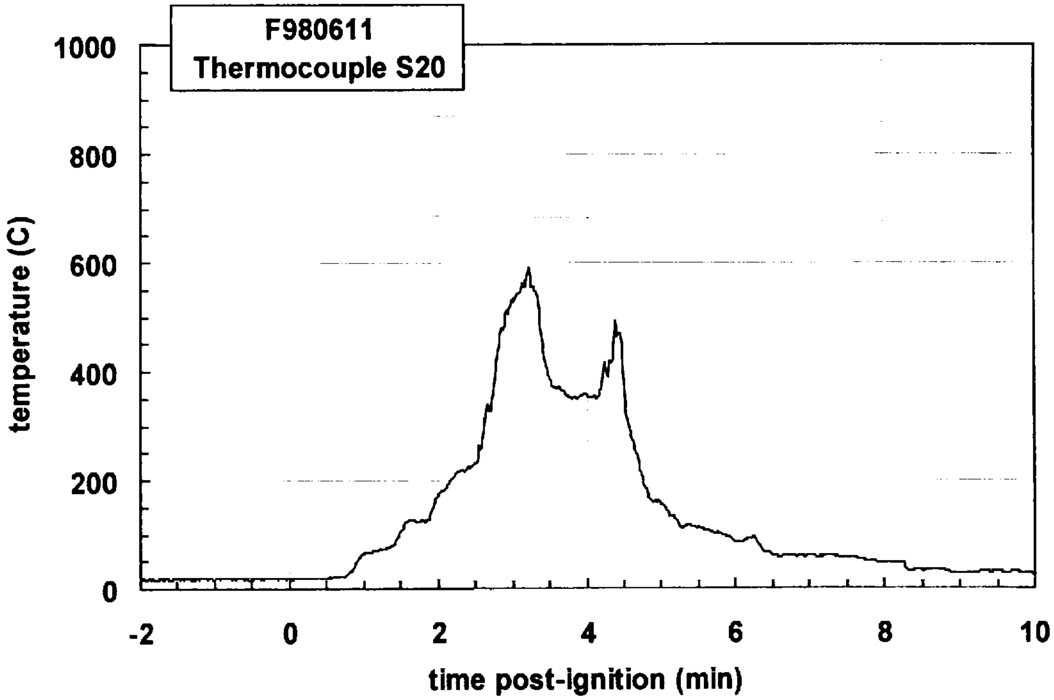

Plot D107. Fire Test F980611. Data plot from thermocouple S20.

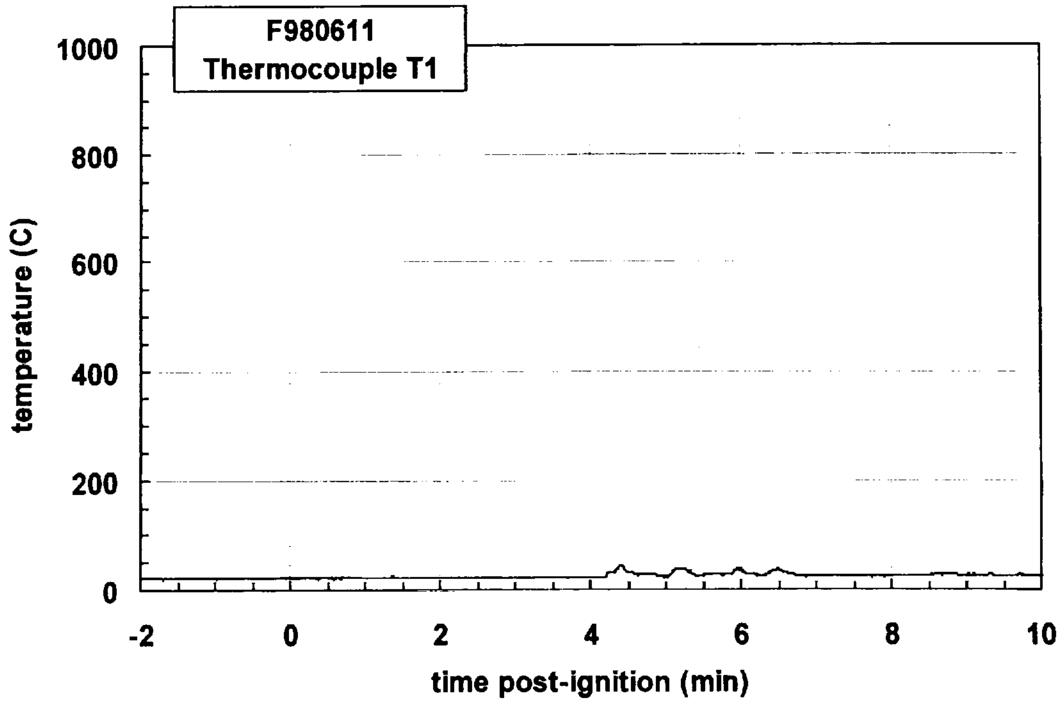

Plot D108. Fire Test F980611. Data plot from thermocouple T1.

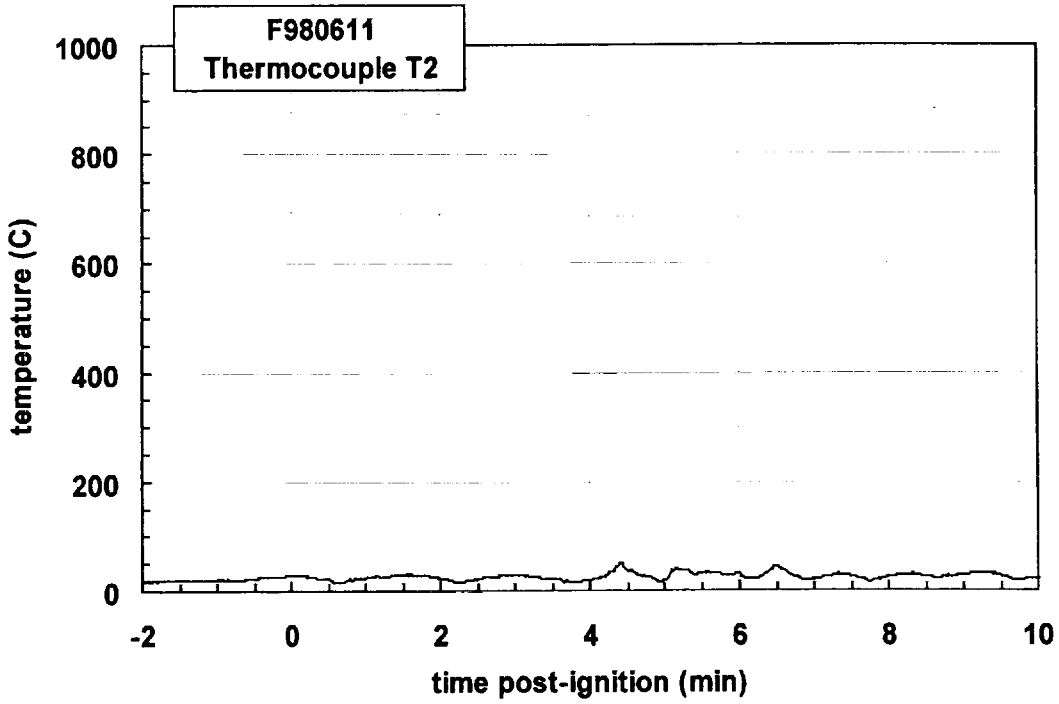

Plot D109. Fire Test F980611. Data plot from thermocouple T2.

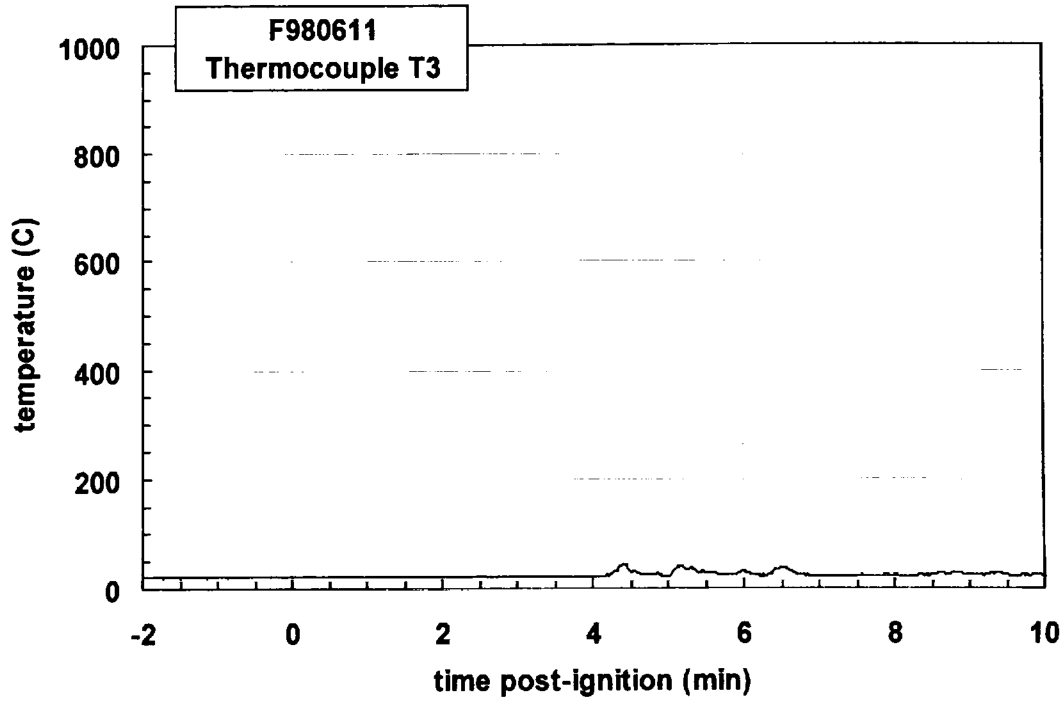

Plot D110. Fire Test F980611. Data plot from thermocouple T3.

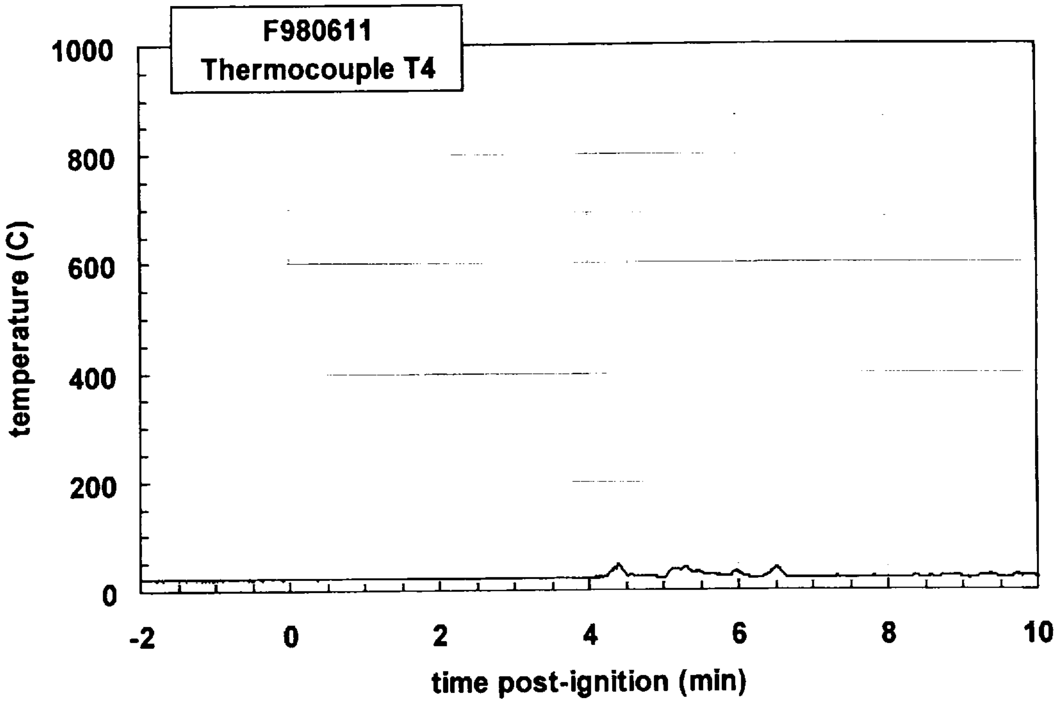

Plot D111. Fire Test F980611. Data plot from thermocouple T4.

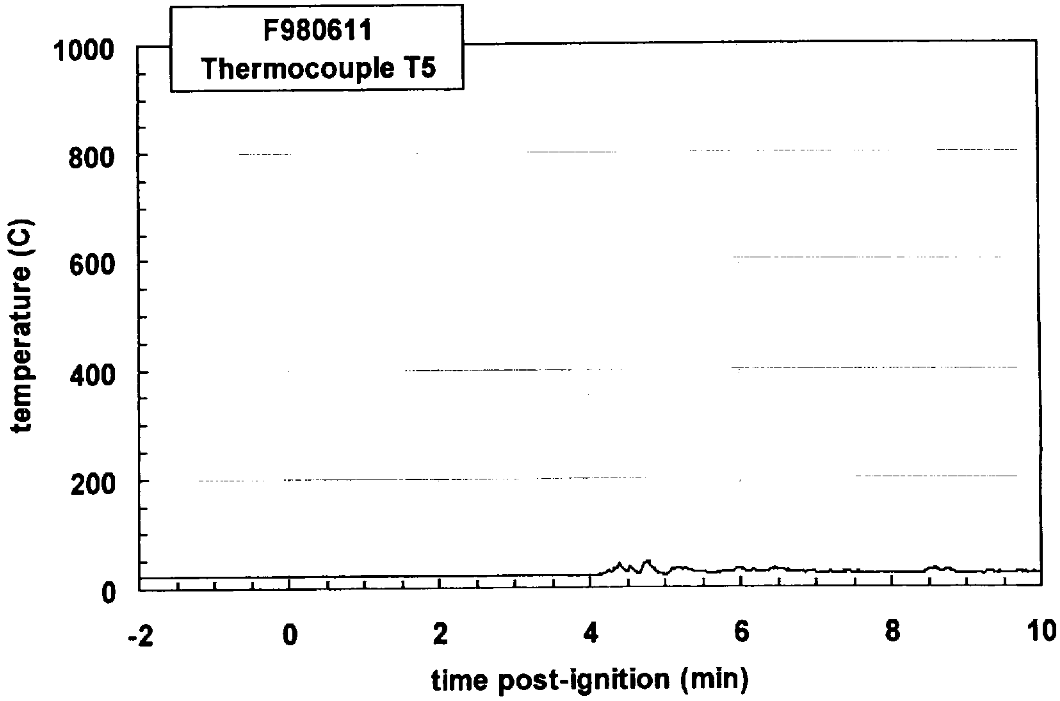

Plot D112. Fire Test F980611. Data plot from thermocouple T5.

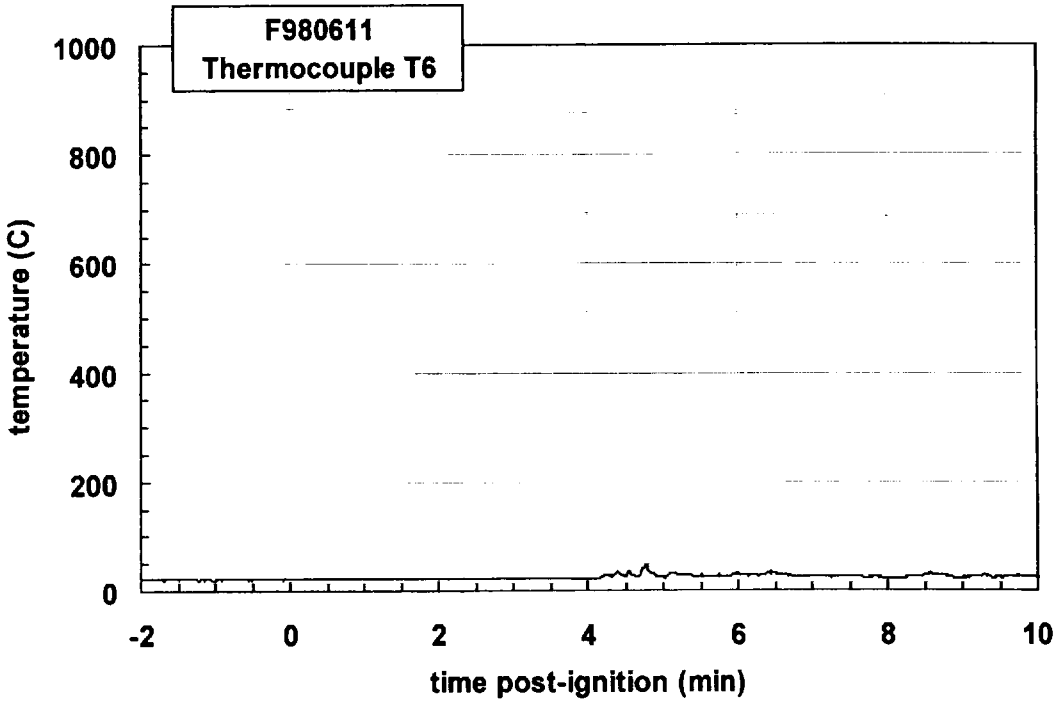

Plot D113. Fire Test F980611. Data plot from thermocouple T6.

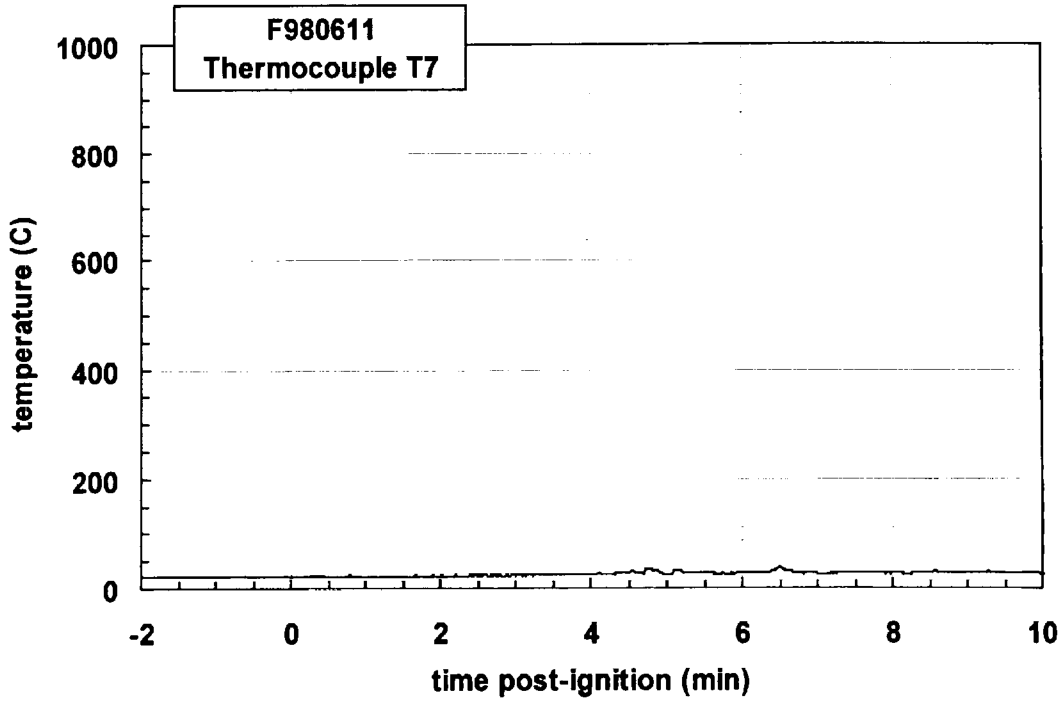

Plot D114. Fire Test F980611. Data plot from thermocouple T7.

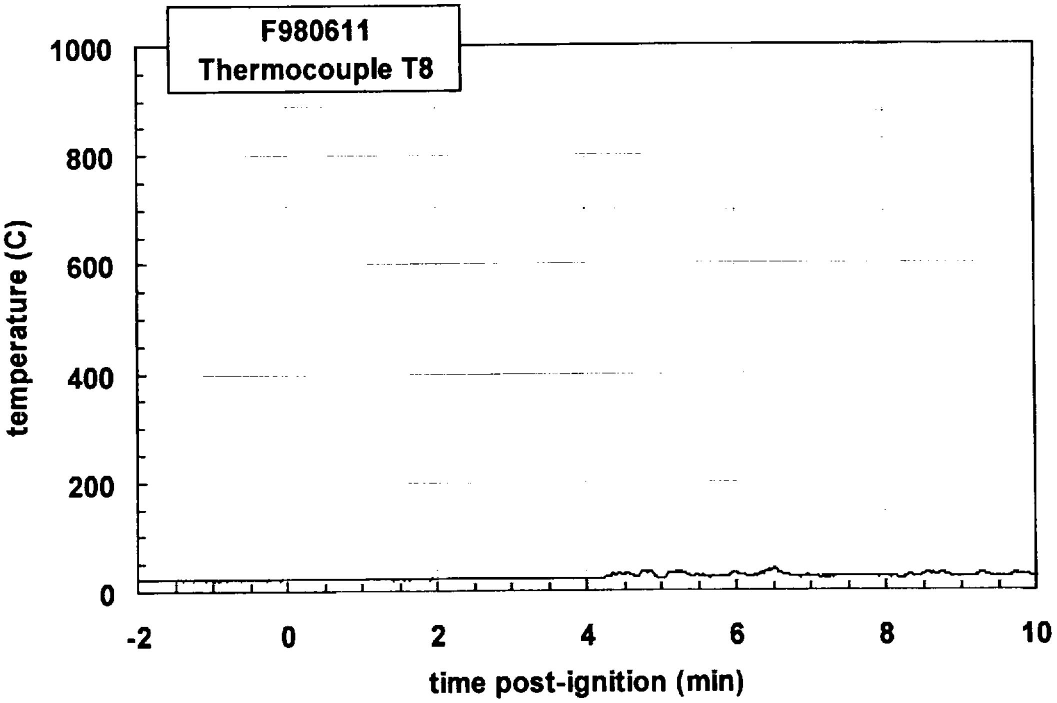

Plot D115. Fire Test F980611. Data plot from thermocouple T8.

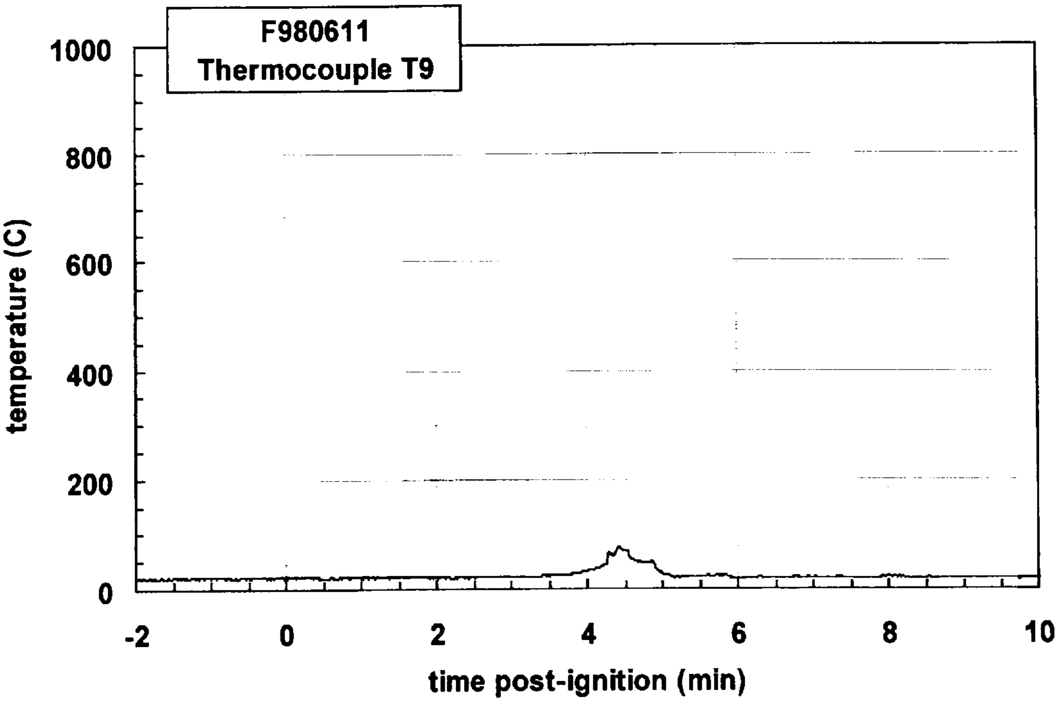

Plot D116. Fire Test F980611. Data plot from thermocouple T9.

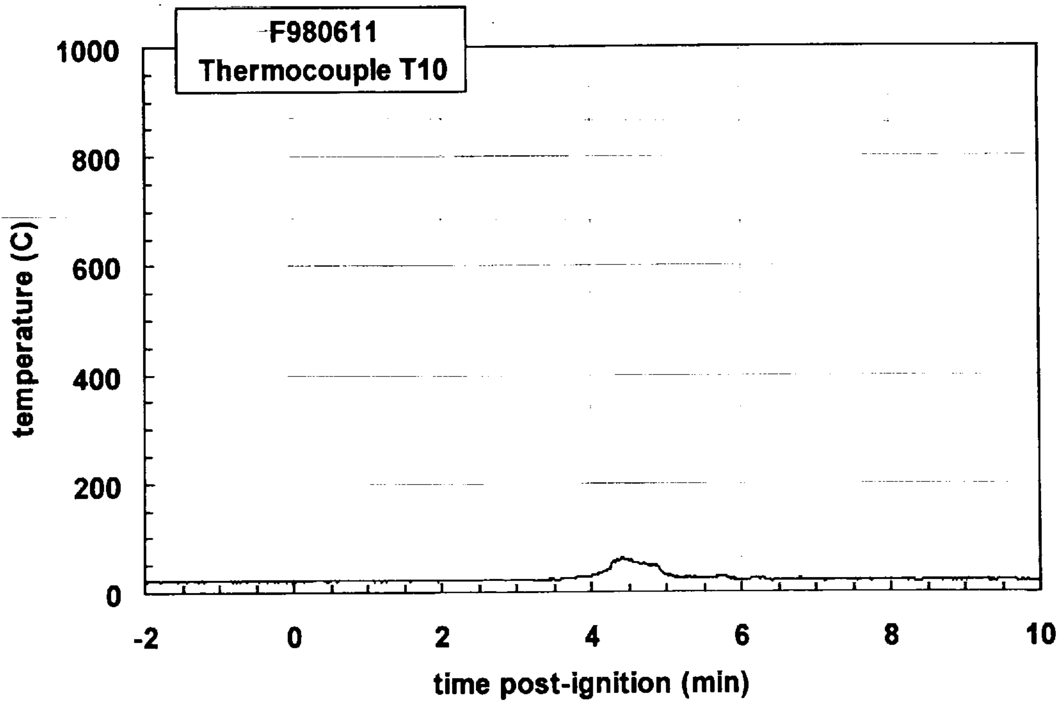

Plot D117. Fire Test F980611. Data plot from thermocouple T10.

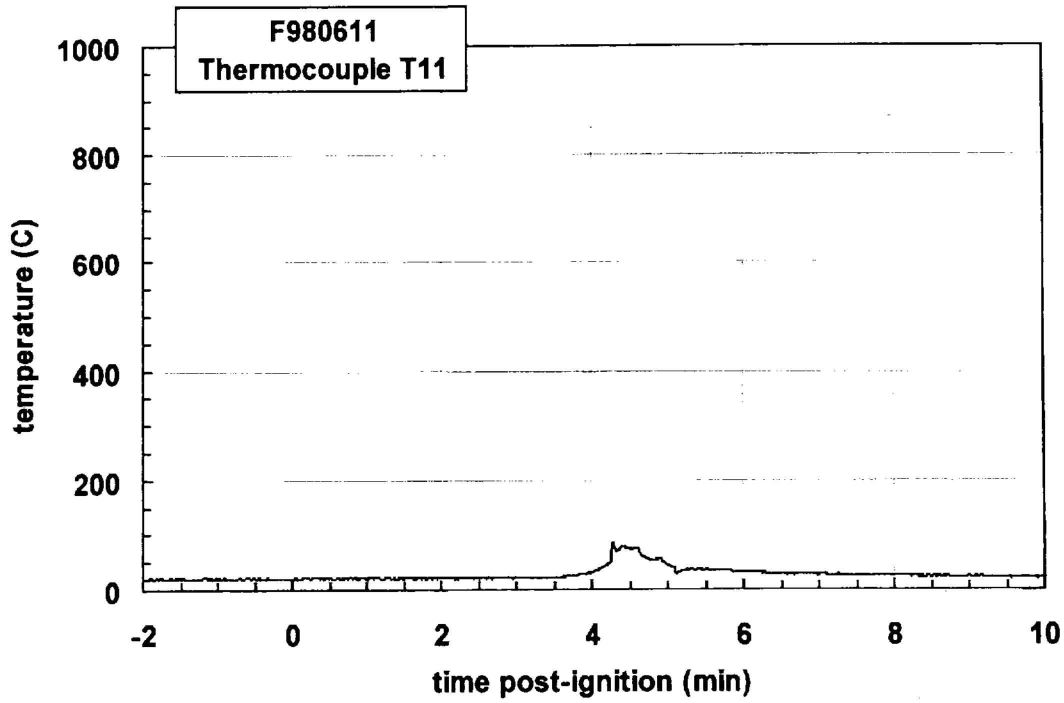

Plot D118. Fire Test F980611. Data plot from thermocouple T11.

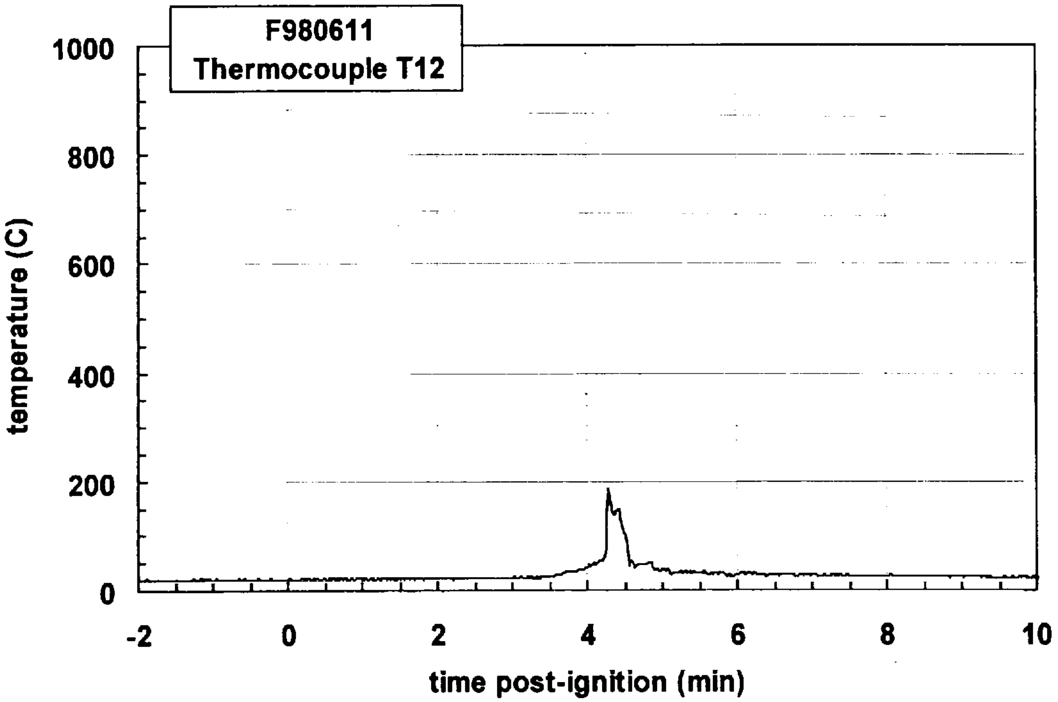

Plot D119. Fire Test F980611. Data plot from thermocouple T12.

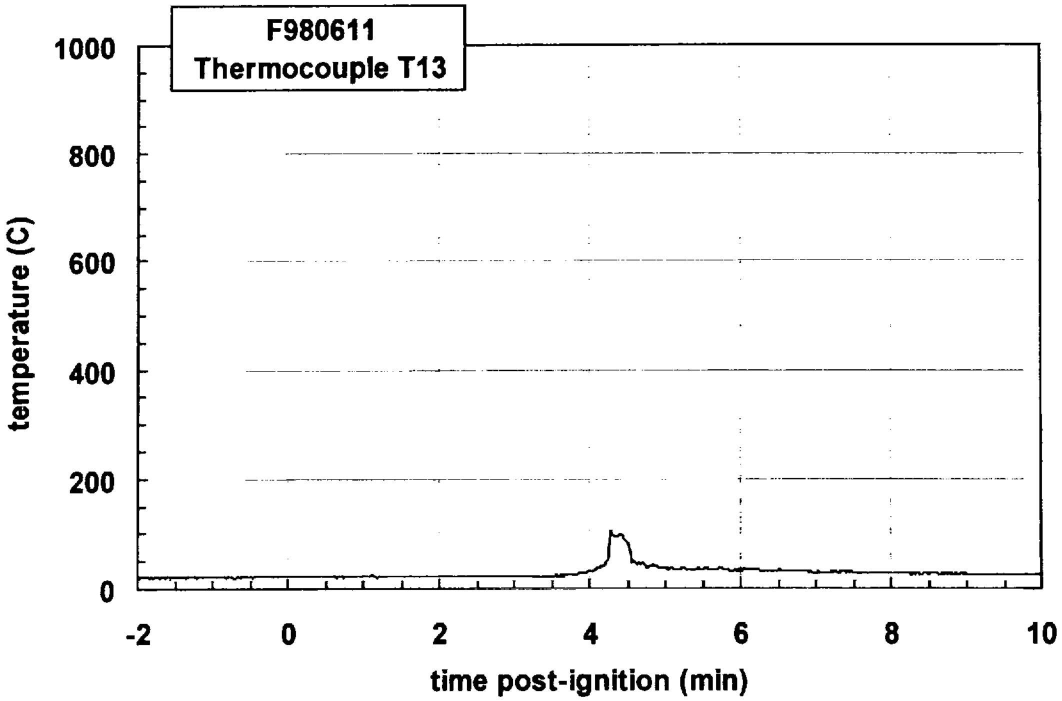

Plot D120. Fire Test F980611. Data plot from thermocouple T13.

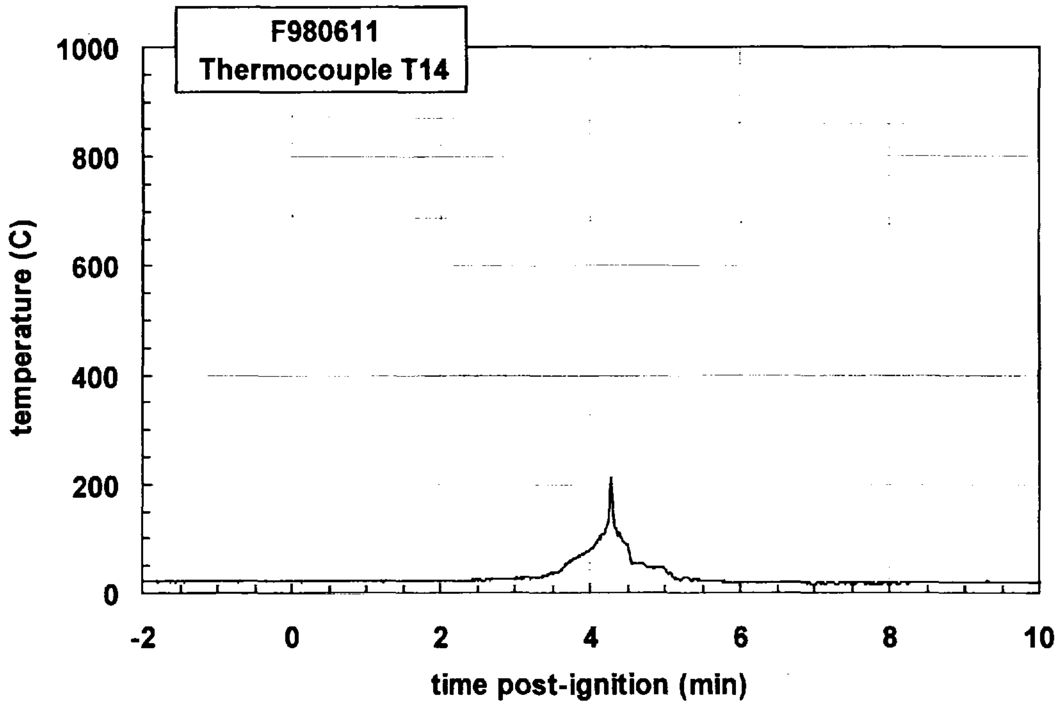

Plot D121. Fire Test F980611. Data plot from thermocouple T14.

APPENDIX E
ASPIRATED THERMOCOUPLE DATA

Two aspirated thermocouple assembly (Medtherm Corporation) was installed in the test vehicle (Fig. E1). The aspirated thermocouple assembly was fabricated from Inconel 600 tubing. Each assembly consisted of a vertical manifold (o.d. = 0.375 in. (9.5 mm), i.d. = 0.25 in. (6.4 mm), length = 16 in. (406 mm)) with six horizontal radiation shields (o.d. = 0.25 in. (6.4 mm), i.d. = 0.19 in. (4.8 mm), length = 1.00 in. (25.4 mm)). The vertical spacing between the radiation shields along the manifold was 3 in. (75 mm). Three radial holes were drilled near the tip of each radiation shield. The holes were sized to approximately balance the airflow-rates over each thermocouple. A Type-N thermocouple inserted into each radiation shield so that the thermocouple junction was positioned approximately 0.2 in. (5.1 mm) down-stream from the inlet holes.

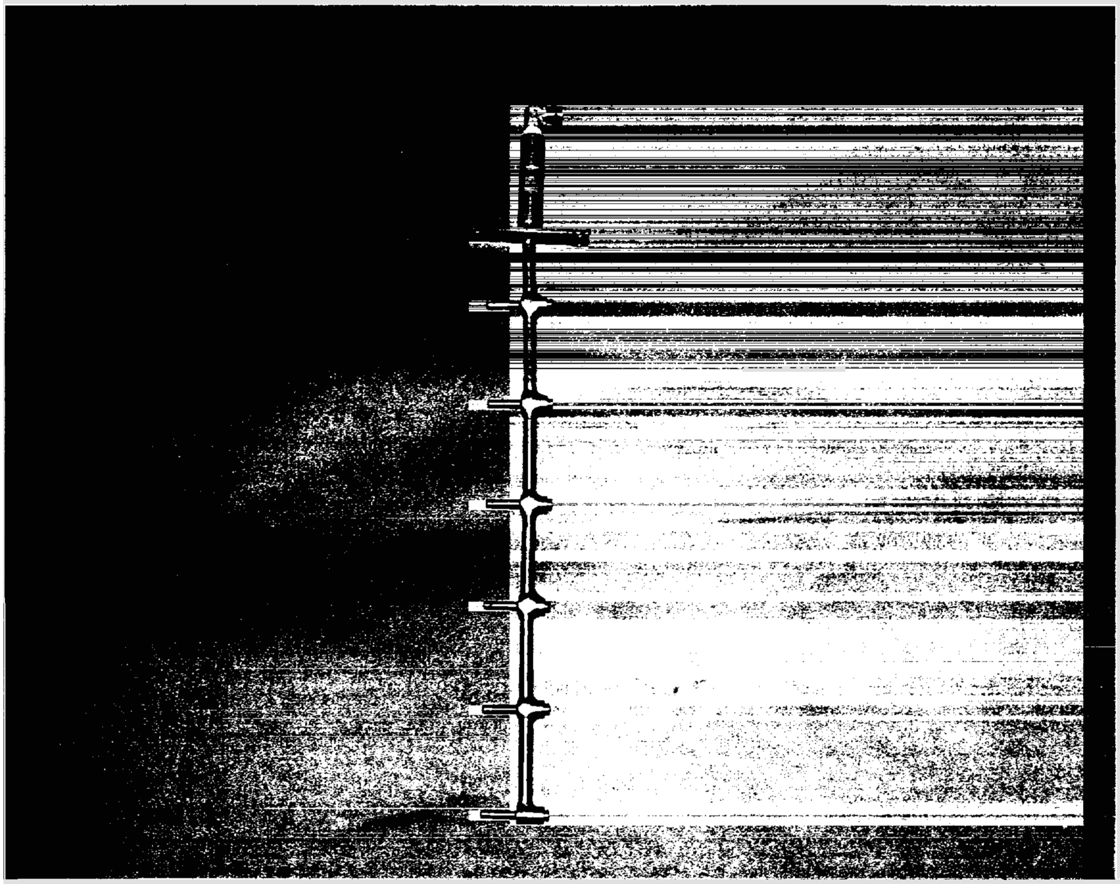

Figure E1. Fire Test F980611. Photograph of the aspirated thermocouple assembly used in the passenger compartment of the test vehicle.

The mounting flange of the aspirated thermocouple probe assembly was attached to the roof of the vehicle. The probe extended into the passenger compartment through a hole in the roof so that all 6 thermocouples were located below the headliner. The probe was vertical and located along the longitudinal mid-line of the vehicle approximately equidistant from the driver and passenger seats. The upper-most aspirated thermocouple was approximately 0.5 in. (12 mm) below the lower surface of the headliner. The manifold was connected to a rotary-vane pump with flexible copper tubing (o.d. = 0.5 in. (12 mm), length = 15 ft. (4.6 m)). The capacity of the pump was 50 L/min at atmospheric pressure.

Figures E2 and E3 show the approximate location of the aspirated thermocouple probe assembly in the test vehicle for this test.

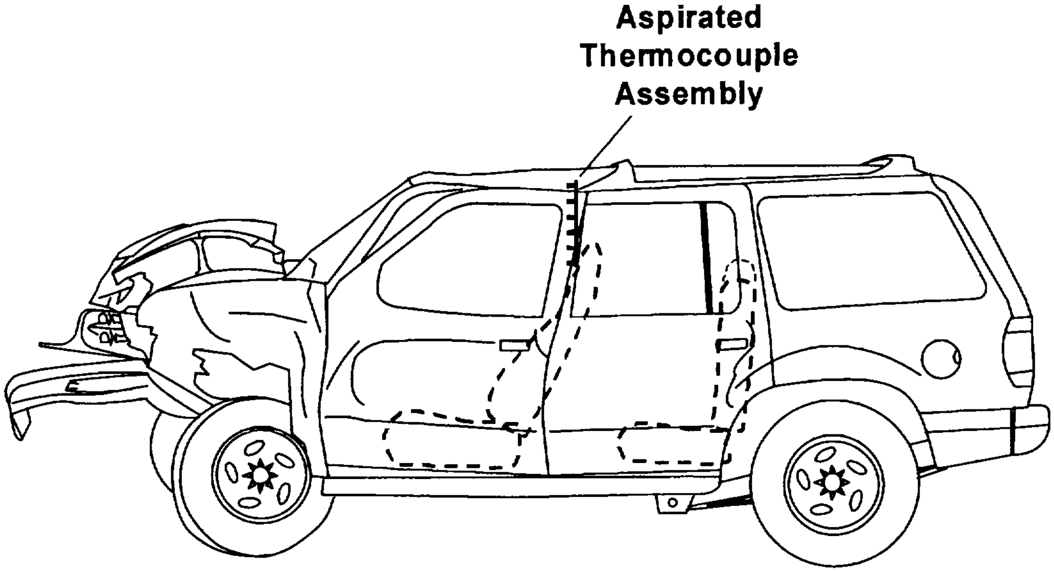

Figure E2. Fire Test F980611. Side view of the test vehicle showing the approximate location of the aspirated thermocouple probe assembly in the passenger compartment.

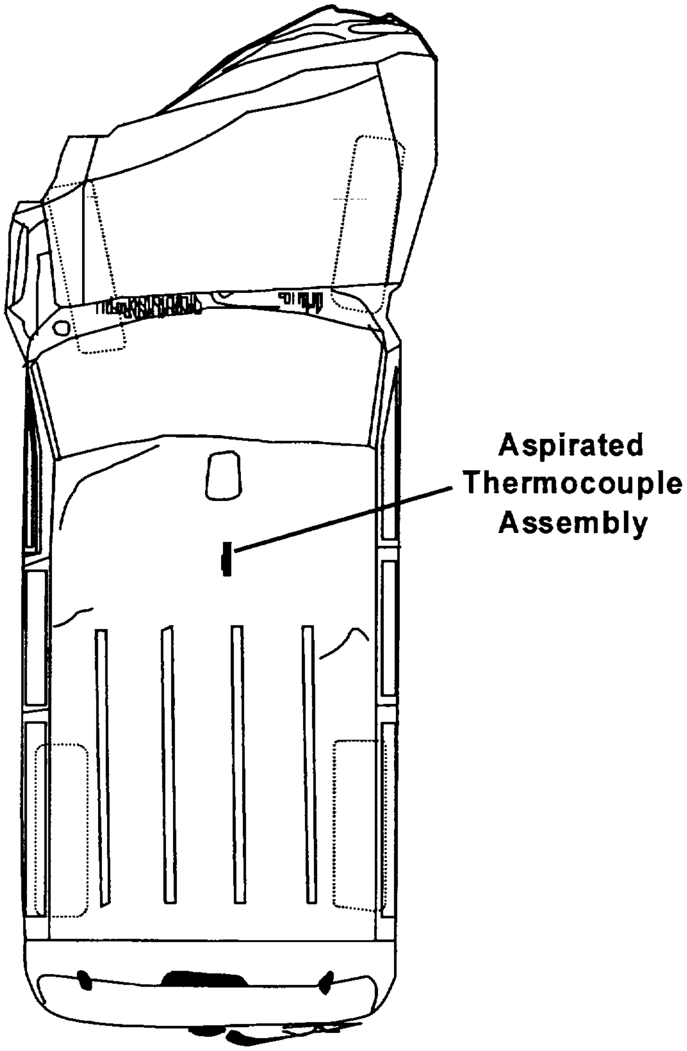

Figure E3. Fire Test F980611. Top view of the test vehicle showing the approximate location of the aspirated thermocouple probe assembly in the passenger compartment.

REFERENCES

E1. J. S. Newman and P. A. Croce. A simple aspirated thermocouple for use in fires. *J. Fire Flamm.* **10**:326-336 (1979).

E2. N. R. Keltner and K. A. Strom. Thermal Measurement Uncertainty and Compensation. Paper in preparation.

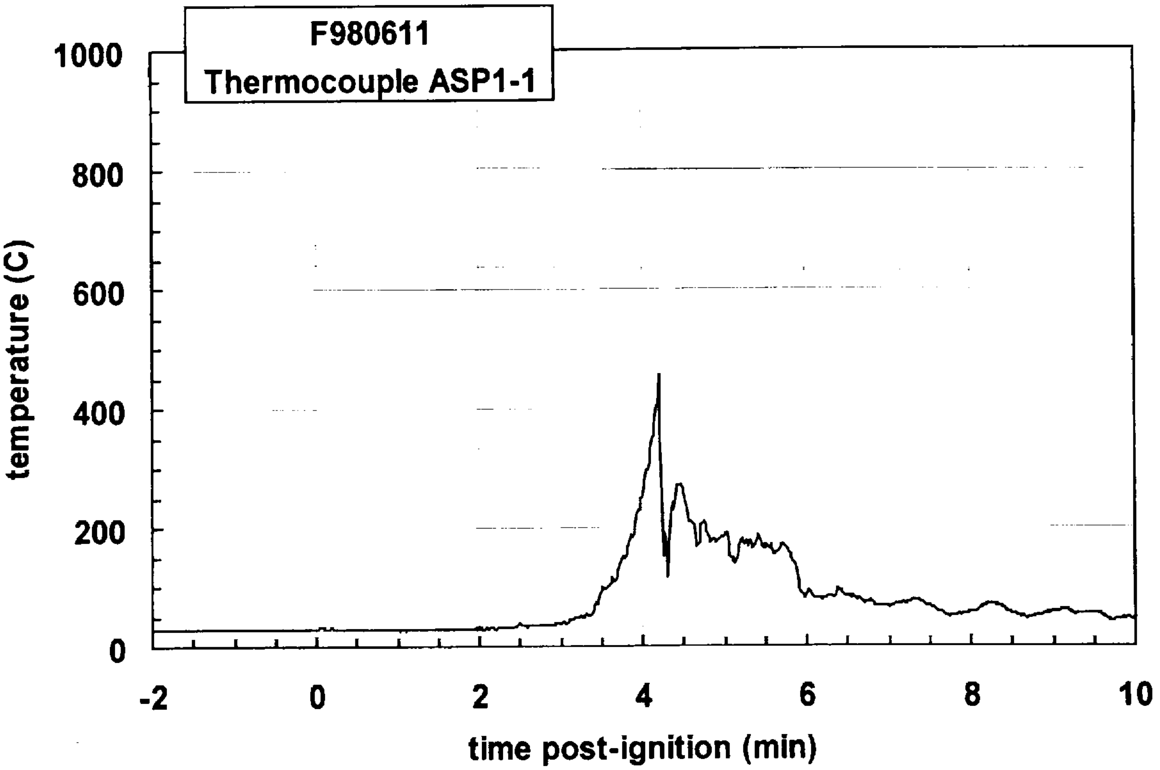

Plot E1. Fire Test F980611. Data plot from thermocouple ASP1-1.

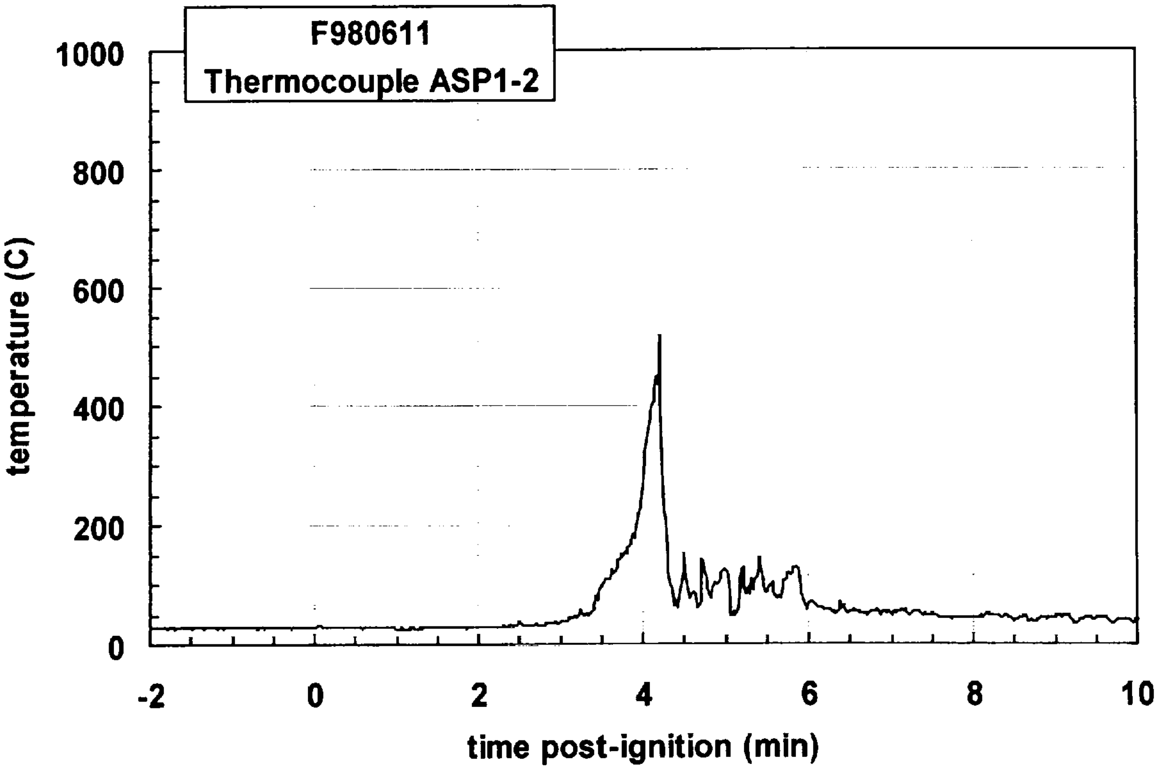

Plot E2. Fire Test F980611. Data plot from thermocouple ASP1-2.

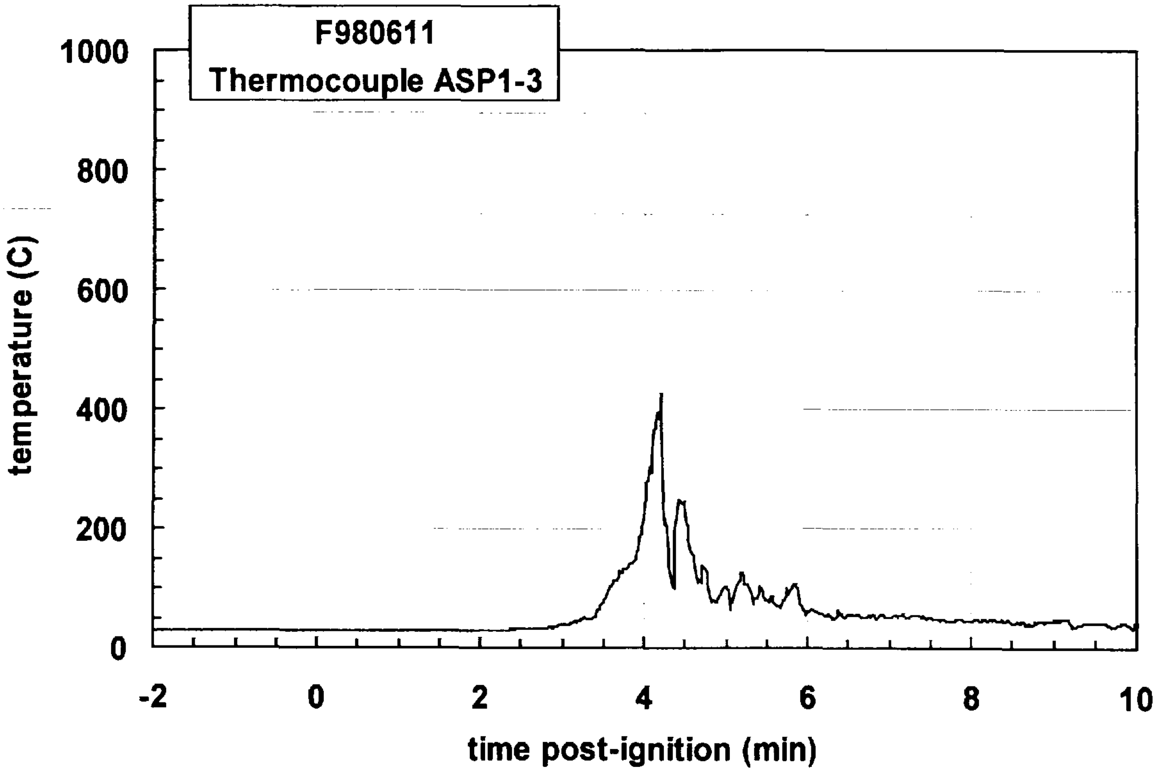

Plot E3. Fire Test F980611. Data plot from thermocouple ASP1-3.

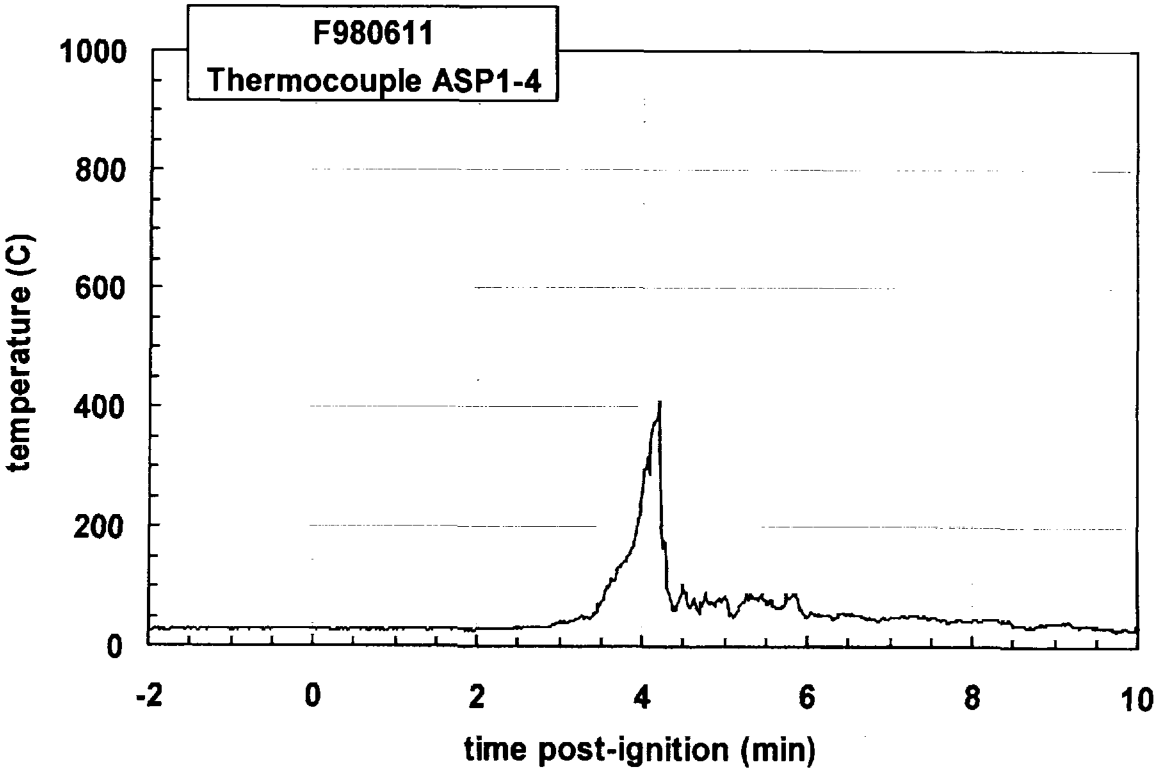

Plot E4. Fire Test F980611. Data plot from thermocouple ASP1-4.

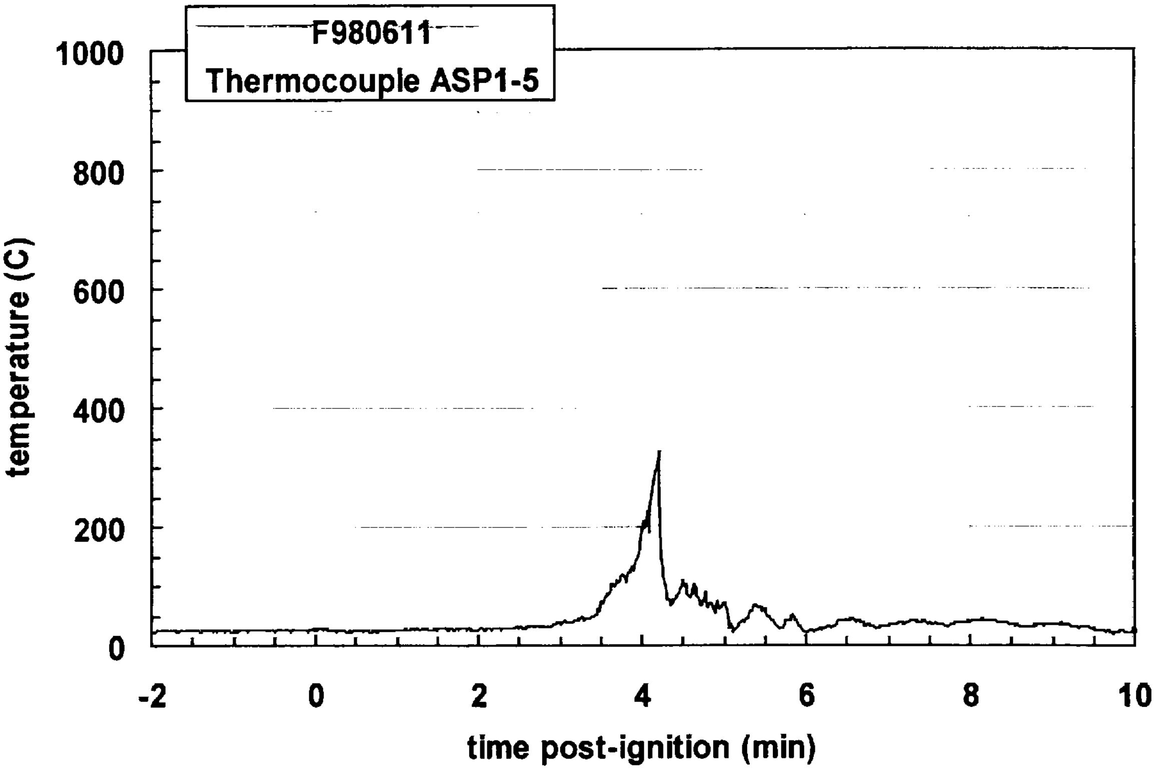

Plot E5. Fire Test F980611. Data plot from thermocouple ASP1-5.

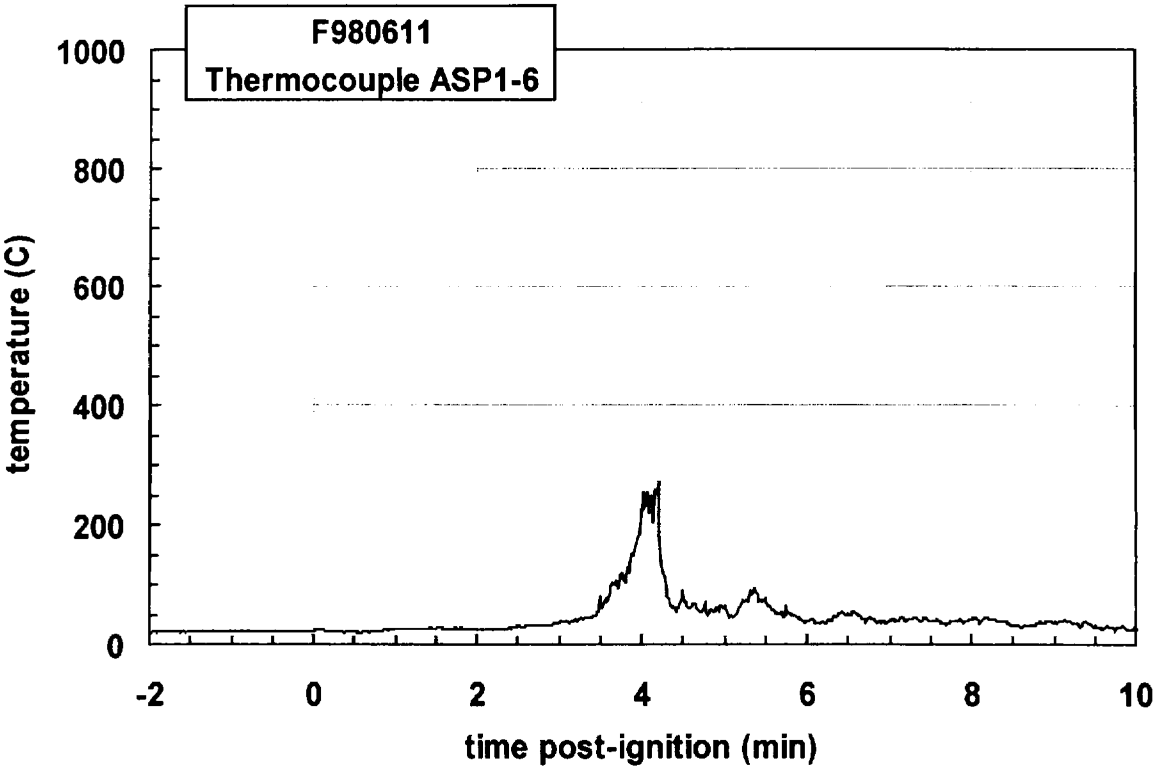

Plot E6. Fire Test F980611. Data plot from thermocouple ASP1-6.

APPENDIX F
HEAT FLUX TRANSDUCER/RADIOMETER DATA

Heat-flux transducer/radiometer assemblies (64 Series, Medtherm Corporation) were used to measure convective and radiative heat transfer to selected objects in the vehicle. Each assembly contained two Schmidt-Boelter thermopiles in a water-cooled copper body (diameter = 1 in. (25.4 mm), length = 1 in. (25.4 mm)). The faces of the heat flux transducers were coated with high-temperature optical black paint. The radiometers had permanent sapphire windows (view-angle = 150°; optical transmittance range 0.4 to 4.2 μm). Both transducers were calibrated to 100 kW/m^2 at a reference temperature of 25°C.

The PC-based data system used to acquire data from the thermocouples (**APPENDIX C**) also was used to acquire data from the heat flux transducers and radiometers. The electrical signal wires from these transducers terminated in a 5-pin circular connector (165 Series, Amphenol). Each connector was plugged into a panel-mounted jack, which was hard wired to an analog-input multiplex expansion card (DBK-12, IOTech, Inc., Cleveland, OH). As with the thermocouples, the electrical shields on the signal cables were connected to the electronic chassis grounds on the analog-input expansion cards. The data acquisition software (DASYLab) was configured to sample each channel at a rate of 10 Hz and store the data in 10-point block averages.

Figures F1 and F2 show the approximate locations of heat flux transducer/radiometer assemblies in the test vehicle.

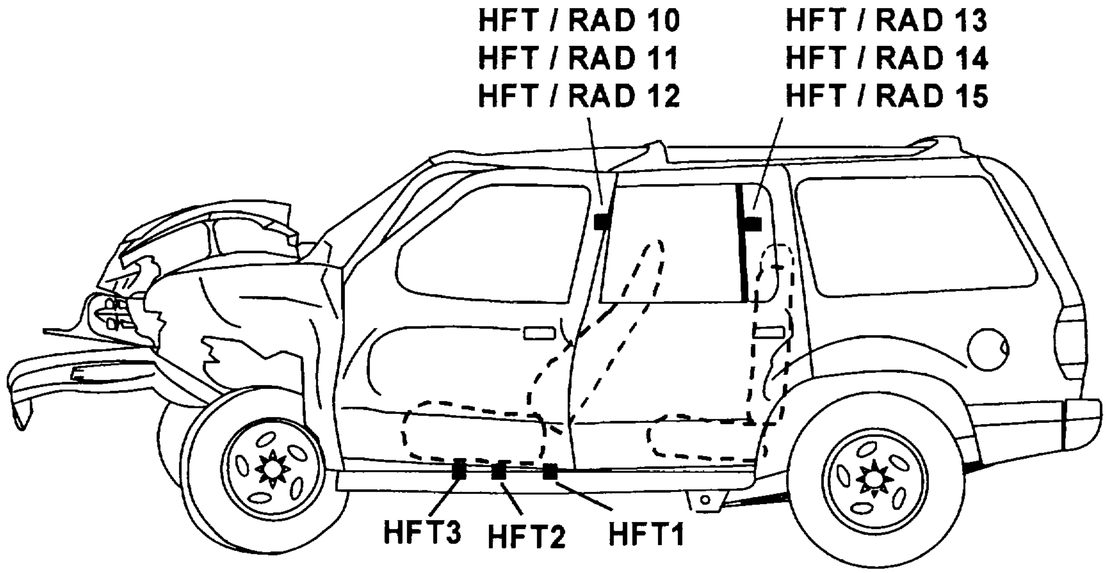

Figure F1. Fire Test F980611. Side view of the test vehicle showing the approximate locations of heat flux transducer/radiometer (HFT/RAD) assemblies in the test vehicle.

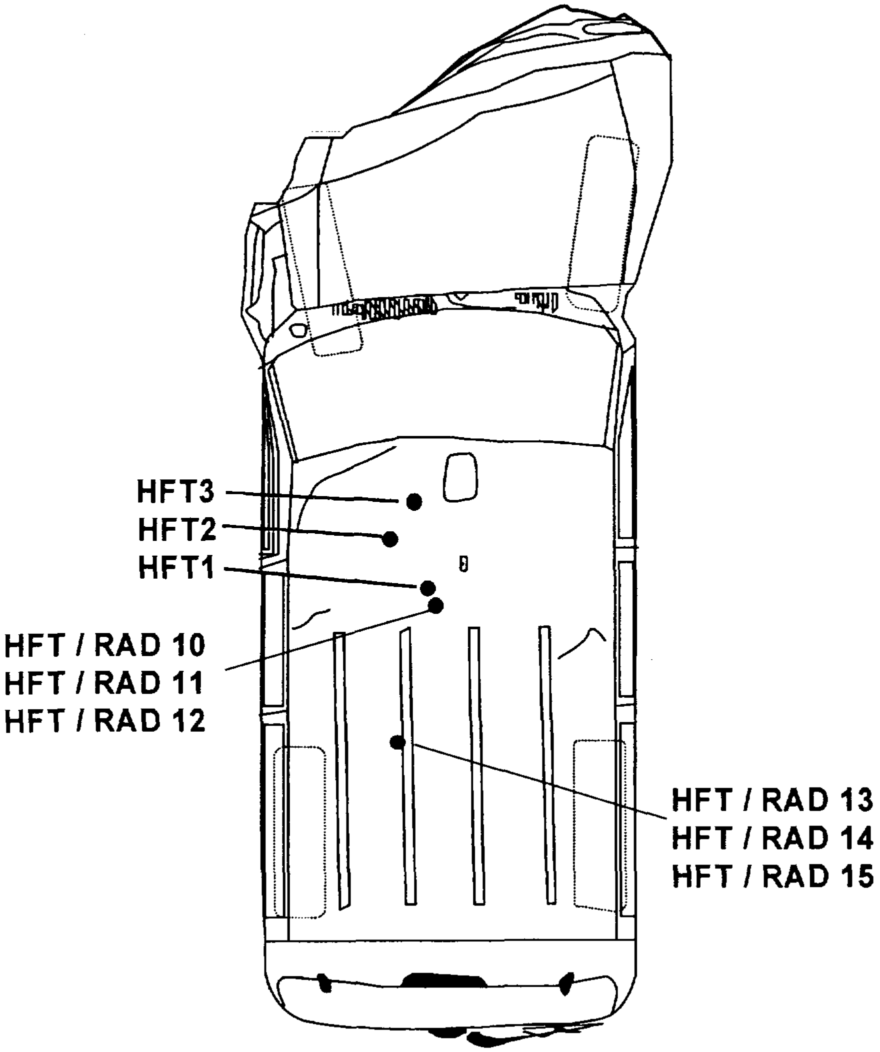

Figure F2. Fire Test F980611. Top view of the test vehicle showing the approximate locations of heat flux transducer/radiometer (HFT/RAD) assemblies mounted in the test vehicle.

Heat flux transducer assemblies mounted to floor panel were inserted into a clearance-hole that was drilled in the metal panel. The transducer was mounted on stand-offs so that the face of the transducer was flush with the exterior metal surface. Head flux transducer/radiometer assemblies located above the front and rear seats were mounted to threaded rods (diameter = ½ in.) inserted through holes drilled in the roof. The lower end of each rod was secured to the floor to stabilize the transducers during the test. Copper tubing (o.d. = 0.25 in. (6.4 mm)) was used for the cooling water supply and waste lines. The temperature of the water supplied to the HFT/RAD assemblies was approximately 80°C, and the flow rate of water through each body was approximately 100 mL/min.

Thermocouples F23, 002 and F15 were located in the bodies of each heat flux transducer or heat flux transducer/radiometer assemblies HFT1, HFT2 and HFT3 respectively. Thermocouples O10, O11, O12, O13, O14, and O15 were located in the bodies of each heat flux transducer or heat flux transducer/radiometer assemblies HFT/RAD10, HFT/RAD11, HFT/RAD12, HFT/RAD13, HFT/RAD14, and HFT/RAD15, respectively.

HTF/RAD10 were located approximately 30 cm above the left front seat cushion with the transducer surface oriented upward. HTF/RAD11 were located approximately 30 cm above the left front seat cushion with the transducer surface facing to the left. HTF/RAD12 were located approximately 30 cm above the left front seat cushion with the transducer surface oriented downward toward the foot area in front of the left front seat. HTF/RAD13 were located approximately 30 cm above the left rear seat cushion with the transducer surface facing the left. HTF/RAD14 were located approximately 30 cm above the left rear seat cushion with the transducer surface oriented upward. HTF/RAD15 were located approximately 30 cm above the left rear seat cushion with the transducer surface oriented forward.

Data recorded from these transducers is shown in Plots F1 through F15.

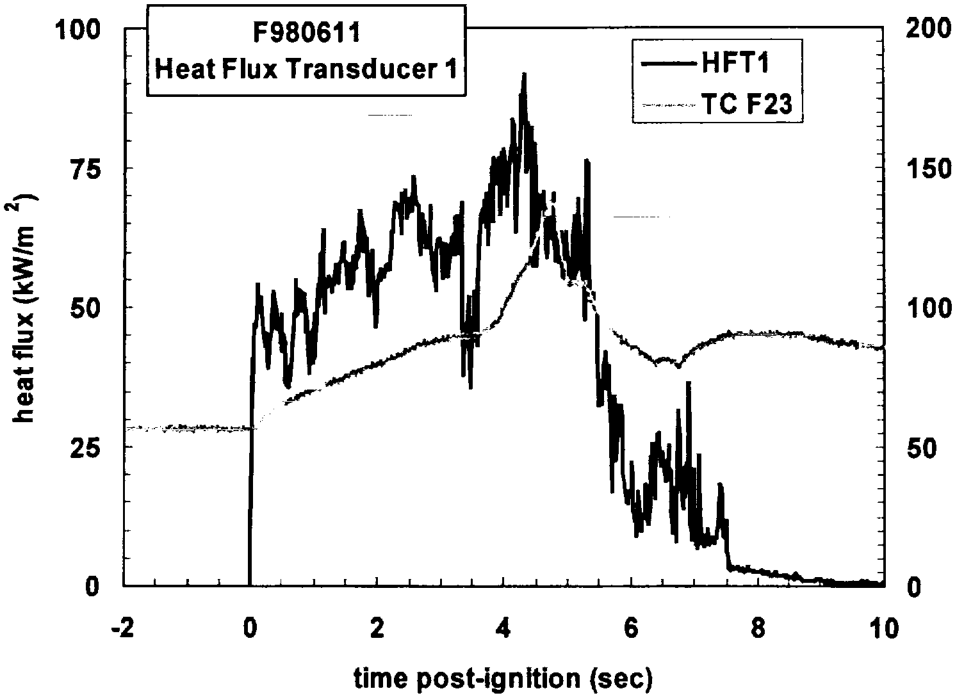

Plot F1. Fire Test F980611. Data plot from Heat Flux Transducer 1 and Thermocouple F23.

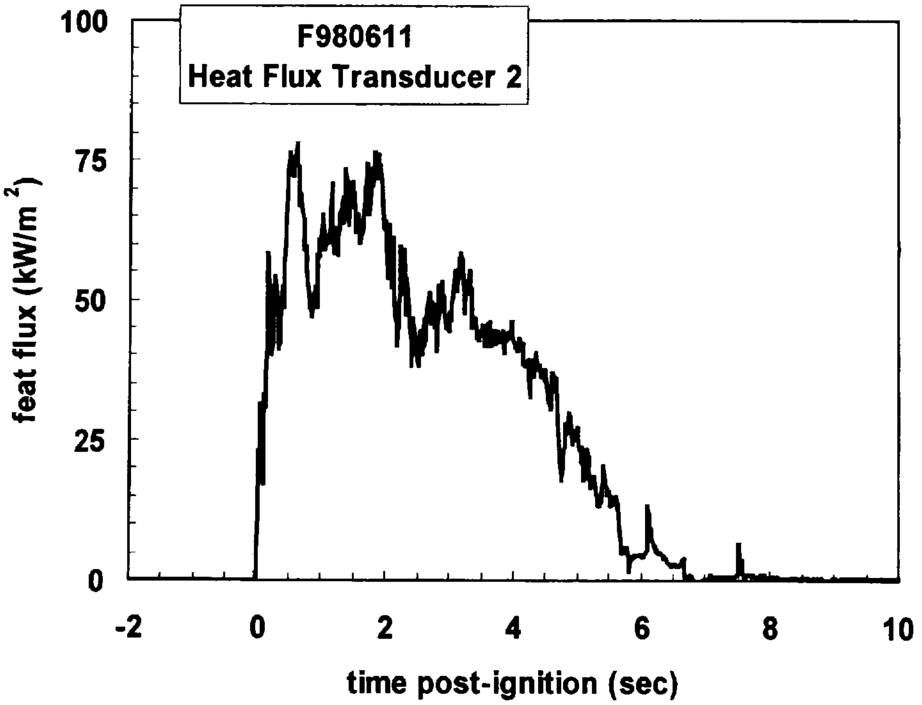

Plot F2. Fire Test F980611. Data plot from Heat Flux Transducer 2. No data was taken for Thermocouple 002.

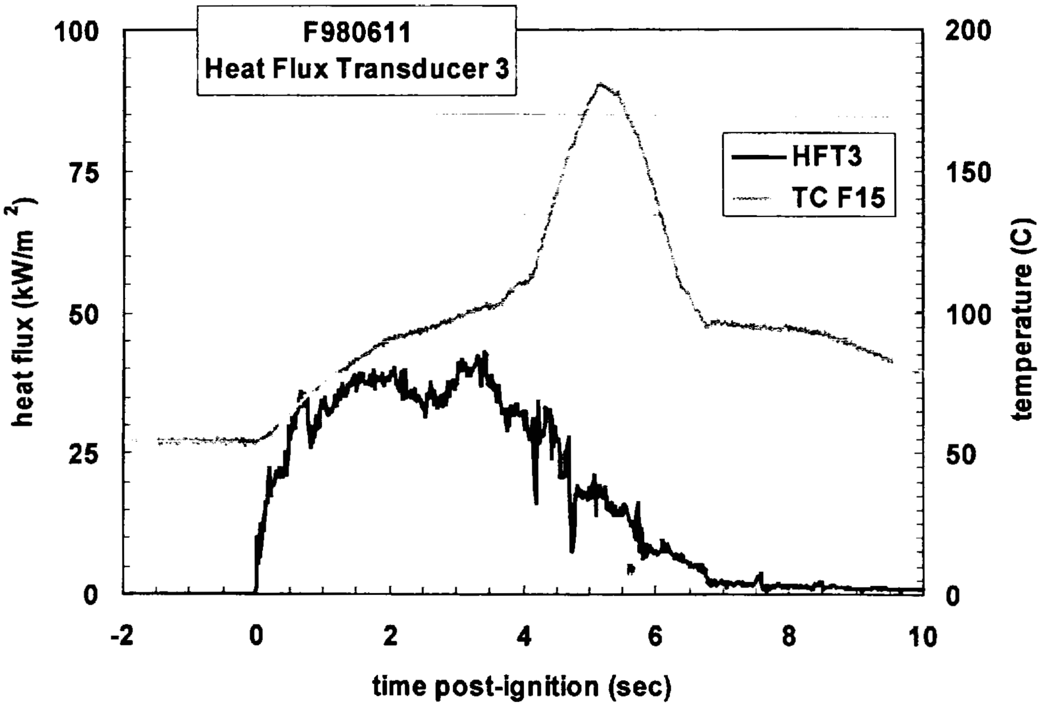

Plot F3. Fire Test F980611. Data plot from Heat Flux Transducer and Thermocouple F15.

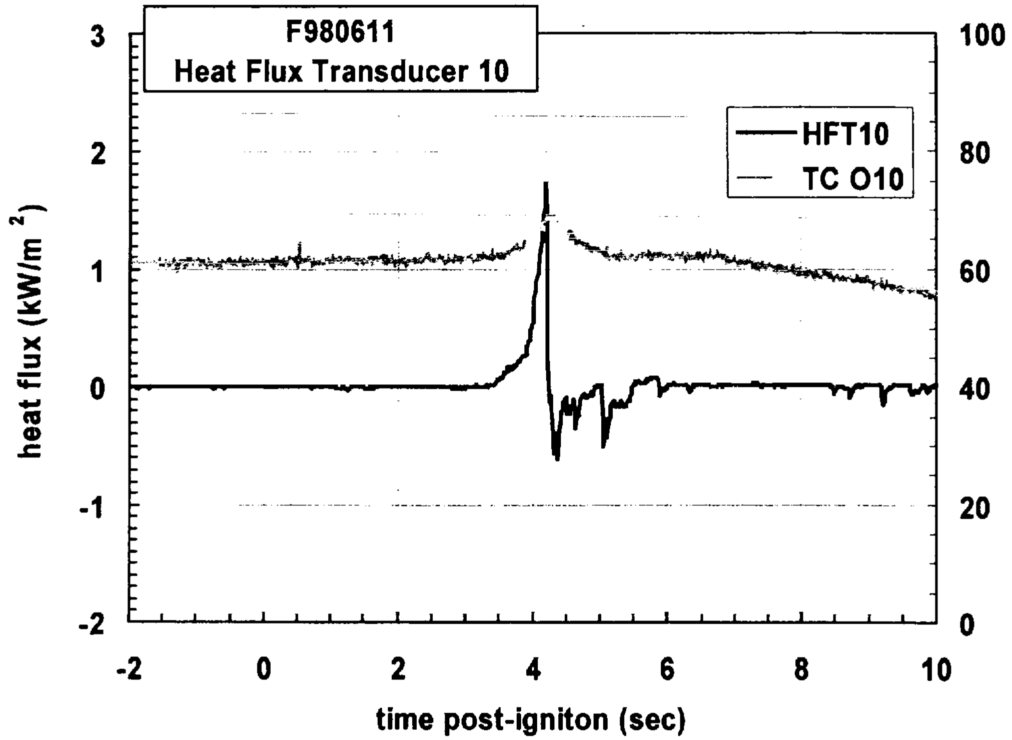

Plot F4. Fire Test F980611. Data plot from Heat Flux Transducer 10 and Thermocouple 010.

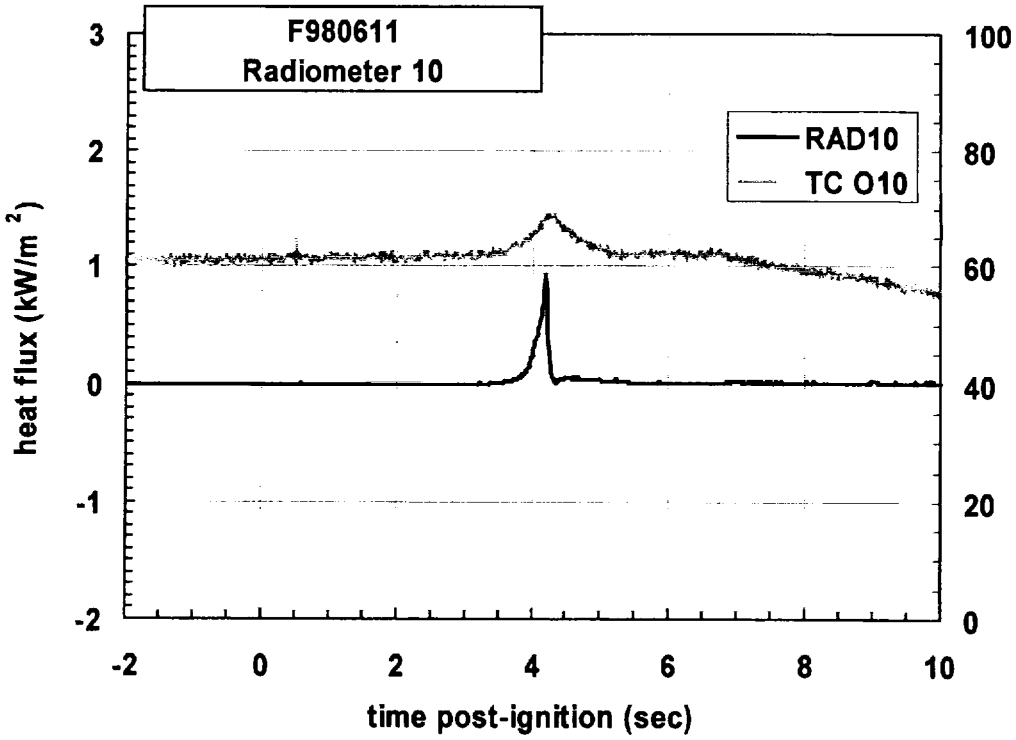

Plot F5. Fire Test F980611. Data plot from Radiometer 10 and Thermocouple 010.

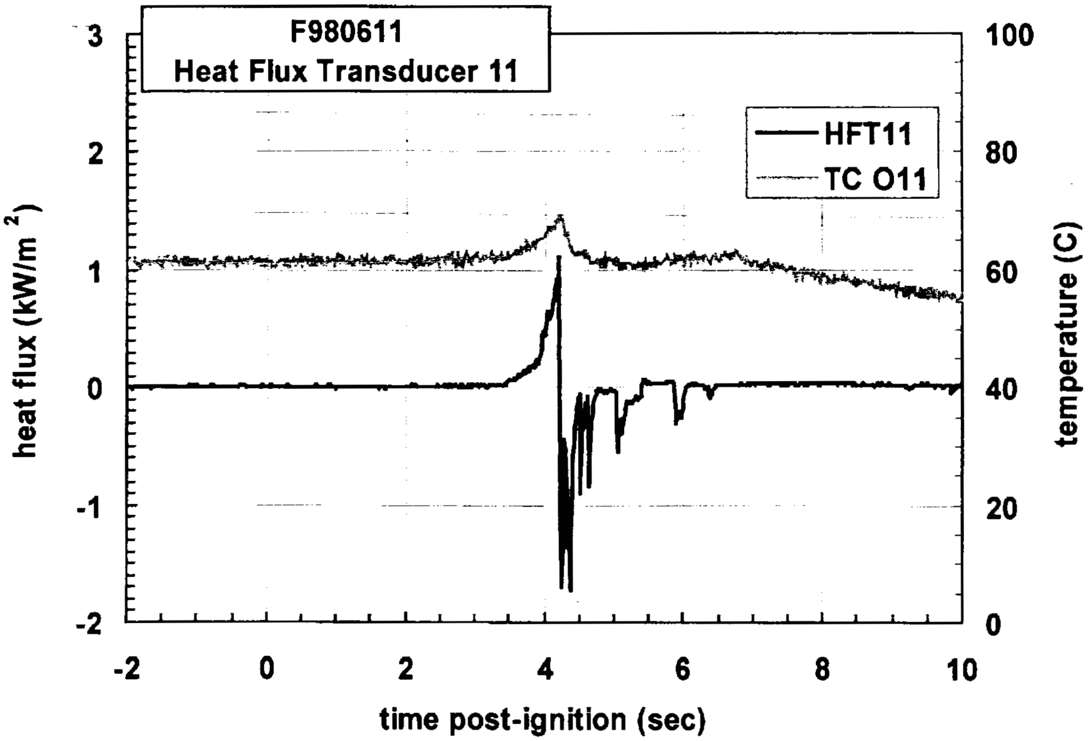

Plot F6. Fire Test F980611. Data plot from Heat Flux Transducer 11 and Thermocouple 011.

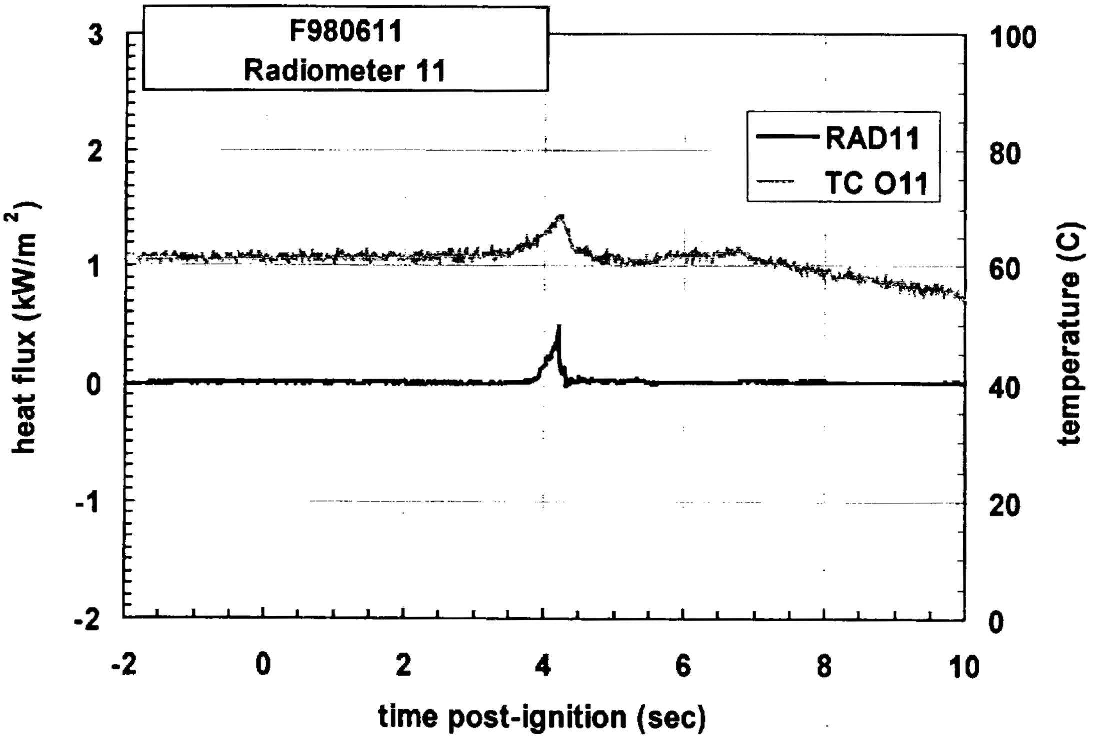

Plot F7. Fire Test F980611. Data plot from Radiometer 11 and Thermocouple 011.

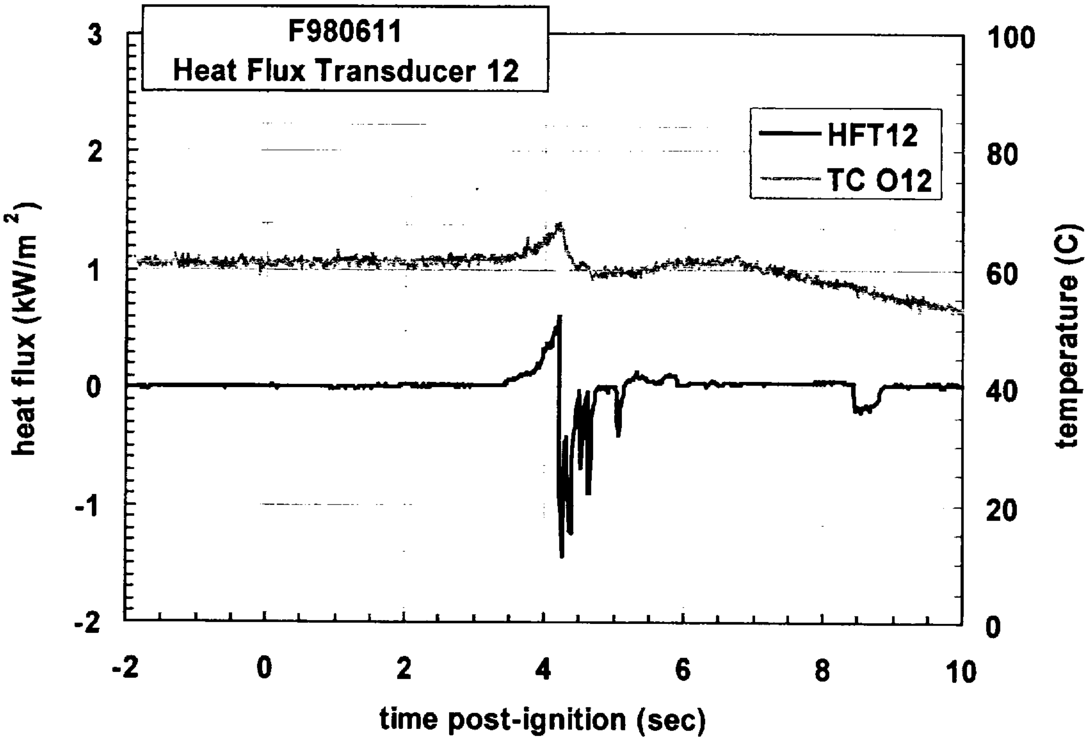

Plot F8. Fire Test F980611. Data plot from Heat Flux Transducer 12 Thermocouple 012.

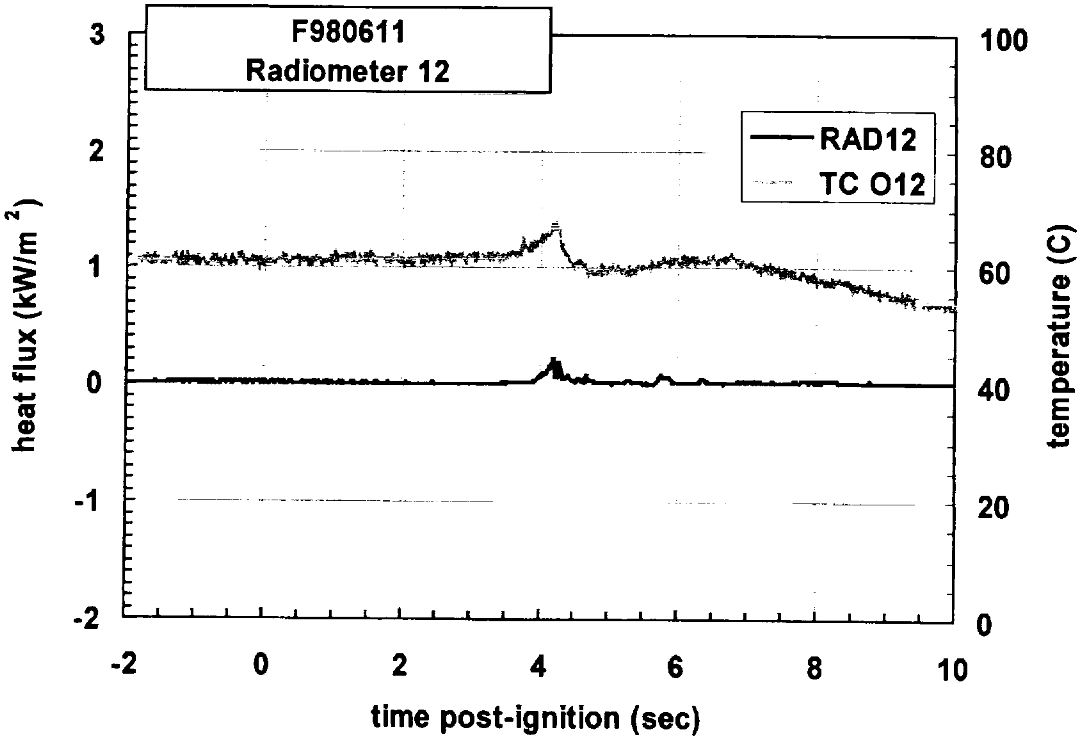

Plot F9. Fire Test F980611. Data plot from Radiometer 12 and Thermocouple 012.

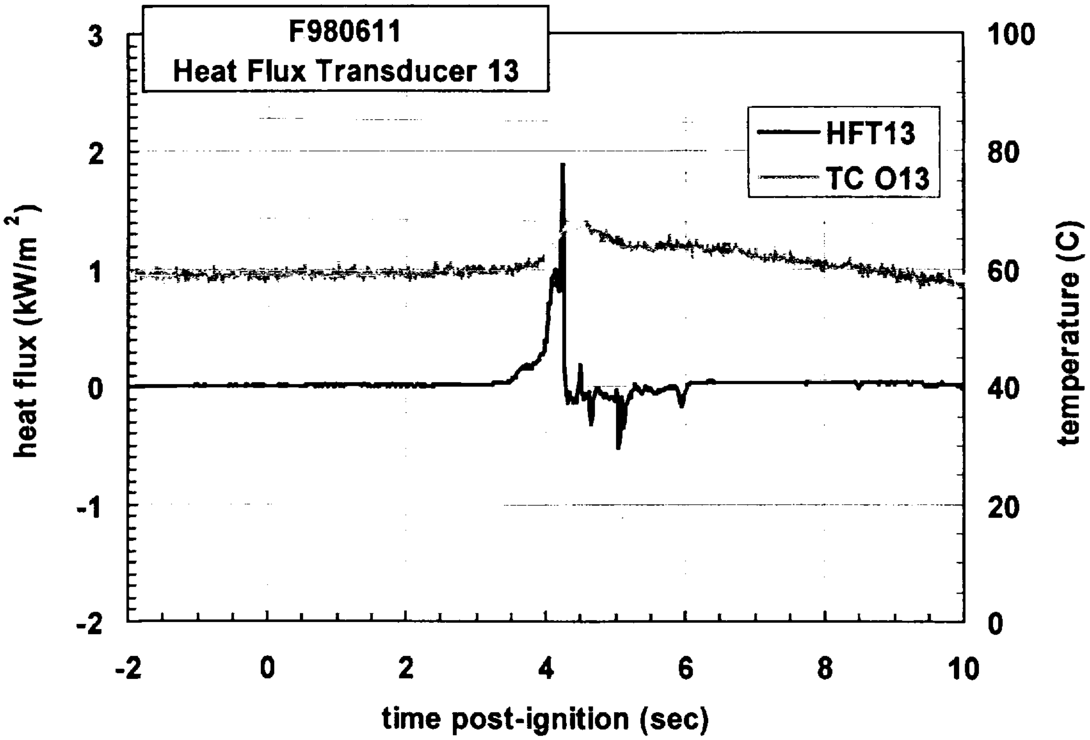

Plot F10. Fire Test F980611. Data plot from Heat Flux Transducer 13 and Thermocouple 013.

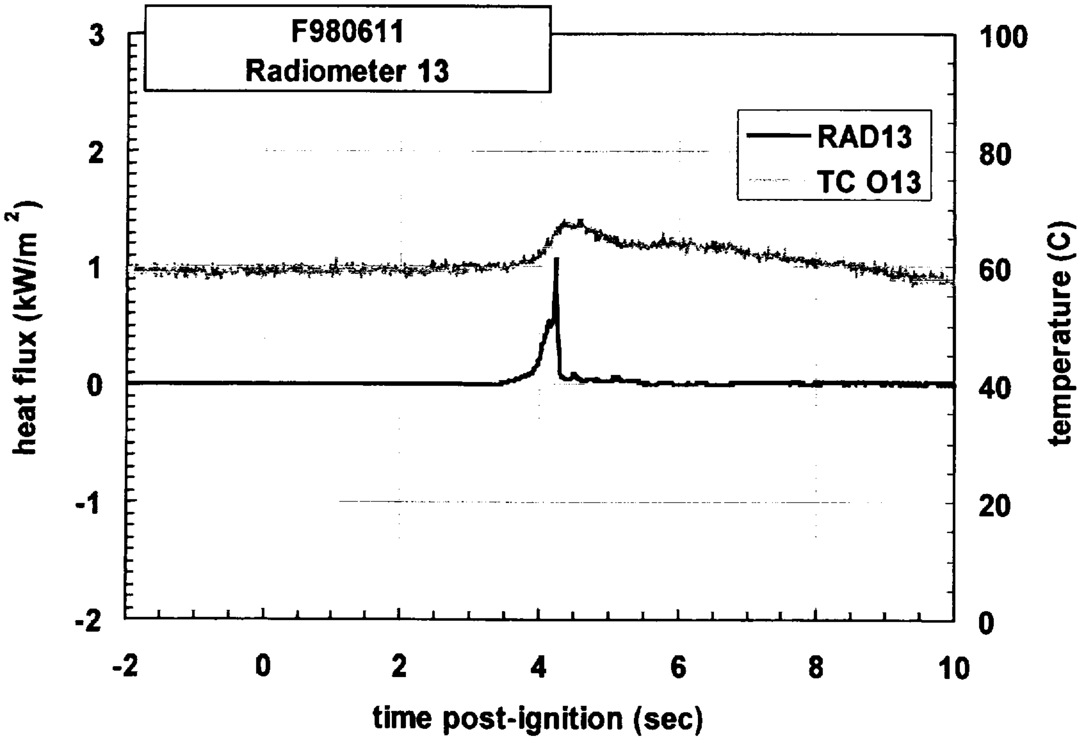

Plot F11. Fire Test F980611. Data plot from Radiometer 13 and Thermocouple 013.

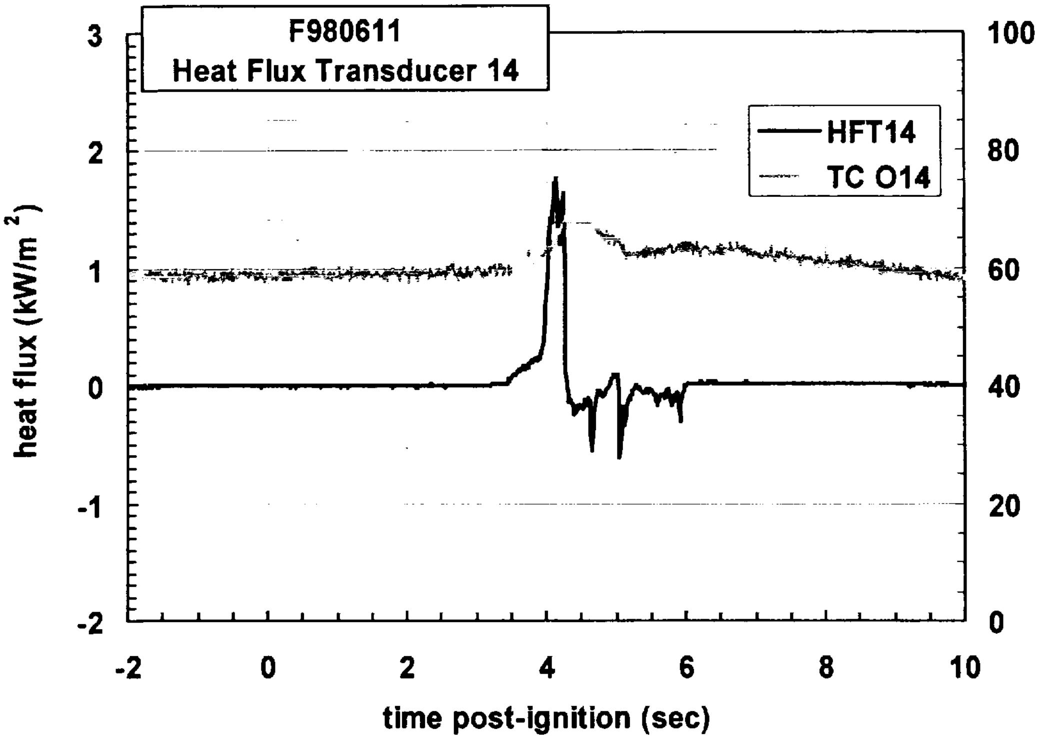

Plot F12. Fire Test F980611. Data plot from Heat Flux Transducer 14 and Thermocouple 014.

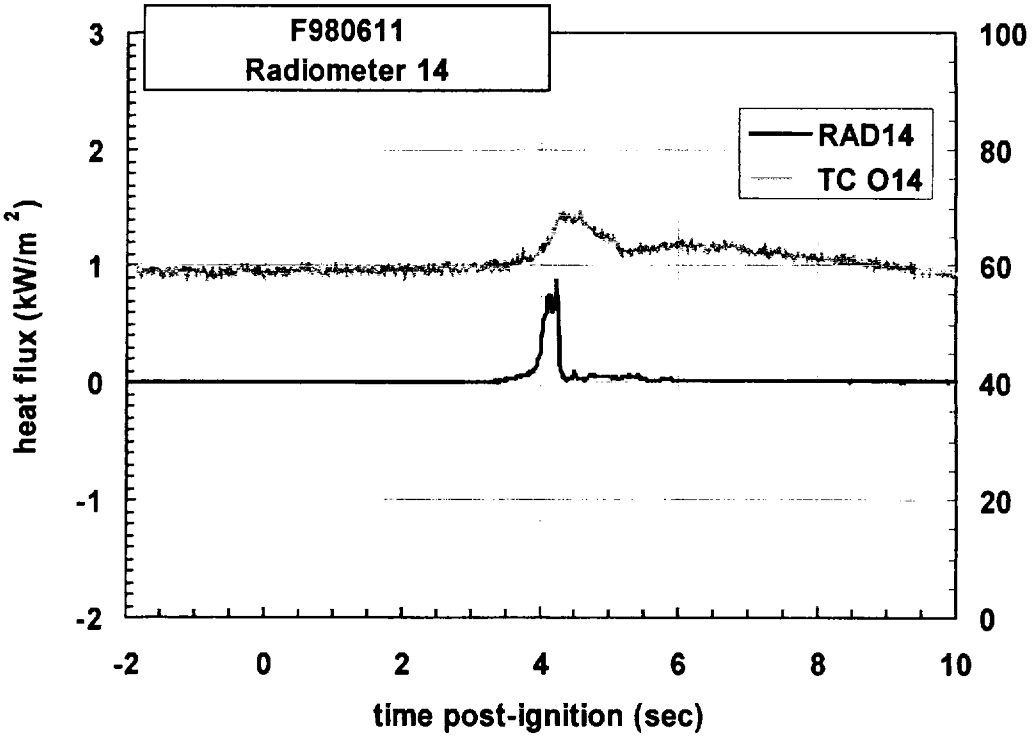

Plot F13. Fire Test F980611. Data plot from Radiometer 14 and Thermocouple 014.

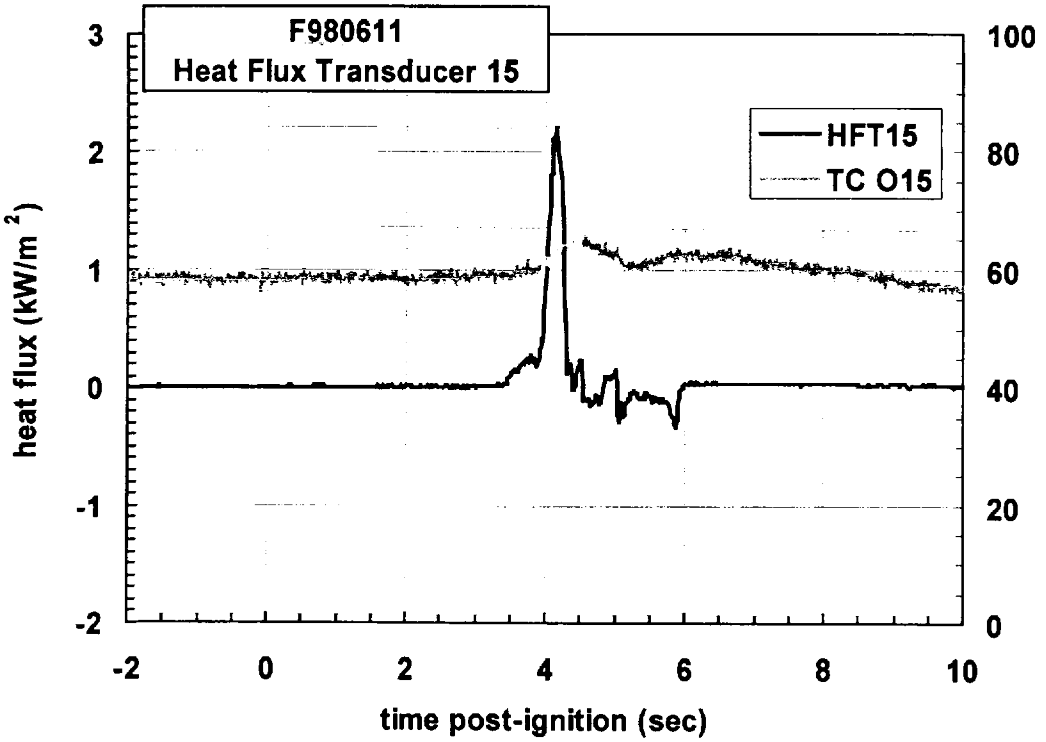

Plot F14. Fire Test F980611. Data Plot from Heat Flux Transducer 15 and Thermocouple 015

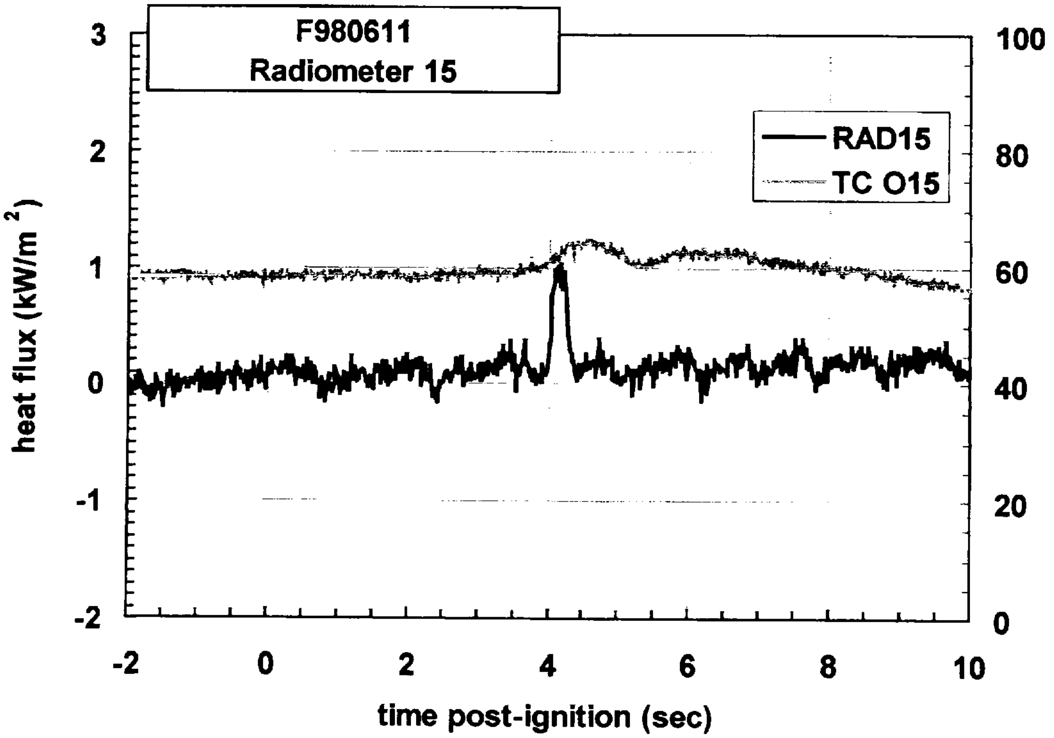

Plot F15. Fire Test F980611. Data Plot from Radiometer 15 and Thermocouple 015

APPENDIX G
PRESSURE AND AIRFLOW MEASUREMENTS

Figures G1 and G2 show the approximate locations of the pressure taps and bi-directional flow probe in the test vehicle.

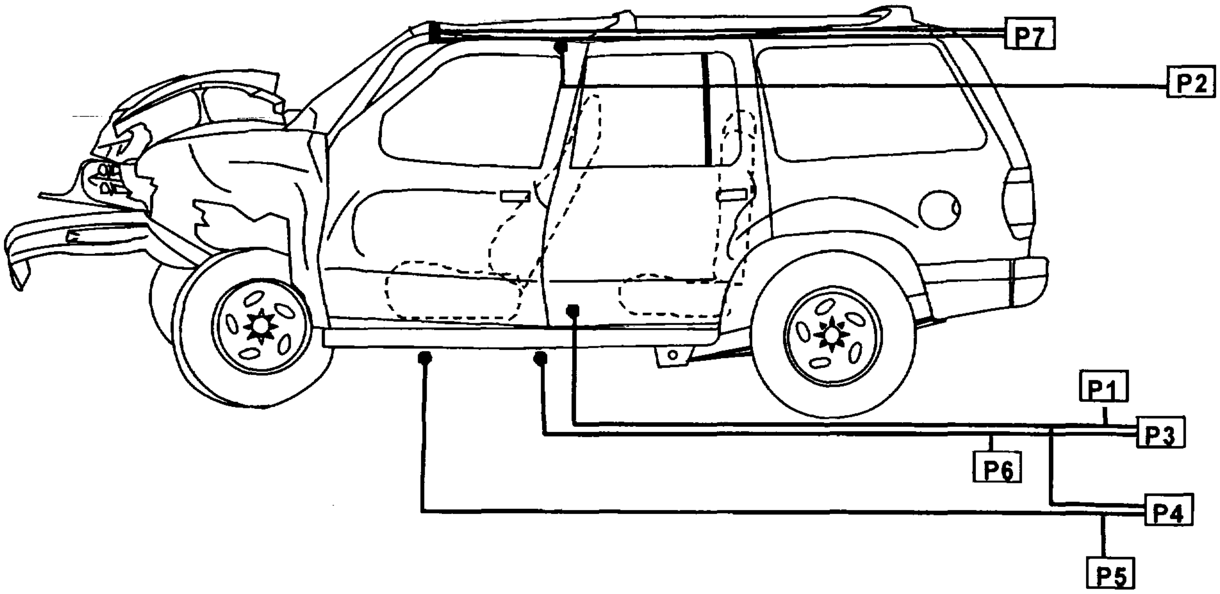

Figure G1. Fire Test F980611. Side view showing the approximate locations of the pressure taps and bi-directional flow probe in the test vehicle.

Four pressure taps were installed in the test vehicle for this test in the following locations: above the carpet in the foot area in front of the right rear seat, below the floor pan on the right side of the drive-line tunnel forward of the right front seat, below the floor pan on the right side of the drive-line tunnel rearward of the right front seat and below the headlining panel in the front compartment.

Each pressure tap was constructed from stainless steel tubing (o.d. = 0.250 in.). A union-T fitting with compression-type couplings (Parker) was attached to the inlet of the stainless steel tubing, with two of the three positions in the union-T fitting were left open. The other end of stainless steel tubing was connected to a pressure gauge with solvent-resistant flexible tubing (Tygon Masterflex® 6049; i.d. = 0.250 in.; o.d. = 0.438 in.). The total length of the stainless steel and flexible tubing was approximately 10 m.

A bi-directional flow probe was installed in the test vehicle so that it was located just outboard of the roof at the top of the center of the opening between the door frame and the roof. This probe was used to determine the velocity and direction of airflow through the opening during the test. The stainless steel tubes leading from the flow probe were connected to pressure gauges with solvent-resistant resistant flexible tubing (Tygon Masterflex® 6049; i.d. = 0.250 in.; o.d. = 0.438 in.). The total length of tubing was approximately 10 m.

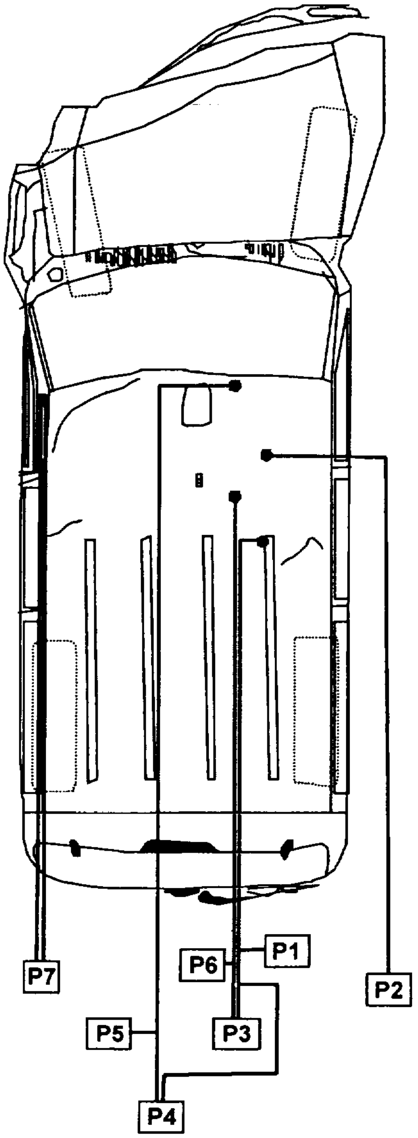

Figure G2. Fire Test F980611. Top view showing the approximate locations of pressure taps and bi-directional probe in the test vehicle.

The velocity of gas flow through the window opening in the driver's door was calculated from the pressure difference measured across the bi-directional probe using the following relationship:

$$V = 0.070\sqrt{T\Delta p} \tag{G1}$$

where V is the gas velocity in m/s, T is the gas temperature in degrees Kelvin, and Δp is the pressure difference in Pascals (N/m^2) [G1 and G2].

Pressure gauges (Model C-264, Setra Systems, Acton, MA) with two pressure ranges were used for this test: - 0.5 to 0.5 (± 0.0013) in. W.C. (-124.5 to 124.5 Pascal) and -0.1 to 0.1 (± 0.0003) in. W.C. (-24.9 to 24.9 Pascal). Both gauges were accurate to 0.25% full scale. The gages were powered with a 24 volt non-regulated power supply (Setra Systems). The high-pressure inlet of Pressure Gauge P1 was connected to the pressure tap located above the carpet in the foot area in front of the right rear seat, and its low-pressure inlet was left open to atmosphere. The high-pressure inlet of Pressure Gauge P2 was connected to the pressure tap located below the headlining panel in the front compartment, and its low-pressure inlet was left open to atmosphere. The high-pressure inlet of Pressure Gauge P3 was connected to the pressure tap located below the floor pan on the right side of the drive-line tunnel rearward of the right front seat. The low-pressure inlet of Pressure Gauge P3 was connected to the pressure tap located above the carpet in the foot area in front of the right rear seat. The high-pressure inlet of Pressure Gauge P4 was connected to the pressure tap located below the floor pan on the right side of the drive-line tunnel forward of the right front seat. The low-pressure inlet of Pressure Gauge P4 was connected to the pressure tap located above the carpet in the foot area in front of the right rear seat. The high-pressure inlet of Pressure Gauge P5 was to the pressure tap located below the floor pan on the right side of the drive-line tunnel forward of the right front seat, and its low-pressure inlet was left open to atmosphere. The high-pressure inlet of Pressure Gauge P6 was connected to the pressure tap located below the floor pan on the right side of the drive-line tunnel rearward of the right front seat, and its low-pressure inlet was left open to atmosphere. Pressure Gauge P7 was to both sides of the bi-directional flow probe.

The PC-based data acquisition system described in **APPENDIX C** also was used to record the electronic signals from the pressure gauges during the test. The signal leads from the pressure gauges were plugged into panel-mounted connectors, which were hard-wired to a low-gain analog-input multiplex expansion card (DBK12, IOTech). The analog-input expansion card was interfaced to the main A/D card in the PC. The signal from each pressure gauge was sampled at a rate of 100 Hz. The analog data was stored to a data file in 100-point block-averages so that the effective sampling rate during the test was 1 Hz.

Plots of the pressures recorded with Pressure Gauges P1 through P7 are shown in Plots G1 through G7. Steam generated by the start of fire suppression caused the positive- and negative-going pressure deflections starting at about 255 seconds post-ignition.

REFERENCERS

G1. N. R. Keltner and J. L. Moya. Defining the thermal environment in fire tests. *Fire and Materials* **14**: 133-138, 1989.

G2. B. J. McCaffrey and G. A. Heskestad. Robust bidirectional low-velocity probe for flame and fire application. *Combustion and Flame* **26**: 125-127, 1976.

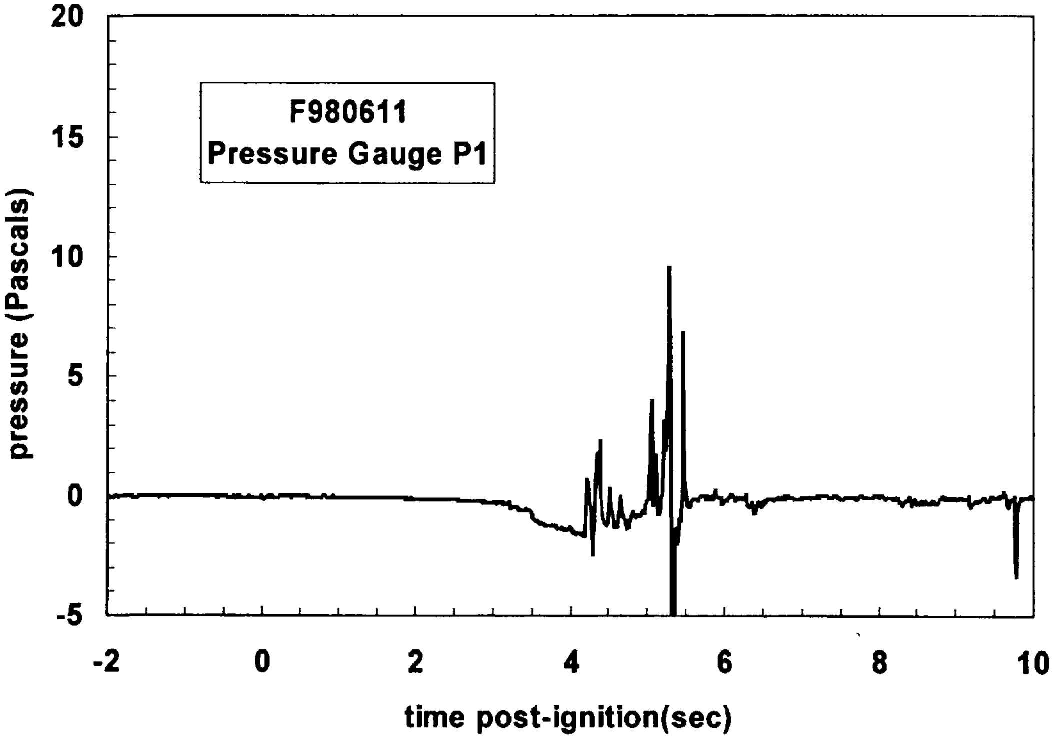

Plot G1. Fire Test F980611. Pressure above the carpet in the foot area in front of the right rear seat relative to atmospheric pressure measured with pressure gauge P1.

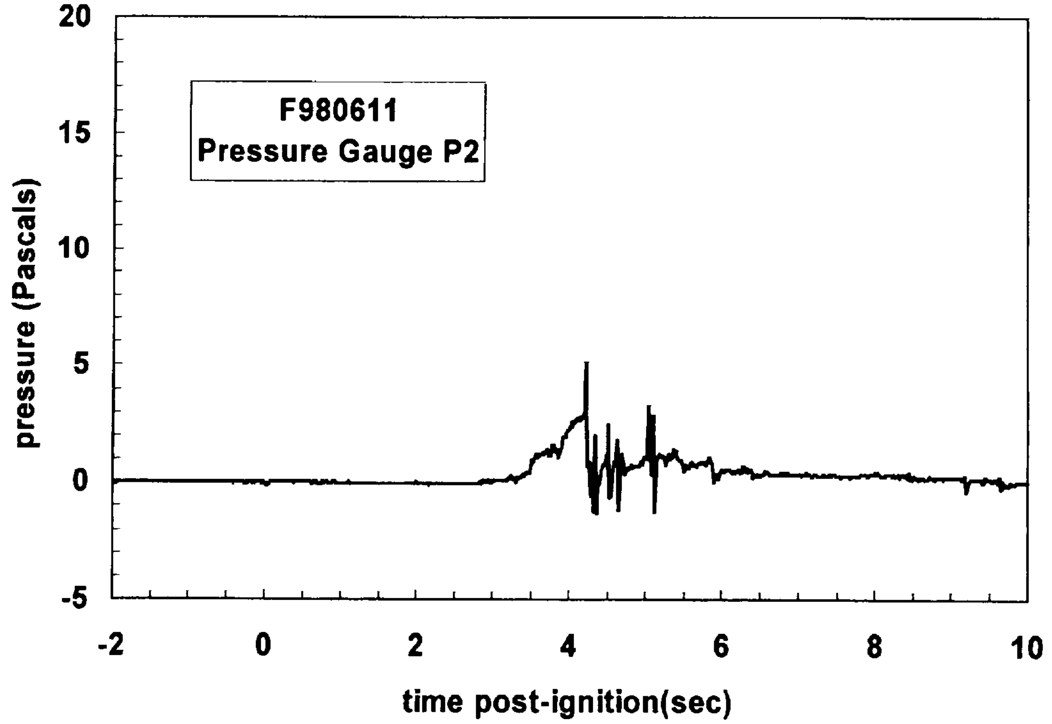

Plot G2. Fire Test F980611. Pressure below the headlining panel in the front compartment relative to atmospheric pressure measured with pressure gauge P2.

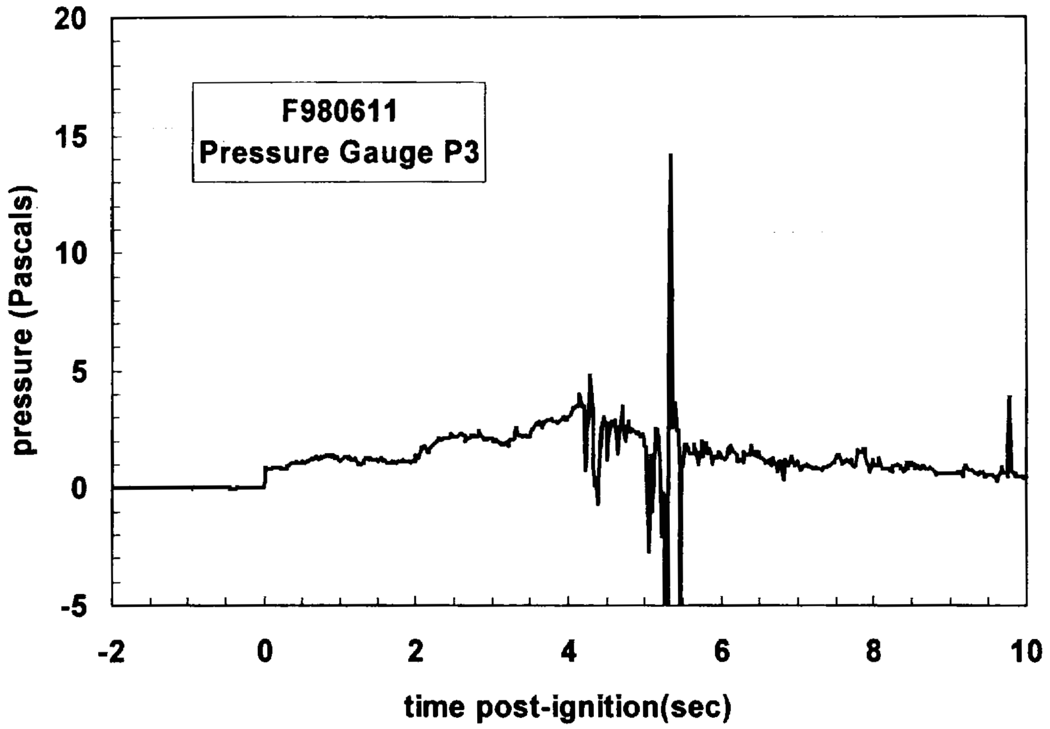

Plot G3. Fire Test F980611. Pressure difference between the foot well in front of the right rear seat and below the floor pan on the right side of the drive line tunnel rearward of the front seat measured with P3.

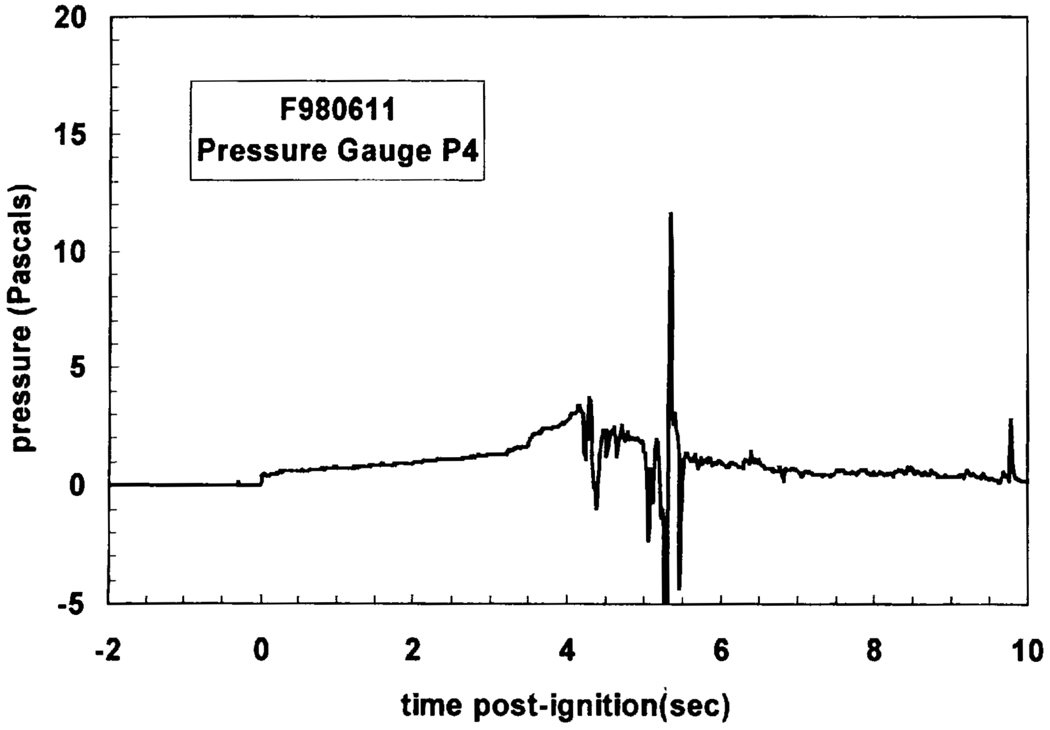

Plot G4. Fire Test F980611. Pressure difference between the foot well in front of the right rear seat and below the floor pan on the right side of the drive line tunnel forward of the front seat measured with P4.

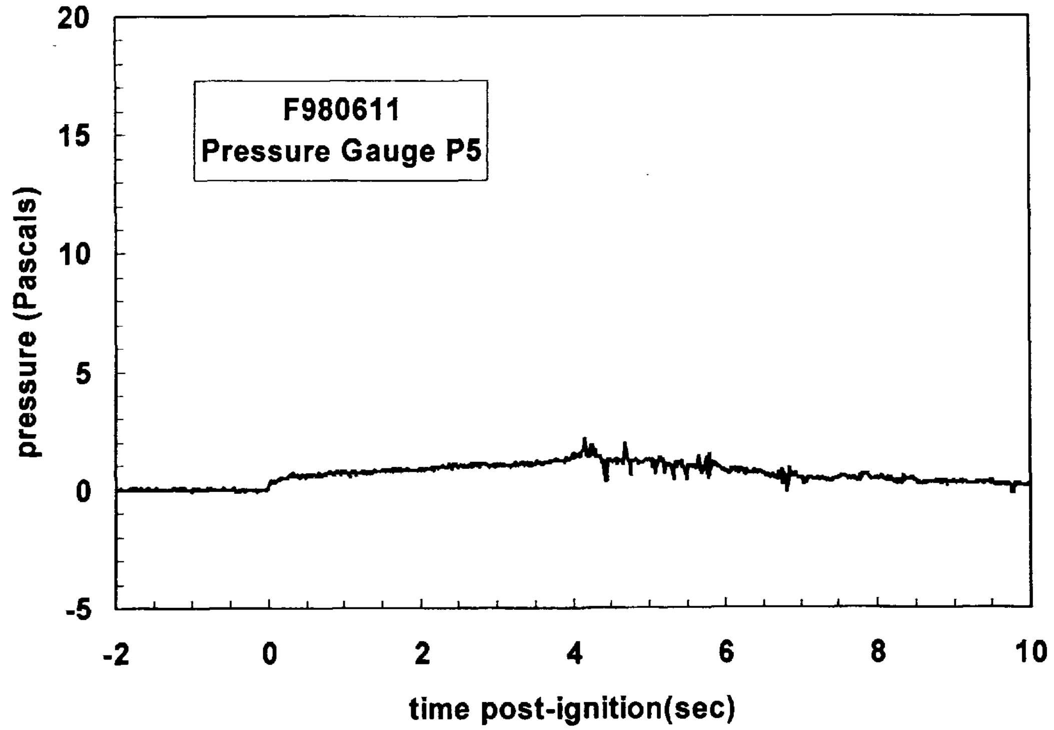

Plot G5. Fire Test F980611. Pressure below the floor pan on the right side of the drive-line tunnel forward of the front seat relative to atmospheric pressure measured with P5.

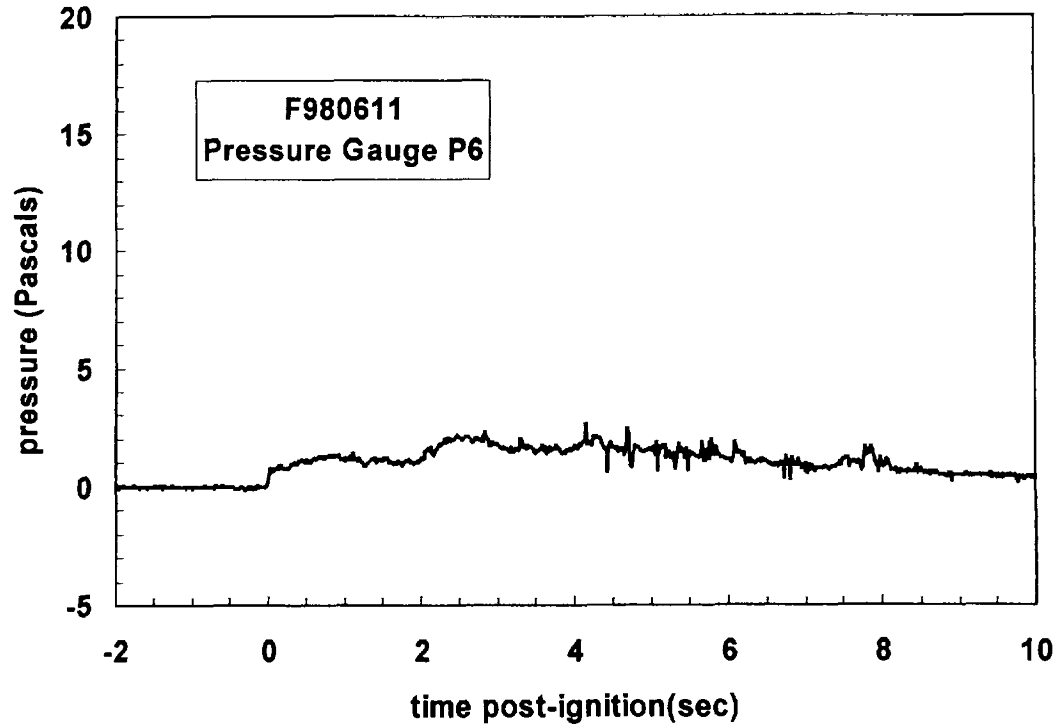

Plot G6. Fire Test F980611. Pressure below the floor pan on the right side of the drive-line tunnel rearward of the front seat relative to atmospheric pressure measured with P6.

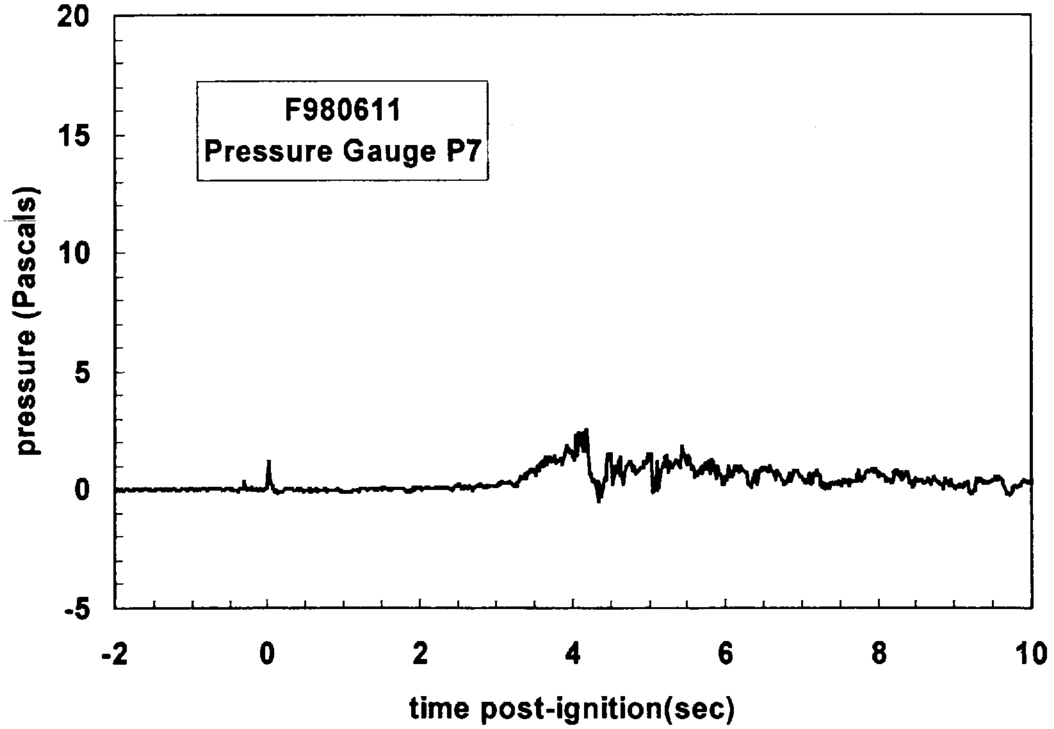

Plot G7. Fire Test F980611. Pressure difference across the bi-directional flow probe measured with P7.

APPENDIX H
FIRE PRODUCTS COLLECTOR DATA

Scientific and technical personnel from Factory Mutual Research Corporation were primarily responsible for obtaining and analyzing data from the Fire Products Collector (FPC) at the Factory Mutual Test Center.

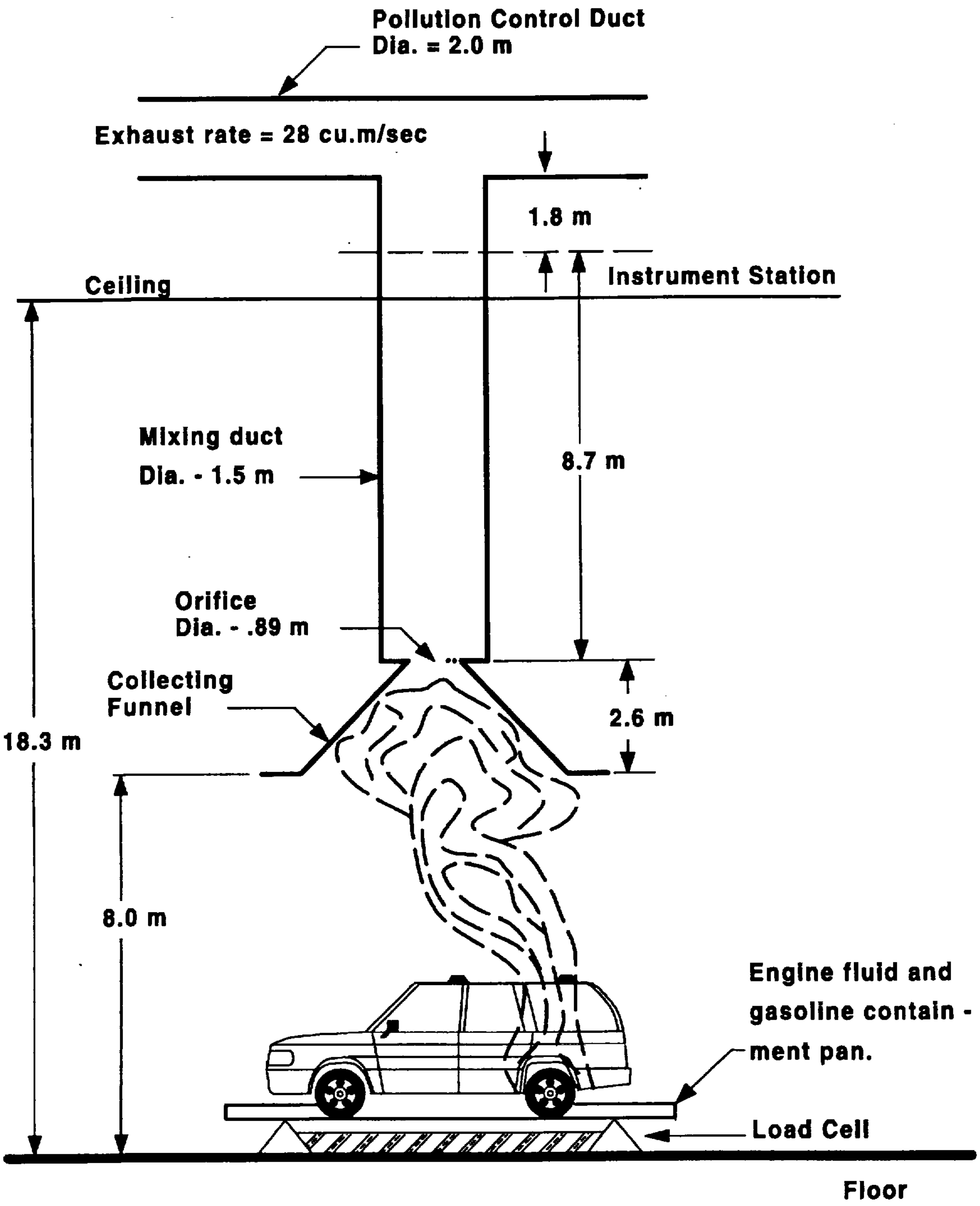

Figure H1. Fire Test F980609. Diagram of the test vehicle under the fire products collector at the Factory Mutual Test Center.

A fire products collector was used to measure heat and combustion gases generated by the burning vehicle during this test (Fig. H1). The fire products collector consisted of a collection funnel (diameter = 6.1 m), an orifice plate (hole = 0.9 m), and a vertical stainless steel sampling duct (diameter = 1.5 m). The sampling duct was connected to the air pollution control system of the Test Center. The blower of the air pollution control system induces gas flow through the sampling duct. Air enters the sampling duct via the orifice plate. The temperature, linear velocity, optical transmission, and chemical composition of the entrained gas were measured in the center of the sampling duct 8.66 m (5.7 duct diameters) downstream from the orifice plate, ensuring a flat velocity profile at the sampling location. The data acquisition system consisted of a Hewlett Packard 2313B analog-to-digital conversion sub-system interfaced to a Hewlett Packard 1000 computer.

Gas temperature in the sampling duct was measured with two Type-K thermocouples (30 gage) with exposed bead-type junctions. The thermocouple leads were housed in stainless steel tubes (o.d. = 6.4 mm). Ambient air temperature in the facility was measured by five Type-K thermocouples attached to the external surface of the duct at 2.44, 5.49, 9.14, 12.8, and 15.9 m above the floor. These thermocouples were shielded from radiation from the fire.

The linear velocity of the gas entrained in the sampling duct was measured with a Pitot ring consisting of four Pitot tubes. A static pressure tap was mounted on the inside wall of the sampling duct. The pressure difference between the Pitot ring and the static wall tap was measured with an electronic manometer (Barocel Model 1173, CGS Scientific Corporation).

The particulate concentration in the entrained air was determined from the optical transmission across the duct measured at 0.4579 μm (blue), 0.6328 μm (red), and 1.06 μm (infrared). The optical path length across the duct was 1.524 m. Gas was withdrawn from the sampling duct through a stainless steel tube (o.d. = 3.9 mm) at a flow rate of 0.17×10^{-3} m^3/s for chemical analysis. The gas flowed through a particulate filter, a water condenser, and a drying agent before entering the analyzers. Carbon dioxide (CO_2) and carbon monoxide (CO) were measured with two dedicated non-disperse infrared analyzers (Beckman Model 864 Infrared Analyzers). Oxygen (O_2) was measured with a paramagnetic oxygen analyzer (Beckman Model 755 Paramagnetic Oxygen Analyzer). Total gaseous hydrocarbons were measured with a flame ionization analyzer (Beckman Model 400 Flame Ionization Analyzer).

The rate of product release was calculated using the following relationship:

$$\left(\frac{dR_j}{dt}\right) = f_j\left(\frac{dV}{dt}\right)\rho_j = f_j\left(\frac{dW}{dt}\right)\left(\frac{\rho_j}{\rho_g}\right) \qquad \text{(H1)}$$

where $d(R_j)/dt$ is the mass release rate of product j in kg/s; f_j is the volume fraction of product j; dV/dt is the total volume flow rate of the gas entrained in the sampling duct in m^3/s; dW/dt is the total mass flow rate of the gas entrained in the sampling duct in kg/s; ρ_j is the density of product j in g/m^3; and ρ_g is the density of the gas entrained in the concentration measurements. The rate of oxygen consumption was calculated using equation (H1), where the volume fraction of oxygen consumed was substituted for f_j.

The volume fraction of smoke particulate was calculated from the following relationship:

$$f_s = \frac{D\lambda \times 10^{-6}}{\Omega} \qquad \text{(H2)}$$

where f_s is the volume fraction of smoke, λ is the wavelength of the light source, Ω is the extinction coefficient of particulate (a value of 0.7 was used in these calculations), and D is the optical density at each of the three wavelengths at which measurements were made:

$$D = \frac{\ln\left({}^{I_0}/_{I}\right)}{L} \qquad \text{(H3)}$$

where I_0 is the intensity of light transmitted through clean air, I is the intensity of light transmitted through air containing smoke particulate, and L is the optical pathlength, which was equal to 1.524 m. A value of 1.1×10^6 g/m^3 was used for the density of smoke particulate (ρ_j) in equation (H1).

The convective heat release rate was calculated using the following relationship:

$$\left(\frac{dE_{conv}}{dt}\right) = \left(\frac{dW}{dt}\right) \times c_p \times \left(T_g - T_a\right) \qquad \text{(H4)}$$

where $d(E_{conv})/dt$ is the convective heat release rate in kW; dW/dt is the mass flow rate of the gas entrained in the sampling duct in kg/s; c_p is the heat capacity of the gas entrained in the sampling duct at the gas temperature in kJ/(kg×K); T_g is the temperature of the gas entrained in the sampling duct in K; and T_a is the ambient air temperature in K.

The chemical heat release rate was calculated from the release rates of carbon dioxide and carbon monoxide as follows:

$$\left(\frac{dE_{ch}}{dt}\right) = \Delta H^{*}_{CO_2} \times \left(\frac{dR_{CO_2}}{dt}\right) + \Delta H^{*}_{CO} \times \left(\frac{dR_{CO}}{dt}\right) \qquad \text{(H5)}$$

where $d(E_{ch})/dt$ is the chemical heat release rate in kW; ΔH^* is the net heat of complete combustion per unit mass of carbon dioxide or carbon monoxide released in the fire in kJ/g; and dR/dt is the mass release rate of carbon dioxide or carbon monoxide in kg/s. Values of ΔH^* for carbon dioxide and carbon monoxide were obtained from the literature [H1 and H2].

The chemical heat release rate also was calculated from the oxygen consumption rate as follows:

$$\left(\frac{dE_{ch}}{dt}\right) = \Delta H^{*}_{O}\left(\frac{dC_{O}}{dt}\right) \qquad \text{(H6)}$$

where $d(E_{ch})/dt$ is the chemical heat release rate in kW; ΔH^*_O is the net heat of complete combustion per unit mass of O_2 consumed in kJ/g; and $d(C_O)/dt$ is the consumption rate of oxygen in kg/s. The value for ΔH^*_O was obtained from the literature [H1 and H2].

The radiative heat release rate was the difference between the chemical heat release rate and the convective heat release rate:

$$\left(\frac{dE_{rad}}{dt}\right) = \left(\frac{dE_{ch}}{dt}\right) - \left(\frac{dE_{conv}}{dt}\right) \qquad \text{(H7)}$$

where $d(E_{rad})/dt$ is the radiative heat release rate; and $d(E_{ch})/dt$ is the average chemical heat release rate calculated using equations (H5) and (H6).

The vehicle was placed in a rectangular steel pan (length = 25 ft., width = 15 ft., height = 4 in.) to prevent spilled and leaking automotive fluids from spreading in the test facility. This fluid containment pan was fabricated from two sheets of carbon steel. Angle-braces were welded to the under-side of the pan to keep it from flexing under the weight of the vehicle. The corners of the support frame rested on load cells. Mass loss was determined from data acquired from the load cells during the test.

The fluid containment pan was lined with a layer of fiberglass-reinforced cement construction board (DuraRock, USG Corporation). A thin layer of sand was used to level the concrete board so that the grade of the surface measured from the center to the edges along the major and minor axes was no greater than 1%. The joints between boards were sealed with latex caulking.

Mass loss from the burning vehicle and any burning fluids retained by the containment pan was measured with a load cell weigh-module system. The fluid containment pan was supported by an I-beam frame a load cell weight-module (KIS Series, BLH Electronics, Inc.) at each corner. These weight-modules contain cylindrical, double cantilever strain gauge transducers that are not generally affected by changes in mass distribution. The weight-module system was calibrated before this test by placing a series of standard weights on the fluid containment pan.

Data from the fire-products collector and load cell weight-module system are shown in Plots H1 through H5. The Fire Products Collector did not detect a fire plume until approximately 30 seconds after the gasoline was ignited. The heat release rate curve showed two upward deflections (Plot H1). The first occurred between 0 and 1 minutes post-ignition and coincided with ignition and steady-state combustion of the liquid gasoline pumped onto the test vehicle. The second started at about 2 minutes post-ignition and continued until the fire was extinguished. This coincided with ignition of combustible materials in the test vehicle. The heat release rate reached a maximum of approximately 475 kW at approximately 4½ minutes post-ignition. Trends in the carbon dioxide, carbon monoxide, and smoke release rate curves (Plots H2, H3, and H4, respectively) were similar to the heat release rate curve, showing an initial increase in the first minute of the test and a second occurring between 2 and 4½ minutes post-ignition. The maximum rate of carbon dioxide release measured during this test was 31.6 g/s (Plot H2). The maximum rate of carbon monoxide release measured during this test was 1.9 g/s (Plot H3). The maximum rate of smoke release measured during this test was 0.65 mg/s and occurred soon after fire suppression began (Plot H4). The mass loss curve indicated that approximately 5 kg of mass was lost from the test vehicle during this test (Plot H5). The resolution of the load cell system used to make the weight measurement was between 0.3 and 0.4 kg (between 6 to 8% of the total mass loss during the test), and was responsible for the high degree of scatter in the mass loss curve (Plot H5).

REFERENCES

H1. G. Heskestad. A Fire Products Collector for Calorimetry into the MW Range, Technical Report J.I. OC2E1.RA. Factory Mutual Research Corporation, Norwood, MA. June, 1981.

H2. Archibald Tewarson. "Generation of Heat and Chemical Compounds in Fires" Section 3/Chapter 4, SFPE Handbook of Fire Protection Engineering, 2nd Edition, 1995, pp. 3:53-124.

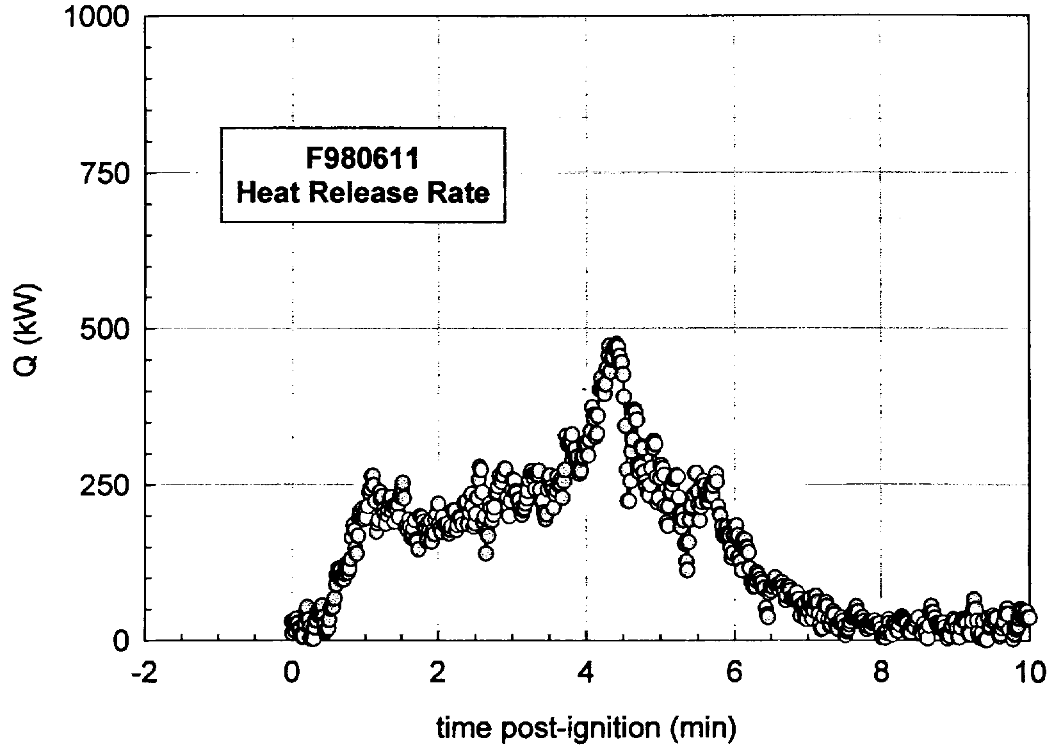

Plot H1. Fire Test F980611. Heat release rate measured using the Fire Products Collector.

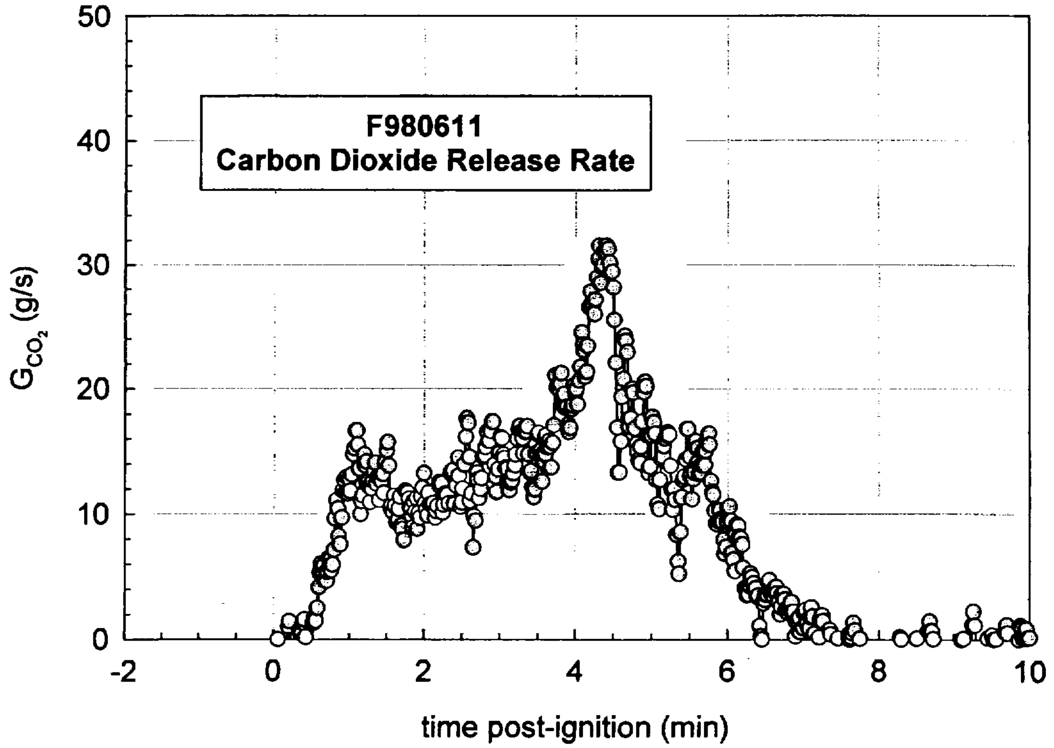

Plot H2. Fire Test F980611. Carbon dioxide release rate measured using the Fire Products Collector.

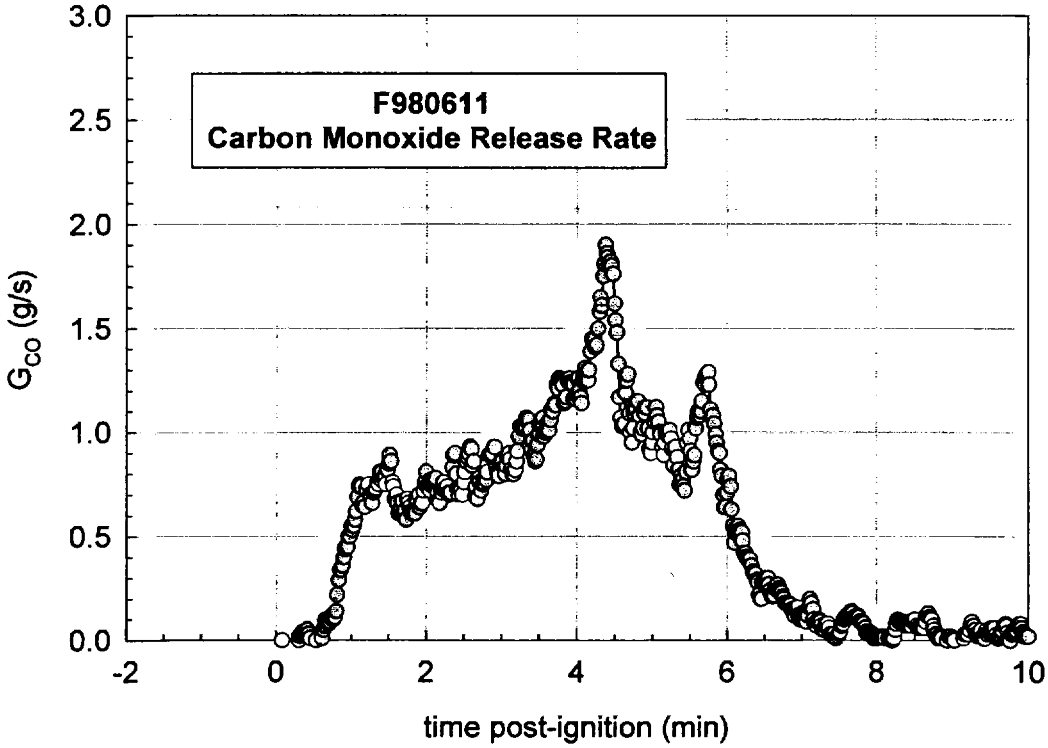

Plot H3. Fire Test F980611. Carbon monoxide release rate measured using the Fire Products Collector.

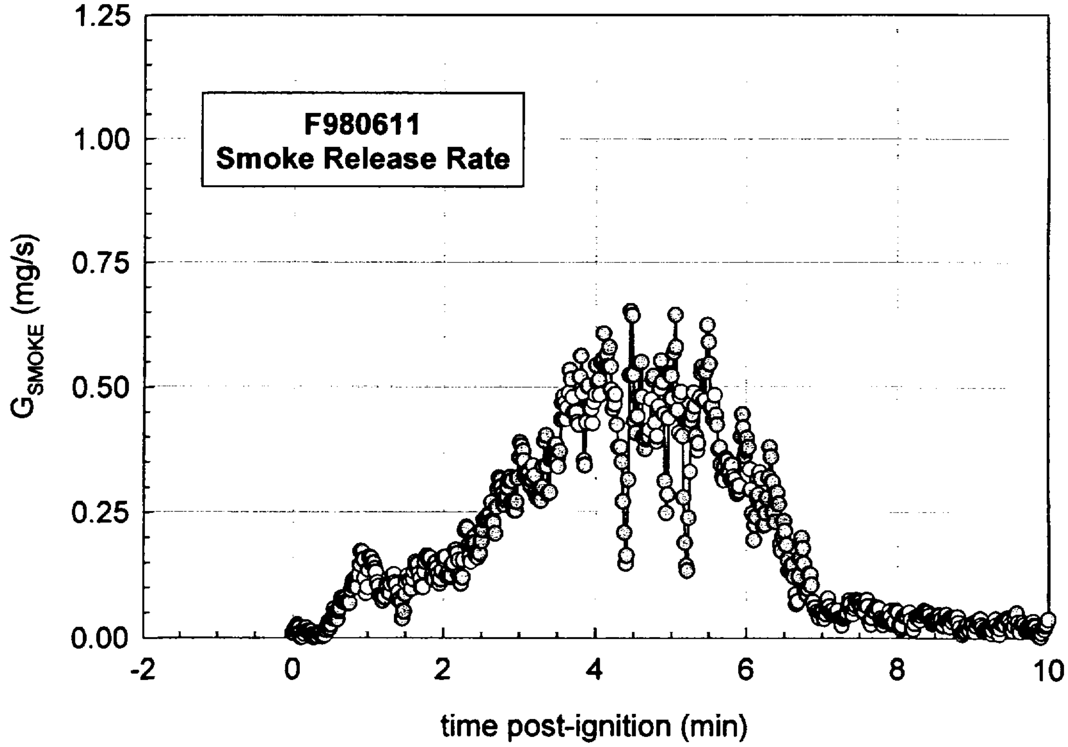

Plot H4. Fire Test F980611. Smoke release rate measured using the Fire Products Collector.

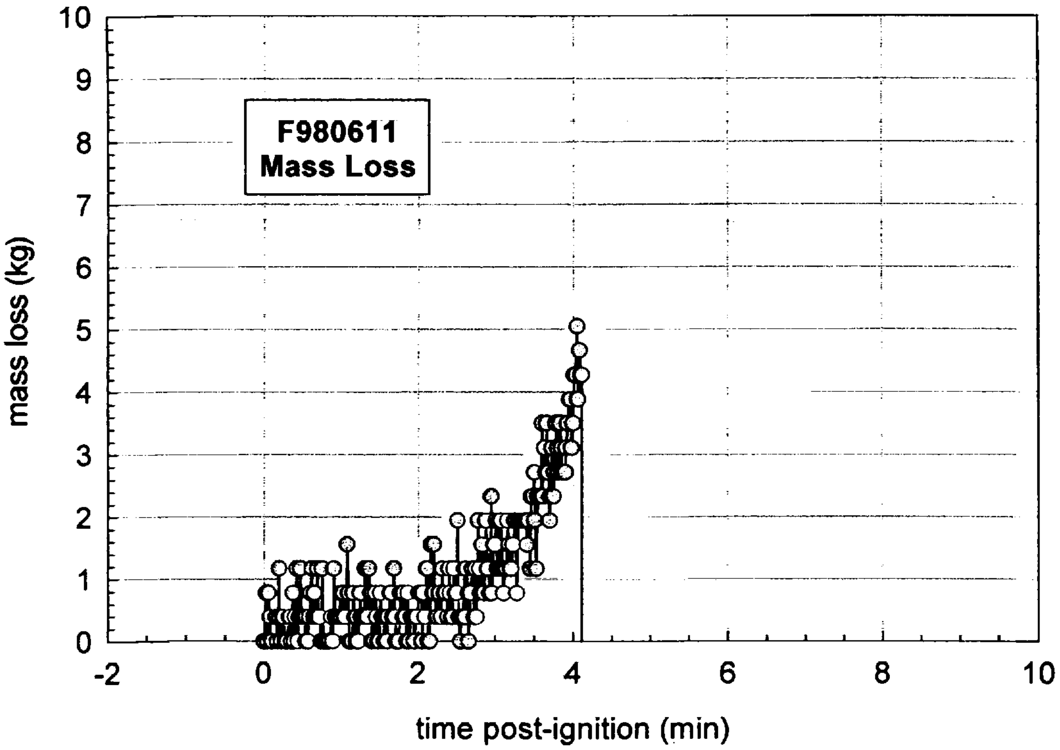

Plot H5. Fire Test F980611. Mass Loss from the test vehicle during the fire test. The mass data was not valid after 4 minutes post-ignition because test personnel stepped onto the fluid containment pan to extinguish the fire.

APPENDIX I
PASSENGER COMPARTMENT COMBUSTION GAS DATA FOURIER TRANSFORM INFRARED SPECTROSCOPY AND AN ELECTROCHEMICAL OXYGEN SENSOR

The sampling-line for FTIR analysis consisted of a stainless-steel tube (o.d. = 0.250 in. (6.4 mm), i.d. = 0.125 in. (3.2 mm), l = 20 ft (6.1 m)) inserted through the roof between the front seats along the longitudinal midline of the test vehicle (Fig.'s I1 and I2). The inlet of the sample-tube extended approximately 10 in. below the headlining. The tube was not heated. The outlet of the sample tube was connected to a heated Teflon® transfer-line (o.d. = 0.250 in. (6.4 mm), i.d. = 0.125 in. (3.2 mm), l = 75 ft. (23 m)), which was connected to the gas cell of the FTIR spectrometer. The transfer-line was heated to 105°C during the test to prevent condensation of water and water-soluble gases (*e.g.*, HCl, HCN, NO, and NO_2). An in-line stainless steel filter holder containing a quartz fiber filter (o.d. = 47 mm) was placed between the sample-tube and the transfer-line to prevent smoke particles from contaminating analytical instrumentation.

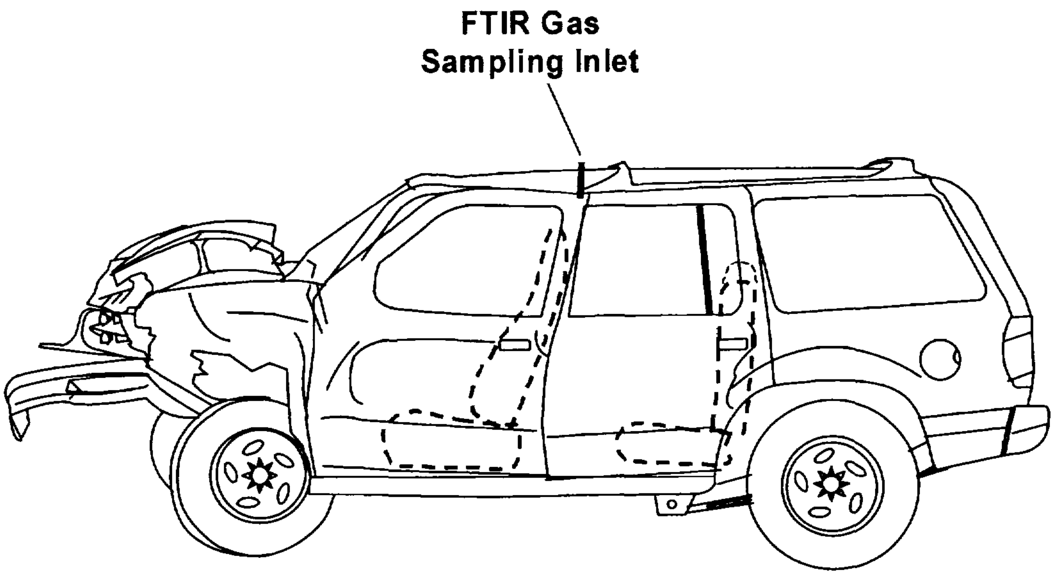

Figure I1. Fire Test F980611. Side-view of the test vehicle show the approximate location of the FTIR gas-sampling inlet in the passenger compartment.

The FTIR spectrometer was a Model I-1000 Series FTIR Spectrometer (MIDAC Corporation, Riverside, California), with a KBr beam-splitter; a liquid nitrogen-cooled Mercury-Cadmium-Telluride detector; and gold-surfaced aluminum optics. This instrument was fitted with a stainless steel, multiple-reflectance gas cell (path length = 10 m) with zinc selenide windows. The gas cell was heated to 105°C. The optical bench was filled with clean, dry argon and hermetically sealed. The usable spectral range of this instrument was approximately 7400-700 cm^{-1}. Pressure in the gas cell during the fire tests was measured with a Baratron pressure gauge (MKS Instruments, Burlington, MA). The spectrometer was operated at a spectral resolution of 0.5 cm^{-1}.

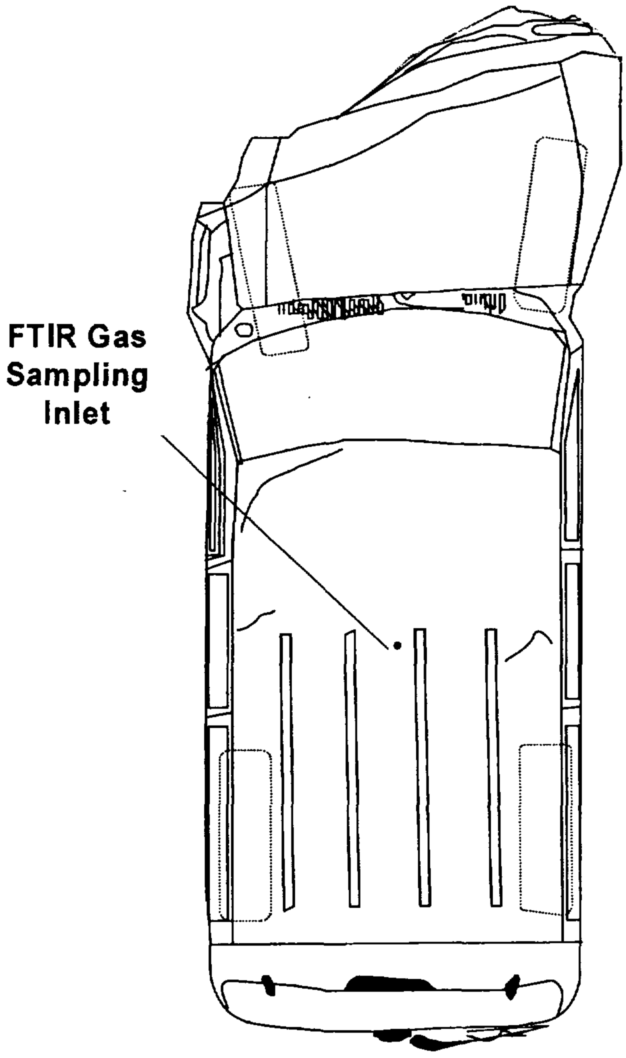

Figure I2. Fire Test F980611. Top view of the test vehicle showing the approximate location of the FTIR gas-sampling inlet in the passenger compartment.

The sampling line and gas cell were equilibrated to 105°C for at least 60 minutes before sample acquisition. A reference spectrum was acquired while the gas cell was evacuated. During the fire tests, the gas cell was purged continuously with air withdrawn from the passenger compartment at a flow rate of 7 L/min. Single-scan absorbance spectra were acquired and stored to disk at intervals of 10 s. After the test, the stored spectra were analyzed using the quantitative analysis software provided by the instrument manufacturer (AutoQuant, MIDAC). This software uses a Classical Least Squares algorithm to determine gas concentrations. The method developed for analysis of combustion gases was calibrated with gas standards (Scott Specialty Gases, Inc., Troy, MI). The standards were either NIST-traceable or produced by a gravimetric blending process.

An electrochemical oxygen sensor (Model SE-25, FIGARO USA, Inc.) was placed in the FTIR sampling line just before the FTIR gas cell. The signal from the oxygen sensor was recorded by the data acquisition system described in **APPENDIX C**. The oxygen sensor was calibrated before this test by recording its responses when purged with room air (21% O_2) and with pure nitrogen (0% O_2).

The gaseous combustion products measured by FTIR in the passenger compartment during this test included carbon dioxide, carbon monoxide, methane, ethylene, acetylene, hydrogen cyanide, nitric oxide, and hydrogen chloride (Plots H1 through H8). Except for carbon dioxide, which has a background concentration in air of approximately 0.05%, and hydrogen chloride, the concentrations of all of these gases were less than their respective lower limits of detection before ignition. The background concentration of carbon dioxide in air is approximately 0.04%. Noise in the Infrared spectra acquired before ignition resulted in an apparent hydrogen chloride concentration of < 1 ppm.

Carbon dioxide, carbon monoxide, methane, ethylene, and acetylene started to accumulate in the passenger compartment between 50 and 75 seconds post-ignition (Plots I1 through I5). The Infrared spectra acquired during this test also contained a broad absorbance band between 2800 and 3200 cm^{-1}, indicating the presence of a mixture of aliphatic hydrocarbons in the air samples from the passenger compartment. The intensity of this absorbance band generally followed the same time-course as that of methane (Plot I3), ethylene (Plot I4), and acetylene (Plot I5). This broad band appeared to contain absorbances from ethane, propane, and butane. However, all of the gaseous species contributing to this absorbance band could not be identified or accurately quantified.

Hydrogen cyanide (Plot I7) and nitric oxide (Plot I8) started to accumulate in the passenger compartment between 50 and 100 seconds post-ignition. Hydrogen chloride (HCl) was not detected during this test (Plot I6).

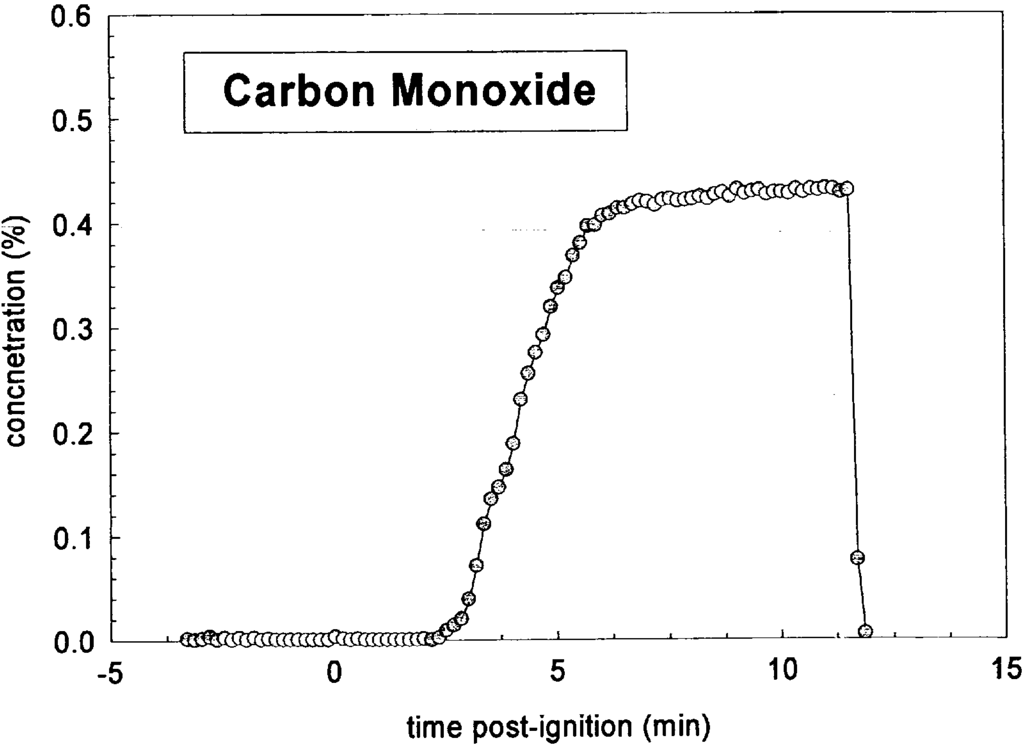

Plot I1. Fire Test F980611. Concentration of carbon monoxide (CO) in the passenger compartment measured by FTIR analysis.

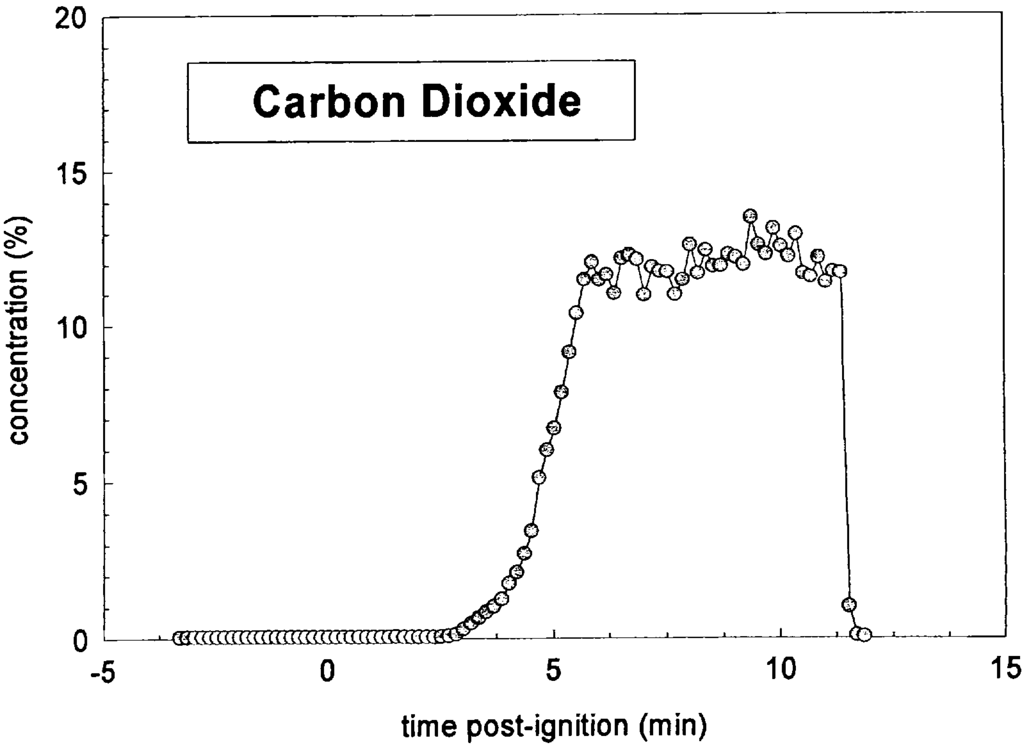

Plot I2. Fire Test F980611. Concentration of carbon dioxide (CO_2) in the passenger compartment measured by FTIR analysis.

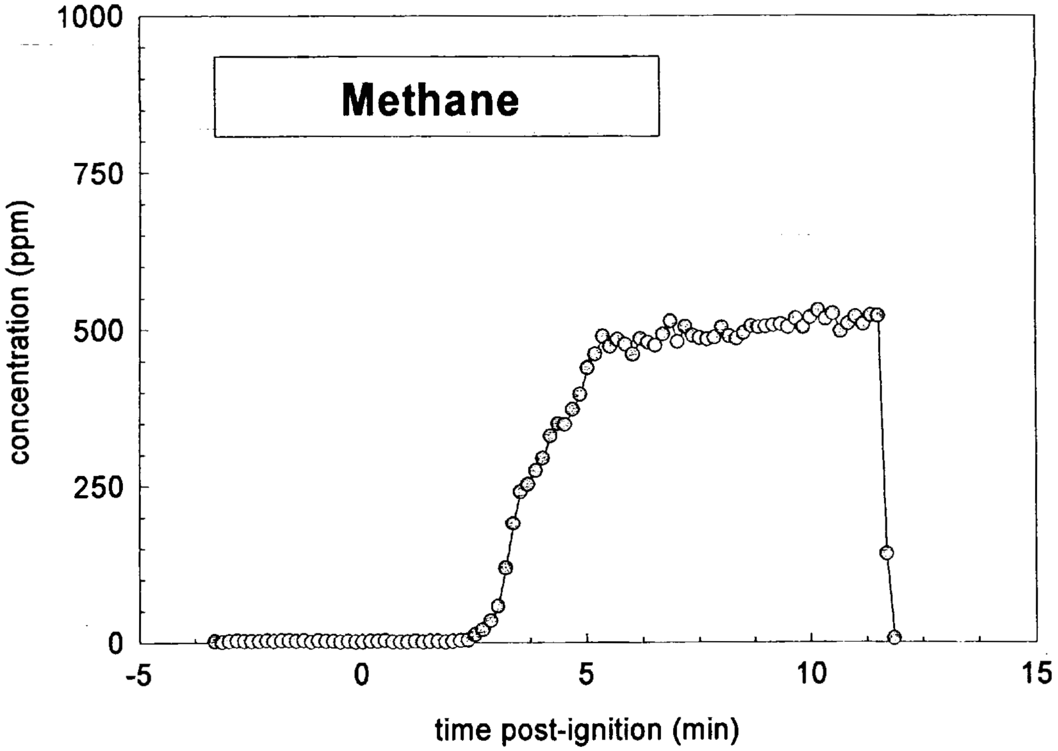

Plot I3. Fire Test F980611. Concentration of methane (CH_4) in the passenger compartment measured by FTIR analysis.

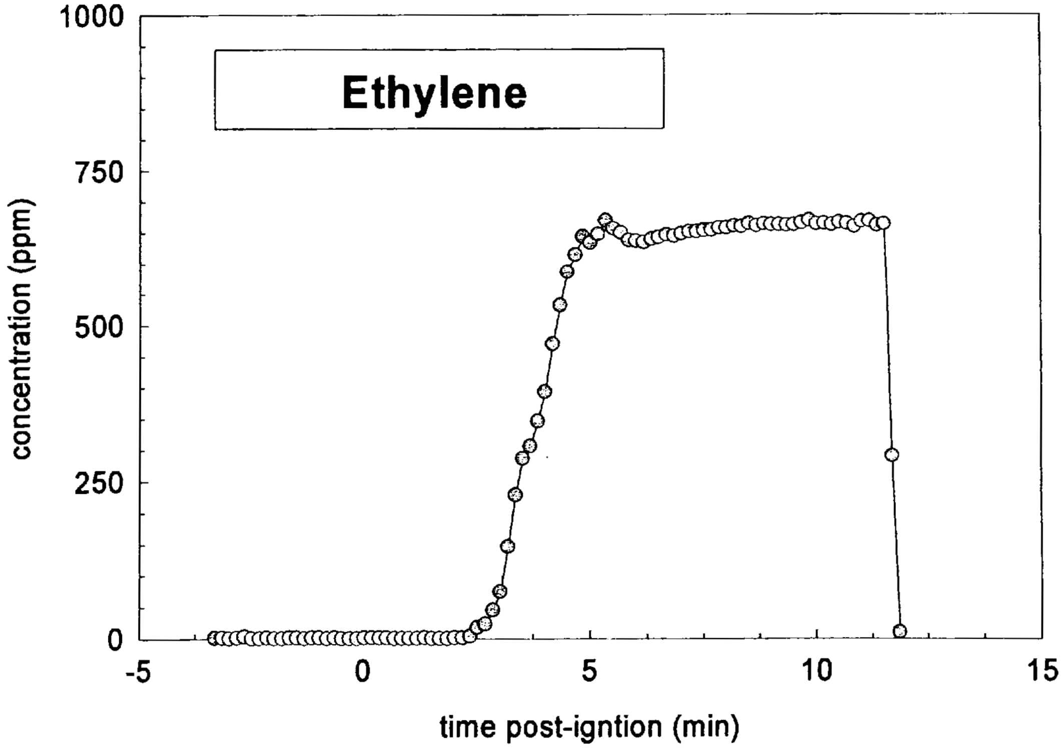

Plot I4. Fire Test F980611. Concentration of ethylene (C_2H_4) in the passenger compartment measured by FTIR analysis.

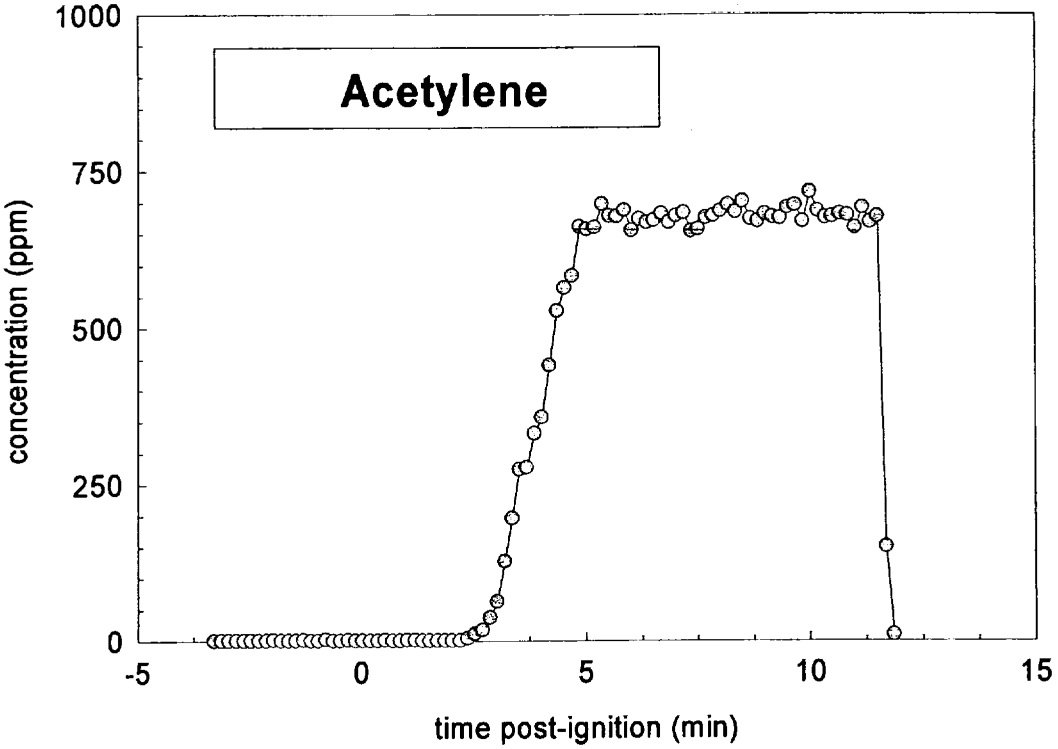

Plot I5. Fire Test F980611. Concentration of acetylene (C_2H_2) in the passenger compartment measured by FTIR analysis.

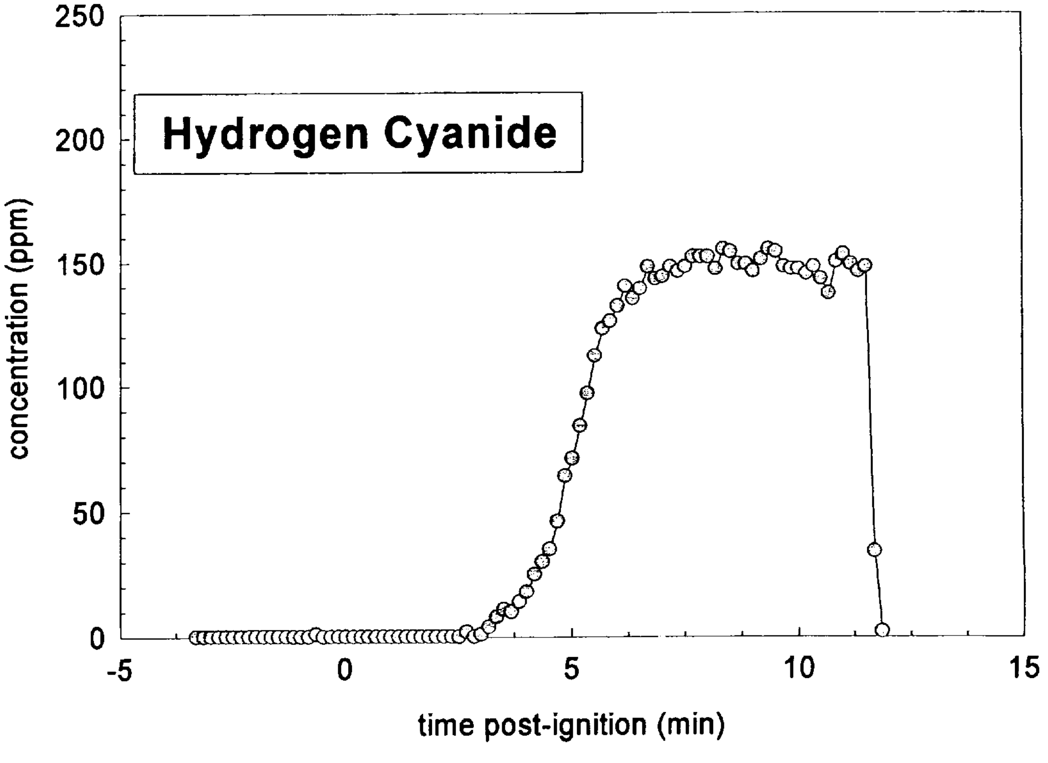

Plot I6. Fire Test F980611. Concentration of hydrogen cyanide (HCN) in the passenger compartment measured by FTIR analysis.

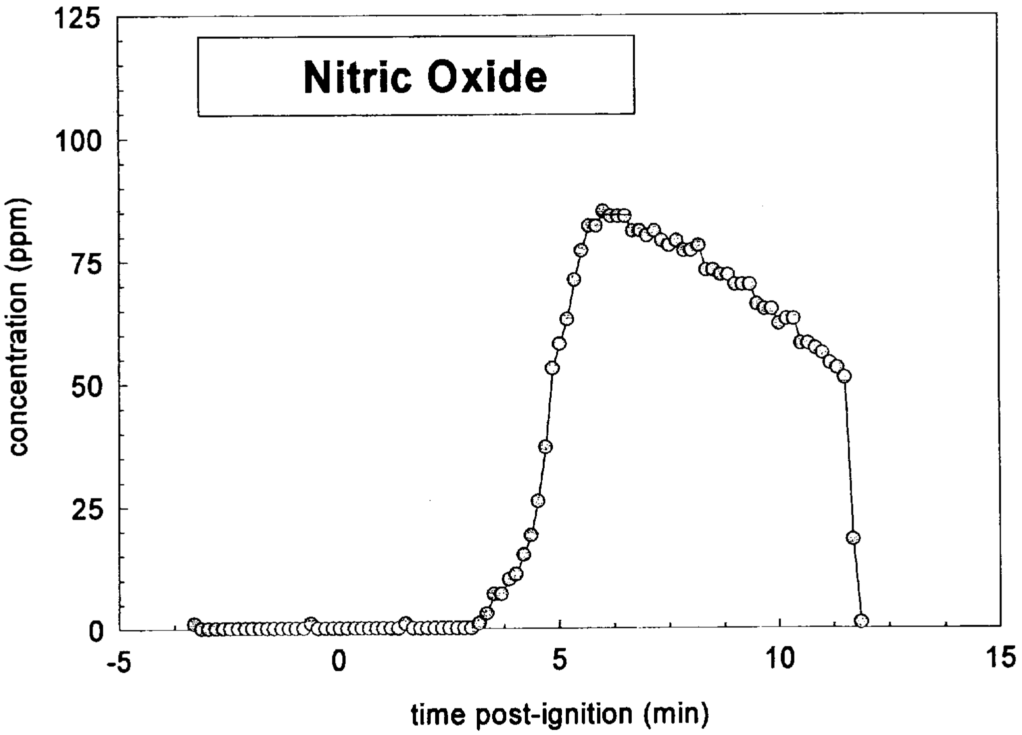

Plot I7. Fire Test F980611. Concentration of nitric oxide (NO) in the passenger compartment measured by FTIR analysis.

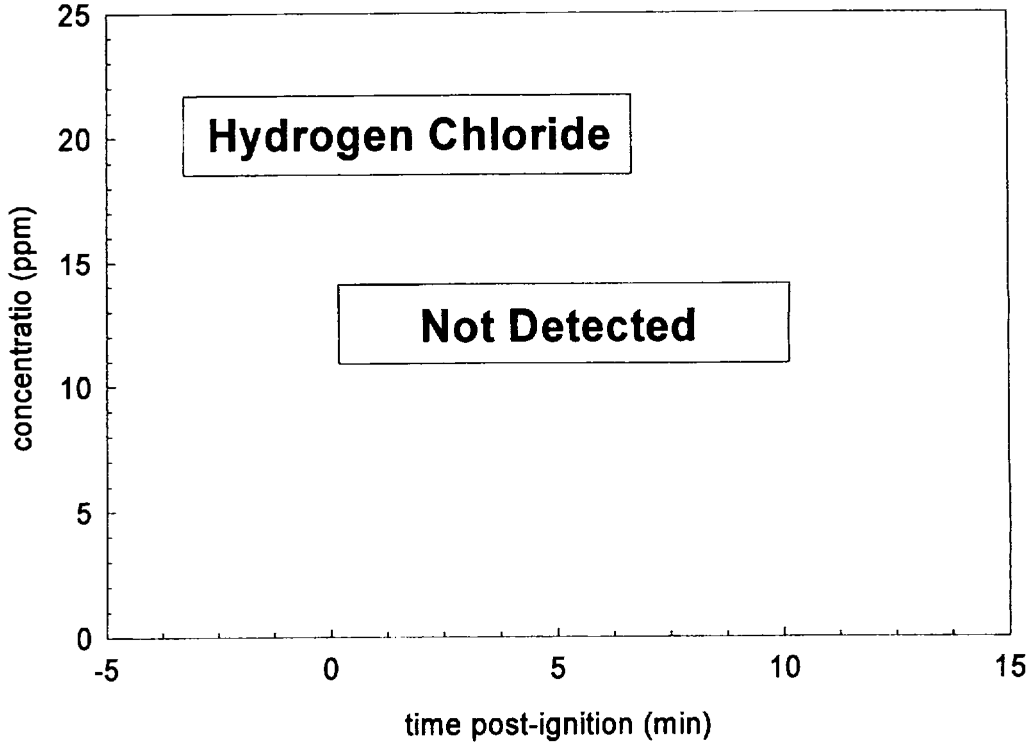

Plot I8. Fire Test F980611. Concentration of hydrogen chloride (HCl) in the passenger compartment measured by FTIR analysis.

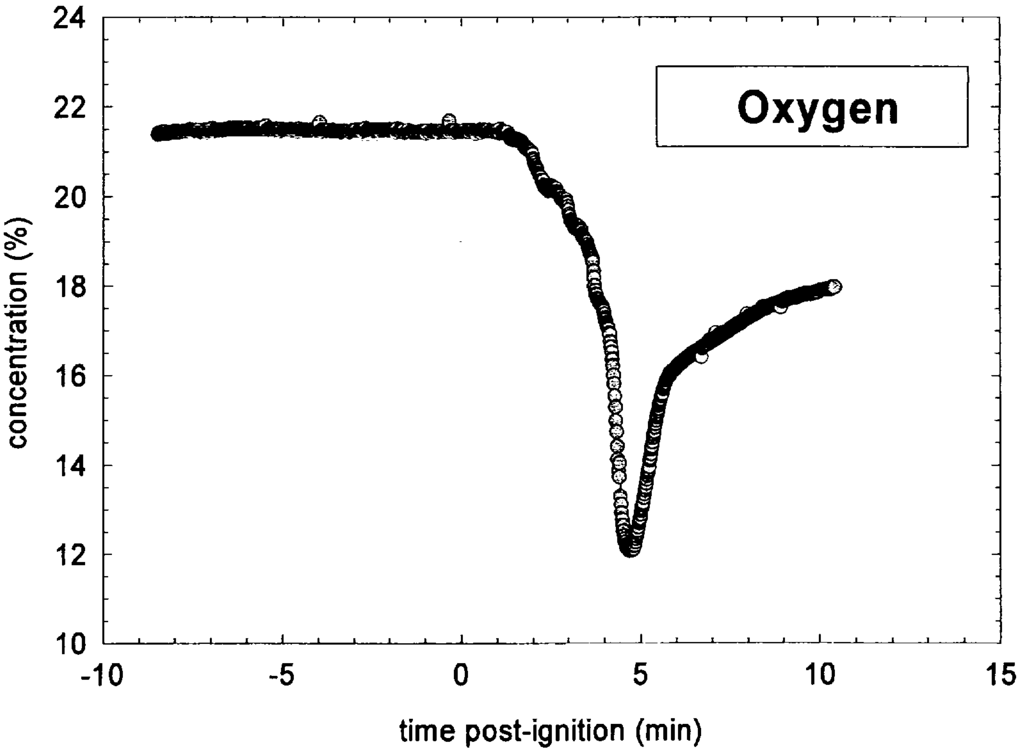

Plot I9. Fire Test F980611. Concentration of oxygen (O_2) in the passenger compartment measured by the electrochemical oxygen sensor.

APPENDIX J
PASSENGER COMPARTMENT COMBUSTION GAS DATA
GAS CHROMATOGRAPHY/MASS SPECTROSCOPY GAS ANALYSIS

The sampling-line for GC/MS samples consisted of a stainless-steel tube (o.d. = 0.250 in. (6.4 mm), i.d. = 0.125 in. (3.2 mm), l = 20 ft (6.1 m)) inserted through the roof between the front seats along the longitudinal midline of the test vehicle (Fig.'s J1 and J2). The inlet of the sample-tube extended approximately 10 in. below the headlining. The outlet of the sample tube was connected to sampling manifold by a length of stainless steel sampling tube (o.d. = ¼ in., length = 25 ft.). The sampling manifold contained five sample cartridges in parallel. Airflow was directed sequentially through the sample cartridges a solenoid-actuated gas-switching manifold. The airflow rate through the cartridges during sampling was adjusted 250 cm^3/min with a rotometer. None of the components of the GC/MS sampling line were heated.

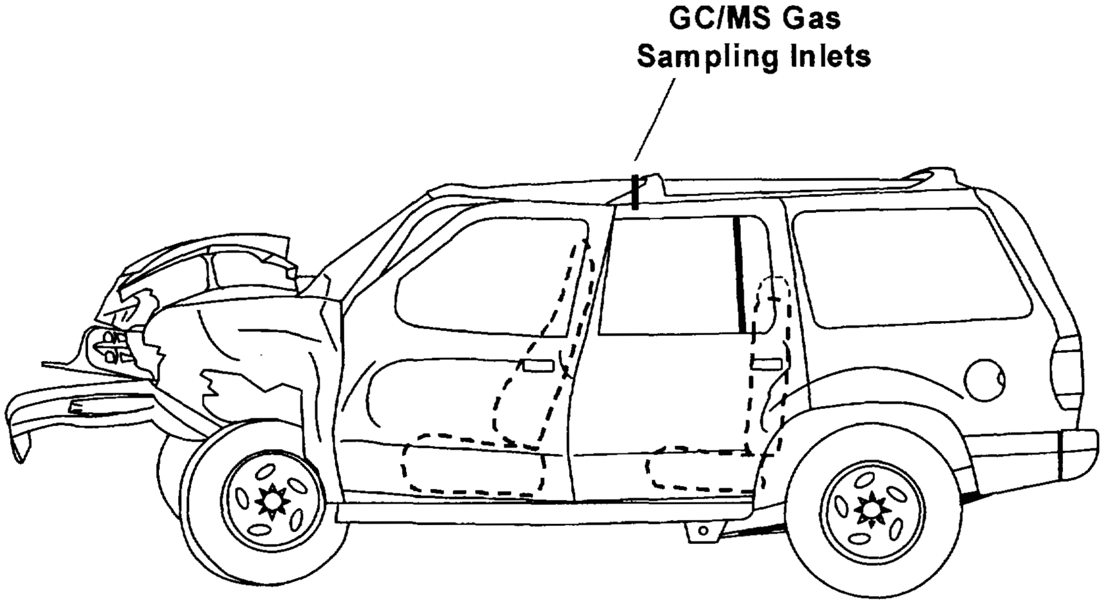

Figure J1. Fire Test F980611. Side-view of the test vehicle show the approximate locations of the GC/MS gas sampling inlets in the passenger compartment.

Each cartridge was a glass-lined stainless steel tube (i.d. = 4 mm; length = 10 cm; Scientific Instrument Services, Inc, Ringoes, NJ) packed with 25 mg of Carbotrap™ C Graphitized Carbon Black (Supelco, Inc.; Bellefonte, PA) in series with 15 mg of Carbotrap™ Graphitized Carbon Black (Supelco).

After the test, the sample cartridges were analyzed by thermal desorption/gas chromatography/mass spectrometry. Deuterated standards dissolved in deuterated methanol were added to each sorbent cartridge to monitor sample recovery. A modified purge-and-trap concentrator was used for thermal desorption (Model 600 Purge-and-Trap Concentrator, CDS Analytical, Oxford, PA). The gas chromatograph was a Model 5890 Series II Plus Gas Chromatograph (Hewlet Packard, Palo Alto, CA). The mass spectrometer was a Hewlet Packard

Model 5989B Mass Spectrometer (Hewlett Packard). The thermal desorption unit was interfaced directly to the split/splitless injector of the gas chromatograph through a cryo-focusing unit. The injector was operated in the split mode with a split of approximately 10 mL/min. The chromatographic column was a fused silica capillary column coated with 100% methyl silicone (HP-1 ; length = 30 m; i.d. = 0.25 mm; film thickness = 0.25 μm).

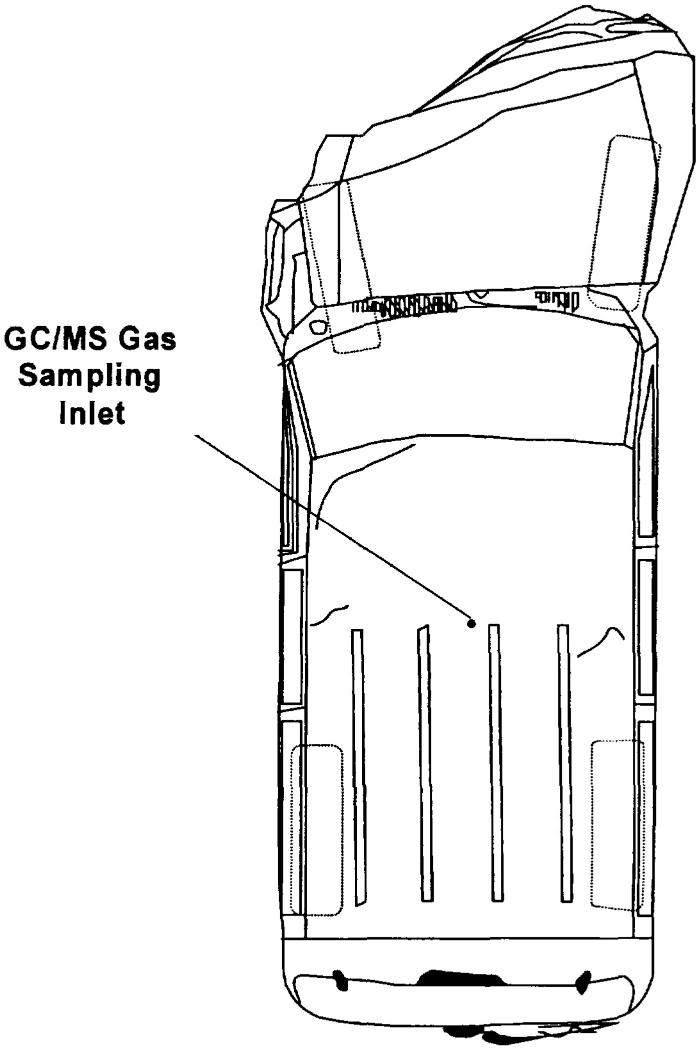

Figure J2. Fire Test F980611. Top view of the test vehicle showing the approximate locations of the GC/MS gas sampling inlet in the passenger compartment.

The sample was desorbed at 320°C for 10 min, and cryofocused onto the head of the chromatographic column -80°C. The temperature of the analytical column was maintained at 0°C while the sample was desorbed and cryo-focused. To start the chromatographic analysis, the cryo-focusing unit was heated bullistically to a temperature of 320°C. The column temperature was programmed from 0 to 325°C at a rate of 5°C/min. Mass spectra were obtained by scanning from m/z 40 to 600 at a rate of 1.2 scan/s.

Plots J1 through J7 show the mass chromatograms of the blank and samples acquired during this test. The sampling intervals in the figure captions were corrected for the time-delay for airflow through the sample-line, which was estimated to have been approximately 25 seconds.

Table J1 lists 41 components tentatively identified from analysis of the mass chromatograms of these samples and shows the abundance of each compound listed relative to the average of the deuterated n-alkanes added as internal standards. The components are listed in order of chromatographic retention time. Identifications were based on the results of a spectral search a commercial mass spectral library (Wiley 275K Mass Spectral Library).

Samples 3, 4, and 5 contained complex mixtures of aliphatic and aromatic hydrocarbons from gasoline vapor. Aromatic compounds such as indene, 1-methyl-1H-indene, naphthalene, 2-methylnaphthalene, and 3-methylnaphthalene in these samples were produced by incomplete combustion of the gasoline pumped below the test vehicle and other materials burning during this test. The presence of 2,4-dimethyl-1-heptene in these samples indicates that materials containing the polymer poly(propylene) were undergoing thermal decomposition when these samples were acquired.

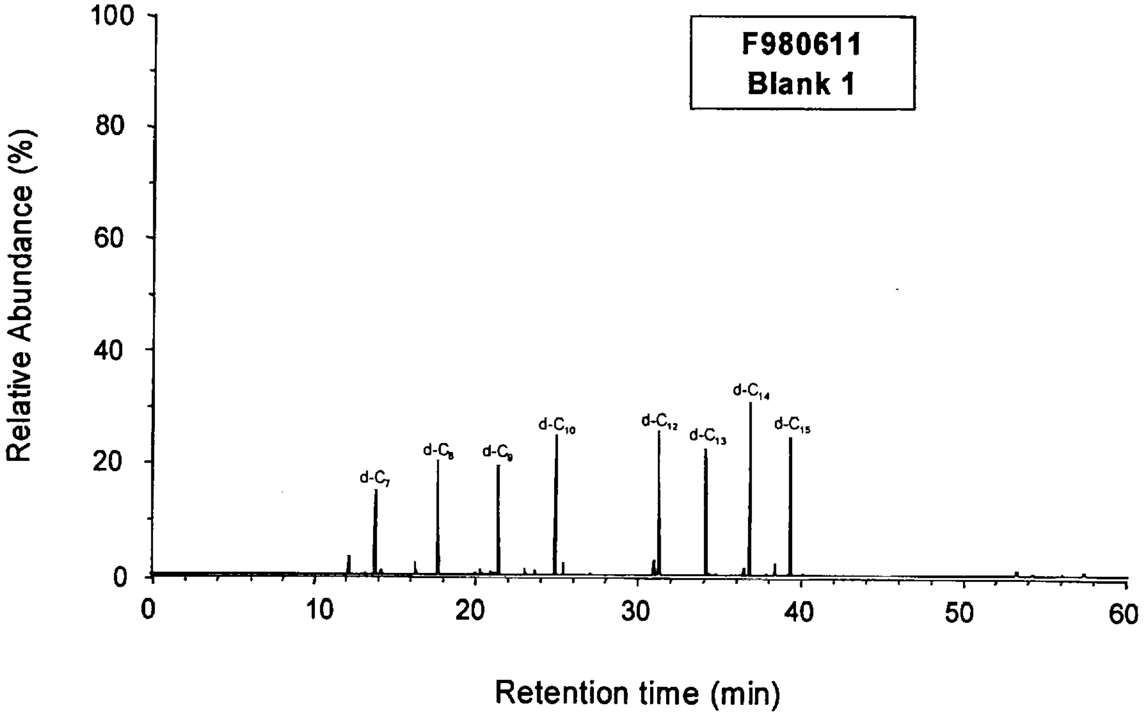

Plot J1. Fire Test F980611. Mass chromatogram from GC/MS analysis of Blank 1 acquired before the test.

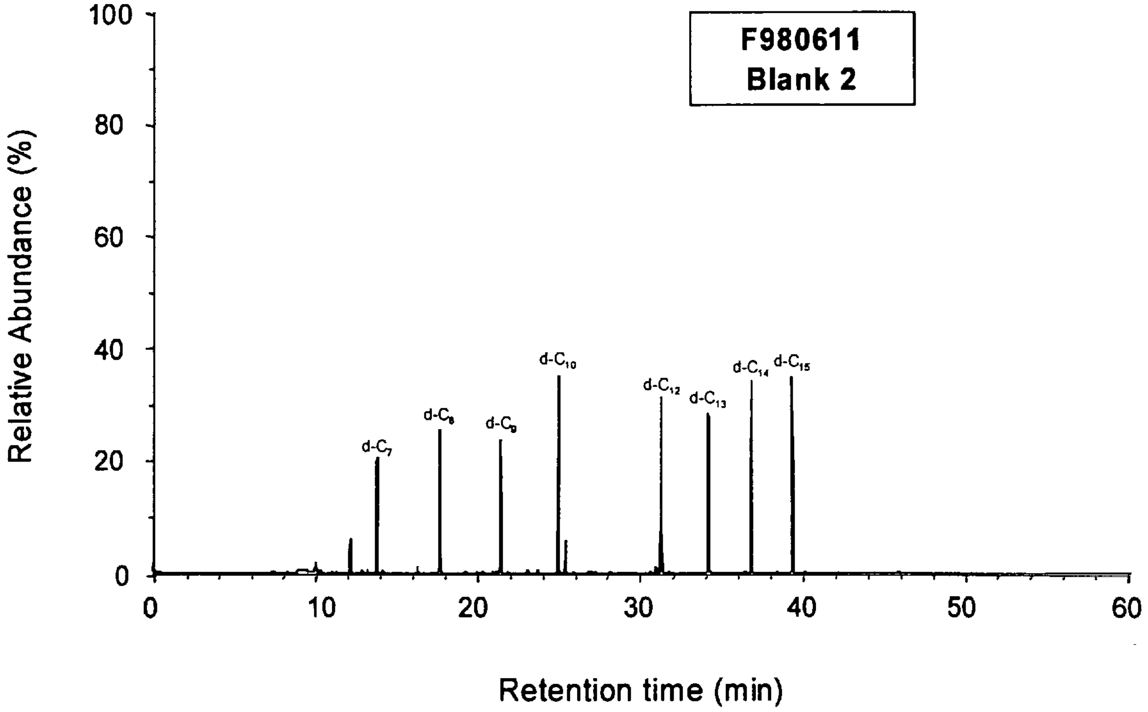

Plot J2. Fire Test F980611. Mass chromatogram from GC/MS analysis of Blank 2 acquired before the test.

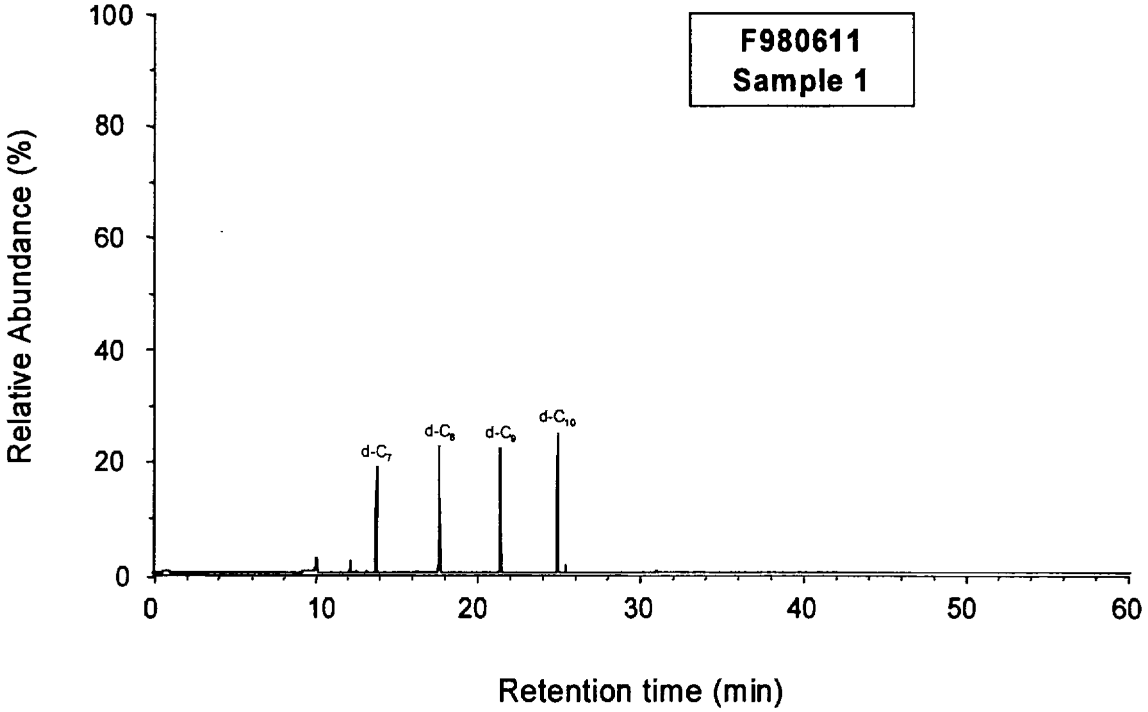

Plot J3. Fire Test F980611. Mass Chromatogram of Sample 1 acquired from -30 to +00 seconds post-ignition.

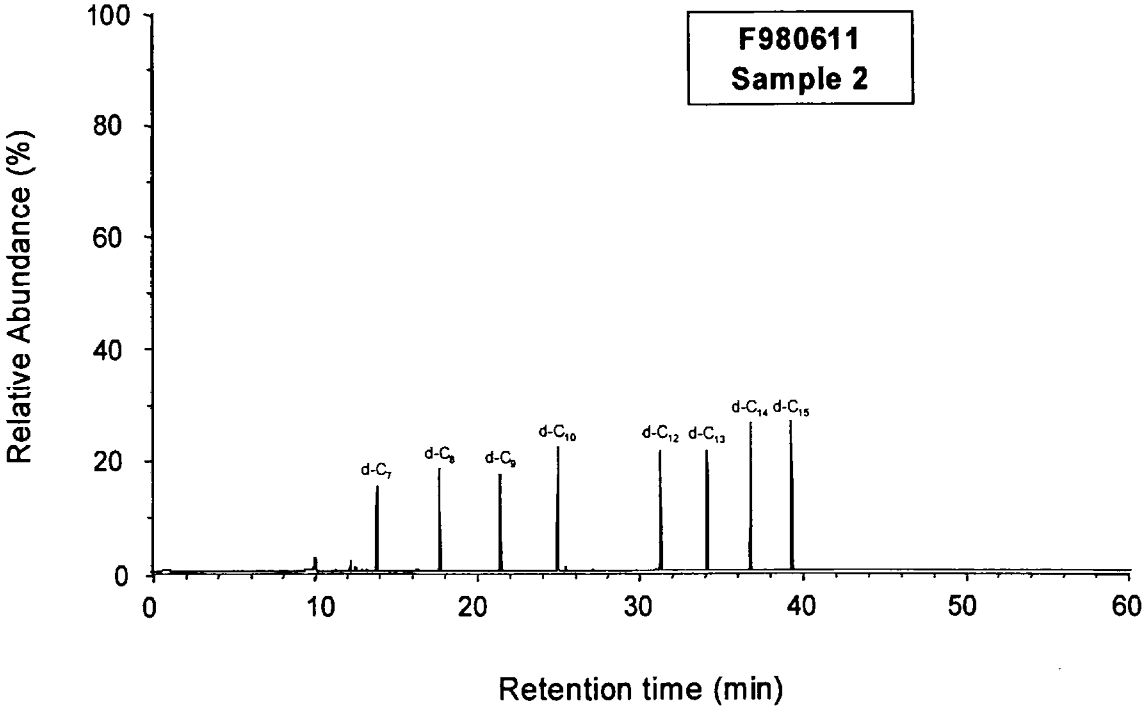

Plot J4. Fire Test F980611. Mass Chromatogram of Sample 2 acquired from +00 to +60 seconds post-ignition.

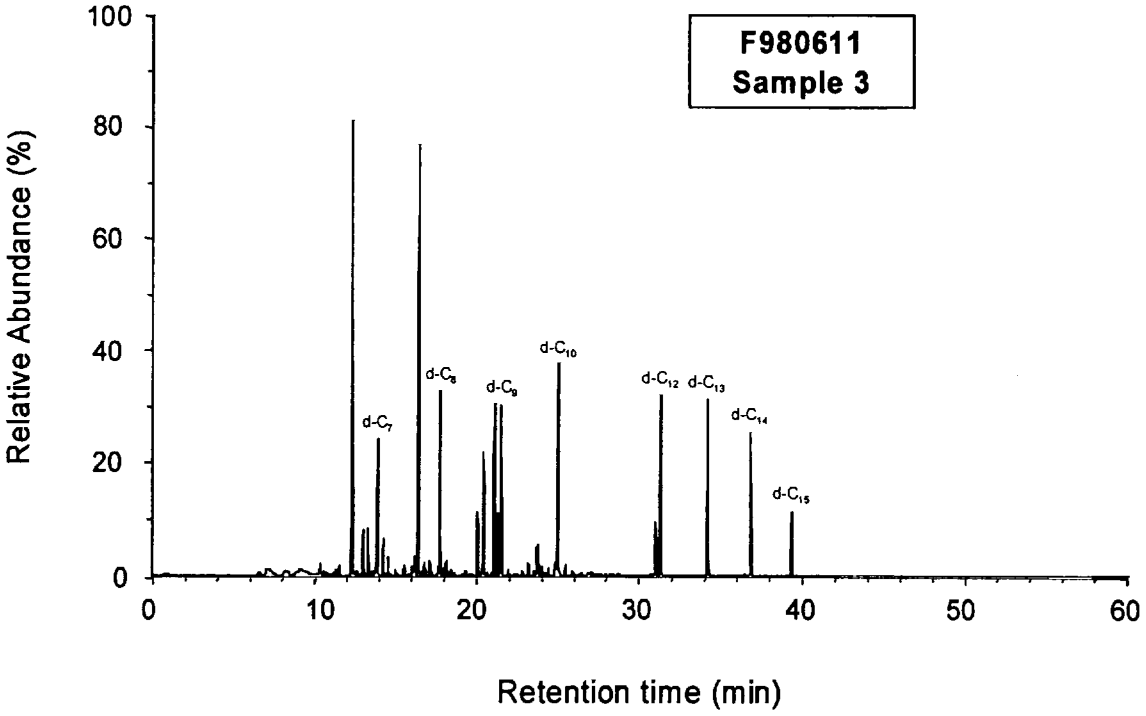

Plot J5. Fire Test F980611. Mass Chromatogram of Sample 3 acquired from +60 to +120 seconds post-ignition.

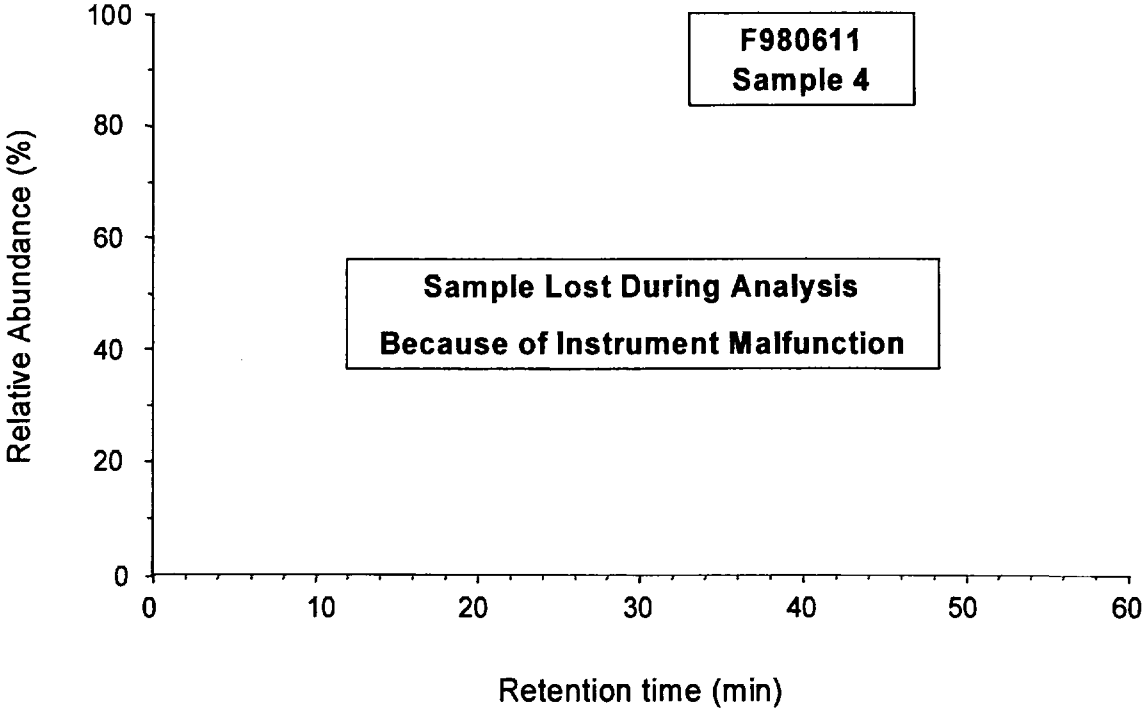

Plot J6. Fire Test F980611. Mass Chromatogram of Sample 4 acquired from +120 to +165 seconds post-ignition.

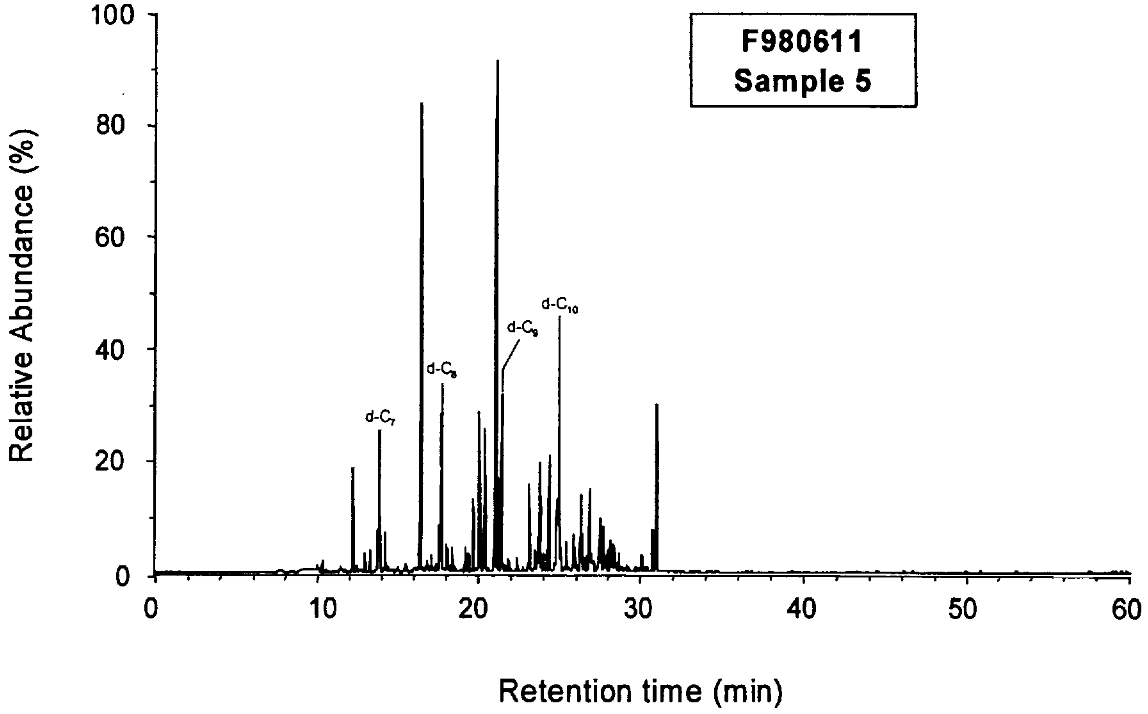

Plot J7. Fire Test F980611. Mass Chromatogram of Sample 5 acquired from +165 to +210 seconds post-ignition.

Table J1
GC/MS Peak Identification

t_R	Compound	CAS	Relative Abundance[1]						
			Blank 1	Blank 2	Sample 1	Sample 2	Sample 3	Sample 4	Sample 5
12.31	benzene	000071-43-2	0.14	0.17	0.09	0.09	3.55	n/a	0.41
13.01	2-methylhexane	000591-76-4	0.00	0.00	0.00	0.00	0.27	n/a	0.10
13.34	3-methylhexane	000589-34-4	0.00	0.00	0.00	0.00	0.22	n/a	0.07
13.84	1-heptene	000592-76-7	0.00	0.00	0.00	0.00	0.00	n/a	0.18
13.92	d_{16}-n-heptane (d-C_7)	33838-52-7	0.62	0.65	0.78	0.66	0.92	n/a	0.56
14.29	n-heptane	000142-82-5	0.00	0.00	0.00	0.00	0.19	n/a	0.13
16.47	methylbenzene	002037-26-5	0.09	0.00	0.00	0.00	3.09	n/a	2.65
17.04	2-methylheptane	000592-27-8	0.00	0.00	0.00	0.00	0.05	n/a	0.08
17.44	3-methylheptane	000589-81-1	0.00	0.00	0.00	0.00	0.08	n/a	0.18
17.79	d_{18}-n-octane (d-C_8)	017252-77-6	0.79	0.78	0.93	0.77	1.05	n/a	0.84
18.20	n-octane	000111-65-9	0.00	0.00	0.00	0.00	0.07	n/a	0.08
19.78	2,4-dimethyl-1-heptene	019549-87-2	0.00	0.00	0.00	0.00	0.00	n/a	0.25
20.11	ethylbenzene	000100-41-1	0.00	0.00	0.00	0.00	0.35	n/a	0.66
20.45	1,4-dimethylbenzene 1,3-diemthylbenzene	000106-42-3 000108-38-3	0.00	0.00	0.00	0.00	1.08	n/a	0.98
21.11	ethynylbenzene	000536-74-3	0.00	0.00	0.00	0.00	0.99	n/a	0.00
21.23	1,2-diemthylbenzene	000095-47-6	0.00	0.00	0.00	0.00	0.32	n/a	3.43

Table J1, continued
GC/MS Peak Identification

t_R	Compound	CAS	Relative Abundance[1]						
			Blank 1	Blank 2	Sample 1	Sample 2	Sample 3	Sample 4	Sample 5
21.52	d20 -n-nonane (d-C9)	121578-11-8	0.89	0.90	1.07	0.86	1.13	n/a	0.98
21.96	n-nonane	000111-84-2	0.00	0.00	0.00	0.00	0.00	n/a	0.05
22.48	1-methylethylbenzene	000098-82-8	0.00	0.00	0.00	0.00	0.00	n/a	0.05
23.20	benzaldehyde	000100-52-7	0.00	0.00	0.00	0.00	0.00	n/a	0.45
23.54	propylbenzene	000103-65-1	0.00	0.00	0.00	0.00	0.00	n/a	0.09
23.72	2,2-dimethyl-3-methylene-bicyclo[2.2.1]heptane	000079-92-5	0.00	0.00	0.00	0.00	0.18	n/a	0.17
23.80	1-methyl-2-ethylbenzene	000611-14-3	0.00	0.00	0.00	0.00	0.12	n/a	0.00
23.84	isocyanobenzene	000931-54-4	0.00	0.00	0.00	0.00	0.00	n/a	0.75
24.08	1-methyl-4-ethylbenzene	000622-96-8	0.00	0.00	0.00	0.00	0.00	n/a	0.07
24.42	1-methylethenylbenzene	000098-83-9	0.00	0.00	0.00	0.00	0.00	n/a	0.49
25.02	d22-n-decane (d-C10)	016416-29-8	1.16	1.05	1.22	1.00	1.49	n/a	1.62
27.32	n-decane	000124-18-5	0.00	0.11	0.00	0.00	0.30	n/a	0.12
26.53	indene	000095-13-6	0.00	0.00	0.00	0.00	0.00	n/a	0.004
30.15	azulene	000275-51-4	0.00	0.00	0.00	0.00	0.00	n/a	0.08
31.02	naphthalene	000091-20-3	0.12	0.00	0.00	0.00	0.00	n/a	0.80
31.32	d26-n-dodecane (d-C12)	121578-12-9	1.17	1.13	0.00	1.09	1.18	n/a	0.00

Table J1, continued
GC/MS Peak Identification

t_R	Compound	CAS	Relative Abundance[1]						
			Blank 1	Blank 2	Sample 1	Sample 2	Sample 3	Sample 4	Sample 5
34.16	d28-n-tridecane (d-C13)	121578-12-9	1.11	1.14	0.00	1.15	1.11	n/a	0.00
36.83	d30-n-tetradecane (d-C14)		1.22	1.18	0.00	1.24	0.81	n/a	0.00
38.40	acenaphthalene	000208-96-8	0.11	0.00	0.00	0.00	0.00	n/a	0.00
39.33	d32-n-pentadecane (d-C15)	036340-20-2	1.03	1.17	0.00	1.22	0.31	n/a	0.00

[1] The abundance values shown in this table are the ratio of the peak area of the compound of interest to the average peak area of the deuterated n-alkanes (internal standards) in each sample.

APPENDIX K
PASSENGER COMPARTMENT
AIRBORNE PARTICULATE ANALYSIS

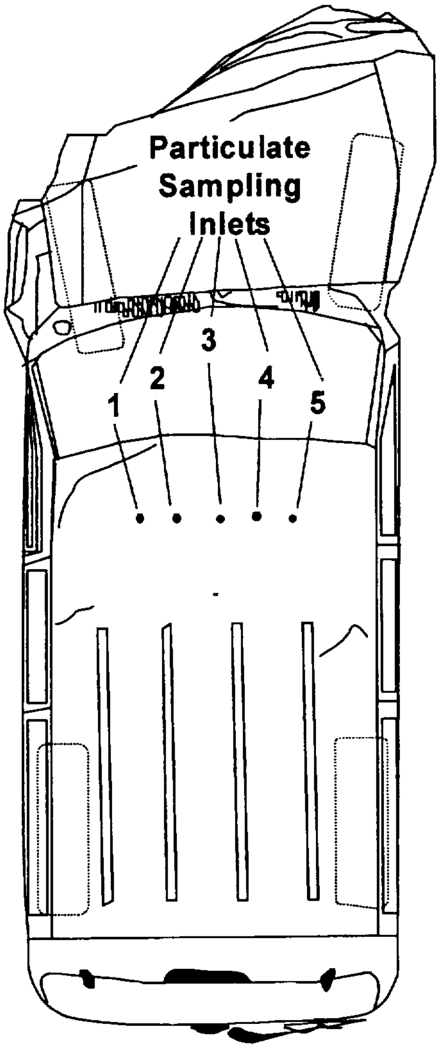

Figure K2. Fire Test F9806011. Top-view of the test vehicle showing the approximate locations of the particulate sampling inlets in the passenger compartment.

After the test, the filters placed in a dissector cabinet overnight to remove water absorbed by the filter media and particulate. The weight of each filter was recorded only after constant weight was achieved. The average concentrations of airborne particulate during each sample interval were determined from the mass of particulate collected, the volume flow rate, and the elapsed time.

A quarter was cut from each filter, weighted, and extracted for quantitative ion chromatographic analysis. The extracting solution was the mobile phase buffer. The chromatography column was an IC-Pak A HC column (Waters, Milford, MA). The mobile phase was a sodium borate/gluconate buffer at a flow rate of 1.8 mL/min [K1]. The chromatographic system consisted of a Model 616 Pump, a Model 717 Autosampler, and a Model 431 Conductivity Detector (Waters). The following anions were measured in the ion chromatographic analysis: fluoride (F^-), bicarbonate (HCO_3^-), chloride (Cl^-), nitrite (NO_2^-), bromide (Br^-), hypochlorite ($HClO_3^-$), nitrate (NO_3^-), phosphate (HPO_4^-), sulfate (SO_4^-), and oxalate ($C_2O_4^-$).

Table JI shows the concentration of airborne particulate in the passenger compartment during this test.

Table K1
Average Airborne Particulate Concentration

Sample	Sampling Interval (sec.)	Sampling Time (sec.)	Airborne Concentration (mg/m^3)
Blank	n/a	600	0
Sample 1	0 to 30	30	22
Sample 2	30 to 84	54	31
Sample 3	84 to 174	90	337
Sample 4	174 to 264	90	1354
Sample 5	264 to 294	30	915

Table K2 shows the results of the average anion concentration in the airborne particulate. The results shown in Table K2 were corrected for bicarbonate, nitrate, phosphate, sulfate, and oxalate detected in the blanks. All samples contained chloride. Sample 4 contained fluoride. Samples 2, 3,4, and 5 contained phosphate and sulfate.

Table K2

Average Anion Concentration in the Airborne Particulate

Sample	Anion Concentration in Airborne Particulate (µg/mg)[1]									
	F^-	HCO_3^-	Cl^-	NO_2^-	Br^-	$HClO_3^-$	NO_3^-	HPO_4^-	SO_4^-	$C_2O_4^-$
Sample 1	n/d[1]	n/d	n/d	n/d	n/d	n/d	n/d	n/d	n/d	n/d
Sample 2	n/d	n/d	53	n/d	n/d	n/d	n/d	42	n/d	n/d
Sample 3	n/d	n/d	92	n/d	5.1	n/d	n/d	3	n/d	n/d
Sample 4	n/d	n/d	86	n/d	3.8	n/d	n/d	0.1	3	n/d
Sample 5	n/d	n/d	187	n/d	10.4	n/d	n/d	10	n/d	n/d

[1] n/d = not detected

REFERENCES FOR APPENDIX K

K1. Method A-102, Waters Innovative Methods for Ion Analysis, Manual Number 22340, Waters Corporation, Milford, MA.